Numerical Evaluation of Forces on Piled Bridge Foundations in Laterally Spreading Soil

Christopher R. McGann

A dissertation
submitted in partial fulfillment of the
requirements for the degree of

Doctor of Philosophy

University of Washington

2013

Reading Committee:

Pedro Arduino, Chair

Peter Mackenzie-Helnwein, Chair

Steven L. Kramer

Program Authorized to Offer Degree:
Department of Civil and Environmental Engineering

University of Washington

Abstract

Numerical Evaluation of Forces on Piled Bridge Foundations in Laterally Spreading Soil

Christopher R. McGann

Co-Chairs of the Supervisory Committee:
Professor Pedro Arduino
Civil and Environmental Engineering

Research Associate Professor Peter Mackenzie-Helnwein
Civil and Environmental Engineering

The response of piled bridge foundations to liquefaction-induced lateral soil deformation is an important design consideration in seismically active regions. Recent research and case history data suggest that three-dimensional deformation of the approach embankment can significantly influence the loads placed on the embedded foundations during a flow failure or lateral spreading event. For example, the 2010 Maule earthquake in Chile caused widespread lateral spreading in the soil surrounding the Mataquito river bridge, however, only insignificant structural damage was observed in the bridge itself. The discrepancy between the amount of soil deformation and structural damage suggests that design procedures for this load case that do not make adequate consideration for 3D soil deformation mechanisms may lead to overly conservative and expensive design solutions.

Finite element models of the Mataquito river bridge are created using the OpenSees computational framework to investigate the reduction in foundation loads during lateral spreading implied by the minimal structural damage at the site. These models include beam on nonlinear Winkler foundation models, dynamic effective stress models of the bridge-foundation-soil system in plane strain, and 3D models of the southern bridge abutment, approach embankment, and surrounding soil. This numerical work focuses on the development of efficient element formulations and appropriate mesh configurations to minimize computational effort, and seeks to frame the load reduction mechanisms in the context of a simplified analysis procedure for the lateral spreading load case.

The results of the numerical models for the Mataquito bridge, along with a parameter study conducted using a second set of 3D finite element models, indicate that consideration for the 3D geometry of the bridge site results in tangible reductions in foundation bending demands and abutment displacements compared to those returned by a plane strain description of the problem. This reduction increases as the depth of the liquefiable layer and the effective width of the approach embankment are decreased. An approach is proposed to estimate the reductions in abutment displacement and associated foundation bending demands for a given site geometry, and an existing simplified analysis procedure is modified to better consider the findings of this work.

TABLE OF CONTENTS

LIST OF FIGURES

LIST OF TABLES

Chapter 1

BACKGROUND AND INTRODUCTION

Seismic design of bridge foundations is a significant aspect to the general design process for bridges in certain parts of the world. For river-spanning bridges, a critical part of the seismic design effort is an assessment of the effects of liquefaction-induced flow failure or lateral spreading on the bridge foundations. Current design procedures for this load case generally prescribe simplified analytical methods based on a two-dimensional description of the site geometry. The assumption of plane strain for this type of analysis is a practical approach that will typically lead to conservative foundation designs. Due to the uncertainty involved in the lateral spreading problem, such conservatism is generally desired, however, for the case of an approach embankment built with finite lateral extents, it is hypothesized that the use of design procedures based on plane strain assumptions may result in overly conservative and expensive design solutions.

Numerous bridges affected by lateral spreading during past earthquakes have displayed three-dimensional soil deformation effects that cannot be captured in a two-dimensional analysis. In many of these cases, it is apparent that the bridge and its foundations have altered the near-field deformation pattern of the laterally spreading soil, and it is likely that the resistance provided by the bridge leads to reductions in foundation demands as compared to those predicted under the assumption of plane strain. The pile pinning analysis procedure (Martin et al., 2002; Ashford et al., 2011), is a simplified approach that has been developed to account for the lateral resistance provided by bridge foundations during lateral spreading, however, this approach does not offer a way to directly evaluate when significant resistance can be expected and when it cannot. The development of such a predictive method represents a highly advantageous supplement to this existing analysis approach.

The objective of this research is to identify and quantify the mechanisms implied by the case history record that may result in potential reductions in the bridge foundation demands developed during lateral spreading through consideration for the three-dimensional geometry of the bridge site. This work involves a review of relevant case histories and recent work, with a focus on numerical modeling strategies, and the development of numerical models that capture the kinematic loading conditions and 3D effects of the problem. The results obtained from the numerical modeling effort are used to evaluate and inform the existing pile pinning analysis approach, and a proposed procedure to assess the expected amount of lateral pinning resistance for a given combination of bridge foundation, soil profile, and approach embankment is presented.

1.1 Representative Case Histories

During liquefaction-induced lateral spreading, a bridge approach embankment, and any native crustal soil above the liquefied zone, will tend to deform towards the river, imposing lateral loads on the bridge foundations in their path. In some cases, due to the combination of the lateral stiffness of the foundation and the limited transverse extents of the embankment there is a tendency for the embankment soil to slump down and flow around the bridge foundation instead of flowing directly into it. This type of 3D embankment deformation has been documented during reconnaissance efforts following multiple earthquakes for which liquefaction-induced lateral spreading was observed along river banks. Several typical cases are discussed in the following sections to provide context and motivation for this research.

1.1.1 Bandai Bridge, 1964 Niigata Earthquake

The Bandai Bridge, finished in 1929, is located in the central part of Niigata City, Japan, spanning the Shinano River. Liquefaction-induced lateral spreading during the M7.5 June 16, 1964 Niigata earthquake caused dramatic bank convergence in the area of the bridge. The Bandai Bridge is an arched reinforced concrete bridge with abutments founded on piles and piers founded on pneumatic caissons (Katayama et al., 1966). The bridge was damaged during the lateral spreading of the river bank, however, the damage was not catastrophic. The abutments settled and rotated with attendant cracking, and the piers settled unevenly. Regardless of the damage sustained, evidence of three-dimensional embankment deformation and foundation pinning effects was observed at this site.

Aerial photographs taken before and after the earthquake were used to measure permanent ground displacements (Hamada and O'Rourke, 1992). These photographs visually demonstrate the restraining effect of the piled bridge abutments on the lateral flow of soil. The ground displacement vectors determined from the photogrammetric analyses, Figure 1.1, support the visual evidence, indicating that river bank displacements near the bridge foundations are lesser than those further away, and that displacements behind the abutments have components parallel to the river bank. The presence of longitudinal cracking near the southern abutment also suggests that the embankment soils spread parallel to the river bank in this area. Further evidence of three-dimensional effects in the embankment deformation is given by Katayama et al. (1966), who report the settlement and swelling-out of the road surface in the vicinity of each abutment.

1.1.2 Landing Road Bridge, 1987 Edgecumbe Earthquake

The Landing Road Bridge, constructed in 1962, spans the Whakatane River in the Bay of Plenty Region of New Zealand. The abutments of the Landing Road Bridge are supported by groups of eight raked piles, and the northern-most spans extend over a wide floodplain

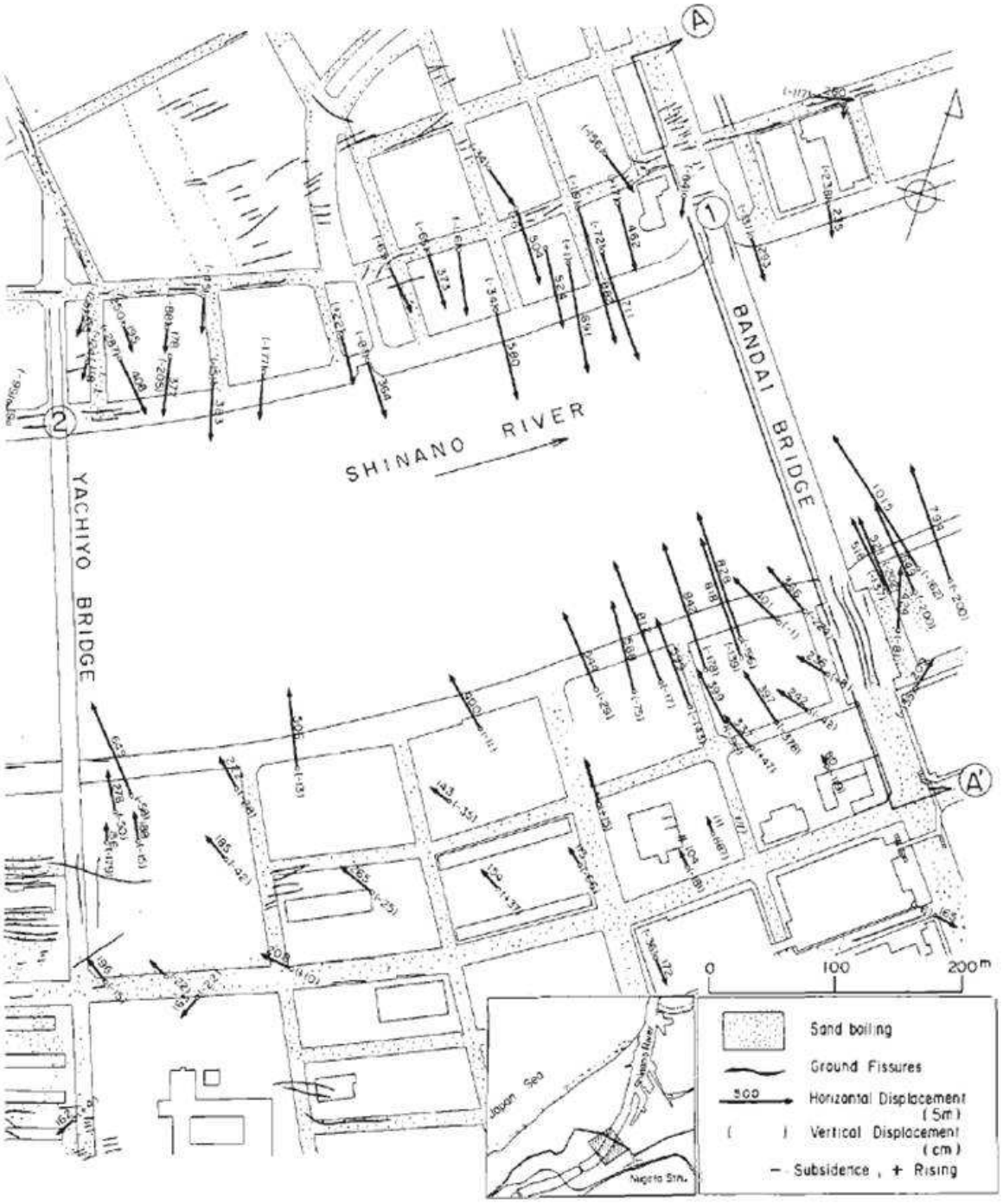

Figure 1.1: Permanent ground displacement vectors in vicinity of Bandai Bridge (Hamada and O'Rourke, 1992).

Figure 1.2: Northern approach to Landing Road Bridge two days after the Edgecumbe event. Ejected sand is visible on the ground surface (Berrill and Yasuda, 2002).

on the bank of the river as shown in Figure 1.2. Extensive liquefaction-induced lateral spreading of the northern river bank occurred near the bridge during the M6.3 March 2, 1987 Edgecumbe earthquake (Pender and Robertson, 1987). Minor rotation of the northern abutment was observed ($\sim 0.5°$), with cracking in the piles taking place near the connection to the pile cap on the river side (Berrill et al., 2001).

Observed cracks due to lateral spreading in the northern floodplain were parallel to the river bank except in the immediate vicinity of the bridge where they met the bridge axis at approximately 45° (Berrill et al., 2001). Settlement took place in the northern approach embankment, with cracks in the roadway observed extending back a distance of approximately 200 m. The general deformation pattern observed at the bridge demonstrates the resistance to ground displacements provided by the bridge foundations and a corresponding three-dimensional aspect to the embankment deformation.

1.1.3 Rio Estrella Highway Bridge, 1991 Costa Rica Earthquake

Liquefaction-induced lateral spreading occurred near several river-spanning bridges due to the M7.5 April 22, 1991 earthquake in Limon Province, Costa Rica (Franke, 2011). Among these, the highway bridge over the Rio Estrella demonstrates the behavior of interest in this work. After the strong shaking, there was evidence of widespread liquefaction and lateral spreading with displacements as large as 1 to 3 m near the southern bridge abutment, which consists of a concrete wall supported on two groups of twenty piles (Priestley et al., 1991; Franke, 2011).

Figure 1.3: Settlement and longitudinal cracking of southern approach embankment at Rio Estrella Highway Bridge (Youd, 1993).

Very little permanent displacement or rotation of the south abutment was observed. Despite this lack of permanent abutment displacement, the southern bridge span became unseated and collapsed into the river. The approach embankment for the southern abutment failed due to the lateral spreading, settling approximately 2 m and spreading perpendicularly to the longitudinal direction of the bridge with large cracks occurring parallel to the bridge axis as shown in Figure 1.3.

1.1.4 Mataquito River Bridge, 2010 Maule Earthquake

The Mataquito River Bridge, constructed in 2006, spans the Mataquito River between Quivolgo and Iloca, Chile. Liquefaction-induced lateral spreading occurred on both banks of the river due to the M_w8.8 February 27, 2010 offshore Maule earthquake. The bridge has seat-type abutments founded on 4×2 drilled shaft groups, and the interior piers are supported by 3×1 groups of shafts. Lateral soil displacements of up to 2.5 m occurred near the northeast abutment, involving the approach embankment and a 100 m floodplain sloping gently toward the river. Similar lateral spreading effects were observed on the opposite bank, however, the corresponding embankment soils were not involved (FHWA, 2011).

The bridge foundations reportedly did not experience significant permanent lateral deformations, and all bridge spans remained intact and functional. The northeast approach embankment settled approximately 0.7 to 1 m relative to the bridge deck, Figure 1.4. Longitudinal roadway cracks suggest that there was a component of embankment deformation perpendicular to the bridge axis of approximately 0.6 m (GEER, 2010a), indicating that some of the soil moved around the abutment rather than directly into it. This 3D effect may have reduced the forces applied to the foundations, contributing to the minimal damage and deformation observed in the bridge.

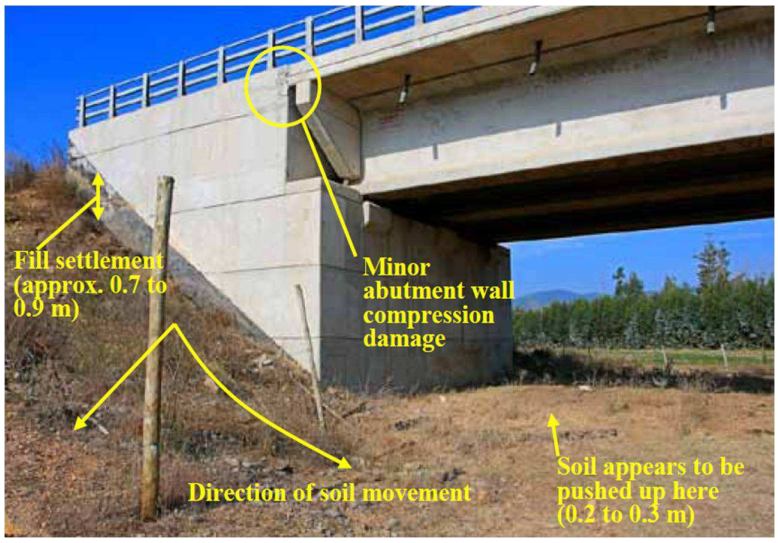

Figure 1.4: Settlement and lateral spreading deformation of northeast approach embankment to Mataquito River Bridge (FHWA, 2011).

1.1.5 Various Bridges, 2010 Darfield and 2011 Christchurch Earthquakes

The M7.1 September 4, 2010 Darfield and M6.3 February 22, 2011 Christchurch earthquakes in New Zealand caused liquefaction to occur over much of the city of Christchurch. Liquefaction-induced lateral spreading affected several bridges spanning the Avon and Heathcote rivers, with most of the associated damage concentrated on the abutments, approaches, and piers rather than the superstructure (Wotherspoon et al., 2011). Three-dimensional deformation of approach embankments during lateral spreading was observed at multiple sites for bridges spanning the Avon River.

The South Brighton Bridge, constructed in 1980, has an approximately 70 m span with seat-type abutments and a single central pier (GEER, 2010b). The abutments and pier are supported on raked prestressed concrete piles. Liquefaction-induced lateral spreading occurred on both banks of the river due to the Darfield earthquake, causing significant cracking in the approach embankments. These cracks were perpendicular to the river bank near the abutments, becoming parallel to the river in the surrounding ground. Similar damage occurred during the Christchurch earthquake, increasing the permanent deformation (Wotherspoon et al., 2011). Figure 1.5(a) shows the observed longitudinal surface cracks in the western approach to the bridge, and Figure 1.5(b) shows and aerial view of the bridge site with visible lateral spreading surface cracks along the river banks.

The ANZAC Drive Bridge, built in 2000, is a newer three span bridge supported by two 2-column bents and concrete abutments with wing-walls, all founded on piles (GEER, 2011). Minor liquefaction and lateral spreading occurred due to the Darfield event with no attendant damage (Wotherspoon et al., 2011). Severe liquefaction and significant lateral

(a) (b)

Figure 1.5: South Brighton Bridge after the Christchurch event. (a) Longitudinal lateral spreading cracks in western approach embankment (Cowan, 2011). (b) Aerial photo with visible lateral spreading cracks on river banks (LINZ, 2011).

(a) (b)

Figure 1.6: ANZAC Drive Bridge after the Christchurch event. (a) Aerial photo (LINZ, 2011). (b) Lateral spreading cracks in southern approach (GEER, 2011).

spreading occurred on both river banks near the bridge due to the Christchurch earthquake, with more pronounced evidence on the southern bank, as shown in Figure 1.6(a). Lateral spreading cracks parallel to the bridge axis were observed on both sides of the southern approach embankment (GEER, 2011), as shown in Figure 1.6(b). Both abutments experienced permanent rotations due to the lateral spreading and the restraint provided by the superstructure.

The Avondale Road Bridge, built in 1962, is a three span bridge supported by two 3-column bents and seat-type abutments with wing-walls, all founded on piles (GEER, 2011). Limited liquefaction was observed due to the Darfield earthquake, with no associated damage to the bridge, however, liquefaction-induced lateral spreading occurred due to the

Figure 1.7: Avondale Road Bridge after the Christchurch event. Lateral spreading cracks are visible near the southern approach and along the river bank (LINZ, 2011).

Christchurch earthquake. During the latter event, lateral spreading occurred on both river banks, causing permanent rotations in the abutments. At the southern abutment, lateral spreading cracks were observed extending from the sides of the abutment, perpendicular to the river bank near the abutment and rotating to a parallel configuration over about 15 m distance (Wotherspoon et al., 2011). Figure 1.7 shows an aerial view of the visible lateral spreading surface cracks at the Avondale Road Bridge site.

1.2 Scope of Work

The research discussed in this document is supported by a review of previous work relevant to the problem and an evaluation of case histories with potential for use in the investigation. Aside from these preliminary efforts, the majority of the research is numerical in nature. All of the numerical work is performed using the OpenSees finite element analysis platform, an open-source computational framework maintained by the Pacific Earthquake Engineering Research (PEER) Center, and several numerical tools are implemented or modified within OpenSees to support this effort. This development includes the efficient continuum elements discussed in Chapter 4 and modifications to the contact constraint enforcement approach for the (Petek, 2006) beam-contact element discussed in Chapter 9.

Three primary numerical analysis approaches are considered as a part of this work, each representing the chosen case study bridge with varying levels of complexity. These models and their general purposes are summarized as follows:

- Dynamic effective stress plane strain finite element models are developed for a full bridge site. These models are used to analyze the site response for a ground motion similar to that which occurred at the bridge, and to assess the liquefaction and lateral spreading susceptibility and response of the site.

- Simplified beam on nonlinear Winkler foundation models and associated limit equilibrium slope stability models are developed to analyze a bridge abutment and foundation using the pile pinning analysis approach adopted by Caltrans (2011). These models are used to assess the viability of this analysis approach in relation to the observed behavior at the site and through comparison with the other modeling approaches.

- 3D finite element models of a bridge abutment and foundation, approach embankment, and the underlying soils are created to simulate the effects of lateral spreading on the embedded foundations. These models consider the inherent three-dimensionally of the site that cannot be directly considered in the other modeling approaches, and are used to identify mechanisms leading to reductions in lateral foundation loads from those estimated using simplified descriptions of the problem.

The general and specific development related to these models, along with a discussion of their respective results, are discussed in Chapters 7 through 9. In addition to the numerical models developed for the case study site, a second set of 3D FE models is created and analyzed in order to quantify the effects of various geometric site parameters on the reduction in foundation demands as compared to a two-dimensional description of the problem. The development and assessment of these parameter study models are discussed in Chapter 10.

1.3 Summary

The loads imposed on embedded structures during liquefaction-induced lateral ground deformation an important consideration in the lateral design of deep foundations for bridges in seismically active regions. A brief review of several case histories documenting bridge performance in past earthquakes demonstrates that the presence of foundation elements influences the deformation of the soil during lateral spreading. In each of the referenced case histories, there is an observed tendency for the approach fill to slump vertically and for the soil to deform perpendicularly to the bridge axis, likely due to the lateral resistance provided by the bridge foundations and superstructure.

An analysis which assumes 2D conditions, i.e., all embankment and native crustal soil behind a bridge abutment will transmit load directly into the foundation during lateral spreading or flow failure, may be overconservative. A simplified analysis procedure for estimating lateral spreading forces which makes consideration for the effects observed in the case histories, or provides guidance on when 2D or 3D assumptions are most applicable, would be a valuable tool for bridge design. The research discussed in this document attempts to provide guidance on such a procedure.

Chapter 2

REVIEW OF PILED BRIDGE FOUNDATION ANALYSIS

A significant amount of research has been dedicated to investigating the response of bridge foundations and general deep foundations in liquefied and laterally spreading soil. These investigations have employed different combinations of numerical modeling, experimental testing, and case history evaluation to reach various conclusions. A review of the recent relevant literature follows. For general reference, the following works provide a fairly comprehensive discussion of the issues related to the seismic analysis of bridge foundations and piles (Ledezma and Bray, 2010, 2008; Martin, 2004; Aviram et al., 2008b; Ashford et al., 2011; Finn, 2005; Cubrinovski and Ishihara, 2007; Berrill and Yasuda, 2002)

2.1 Experimental Analysis

The behavior of piled bridge abutments, as well as isolated piles or pile groups, during lateral spreading and other lateral load cases has been studied via numerous experiments. These experiments include centrifuge tests (e.g., Armstrong et al., 2008; Gonzalez Lagos et al., 2007; Tobita et al., 2006; Bhattacharya et al., 2005; Brandenberg et al., 2005; Boulanger et al., 2003; Kondoh and Tamura, 2003; Abdoun and Dobry, 2002), full-size or scaled shake table tests (e.g., Suzuki et al., 2006; Dungca et al., 2006; Cubrinovski et al., 2006; Tokimatsu et al., 2005), and full-scale field tests (e.g., Lemitzer et al., 2010, 2009; Bozorgzadeh et al., 2008; Stewart et al., 2007; Rollins et al., 2005; Wallace et al., 2001; Mokwa and Duncan, 2000; Romstad et al., 1995).

These experiments have provided insights into such phenomena as pile pinning effects during lateral spreading (Armstrong et al., 2008; Gonzalez Lagos et al., 2007), pile buckling in liquefied soil (Bhattacharya et al., 2005), the lateral behavior of pile caps, bridge abutments, and backfill soil (Lemitzer et al., 2009; Bozorgzadeh et al., 2008; Mokwa and Duncan, 2000; Romstad et al., 1995), induced earth pressures on bridge abutments during lateral spreading (Kondoh and Tamura, 2003), the interaction of piles and laterally spreading crustal layers (Knappett et al., 2010; Brandenberg et al., 2007a), and the general response of piles and pile groups to liquefaction and lateral spreading.

2.2 Numerical Analysis

Numerical analysis techniques have become the most viable method of analysis for design purposes, and extensive numerical analyses have been conducted in order to validate and re-

fine existing approaches. As confidence has increased, it has become common for researchers to use numerical analysis to gain further insight on the behavior of deep foundations in liquefied and laterally spreading soil. The majority of the numerical analyses present in the literature can be separated into three broad groups; (1) those that exclusively use a beam on nonlinear Winkler foundation (BNWF) approach to represent soil-foundation interaction, (2) those that model the soil-foundation system in 2D with a plane strain soil continuum, and (3) those that model the full three-dimensionality of the problem. There are obviously hybrid approaches which fit in between these broad categories, however, they serve as useful separators for a survey of the literature.

2.2.1 Beam on Nonlinear Winkler Foundation Models

The use of a BNWF model to represent the interaction between deep foundations and the surrounding soil is prevalent. In this approach, the deep foundation is modeled as a beam-column and the soil is modeled using a series of discrete nonlinear force density-displacement springs. These springs are used to represent both lateral (normal to the pile) and vertical (parallel to the pile) soil response, and are typically derived from experimental testing. In the generally accepted nomenclature for this approach, p-y springs (e.g., Reese and Van Impe, 2001; API, 2007) refer to lateral soil-pile interaction, t-z springs (e.g., Seed and Reese, 1957; Kraft et al., 1981; Reese et al., 2006) to frictional side resistance, and Q-z springs (e.g., Meyerhof, 1976; Vijayvergiya, 1977) to pile end bearing.

BNWF analyses of piles and pile groups have been compared and validated against experimental data or case histories in numerous studies using both pseudo-static pushover approaches (e.g., Boulanger et al., 2003; Tokimatsu et al., 2005; Brandenberg et al., 2007b; Takahashi et al., 2006a; Ashford and Juirnarongrit, 2006; Khalili-Tehrani et al., 2007) and dynamic analysis (e.g., Miwa et al., 2006; Boulanger et al., 2003). In general, good agreement has been observed between the analytical and experimental results for different configurations and loading types, though thoughtful definition of the included nonlinear springs is often required. These types of correlations have increased the viability of the BNWF analysis approach, leading to its ubiquity in current practice.

BNWF methods have been used to model soil-structure interaction in both 2D and 3D, and have been applied to single piles, pile groups, and complete bridge foundations. The BNWF approach has been incorporated into models investigating thermal loads on bridges (e.g., Faraji et al., 2001), models examining the effects of live load distribution on integral abutment bridges (Dicleli and Erhan, 2005), and in pseudo-static pushover analyses of piles and piled bridge abutments (Silva and Manzari, 2008; Dicleli, 2005). Force-displacement curves representing the lateral response of pile caps and abutments with native and backfill soil have also been investigated (e.g., Dicleli, 2005; Dicleli and Erhan, 2005; Shamsabadi et al., 2007, 2005; Mokwa and Duncan, 2000).

Other work which has employed a BNWF approach includes an examination of the stiffness of piles subject to dynamic shaking in liquefiable soils (Arduino et al., 2006), an analysis of a base-isolated curved bridge using dynamic nonlinear 3D finite element analysis (Ates and Constantinou, 2011), an evaluation of the effects of various bridge abutment modeling decisions on the global seismic response of bridges (Aviram et al., 2008a), and investigations into pile stability and bending-buckling interaction in liquefiable soils (Dash et al., 2010; Knappett and Madabhushi, 2006).

Proposed simplified analysis and design procedures have been developed based on BNWF representations of soil-foundation interaction. Ashour and Ardalan (2011) proposed an analytical method for piles subject to lateral spreading which considers strain wedge effects and accounts for the differing responses of the crust, liquefied soil, and non-liquefied soil. Bradley et al. (2011) proposed a probabilistic framework for pseudo-static analysis of piles in liquefied and laterally spreading soils. Valsamis et al. (2011) proposed a simplified design procedure for single piles in liquefaction-induced lateral spreading based on a parametric analysis. Design charts for the maximum bending moment and displacement of the pile are presented. Brandenberg et al. (2011) developed demand fragility curves for bridges in liquefied and laterally spreading ground using nonlinear equivalent static analysis with inputs sampled using Monte Carlo simulation. Franke (2011) analyzed case history results within the context of performance-based evaluation of bridge foundations.

Cubrinovski and Ishihara (2004) proposed a simplified analysis procedure for piles subject to lateral spreading based on a closed-form solution to the beam on elastic foundation equation. Linear properties were assumed for the soil and pile for this solution, however, simplified models for nonlinear behavior can be incorporated using an equivalent linear approach. Cubrinovski and Ishihara (2006) extended this method to consider pile groups. Meera et al. (2007) and Chang et al. (2008) presented similar finite difference solutions to the beam on Winkler foundation problem for use in the analysis of piles subject to lateral spreading.

2.2.2 Two-Dimensional Finite Element and Finite Difference Models

Plane strain analysis of bridge-foundation-soil systems is an approach which offers refinements over the BNWF approach (e.g., effective stress analysis) at a lower computational cost than fully three-dimensional analysis. Plane strain finite element analysis (FEA) has been used to model pile groups subject to lateral spreading (Chang et al., 2006), to investigate the relationship between ground motion intensity measures and pile response (Bradley et al., 2009), to model bridge abutments subject to lateral loads and seismic shaking (Shamsabadi et al., 2010; Ooi et al., 2010; Hara et al., 2004), and to model the seismic response of bridge-foundation-soil systems using an effective stress approach (Shin et al., 2008; Bradley et al., 2010).

Despite the applications listed above, plane strain analysis is the least common analytical approach in the literature, likely due to the associated difficulty in modeling deep foundations appropriately. The assumption of plane strain is perfectly applicable to the soil domain in most conditions, and bridge foundations without piles can be modeled effectively (e.g., Shamsabadi et al., 2010). However, plane strain is not applicable to deep foundation bodies, which have inherently small out-of-plane dimensions and interact with the soil in a fundamentally three-dimensional manner.

Several approaches have been used to overcome the non-applicability of deep foundations to plane strain conditions. The most effective and common approach is to use *p-y* curves, which are based on 3D soil-pile interaction, to connect piles modeled as beam-column elements to the adjacent solid elements representing the soil domain (e.g., Shin et al., 2008; Chang et al., 2006). Hara et al. (2004) modeled a pile group using several columns of solid elements, assuming the row of piles to act as a plane strain wall. Ooi et al. (2010), Bradley et al. (2009), and Bradley et al. (2010) used a similar assumption with a pile row acting as a wall in plane strain, but modeled the piles as beam-column elements.

Neither of these approaches are perfect. For example, the assumptions involved with the plane strain wall approach are not applicable to all pile spacings and cannot account for a single pile. When using the *p-y* curve approach, it is important to address the effects of representing the soil using both solid elements and soil-pile interaction springs. It is often assumed that the solid elements represent the far-field soil response while the *p-y* curves represent the near-field response. Modifications to the stiffness of the soil-pile interaction curves such that the combined lateral response of the spring and solid elements approximates a target *p-y* response is another alternative (Armstrong, 2010).

2.2.3 Three-Dimensional Finite Element and Finite Difference Models

Three-dimensional analysis possesses the greatest potential for accurately capturing the full behavior of soil-foundation systems, though it also presents the greatest computational expense. As computing power has increased, the relative cost of 3D numerical analysis has become less prohibitive, and the use of this technique has become more common in both research and practice.

Much of the early work in 3D numerical analysis of deep foundations was conducted by Desai and his colleagues (e.g., Desai and Appel, 1976; Faruque and Desai, 1982; Muqtadir and Desai, 1986). Other examples of relatively early work in this field include Brown et al. (1989) and Brown and Shie (1990, 1991). These early studies showed that 3D analysis is a viable approach for single and grouped deep foundations, able to incorporate nonlinear constitutive behavior, geometric nonlinearity, interface friction, sloping ground, and other influential factors.

The research program discussed in this document primarily involves the use of 3D FEA

as a numerical modeling tool. In order to gain a better understanding of the 3D modeling process, as related to the particular problem under consideration, the literature summary for this topic is presented in greater detail. Each aspect of the full 3D model is separately discussed to provide a more comprehensive survey of the different approaches which have been previously undertaken. These aspects include soil constitutive behavior, the use of mixed elements for fluid-solid coupling, treatments for deep foundations and the soil-foundation interface, and boundary and loading conditions.

2.2.3.1 Soil Constitutive Modeling

Soil constitutive modeling approaches in 3D analyses of soil-foundation systems have ranged from relatively simple Von Mises, Drucker-Prager, and Mohr-Coulomb plasticity models (e.g., Yang and Jeremic, 2002, 2003, 2005; Khalili-Tehrani et al., 2007; Ooi et al., 2010) to more sophisticated alternatives as computing power has increased. An extension of the Duncan and Chang (1970) hyperbolic constitutive model with a yield cap and consideration for soil dilatancy effects was used by Shamsabadi et al. (2010). Multi-surface plasticity models (Prevost, 1977, 1985a; Elgamal et al., 2003) have been used to represent the constitutive behavior of both cohesive and cohesionless soils in total and effective stress analyses, respectively (e.g., Elgamal et al., 2006, 2008).

Other approaches are found in the work of Cubrinovski et al. (2008) and Uzuoka et al. (2008), who used a critical state constitutive model for cohesionless soil (Cubrinovski and Ishihara, 1998a,b) in effective stress analyses, Cheng and Jeremic (2009), who used a soil constitutive model based on the work of Manzari and Dafalias (1997) and Dafalias and Manzari (2004), and Takahashi et al. (2006b, 2010) who used a plasticity model with a subloading surface and rotational hardening after Hashiguchi and Chen (1998).

2.2.3.2 Coupled Fluid-Solid Elements

Effective stress analysis requires a method to account for the interaction between the pore fluid and soil skeleton in saturated or partially saturated soil. Various approaches derived from the work of Biot (1941, 1956, 1962) have been developed to accomplish this goal in a numerical setting, each adding fluid degrees-of-freedom to the system according to different assumptions. Three primary approaches are discussed by Zienkiewicz and Shiomi (1984). These approaches are the **u**-*p*-**U** element formulation, which uses the full system of equations developed for the saturated problem, the **u**-**U** formulation, a simplification of the **u**-*p*-**U** approach which assumes incompressibility for each medium, and the **u**-*p* approach, which simplifies the system by assuming that fluid acceleration can be neglected. The theory behind these approaches is discussed in further detail in Section 3.2.

Each of these primary finite element formulations is represented in the literature related to 3D effective stress analyses of soil-foundation systems. Cubrinovski et al. (2008) and

Uzuoka et al. (2008) used the **u**-**U** and **u**-p element formulations, respectively, in their 3D simulations of shake table tests. Cheng and Jeremic (2009) used the **u**-p-**U** element formulation in their numerical simulations of a single pile in liquefiable soil.

2.2.3.3 Deep Foundation Elements and Treatment of Soil-Foundation Interface

Deep foundations have typically been incorporated into 3D FEA using either solid elements (e.g., Yang and Jeremic, 2002, 2003, 2005) or beam-column elements (e.g., Petek, 2006; Cheng and Jeremic, 2009; Elgamal et al., 2008). For solid element approaches, linear elastic foundation constitutive behavior is the predominant choice, though elastoplastic behavior has been considered in some cases. An example of the latter is presented by Khalili-Tehrani et al. (2007), who used a combination of truss and solid elements to represent the elastoplastic response of reinforced concrete piles.

When using solid elements for deep foundations, it is prevalent in the literature to simulate the interface between the foundation and surrounding soil by equating some or all of the displacement degrees-of-freedom at the soil-foundation interface (e.g., Cubrinovski et al., 2008; Uzuoka et al., 2008), or by simulating a frictional interface via a thin layer of solid elements (e.g., Yang and Jeremic, 2002, 2003, 2005) or interface elements with frictional constitutive behavior (e.g., Ooi et al., 2010; Khalili-Tehrani et al., 2007).

The use of beam-column elements to model piles is beneficial, as it simplifies post-processing interpretation of pile shear and moment values, however, it also necessitates special treatment of the soil-pile interface due to the incompatibility of the pile and soil element types. Another advantage of this approach lies in the relative ease with which to consider elastoplastic pile constitutive behavior via fiber section models (e.g., Cheng and Jeremic, 2009; Jeremic et al., 2009; Elgamal et al., 2008).

Interface approaches for models with beam-column pile elements have typically involved rigid no-slip node-to-node contact links (e.g., Elgamal et al., 2008; Jeremic et al., 2009), though other treatments have been used. Cheng and Jeremic (2009) used a combination of rigid links and impermeable solid elements to ensure compatibility for both the solid and fluid degrees-of-freedom at the soil-foundation interface. Petek (2006) introduced a 3D beam-solid contact element which creates a frictional stick-slip interface between the beam-column and solid elements, allowing for more realistic soil-foundation interaction. This beam-solid contact element was used to examine numerical p-y curves in the 3D FEA of McGann et al. (2010, 2011).

2.2.3.4 Boundary and Loading Conditions

Proper boundary conditions must be devised to ensure the success of a 3D analysis of a soil-foundation system. Boundary conditions for foundation elements typically replace structural components which are not critical to the model, and vary depending upon the particular

support conditions assumed at the connection between the critical and non-critical components. Rigid-type connections are commonly represented using rotational fixity, while more flexible connections may be more appropriately modeled with rotational freedom. Translational degrees-of-freedom for foundation elements may also require restriction depending upon the geometry of the model.

Boundary conditions for the soil continuum require somewhat greater care to ensure appropriate results. At a minimum, the boundaries must be fixed such that all rigid body displacement modes are restricted. In static or pseudo-static analyses, the main concern is related to diminishing the effects of the boundary on the portions of the model which are of primary interest. Boundary effects can be controlled for an analysis of a soil-foundation system by extending the limits of the soil continuum away from the location of the foundation elements. The optimal extents are those which minimize the boundary effects while maximizing computational efficiency. A brief study demonstrating boundary effects in analysis of laterally loaded piles is given by McGann (2009).

Minimization of boundary effects is also critical in dynamic analysis, however, devising proper boundary conditions is more difficult than in static or pseudo-static cases. The particular method used for this purpose depends upon the objective of the numerical model. For example, Cubrinovski et al. (2008) and Uzuoka et al. (2008) compared numerical results to shake table tests, therefore, the geometry and boundaries in the model mirrored those in the experiment. All lateral boundaries were fixed against out-of-plane translation to be consistent with the rigid container used in the shake table tests, and input excitations were applied at the fixed base of the model. Specification of boundary and loading conditions in this manner is common for simulations of experimental analysis.

When creating a numerical model for a site in the field, the assumption of rigid boundaries is typically no longer valid. Several strategies have been developed to include the effect of semi-infinite subsurface extents in a numerical model of finite size. The use of periodic boundary conditions, in which the lateral extents of the model share translational degrees-of-freedom, is one such approach which attempts to appropriately account for the free-field response of the soil domain. Elgamal et al. (2008) used this approach in their model of a complete bridge-foundation-soil system.

Lysmer and Kuhlemeyer (1969) introduced a technique to capture a transmitting boundary through the use of viscous dashpots. By defining the viscous response of the dashpots based on the density and shear wave velocity of the material beyond the boundary, this approach appropriately captures the dissipation of wave energy in the numerical model. When defining transmitting boundaries using the Lysmer and Kuhlemeyer (1969) method, accelerations are not directly applied to the model. Instead, a force is applied using the technique developed by Joyner and Chen (1975). This applied force is proportional to the input velocity and the constitutive properties of the material beyond the boundary. This

approach is commonly used in numerical analysis for geotechnical problems to account for the compliance between the soil domain of the model and the semi-infinite media outside of the considered domain. For example, Elgamal et al. (2008) represented an underlying elastic half-space in this manner via dashpots in the three Cartesian directions at each node on the base of their 3D FE model of a full bridge-foundation-soil system.

Another technique which can be used in geotechnical simulations to properly account for the differences in wave behavior inside the finite soil domain represented by the model and the wave behavior in the semi-infinite soil medium is the domain reduction method (Bielak et al., 2003; Yoshimura et al., 2003). The domain reduction method (DRM) consists of two phases. The initial phase involves a background geological model which includes both the source of the earthquake and the region of interest. This background model is used to compute the free-field displacement wave-field demands on the boundary of the smaller region of interest. The second phase involves only the reduced region of interest. In this phase, effective seismic forces are applied at the boundary of the local region. These effective forces are derived from the boundary displacement demand obtained in the initial phase. Jeremic et al. (2009) applied a vertically propagating wave field to their model using the DRM, utilizing equivalent linear site response analysis for the initial analysis phase.

Representation of the initial state of stress is of paramount importance in geotechnical simulations. The soil response (i.e., stress, strain) greatly depends on these initial conditions. Several approaches can be used to create an appropriate initial state. The typical method is to apply gravitational body forces to the elements in the numerical model prior to any further analysis steps. Jeremic et al. (2009) and Cheng and Jeremic (2009) took this a step further, using a staged modeling procedure in which gravitational stresses were first developed in a base soil mesh. After this stage, the soil elements were removed and replaced by foundation elements and gravitational stresses were developed for the new configuration.

2.2.4 Other Numerical and Analytical Approaches

Investigations into the response of bridge foundations to lateral loads have not always taken a form which fits conveniently into one of the three categories discussed previously. The primary exception to the former categorization is analyses based on slope stability approaches. Such analytical methods have been used to examine pile pinning effects (Boulanger et al., 2006), to assess the nonlinear force-displacement behavior of bridge abutments (Shamsabadi et al., 2007, 2005), to examine displacements of bridge abutments (Basha and Babu, 2009), and to estimate lateral spreading forces on bridge piles (Zha, 2006). Other examples of alternative analytical approaches include the work of Sextos and Taskari (2008), who proposed a multi-platform analysis approach for the analysis of bridge-foundation-soil systems in seismic conditions, and the work of Kotsoglou and Pantazopoulou (2009), who analyzed a bridge-foundation-soil system as an equivalent single degree-of-freedom system.

2.3 Summary

A brief overview of the extensive amount of research related to the effects of liquefaction-induced lateral ground deformation on bridge foundations has been presented. This work has been conducted via experimental and numerical analysis, and significant progress has been made in improving the general understanding of this complex problem. Numerical analyses for this problem have most often used BNWF assumptions, though continuum analyses in two- and three-dimensions have also been explored. Simplified approaches are prevalent because they are efficient and effective, however, it is recognized that certain simplifying assumptions can lead to overconservative solutions.

Chapter 3

BRIEF REVIEW OF FINITE ELEMENT TECHNOLOGY

Finite element simulations of geotechnical problems often involve complex constitutive models, may consider spatial domains requiring a large number of degrees-of-freedom, and, for undrained conditions, must make appropriate consideration for the coupled response of the pore fluid and solid soil particles which drives the overall soil behavior. Finite element formulations which reduce computational demand via coarse mesh accuracy, effective assimilation of nonlinear constitutive models, or general efficiency are ideal in this context.

Extensive research has been devoted to establishing finite element formulations for solid mechanics that are equally applicable to any arbitrarily-posed problem. This work has focused on the development of elements that are computationally efficient, are free from volumetric locking for incompressible problems, possess good bending behavior, have little or no sensitivity to mesh distortion, are accurate in a coarse mesh, and can incorporate nonlinear constitutive equations in a simple manner (Wriggers, 2008). Several families of techniques have emerged in pursuit of satisfying these interrelated objectives, and those most applicable to this research are briefly summarized in the following sections.

3.1 Reduced Integration

The computational demand related to the relatively large soil domain necessary in most geotechnical continuum models can be lessened through reduced integration techniques. Early applications include the work of Doherty et al. (1969), Zienkiewicz et al. (1971), and Naylor (1974), who showed that in addition to reducing computational demand over full numerical integration, reduced integration can improve element behavior for certain problems. The initial response to reduced integration was poor, as many viewed it as more of a trick than a method, however, Malkus and Hughes (1978) proved the equivalence of reduced integration techniques with mixed methods firmly grounded in mathematical theory, thus legitimizing the approach.

One of the non-efficiency related benefits of reduced integration is in the mitigation of locking in low-order elements. Selectively applying reduced integration to the volumetric portion of the element while applying full integration to the deviatoric portion effectively eliminates volumetric locking in four-node quadrilateral and eight-node hexahedral elements. The removal of locking comes with a price, as use of this technique leads to a spatial instability in the pressure field known as checkerboarding (Belytschko et al., 2000). Fully

reduced integration offers the least computational effort possible for these elements, however, in addition to the pressure instability of selectively-reduced integration, fully reduced integration results in instabilities in the displacement field known as spurious modes or hourglassing (Belytschko et al., 2000; Wriggers, 2008).

Hourglass stabilization techniques (Flanagan and Belytschko, 1981; Belytschko et al., 1984; Jacquotte and Oden, 1984; Wissmann et al., 1987) are an effective means of controlling the instabilities related to reduced integration. Hourglass stabilized reduced integration has been shown to be effective in numerous applications. This technique has been specialized for incompressible elasticity and beam bending (Belytschko and Bachrach, 1986), extended to include assumed strain fields (Belytschko and Bindeman, 1991, 1993), and incorporated into finite deformation elements (Reese, 2003, 2005). Hourglass stabilized single-point integration is a natural approach to reduce computational demand for the 2D and 3D elements developed in this work.

3.2 Analysis of Saturated Porous Media

Elements developed for modeling saturated soil (e.g., Prevost, 1982, 1985b; Zienkiewicz, 1981; Zienkiewicz and Shiomi, 1984), are typically derived from mixed formulations that consider the coupled response of the fluid and solid phases comprising the soil, often within the framework of the early work of Biot (1941, 1956, 1962). In the established approach, the saturated porous medium is described in terms of the displacement of the solid skeleton, $\mathbf{u}$, the pressure in the pore fluid, p, and the displacement of the fluid phase relative to the solid phase, $\mathbf{w}$.

The system of equations resulting for this description of the problem contains an inconvenient coupling in the mass matrix, however, a modification of variables introduced by Zienkiewicz and Shiomi (1984)

$$\mathbf{U} = \mathbf{u} + \frac{\mathbf{w}}{n} \tag{3.1}$$

where n is the porosity, ensures an uncoupled mass matrix that is more convenient in temporal integration. The new system of equations for $\mathbf{u}$, p, and $\mathbf{U}$ can be discretized using mixed finite element procedures, and is sometimes referred to as the $\mathbf{u}$-p-$\mathbf{U}$ formulation. Deibels and Ehlers (1996) present such an element formulated to account for material and geometric nonlinearities.

The system of equations can be further simplified by assuming idealized conditions for the fluid-solid mixture, with different assumptions leading to the elimination of different variables. Assuming incompressibility for both the pore fluid and the soil skeleton (Prevost, 1982) removes the pore pressure from the system of equations, resulting in a $\mathbf{u}$-$\mathbf{U}$ (or $\mathbf{u}$-$\mathbf{w}$) element formulation. Assuming that the fluid acceleration relative to the solid skeleton is negligible (Zienkiewicz, 1981) results in a formulation which can be written entirely in terms

of **u** and p. Of the available options, the **u**-p formulation (Zienkiewicz and Shiomi, 1984) is particularly attractive in the context of an efficient solution and is the method chosen in this work. The solid displacement and fluid pressure are typically of interest in geotechnical analysis, and the assumptions leading to the formulations are valid for most soil dynamics problems.

3.3 Numerical Stability for Incompressible Problems

Low mixture permeabilities and nearly incompressible pore fluids are commonly encountered in geotechnical problems. For the **u**-p formulation, the system of equations in this incompressible-impermeable limit corresponds to similar to mixed formulations in incompressible elasticity, Darcy flow, and Stokes flow where proof of convergence coincides with satisfaction of the *inf-sup* condition (Brezzi and Fortin, 1991; Wriggers, 2008). Fulfillment of the *inf-sup* condition is related to ensuring full rank for the coupling terms in the linearized system of equations. Element formulations which do not satisfy the *inf-sup* condition are not automatically useless (Wriggers, 2008), however, the stability of such elements cannot be guaranteed in the limiting case.

Stability can be ensured by using interpolation functions for displacement that are of higher order than those used for the pressure (Zienkiewicz et al., 2005), or otherwise satisfying]the *inf-sup* condition, but there are several available techniques which can be used to enhance the stability of low-order elements. These include special time stepping algorithms (Huang et al., 2001), direct stabilization techniques (Huang et al., 2004; Zienkiewicz et al., 1994), approaches based on the Galerkin Least-Squares method (Hughes et al., 1986; Truty, 2001), and variational multiscale methods (Hughes, 1995; Hughes et al., 1998; Xia and Masud, 2009), among others. A direct stabilization technique is adopted for the coupled fluid-solid elements developed for this work. Further discussion on the implemented pressure field stabilization formulation is available in Section 4.6.

3.4 Summary

A short review of finite element technology applicable to geotechnical analysis in two- and three-dimensions has been presented. These techniques are applied to the development of efficient continuum element formulations for the analysis of solid and fluid-solid coupled problems. The resulting elements, discussed in Chapter 4, are used during the numerical investigations presented in the remainder of this work.

Chapter 4

STABILIZED SINGLE-POINT INTEGRATION CONTINUUM ELEMENTS

The present chapter discusses new low-order four-node quadrilateral and eight-node hexahedral elements with a **u**-p formulation which combine hourglass-stabilized single-point integration in the solid phase with non-residual based stabilization of the pressure field for enhanced stability in the incompressible-impermeable limit. The presented formulations result in stable, accurate, and computationally efficient elements suitable for dynamic analysis of saturated soils in 2D and 3D. In addition, the solid phase formulations for these elements stand alone as efficient displacement-based elements suitable for general static and dynamic analysis of continua.

4.1 General Mixed Element Formulation

The **u**-p element formulation (Zienkiewicz and Shiomi, 1984) is derived from two coupled equations, the equation of motion for the mixture neglecting the acceleration of the fluid,

$$\boldsymbol{\nabla} \cdot \left(\boldsymbol{\sigma}' - p\mathbf{1}\right) + \rho\mathbf{g} - \rho\ddot{\mathbf{u}} = \mathbf{0} \tag{4.1}$$

and the combined equation of motion for the fluid phase and mass balance for the mixture,

$$\operatorname{tr}\dot{\boldsymbol{\varepsilon}} + \frac{n}{K_f}\dot{p} + \boldsymbol{\nabla} \cdot \left[\mathbf{k}\left(-\boldsymbol{\nabla}p + \rho_f\mathbf{g}\right)\right] = 0 \tag{4.2}$$

where $\mathbf{u}$ is the displacement of the solid phase, $\boldsymbol{\sigma}'$ is the effective stress, $\mathbf{1}$ is the second-order identity tensor, ρ is the mixture mass density, $\mathbf{g}$ is a vector of body forces, $\operatorname{tr}\dot{\boldsymbol{\varepsilon}}$ is the volumetric strain rate in the solid phase, n is the porosity, K_f and ρ_f are the pore fluid bulk modulus and mass density, respectively, and $\mathbf{k}$ is the permeability tensor. In this and all subsequent discussion, compression is taken as negative.

Using the approximations $\mathbf{u} \approx \mathbf{N}_u\mathbf{d}$ and $p \approx \mathbf{N}_p\mathbf{p}$, where $\mathbf{N}_u$ and $\mathbf{N}_p$ are arrays of interpolation functions for displacement and pressure, respectively, and $\mathbf{d}$ and $\mathbf{p}$ are vectors of nodal displacements and pore pressures, the following discretized functions are obtained from (4.1) and (4.2) via the standard Galerkin technique:

$$\mathbf{M}\ddot{\mathbf{d}} + \int_\Omega \mathbf{B}^T\boldsymbol{\sigma}'\, d\Omega - \mathbf{Q}\mathbf{p} = \mathbf{f}_u^{\text{ext}} \tag{4.3}$$

$$\mathbf{Q}^T\dot{\mathbf{d}} + \mathbf{S}\dot{\mathbf{p}} + \mathbf{H}\mathbf{p} = \mathbf{f}_p^{\text{ext}} \tag{4.4}$$

where

$$\mathbf{M} = \int_\Omega \mathbf{N}_u^T \rho \mathbf{N}_u \, d\Omega \tag{4.5}$$

$$\mathbf{Q} = \int_\Omega \mathbf{B}^T \mathbf{1} \mathbf{N}_p \, d\Omega \tag{4.6}$$

$$\mathbf{S} = \int_\Omega \mathbf{N}_p^T \frac{n}{K_f} \mathbf{N}_p \, d\Omega \tag{4.7}$$

$$\mathbf{H} = \int_\Omega \boldsymbol{\nabla} \mathbf{N}_p^T \mathbf{k} \boldsymbol{\nabla} \mathbf{N}_p \, d\Omega \tag{4.8}$$

$$\mathbf{f}_u^{\text{ext}} = \int_\Omega \mathbf{N}_u^T \rho \mathbf{g} \, d\Omega + \int_\Gamma \mathbf{N}_u^T \mathbf{t} \, d\Gamma \tag{4.9}$$

$$\mathbf{f}_p^{\text{ext}} = \int_\Gamma \mathbf{N}_p^T \mathbf{k} \mathbf{q} \, d\Gamma - \int_\Omega \boldsymbol{\nabla} \mathbf{N}_p^T \rho_f \mathbf{k} \mathbf{g} \, d\Omega \tag{4.10}$$

where $\mathbf{B}$ is the standard kinematic matrix for the solid phase, and $\mathbf{1} = [1, 1, 0]^T$ in 2D or $\mathbf{1} = [1, 1, 1, 0, 0, 0]^T$ in 3D. Voight notation is adopted in equations (4.3)-(4.10) and all subsequent development. In the following sections, expressions for the matrices in (4.3) and (4.4) are developed for single-point integration 2D and 3D elements.

4.2 Evaluation of Solid Phase for Four-Node Quadrilateral Element

The solid phase constituents of the discretized field equations (4.3) and (4.4) are evaluated using a single integration point located in the center of the element (local coordinates, $\xi = \eta = 0$) using linear interpolation functions. The single-point strategy involves an assumed strain field for locking-free behavior and physical hourglass stabilization to eliminate the spurious zero-energy modes associated with reduced integration.

4.2.1 Element Kinematics

The displacement field for the element is expressed in the form given by Belytschko and Bachrach (1986)

$$\mathbf{u} = (a_{0x} + a_{1x}x + a_{2x}y + a_{3x}h)\mathbf{i} + (a_{0y} + a_{1y}x + a_{2y}y + a_{3y}h)\mathbf{j} \tag{4.11}$$

where a_{ix} and a_{iy} are scalar coefficients, x and y are global coordinates, and $h = \xi\eta$ is the local coordinate product. Using this form, the nodal displacements, $\mathbf{d}_x = [u_1, u_2, u_3, u_4]^T$

and $\mathbf{d}_y = [v_1, v_2, v_3, v_4]^T$, can be expressed as

$$\mathbf{d}_x = a_{0x}\mathbf{r} + a_{1x}\mathbf{x} + a_{2x}\mathbf{y} + a_{3x}\mathbf{h} \tag{4.12}$$

$$\mathbf{d}_y = a_{0y}\mathbf{r} + a_{1y}\mathbf{x} + a_{2y}\mathbf{y} + a_{3y}\mathbf{h} \tag{4.13}$$

where

$$\mathbf{r} = [1, 1, 1, 1]^T \tag{4.14}$$

$$\mathbf{x} = [x_1, x_2, x_3, x_4]^T \tag{4.15}$$

$$\mathbf{y} = [y_1, y_2, y_3, y_4]^T \tag{4.16}$$

$$\mathbf{h} = h(\boldsymbol{\xi}, \boldsymbol{\eta}) = [1, -1, 1, -1]^T \tag{4.17}$$

with local coordinate vectors

$$\boldsymbol{\xi} = [-1, 1, 1, -1]^T \tag{4.18}$$

$$\boldsymbol{\eta} = [-1, -1, 1, 1]^T \tag{4.19}$$

The kinematic equations for the element are defined in two parts. The first part is obtained by computing the components of the small strain field from (4.11). This defines a link between the strain, $\boldsymbol{\varepsilon}$, and a vector $\mathbf{a}$ which contains the a_{ix} and a_{iy} coefficients of (4.11), (4.12), and (4.13). This link is expressed as

$$\boldsymbol{\varepsilon} = \tilde{\mathbf{B}}\mathbf{a} = \begin{bmatrix} 1 & 0 & 0 & h_{,x} & 0 \\ 0 & 1 & 0 & 0 & h_{,y} \\ 0 & 0 & 1 & h_{,y} & h_{,x} \end{bmatrix} \begin{Bmatrix} a_{1x} \\ a_{2y} \\ a_{xy} \\ a_{3x} \\ a_{3y} \end{Bmatrix} \tag{4.20}$$

where

$$a_{xy} = \frac{1}{2}(a_{2x} + a_{1y}) \tag{4.21}$$

and

$$h_{,\alpha} = \frac{\partial h}{\partial \alpha} = \eta\xi_{,\alpha} + \xi\eta_{,\alpha} \tag{4.22}$$

for $\alpha = x, y$.

The element kinematic equations are completed by determining a mapping between the

coefficient vector $\mathbf{a}$ and the nodal displacements $\mathbf{d}$ as

$$\mathbf{a} = \mathbf{L}\mathbf{d} = \begin{bmatrix} \mathbf{b}_x & 0 \\ 0 & \mathbf{b}_y \\ \mathbf{b}_y & \mathbf{b}_x \\ \boldsymbol{\gamma} & 0 \\ 0 & \boldsymbol{\gamma} \end{bmatrix} \begin{Bmatrix} \mathbf{d}_x \\ \mathbf{d}_y \end{Bmatrix} \tag{4.23}$$

in which the $\mathbf{b}$-vectors are the derivatives of the linear shape function vector

$$\mathbf{N}(\xi, \eta) = \frac{1}{4} \left(\mathbf{r} + \boldsymbol{\xi}\xi + \boldsymbol{\eta}\eta + \mathbf{h}\xi\eta \right)^T \tag{4.24}$$

evaluated at $\xi = \eta = 0$, i.e.,

$$\mathbf{b}_x = \frac{\partial \mathbf{N}}{\partial x}\Big|_{\xi=\eta=0} \tag{4.25}$$

$$\mathbf{b}_y = \frac{\partial \mathbf{N}}{\partial y}\Big|_{\xi=\eta=0} \tag{4.26}$$

and

$$\boldsymbol{\gamma} = \frac{1}{4} \left(\mathbf{h}^T - (\mathbf{h}^T \cdot \mathbf{x})\mathbf{b}_x - (\mathbf{h}^T \cdot \mathbf{y})\mathbf{b}_y \right) \tag{4.27}$$

is the projection operator of Flanagan and Belytschko (1981).

The full kinematic link between the small strain field and the nodal displacements can be expressed by combining (4.20) and (4.23), resulting in

$$\boldsymbol{\varepsilon} = \tilde{\mathbf{B}}\mathbf{L}\mathbf{d} \tag{4.28}$$

This form for the element kinematics provides the means to decompose the strain field into two portions, a constant portion, and non-constant (stabilizing) portion associated with the hourglass modes for the element. This decomposition is expressed as

$$\boldsymbol{\varepsilon} = \left(\mathbf{B}_0 + \mathbf{F}\mathbf{L}_b \right) \mathbf{d} \tag{4.29}$$

In this expression, the constant portion, $\mathbf{B}_0$, is the product of the 3×3 identity matrix in the first three columns of $\tilde{\mathbf{B}}$ with the first three rows of $\mathbf{L}$, and is equivalent to the standard kinematic matrix $\mathbf{B}$ evaluated at the center of the element. The 3×8 sub-matrix $\mathbf{B}_0 = [\mathbf{B}_{0\,1}, \ldots, \mathbf{B}_{0\,I}, \ldots, \mathbf{B}_{0\,4}]$ has the form

$$\mathbf{B}_{0\,I} = \begin{bmatrix} \mathbf{b}_{x\,I} & 0 \\ 0 & \mathbf{b}_{y\,I} \\ \mathbf{b}_{y\,I} & \mathbf{b}_{x\,I} \end{bmatrix} \tag{4.30}$$

where, e.g., $\mathbf{b}_{x\,I}$ is component I of the 1×4 vector $\mathbf{b}_x$.

The non-constant portion of (4.29) involves the sub-matrices formed by the remaining columns of $\tilde{\mathbf{B}}$, here referred to as $\mathbf{F}$, and the remaining rows of $\mathbf{L}$, which are designated as $\mathbf{L}_b$. The 3×2 sub-matrix $\mathbf{F}$ is given by

$$\mathbf{F} = \begin{bmatrix} h_{,x} & 0 \\ 0 & h_{,y} \\ h_{,y} & h_{,x} \end{bmatrix} \tag{4.31}$$

and the 2×8 sub-matrix $\mathbf{L}_b = [\mathbf{L}_{b\,1}, \ldots, \mathbf{L}_{b\,I}, \ldots, \mathbf{L}_{b\,4}]$ has the form

$$\mathbf{L}_{b\,I} = \begin{bmatrix} \gamma_I & 0 \\ 0 & \gamma_I \end{bmatrix} \tag{4.32}$$

in which $\boldsymbol{\gamma}_I$ is component I of the 1×4 vector $\boldsymbol{\gamma}$.

4.2.2 Assumed Strain Field for Stabilization

A single-point quadrilateral element formulated from the kinematic relation given in (4.29) reproduces the behavior of a standard displacement element with full 2×2 numerical integration with less computational effort. The downside to this is that the locking phenomena associated with the full-integration element are also reproduced. As a remedy, the non-constant portion of the strain field is modified based on an assumed strain field such that parasitic shear and volumetric locking are eliminated.

Volumetric locking near the incompressible limit is eliminated by assuming a strain field in which the dilation in the non-constant (hourglass) modes is zero (Belytschko and Bindeman, 1991). Parasitic shear is eliminated by ensuring that the shear strain in the non-constant modes is zero. An assumed strain field which fulfills these goals is constructed based on a general form of the kinematic hourglass matrix $\mathbf{F}$, defined as

$$\hat{\mathbf{F}} = \begin{bmatrix} e_1 h_{,x} & e_2 h_{,y} \\ e_2 h_{,x} & e_1 h_{,y} \\ e_3 h_{,y} & e_3 h_{,x} \end{bmatrix} \tag{4.33}$$

where e_1, e_2, and e_3 are arbitrary scalar constants. Substituting this general form for $\mathbf{F}$ in (4.29) yields a strain field which can be expressed as

$$\boldsymbol{\varepsilon} = \begin{Bmatrix} \varepsilon_x \\ \varepsilon_y \\ \gamma_{xy} \end{Bmatrix} = \begin{Bmatrix} \bar{\varepsilon}_x + e_1 h_{,x}\, \boldsymbol{\gamma} \cdot \mathbf{d}_x + e_2 h_{,y}\, \boldsymbol{\gamma} \cdot \mathbf{d}_y \\ \bar{\varepsilon}_y + e_2 h_{,x}\, \boldsymbol{\gamma} \cdot \mathbf{d}_x + e_1 h_{,y}\, \boldsymbol{\gamma} \cdot \mathbf{d}_y \\ \bar{\gamma}_{xy} + e_3 h_{,y}\, \boldsymbol{\gamma} \cdot \mathbf{d}_x + e_3 h_{,x}\, \boldsymbol{\gamma} \cdot \mathbf{d}_y \end{Bmatrix} \tag{4.34}$$

where $\bar{\varepsilon}_x$, $\bar{\varepsilon}_y$, and $\bar{\gamma}_{xy}$ are the constant part of the strain field, i.e., $\bar{\boldsymbol{\varepsilon}} = \mathbf{B}_0\mathbf{d}$, and the remaining terms are the non-constant portion.

The shear strain in the non-constant modes is simply the non-constant portion of γ_{xy}. From (4.34), it is clear that parasitic shear will be eliminated from the element for $e_3 = 0$. The dilation, Δ, in the hourglass modes is computed as the sum of the non-constant portion of the normal strain components

$$\Delta = (e_1 + e_2)\left(h_{,x}\,\boldsymbol{\gamma}\cdot\mathbf{d}_x + h_{,y}\,\boldsymbol{\gamma}\cdot\mathbf{d}_y\right) \tag{4.35}$$

from which it is apparent that $\Delta = 0$ for a general displacement, $\mathbf{d}$, when $e_1 = -e_2$. It is shown in Belytschko and Bindeman (1991) that the strain energy in the non-constant modes is finite for this choice of coefficients, which, in combination with the zero dilation property, ensures an element free from volumetric locking.

Since e_1 and e_2 are arbitrary coefficients, their magnitude must be specified. Different selections for these coefficients are available, each with certain advantages and disadvantages. The particular magnitudes chosen in this work are $e_1 = 0.5$ and $e_2 = -0.5$. It was shown in Belytschko and Bindeman (1991) that this selection yields good overall behavior for a stabilized element. With this choice for e_1 and e_2, and taking $e_3 = 0$, the kinematic hourglass matrix $\hat{\mathbf{F}}$ takes the form

$$\hat{\mathbf{F}} = \frac{1}{2}\begin{bmatrix} h_{,x} & -h_{,y} \\ -h_{,x} & h_{,y} \\ 0 & 0 \end{bmatrix} \tag{4.36}$$

4.2.3 Element Stiffness

The element stiffness matrix for the solid phase is computed using the decomposed form of the kinematic relation given by

$$\boldsymbol{\varepsilon} = \left(\mathbf{B}_0 + \hat{\mathbf{F}}\mathbf{L}_b\right)\mathbf{d} \tag{4.37}$$

which is identical to that originally shown in (4.29) but with the substitution of the assumed strain hourglass matrix $\hat{\mathbf{F}}$. Using this kinematic basis, the element stiffness, $\mathbf{K}_E$, can be similarly decomposed into the sum

$$\mathbf{K}_E = \mathbf{K}_0 + \mathbf{K}_{\text{stab}} \tag{4.38}$$

where $\mathbf{K}_0$ and $\mathbf{K}_{\text{stab}}$ are the constant and stabilization portions, respectively.

The constant portion of the element stiffness is evaluated using single-point integration as

$$\mathbf{K}_0 = \int_{\Omega_E} \mathbf{B}_0^T\mathbb{C}\mathbf{B}_0 d\Omega_E = 4tJ_0\mathbf{B}_0^T\mathbb{C}\mathbf{B}_0 \tag{4.39}$$

where t is the out-of-plane element thickness, $\mathbb{C}$ is the current material tangent operator, and J_0 is the Jacobian determinant evaluated at $\xi = \eta = 0$, which, after Belytschko et al. (2000), can be computed as

$$J_0 = \frac{1}{8}\left(x_{24}y_{31} + x_{31}y_{42}\right) \tag{4.40}$$

with $x_{ij} = x_i - x_j$ and $y_{ij} = y_i - y_j$ where, e.g., x_i is component i of the nodal position vector $\mathbf{x}$.

The stabilization stiffness matrix for the element,

$$\mathbf{K}_{\text{stab}} = \mathbf{L}_b^T \left(\int_{\Omega_E} \hat{\mathbf{F}}^T \hat{\mathbb{C}} \hat{\mathbf{F}} d\Omega_E \right) \mathbf{L}_b \tag{4.41}$$

where $\hat{\mathbb{C}}$ is the initial material tangent operator, is evaluated through analytical integration. The terms inside the integral can be expressed as

$$\hat{\mathbf{F}}^T \hat{\mathbb{C}} \hat{\mathbf{F}} = \begin{bmatrix} C_1 h_{,x}^2 & C_2 h_{,x}\, h_{,y} \\ C_2 h_{,x}\, h_{,y} & C_1 h_{,y}^2 \end{bmatrix} \tag{4.42}$$

in which

$$C_1 = \hat{\mathbb{C}}_{11} - 2\hat{\mathbb{C}}_{12} + \hat{\mathbb{C}}_{22} \tag{4.43}$$

$$C_2 = 2\hat{\mathbb{C}}_{12} - \hat{\mathbb{C}}_{11} - \hat{\mathbb{C}}_{22} \tag{4.44}$$

where $\hat{\mathbb{C}}_{ij}$ are the components of the initial material tangent operator.

Constitutive behavior is assumed constant over the domain of the element. Only the h-terms in (4.42) need to be integrated. Integrating $h_{,x}^2$ over the element domain gives

$$\int_{\Omega_E} h_{,x}^2 \, d\Omega_E = t \int_A h_{,x}^2 \, dA \tag{4.45}$$

where t and A are the out-of-plane thickness and planar area of the element, respectively. Expanding the area integral via (4.22) results in

$$\int_A h_{,x}^2 \, dA = \eta_{,x}^2 \int_A \xi^2 dA + \xi_{,x}\, \eta_{,x} \int_A \xi\eta dA + \xi_{,x}^2 \int_A \eta^2 dA \tag{4.46}$$

The remaining integral terms are the moments and product of inertia for the element in local coordinates, e.g.,

$$I_{\xi\xi} = \int_A \xi^2 dA \tag{4.47}$$

allowing for the definition of the following term

$$H_{xx} := \int_A h_{,x}^2 \, dA = \eta_{,x}^2 \, I_{\xi\xi} + \xi_{,x} \, \eta_{,x} \, I_{\xi\eta} + \xi_{,x}^2 \, I_{\eta\eta} \tag{4.48}$$

The remaining h-terms from (4.42) follow similarly, resulting in the definitions

$$H_{yy} := \int_A h_{,y}^2 \, dA = \eta_{,y}^2 \, I_{\xi\xi} + \xi_{,y} \, \eta_{,y} \, I_{\xi\eta} + \xi_{,y}^2 \, I_{\eta\eta} \tag{4.49}$$

and

$$\begin{aligned} H_{xy} &:= \int_A h_{,x} \, h_{,y} \, dA \\ &= \eta_{,x} \, \eta_{,y} \, I_{\xi\xi} + \left(\eta_{,x} \, \xi_{,y} + \eta_{,y} \, \xi_{,x} \right) I_{\xi\eta} + \xi_{,x} \, \xi_{,y} \, I_{\eta\eta} \end{aligned} \tag{4.50}$$

The moment and product of inertia terms are evaluated by computing the moment of inertia matrix

$$\mathbf{I} = \frac{4}{3} J_0 \left(\hat{\mathbf{g}}_1 \hat{\mathbf{g}}_1^T + \hat{\mathbf{g}}_2 \hat{\mathbf{g}}_2^T \right) = \begin{bmatrix} I_{\xi\xi} & I_{\xi\eta} \\ I_{\xi\eta} & I_{\eta\eta} \end{bmatrix} \tag{4.51}$$

in which $\hat{\mathbf{g}}_i$ are the normalized general base vectors for the element,

$$\hat{\mathbf{g}}_i = \frac{\mathbf{g}_i}{||\mathbf{g}_i||} \tag{4.52}$$

where

$$\mathbf{g}_1 = \left[\frac{\partial x}{\partial \xi}, \frac{\partial y}{\partial \xi} \right]^T ; \qquad \mathbf{g}_2 = \left[\frac{\partial x}{\partial \eta}, \frac{\partial y}{\partial \eta} \right]^T \tag{4.53}$$

The analytically integrated form of $\mathbf{K}_{\text{stab}}$ can now be expressed as

$$\mathbf{K}_{\text{stab}} = t \mathbf{L}_b^T \begin{bmatrix} C_1 H_{xx} & C_2 H_{xy} \\ C_2 H_{xy} & C_1 H_{yy} \end{bmatrix} \mathbf{L}_b \tag{4.54}$$

in which the H-terms are evaluated according to (4.48)-(4.50) using moment and product of inertia terms computed from (4.51). The stabilization stiffness is computed upon initialization of the element, and is held constant for the duration of the analysis.

4.2.4 Internal and External Forces

The internal force vector for the solid phase, $\mathbf{f}_u^{\text{int}}$, is evaluated in a manner similar to that used for the solid phase stiffness, with a decomposition into a sum of constant and stabilization portions

$$\mathbf{f}_u^{\text{int}} = \mathbf{f}_0^{\text{int}} + \mathbf{f}_{\text{stab}}^{\text{int}} \tag{4.55}$$

The constant portion of the internal force vector, $\mathbf{f}_0^{\text{int}}$, is evaluated using single-point integration as

$$\mathbf{f}_0^{\text{int}} = \int_{\Omega_E} \mathbf{B}_0^T \boldsymbol{\sigma}'(\boldsymbol{\varepsilon}) d\Omega_E = 4tJ_0 \mathbf{B}_0^T \boldsymbol{\sigma}'(\boldsymbol{\varepsilon}) \tag{4.56}$$

where, as before, t is the out-of-plane element thickness, J_0 is the Jacobian determinant at the central integration point, and $\boldsymbol{\sigma}'$ is the stress returned by the constitutive model as a function of the strain, $\boldsymbol{\varepsilon}$, in the element.

The stabilization portion is computed directly from the stabilization stiffness matrix,

$$\mathbf{f}_{\text{stab}}^{\text{int}} = \mathbf{K}_{\text{stab}} \mathbf{d} \tag{4.57}$$

where $\mathbf{d}$ is the current nodal displacement vector for the element.

The external nodal forces for the solid phase resulting from an applied body force, $\mathbf{g}$, are evaluated analytically from (4.9) as

$$\mathbf{f}_I^{\text{ext}} = \mathbf{g}t \left(J_0 + \frac{1}{3} J_1 \xi_I + \frac{1}{3} J_2 \eta_I \right) \tag{4.58}$$

by taking advantage of the linear nature of the Jacobian determinant,

$$J = J_0 + J_1 \xi + J_2 \eta \tag{4.59}$$

where J_0 is as given in (4.40) and

$$J_1 = \frac{1}{8} \left(x_{21} y_{34} + x_{34} y_{12} \right) \tag{4.60}$$

$$J_2 = \frac{1}{8} \left(x_{14} y_{32} + x_{32} y_{41} \right) \tag{4.61}$$

with $x_{ij} = x_i - x_j$ and $y_{ij} = y_i - y_j$ where, e.g., x_i is component i of the nodal position vector $\mathbf{x}$. Surface force contributions to the internal force vector from a traction, $\mathbf{t}$, are identical to a standard displacement element.

4.2.5 Mass Matrix for the Mixture

The mass matrix for the mixture, (4.5), is approximated as a lumped mass matrix. The nodal masses in this matrix are determined using the strategy used for nodal forces, thus,

$$M_{II} = \rho t \left(J_0 + \frac{1}{3} J_1 \xi_I + \frac{1}{3} J_2 \eta_I \right) \tag{4.62}$$

where M_{II} is component I, I of the diagonal mass matrix and ρ is the mixture mass density.

4.3 Evaluation of Fluid Phase for Four-Node Quadrilateral Element

The constituents of the discretized field equations, (4.3) and (4.4), corresponding to the pore fluid are evaluated using a single integration point located at the center of the element. The interpolation functions used for the pore pressure degrees-of-freedom are of the same order as those used for the displacements, therefore, a stabilization technique is used to circumvent violation of the *inf-sup* condition and create stability in the incompressible-impermeable limit (see Section 4.6).

4.3.1 Compressibility Matrix

The compressibility matrix, $\mathbf{S}$, is evaluated from (4.7) using single-point integration, resulting in

$$\mathbf{S} = 4J_0 t \frac{n}{K_f} \mathbf{N}_p^T(0,0)\mathbf{N}_p(0,0) \tag{4.63}$$

where $\mathbf{N}_p(0,0)$ is a 1×4 vector of linear shape functions, (4.24), evaluated at $\xi = \eta = 0$.

In an implementation of this element, the computation of the compressibility matrix can be further simplified by recognizing that $\mathbf{S}$ is a fully-populated 4×4 matrix in which the components are identical, i.e.,

$$S_{ij} = J_0 t \frac{n}{4K_f} \tag{4.64}$$

4.3.2 Permeability Matrix

The 4×4 permeability matrix, $\mathbf{H}$, is evaluated from (4.8) using single-point integration as

$$\mathbf{H} = 4J_0 t \boldsymbol{\nabla}\mathbf{N}_p^T(0,0)\mathbf{k}\boldsymbol{\nabla}\mathbf{N}_p(0,0) \tag{4.65}$$

where $\boldsymbol{\nabla}\mathbf{N}_p(0,0)$ is the 2×4 gradient of the shape function vector $\mathbf{N}_p$ evaluated at $\xi = \eta = 0$ and $\mathbf{k}$ is the 2×2 permeability matrix. For isotropic permeability conditions, $\mathbf{k}$ reduces to a single scalar value.

4.3.3 Coupling Matrix

The 8×4 coupling matrix, $\mathbf{Q}$, is evaluated from (4.6) using the decomposed form of the kinematic relation given by (4.37), resulting in the expression

$$\mathbf{Q} = \int_{\Omega_E} \mathbf{B}_0^T \mathbf{1}\mathbf{N}_p(0,0)d\Omega_E + \int_{\Omega_E} \mathbf{L}_b^T \hat{\mathbf{F}}^T \mathbf{1}\mathbf{N}_p(0,0)d\Omega_E \tag{4.66}$$

where $\mathbf{1} = [1, 1, 0]^T$. Because, $\hat{\mathbf{F}}^T\mathbf{1} = \mathbf{0}$, the second term vanishes, simplifying (4.66) to only the first integral term. This term is evaluated using single-point integration as

$$\mathbf{Q} = 4J_0 t \mathbf{B}_0^T \mathbf{1} \mathbf{N}_p(0,0) \tag{4.67}$$

4.3.4 Internal and External Forces

The internal nodal force vector for the fluid phase, $\mathbf{f}_p^{\text{int}}$, is a combination of compressibility and permeability forces. This vector is computed as

$$\mathbf{f}_p^{\text{int}} = \mathbf{S}\dot{\mathbf{p}} + \mathbf{H}\mathbf{p} \tag{4.68}$$

The external nodal forces for the fluid phase resulting from an applied body force, $\mathbf{g}$, are evaluated from (4.10) using single-point integration as

$$\mathbf{f}_p^{\text{ext}} = 4J_0 t \rho_f \boldsymbol{\nabla}\mathbf{N}_p^T(0,0)\mathbf{k}\mathbf{g} \tag{4.69}$$

where ρ_f is the pore fluid mass density. The contributions from a surface flux, $\mathbf{q}$, are identical to those computed for a standard element formulation.

4.4 Evaluation of Solid Phase for Eight-Node Hexahedral Element

As with the 2D element presented in the previous sections, the terms representing the solid phase in (4.3) and (4.4) are evaluated in the efficient hexahedral element using single-point numerical and analytical integration techniques. Locking is addressed via the assumption of an enhanced assumed strain field. Physical hourglass stabilization is used to control the spurious modes associated with reduced integration. Many of the terms used in this formulation are shared with its 2D counterpart. These terms are redefined as applicable.

4.4.1 Polynomial Expansion of the Jacobian Determinant

The integration scheme for the 3D element is similar to the 2D element in that the stabilizing portion of the element stiffness is evaluated analytically. To facilitate this process, the Jacobian determinant must be expressed as a polynomial function of the local coordinates for the element. Yuan et al. (1994) provide a derivation of the necessary expression. The applicable portion of their work is summarized in this section.

The isoparametric map for an 8-node linear element can be expressed as

$$\begin{Bmatrix} x \\ y \\ z \end{Bmatrix} = \begin{Bmatrix} \mathbf{N}\cdot\mathbf{x} \\ \mathbf{N}\cdot\mathbf{y} \\ \mathbf{N}\cdot\mathbf{z} \end{Bmatrix} = \begin{Bmatrix} a_0 + a_1\xi + a_2\eta + a_3\zeta + a_4 h_{\zeta\eta} + a_5 h_{\zeta\xi} + a_6 h_{\xi\eta} + a_7 h_{\xi\eta\zeta} \\ b_0 + b_1\xi + b_2\eta + b_3\zeta + b_4 h_{\zeta\eta} + b_5 h_{\zeta\xi} + b_6 h_{\xi\eta} + b_7 h_{\xi\eta\zeta} \\ c_0 + c_1\xi + c_2\eta + c_3\zeta + c_4 h_{\zeta\eta} + c_5 h_{\zeta\xi} + c_6 h_{\xi\eta} + c_7 h_{\xi\eta\zeta} \end{Bmatrix} \tag{4.70}$$

where

$$\begin{aligned} a_0 &= \frac{1}{8}\mathbf{x}\cdot\mathbf{r}, \quad a_1 = \frac{1}{8}\mathbf{x}\cdot\boldsymbol{\xi}, \quad a_2 = \frac{1}{8}\mathbf{x}\cdot\boldsymbol{\eta}, \quad a_3 = \frac{1}{8}\mathbf{x}\cdot\boldsymbol{\zeta}, \\ a_4 &= \frac{1}{8}\mathbf{x}\cdot\mathbf{h}_{\zeta\eta}, \quad a_5 = \frac{1}{8}\mathbf{x}\cdot\mathbf{h}_{\zeta\xi}, \quad a_6 = \frac{1}{8}\mathbf{x}\cdot\mathbf{h}_{\xi\eta}, \quad a_7 = \frac{1}{8}\mathbf{x}\cdot\mathbf{h}_{\xi\eta\zeta} \end{aligned} \tag{4.71}$$

The b- and c-coefficients are defined similarly in terms of $\mathbf{y}$ and $\mathbf{z}$, respectively. As discussed in Yuan et al. (1994), from the mapping of (4.70), the Jacobian matrix can be written as

$$\mathbf{J} = \begin{bmatrix} a_1 + a_5\zeta + a_6\eta + a_7 h_{\zeta\eta} & b_1 + b_5\zeta + b_6\eta + b_7 h_{\zeta\eta} & c_1 + c_5\zeta + c_6\eta + c_7 h_{\zeta\eta} \\ a_2 + a_4\zeta + a_6\xi + a_7 h_{\zeta\xi} & b_2 + b_4\zeta + b_6\xi + b_7 h_{\zeta\xi} & c_2 + c_4\zeta + c_6\xi + c_7 h_{\zeta\xi} \\ a_3 + a_4\eta + a_5\xi + a_7 h_{\xi\eta} & b_3 + b_4\eta + b_5\xi + b_7 h_{\xi\eta} & c_3 + c_4\eta + c_5\xi + c_7 h_{\xi\eta} \end{bmatrix} \tag{4.72}$$

from which the inverse can be found using the adjunct as

$$\mathbf{J}^{-1} = \begin{bmatrix} \xi_{,x} & \eta_{,x} & \zeta_{,x} \\ \xi_{,y} & \eta_{,y} & \zeta_{,y} \\ \xi_{,z} & \eta_{,z} & \zeta_{,z} \end{bmatrix} = \frac{1}{J}\begin{bmatrix} J_{22}J_{33} - J_{23}J_{32} & J_{13}J_{32} - J_{12}J_{33} & J_{12}J_{23} - J_{13}J_{22} \\ J_{23}J_{31} - J_{21}J_{33} & J_{11}J_{33} - J_{13}J_{31} & J_{13}J_{21} - J_{11}J_{23} \\ J_{21}J_{32} - J_{22}J_{31} & J_{12}J_{31} - J_{11}J_{32} & J_{11}J_{22} - J_{12}J_{21} \end{bmatrix} \tag{4.73}$$

where J is the Jacobian determinant and J_{ij} are the components of the Jacobian Matrix. By collecting the a-, b-, and c-coefficients into vectors of the form

$$\mathbf{e}_i = \begin{Bmatrix} a_i \\ b_i \\ c_i \end{Bmatrix}, \qquad i = 0 \text{ to } 7 \tag{4.74}$$

and making the following definition

$$p_{ijk} = \mathbf{e}_i \cdot (\mathbf{e}_j \times \mathbf{e}_k), \quad i \neq j \neq k, \quad i, j, k = 1 \text{ to } 7 \tag{4.75}$$

the Jacobian determinant can be expressed in the expanded polynomial form

$$\begin{aligned} J = J_0 &+ J_1\xi + J_2\eta + J_3\zeta + J_4 h_{\eta\zeta} + J_5 h_{\xi\zeta} + J_6 h_{\xi\eta} + J_7\xi^2 + J_8\eta^2 + J_9\zeta^2 + J_{10}\eta^2\zeta + J_{11}\zeta^2\eta \\ &+ J_{12}\zeta^2\xi + J_{13}\xi^2\zeta + J_{14}\xi^2\eta + J_{15}\eta^2\xi + J_{16}h_{\xi\eta\zeta} + J_{17}h_{\zeta\eta}\xi^2 + J_{18}h_{\zeta\xi}\eta^2 + J_{19}h_{\xi\eta}\zeta^2 \end{aligned} \tag{4.76}$$

where

$$\begin{aligned}
&J_0 = p_{123} && J_1 = p_{125} + p_{163} && J_2 = p_{124} + p_{623} && J_3 = p_{523} + p_{143} \\
&J_4 = p_{723} + p_{452} + p_{436} && J_5 = p_{173} + p_{451} + p_{356} && J_6 = p_{127} + p_{416} + p_{256} && J_7 = -p_{156} \\
&J_8 = -p_{426} && J_9 = -p_{453} && J_{10} = p_{247} && J_{11} = -p_{347} \\
&J_{12} = p_{357} && J_{13} = -p_{157} && J_{14} = p_{167} && J_{15} = -p_{267} \\
&J_{16} = 2p_{456} && J_{17} = p_{756} && J_{18} = p_{476} && J_{19} = p_{457}
\end{aligned} \tag{4.77}$$

The form of the Jacobian determinant given by (4.76) facilitates the analytical evaluation of the integrals in the element formulation via the integration of simple polynomial functions over the bi-unit cube ($-1 \leq \xi \leq 1;\ -1 \leq \eta \leq 1;\ -1 \leq \zeta \leq 1$). For example, the element volume is evaluated as

$$V = \int_{\Omega_E} d\Omega_E = \int_{-1}^{1}\int_{-1}^{1}\int_{-1}^{1} J d\xi d\eta d\zeta = 8J_0 + \frac{8}{3}(J_7 + J_8 + J_9) \tag{4.78}$$

4.4.2 Element Kinematics

The displacement field for the element is expressed in the form given by Belytschko and Bachrach (1986)

$$\begin{aligned}
\mathbf{u} = &(a_{0x} + a_{1x}x + a_{2x}y + a_{3x}z + c_{1x}h_{\xi\eta} + c_{2x}h_{\zeta\eta} + c_{3x}h_{\zeta\xi} + c_{4x}h_{\xi\eta\zeta})\mathbf{i} \\
&+ (a_{0y} + a_{1y}x + a_{2y}y + a_{3y}z + c_{1y}h_{\xi\eta} + c_{2y}h_{\zeta\eta} + c_{3y}h_{\zeta\xi} + c_{4y}h_{\xi\eta\zeta})\mathbf{j} \\
&+ (a_{0z} + a_{1z}x + a_{2z}y + a_{3z}z + c_{1z}h_{\xi\eta} + c_{2z}h_{\zeta\eta} + c_{3z}h_{\zeta\xi} + c_{4z}h_{\xi\eta\zeta})\mathbf{k}
\end{aligned} \tag{4.79}$$

where a_{ix}, a_{iy}, a_{ix}, c_{ix}, c_{iy}, and c_{iz} are scalar coefficients, x, y, and z are global coordinates, and

$$h_{\xi\eta} = \xi\eta \tag{4.80}$$
$$h_{\zeta\eta} = \zeta\eta \tag{4.81}$$
$$h_{\zeta\xi} = \zeta\xi \tag{4.82}$$
$$h_{\xi\eta\zeta} = \xi\eta\zeta \tag{4.83}$$

are the local coordinate products. Using this form, the nodal displacements,

$$\mathbf{d}_x = [u_1, u_2, u_3, u_4, u_5, u_6, u_7, u_8]^T \tag{4.84}$$
$$\mathbf{d}_y = [v_1, v_2, v_3, v_4, v_5, v_6, v_7, v_8]^T \tag{4.85}$$
$$\mathbf{d}_z = [w_1, w_2, w_3, w_4, w_5, w_6, w_7, w_8]^T \tag{4.86}$$

can be expressed as

$$\mathbf{d}_x = a_{0x}\mathbf{r} + a_{1x}\mathbf{x} + a_{2x}\mathbf{y} + a_{3x}\mathbf{z} + c_{1x}\mathbf{h}_{\xi\eta} + c_{2x}\mathbf{h}_{\zeta\eta} + c_{3x}\mathbf{h}_{\zeta\xi} + c_{4x}\mathbf{h}_{\xi\eta\zeta} \tag{4.87}$$

$$\mathbf{d}_y = a_{0y}\mathbf{r} + a_{1y}\mathbf{x} + a_{2y}\mathbf{y} + a_{3y}\mathbf{z} + c_{1y}\mathbf{h}_{\xi\eta} + c_{2y}\mathbf{h}_{\zeta\eta} + c_{3y}\mathbf{h}_{\zeta\xi} + c_{4y}\mathbf{h}_{\xi\eta\zeta} \tag{4.88}$$

$$\mathbf{d}_z = a_{0z}\mathbf{r} + a_{1z}\mathbf{x} + a_{2z}\mathbf{y} + a_{3z}\mathbf{z} + c_{1z}\mathbf{h}_{\xi\eta} + c_{2z}\mathbf{h}_{\zeta\eta} + c_{3z}\mathbf{h}_{\zeta\xi} + c_{4z}\mathbf{h}_{\xi\eta\zeta} \tag{4.89}$$

where

$$\mathbf{r} = [1,1,1,1,1,1,1,1]^T \tag{4.90}$$

$$\mathbf{x} = [x_1,x_2,x_3,x_4,x_5,x_6,x_7,x_8]^T \tag{4.91}$$

$$\mathbf{y} = [y_1,y_2,y_3,y_4,y_5,y_6,y_7,y_8]^T \tag{4.92}$$

$$\mathbf{z} = [z_1,z_2,z_3,z_4,z_5,z_6,z_7,z_8]^T \tag{4.93}$$

and

$$\mathbf{h}_{\xi\eta} = h_{\xi\eta}(\boldsymbol{\xi},\boldsymbol{\eta},\boldsymbol{\zeta}) = [1,-1,1,-1,1,-1,1,-1]^T \tag{4.94}$$

$$\mathbf{h}_{\zeta\eta} = h_{\zeta\eta}(\boldsymbol{\xi},\boldsymbol{\eta},\boldsymbol{\zeta}) = [1,1,-1,-1,-1,-1,1,1]^T \tag{4.95}$$

$$\mathbf{h}_{\zeta\xi} = h_{\zeta\xi}(\boldsymbol{\xi},\boldsymbol{\eta},\boldsymbol{\zeta}) = [1,-1,-1,1,-1,1,1,-1]^T \tag{4.96}$$

$$\mathbf{h}_{\xi\eta\zeta} = h_{\xi\eta\zeta}(\boldsymbol{\xi},\boldsymbol{\eta},\boldsymbol{\zeta}) = [-1,1,-1,1,1,-1,1,-1]^T \tag{4.97}$$

with local coordinate vectors

$$\boldsymbol{\xi} = [-1,1,1,-1,-1,1,1,-1]^T \tag{4.98}$$

$$\boldsymbol{\eta} = [-1,-1,1,1,-1,-1,1,1]^T \tag{4.99}$$

$$\boldsymbol{\zeta} = [-1,-1,-1,-1,1,1,1,1]^T \tag{4.100}$$

The kinematic equations for the element are defined in two parts. The first part is obtained by computing the components of the small strain field, $\boldsymbol{\varepsilon}$, from (4.79) as

$$\boldsymbol{\varepsilon} = \tilde{\mathbf{B}}\mathbf{a} \tag{4.101}$$

where

$$\mathbf{a} = [a_{1x},a_{2y},a_{3z},a_{xy},a_{yz},a_{xz},c_{1x},c_{1y},c_{1z},c_{2x},c_{2y},c_{2z},c_{3x},c_{3y},c_{3z},c_{4x},c_{4y},c_{4z}]^T \tag{4.102}$$

with

$$a_{xy} = \frac{1}{2}(a_{2x} + a_{1y}); \qquad a_{yz} = \frac{1}{2}(a_{3y} + a_{2z}); \qquad a_{xz} = \frac{1}{2}(a_{3x} + a_{1z}) \tag{4.103}$$

In (4.101), $\tilde{\mathbf{B}}$ is a 6×18 matrix which can be expressed in terms of 5 sub-matrices as

$$\tilde{\mathbf{B}} = [\mathbf{A}, \mathbf{R}_{\xi\eta}, \mathbf{R}_{\zeta\eta}, \mathbf{R}_{\zeta\xi}, \mathbf{R}_{\xi\eta\zeta}] \tag{4.104}$$

where $\mathbf{A}$ is a 6×6 identity matrix, and the remaining 6×3 sub-matrices are defined as

$$\mathbf{R}_{\xi\eta} = \begin{bmatrix} h_{\xi\eta,x} & 0 & 0 \\ 0 & h_{\xi\eta,y} & 0 \\ 0 & 0 & h_{\xi\eta,z} \\ h_{\xi\eta,y} & h_{\xi\eta,x} & 0 \\ 0 & h_{\xi\eta,z} & h_{\xi\eta,y} \\ h_{\xi\eta,z} & 0 & h_{\xi\eta,x} \end{bmatrix} \tag{4.105}$$

$$\mathbf{R}_{\zeta\eta} = \begin{bmatrix} h_{\zeta\eta,x} & 0 & 0 \\ 0 & h_{\zeta\eta,y} & 0 \\ 0 & 0 & h_{\zeta\eta,z} \\ h_{\zeta\eta,y} & h_{\zeta\eta,x} & 0 \\ 0 & h_{\zeta\eta,z} & h_{\zeta\eta,y} \\ h_{\zeta\eta,z} & 0 & h_{\zeta\eta,x} \end{bmatrix} \tag{4.106}$$

$$\mathbf{R}_{\zeta\xi} = \begin{bmatrix} h_{\zeta\xi,x} & 0 & 0 \\ 0 & h_{\zeta\xi,y} & 0 \\ 0 & 0 & h_{\zeta\xi,z} \\ h_{\zeta\xi,y} & h_{\zeta\xi,x} & 0 \\ 0 & h_{\zeta\xi,z} & h_{\zeta\xi,y} \\ h_{\zeta\xi,z} & 0 & h_{\zeta\xi,x} \end{bmatrix} \tag{4.107}$$

$$\mathbf{R}_{\xi\eta\zeta} = \begin{bmatrix} h_{\xi\eta\zeta,x} & 0 & 0 \\ 0 & h_{\xi\eta\zeta,y} & 0 \\ 0 & 0 & h_{\xi\eta\zeta,z} \\ h_{\xi\eta\zeta,y} & h_{\xi\eta\zeta,x} & 0 \\ 0 & h_{\xi\eta\zeta,z} & h_{\xi\eta\zeta,y} \\ h_{\xi\eta\zeta,z} & 0 & h_{\xi\eta\zeta,x} \end{bmatrix} \tag{4.108}$$

with the derivatives of the local coordinate products defined as (for $\alpha = x, y, z$)

$$h_{\xi\eta,\alpha} = \frac{\partial h_{\xi\eta}}{\partial \alpha} = \xi\eta_{,\alpha} + \eta\xi_{,\alpha} \tag{4.109}$$

$$h_{\zeta\eta,\alpha} = \frac{\partial h_{\zeta\eta}}{\partial \alpha} = \zeta\eta_{,\alpha} + \eta\zeta_{,\alpha} \tag{4.110}$$

$$h_{\zeta\xi,\alpha} = \frac{\partial h_{\zeta\xi}}{\partial \alpha} = \zeta\xi_{,\alpha} + \xi\zeta_{,\alpha} \tag{4.111}$$

$$h_{\xi\eta\zeta,\alpha} = \frac{\partial h_{\xi\eta\zeta}}{\partial \alpha} = \xi\eta\zeta_{,\alpha} + \xi\zeta\eta_{,\alpha} + \eta\zeta\xi_{,\alpha} \tag{4.112}$$

The element kinematic equations are completed by defining the following mapping between the coefficient vector $\mathbf{a}$ and the nodal displacements $\mathbf{d}$

$$\mathbf{a} = \mathbf{L}\mathbf{d} = \begin{bmatrix} \mathbf{b}_x & 0 & 0 \\ 0 & \mathbf{b}_y & 0 \\ 0 & 0 & \mathbf{b}_z \\ \mathbf{b}_y & \mathbf{b}_x & 0 \\ 0 & \mathbf{b}_z & \mathbf{b}_y \\ \mathbf{b}_z & 0 & \mathbf{b}_x \\ \boldsymbol{\gamma}_{\xi\eta} & 0 & 0 \\ 0 & \boldsymbol{\gamma}_{\xi\eta} & 0 \\ 0 & 0 & \boldsymbol{\gamma}_{\xi\eta} \\ \boldsymbol{\gamma}_{\zeta\eta} & 0 & 0 \\ 0 & \boldsymbol{\gamma}_{\zeta\eta} & 0 \\ 0 & 0 & \boldsymbol{\gamma}_{\zeta\eta} \\ \boldsymbol{\gamma}_{\zeta\xi} & 0 & 0 \\ 0 & \boldsymbol{\gamma}_{\zeta\xi} & 0 \\ 0 & 0 & \boldsymbol{\gamma}_{\zeta\xi} \\ \boldsymbol{\gamma}_{\xi\eta\zeta} & 0 & 0 \\ 0 & \boldsymbol{\gamma}_{\xi\eta\zeta} & 0 \\ 0 & 0 & \boldsymbol{\gamma}_{\xi\eta\zeta} \end{bmatrix} \begin{Bmatrix} \mathbf{d}_x \\ \mathbf{d}_y \\ \mathbf{d}_z \end{Bmatrix} \tag{4.113}$$

in which the $\mathbf{b}$-vectors[1] are the derivatives of the linear shape function vector

$$\mathbf{N}(\xi, \eta, \zeta) = \frac{1}{8}\left(\mathbf{r} + \boldsymbol{\xi}\xi + \boldsymbol{\eta}\eta + \boldsymbol{\zeta}\zeta + \mathbf{h}_{\xi\eta}h_{\xi\eta} + \mathbf{h}_{\zeta\eta}h_{\zeta\eta} + \mathbf{h}_{\zeta\xi}h_{\zeta\xi} + \mathbf{h}_{\xi\eta\zeta}h_{\xi\eta\zeta}\right)^T \tag{4.114}$$

averaged over the element domain, i.e., for $\alpha = x, y, z$

$$\mathbf{b}_\alpha = \frac{1}{V}\int_{\Omega_E} \mathbf{N}_{,\alpha}(\xi, \eta, \zeta)\, d\Omega_E \tag{4.115}$$

where V is the element volume as defined in (4.78), and the $\boldsymbol{\gamma}$-vectors are the projection operators of Flanagan and Belytschko (1981), which, using a nomenclature similar to that of Reese (2005), can be expressed as

$$\boldsymbol{\gamma}_{\xi\eta} = \frac{1}{8}\left(\mathbf{G}\mathbf{h}_{\xi\eta}\right)^T \tag{4.116}$$

$$\boldsymbol{\gamma}_{\zeta\eta} = \frac{1}{8}\left(\mathbf{G}\mathbf{h}_{\zeta\eta}\right)^T \tag{4.117}$$

$$\boldsymbol{\gamma}_{\zeta\xi} = \frac{1}{8}\left(\mathbf{G}\mathbf{h}_{\zeta\xi}\right)^T \tag{4.118}$$

$$\boldsymbol{\gamma}_{\xi\eta\zeta} = \frac{1}{8}\left(\mathbf{G}\mathbf{h}_{\xi\eta\zeta}\right)^T \tag{4.119}$$

where

$$\mathbf{G} = \mathbf{1} - \left[\mathbf{b}_x^T, \mathbf{b}_y^T, \mathbf{b}_z^T\right] \begin{Bmatrix} \mathbf{x}^T \\ \mathbf{y}^T \\ \mathbf{z}^T \end{Bmatrix} \tag{4.120}$$

and $\mathbf{1}$ is the 8×8 identity matrix.

Evaluation of the $\mathbf{b}$-vectors involves the volume integrals of the derivatives of the linear shape function vector (4.114), which, for $\alpha = x, y, z$, can be expressed as

$$\mathbf{N}_{,\alpha} = \frac{1}{8}\left(\boldsymbol{\xi}\xi_{,\alpha} + \boldsymbol{\eta}\eta_{,\alpha} + \boldsymbol{\zeta}\zeta_{,\alpha} + \mathbf{h}_{\zeta\eta}h_{\zeta\eta,\alpha} + \mathbf{h}_{\zeta\xi}h_{\zeta\xi,\alpha} + \mathbf{h}_{\xi\eta}h_{\xi\eta,\alpha} + \mathbf{h}_{\xi\eta\zeta}h_{\xi\eta\zeta,\alpha}\right)^T \tag{4.121}$$

From the inverse Jacobian matrix (4.73), the derivatives of the local coordinates (ξ, η, ζ) and local coordinate products $(h_{\zeta\eta}, h_{\zeta\xi}, h_{\xi\eta}, h_{\xi\eta\zeta})$ can be expressed in terms of polynomial functions of the local coordinates. When substituted into (4.121), this facilitates the analytical evaluation of (4.115) via a series of simple polynomial integrals, resulting in

$$\begin{aligned}\mathbf{b}_x = \frac{8}{V}\Bigg(&\left[b_2c_3 - c_2b_3 + \frac{1}{3}(b_6c_5 - c_6b_5)\right]\boldsymbol{\xi} + \left[b_3c_1 - c_3b_1 + \frac{1}{3}(b_4c_6 - c_4b_6)\right]\boldsymbol{\eta} \\ &+ \left[b_1c_2 - c_1b_2 + \frac{1}{3}(b_5c_4 - c_5b_4)\right]\boldsymbol{\zeta} + \frac{1}{3}(b_5c_1 - c_5b_1 + b_2c_4 - c_2b_4)\mathbf{h}_{\xi\eta} \\ &+ \frac{1}{3}(b_6c_2 - c_6b_2 + b_3c_5 - c_3b_5)\mathbf{h}_{\zeta\eta} + \frac{1}{3}(b_1c_6 - c_1b_6 + b_4c_3 - c_4b_3)\mathbf{h}_{\zeta\xi}\Bigg)\end{aligned} \tag{4.122}$$

---

[1] In the 2D single-point element formulation, the $\mathbf{b}$-vectors are defined as the derivatives of the shape function vector at the center of the element. In 3D, a similar definition has been found to be insufficient, leading to an unstable element. This observation corresponds with the work of Belytschko and Bindeman (1993), who introduced the volume-averaged form adopted in (4.115) as a remedy.

$$\mathbf{b}_y = \frac{8}{V}\left(\left[c_2a_3 - a_2c_3 + \frac{1}{3}(c_6a_5 - a_6c_5)\right]\boldsymbol{\xi} + \left[c_3a_1 - a_3c_1 + \frac{1}{3}(c_4a_6 - a_4c_6)\right]\boldsymbol{\eta} \right.$$
$$+ \left[c_1a_2 - a_1c_2 + \frac{1}{3}(c_5a_4 - a_5c_4)\right]\boldsymbol{\zeta} + \frac{1}{3}(c_5a_1 - a_5c_1 + c_2a_4 - a_2c_4)\mathbf{h}_{\xi\eta}$$
$$\left. + \frac{1}{3}(c_6a_2 - a_6c_2 + c_3a_5 - a_3c_5)\mathbf{h}_{\zeta\eta} + \frac{1}{3}(c_1a_6 - a_1c_6 + c_4a_3 - a_4c_3)\mathbf{h}_{\zeta\xi}\right) \quad (4.123)$$

$$\mathbf{b}_z = \frac{8}{V}\left(\left[b_2c_3 - c_2b_3 + \frac{1}{3}(b_6c_5 - c_6b_5)\right]\boldsymbol{\xi} + \left[a_3b_1 - b_3a_1 + \frac{1}{3}(a_4b_6 - b_4a_6)\right]\boldsymbol{\eta} \right.$$
$$+ \left[a_1b_2 - b_1a_2 + \frac{1}{3}(a_5b_4 - b_5a_4)\right]\boldsymbol{\zeta} + \frac{1}{3}(a_5b_1 - b_5a_1 + a_2b_4 - b_2a_4)\mathbf{h}_{\xi\eta}$$
$$\left. + \frac{1}{3}(a_6b_2 - b_6a_2 + a_3b_5 - b_3a_5)\mathbf{h}_{\zeta\eta} + \frac{1}{3}(a_1b_6 - b_1a_6 + a_4b_3 - b_4a_3)\mathbf{h}_{\zeta\xi}\right) \quad (4.124)$$

in which the a_n-, b_n-, and c_n-coefficients are taken from the isoparametric mapping of (4.70).

The full kinematic link between the small strain field and nodal displacements is expressed by combining (4.101) and (4.113), resulting in

$$\boldsymbol{\varepsilon} = \tilde{\mathbf{B}}\mathbf{L}\mathbf{d} \quad (4.125)$$

This form for the element kinematics provides the means to decompose the strain field into two portions, a constant portion, and a non-constant (stabilizing) portion associated with the hourglass modes for the element. This decomposition is expressed as

$$\boldsymbol{\varepsilon} = (\mathbf{B}_0 + \mathbf{F}\mathbf{L}_b)\,\mathbf{d} \quad (4.126)$$

The constant portion, $\mathbf{B}_0$, is the product of the sub-matrix $\mathbf{A}$ in the first six columns of $\tilde{\mathbf{B}}$ with the first three rows of $\mathbf{L}$, and is equivalent to the standard kinematic matrix $\mathbf{B}$ evaluated at the center of the element. The 6×24 sub-matrix $\mathbf{B}_0 = [\mathbf{B}_{0\,1}, \ldots, \mathbf{B}_{0\,I}, \ldots, \mathbf{B}_{0\,8}]$ has the form

$$\mathbf{B}_{0\,I} = \begin{bmatrix} \mathbf{b}_{x\,I} & 0 & 0 \\ 0 & \mathbf{b}_{y\,I} & 0 \\ 0 & 0 & \mathbf{b}_{z\,I} \\ \mathbf{b}_{y\,I} & \mathbf{b}_{x\,I} & 0 \\ 0 & \mathbf{b}_{z\,I} & \mathbf{b}_{y\,I} \\ \mathbf{b}_{z\,I} & 0 & \mathbf{b}_{x\,I} \end{bmatrix} \quad (4.127)$$

where, e.g., $\mathbf{b}_{x\,I}$ is component I of the 1×8 vector $\mathbf{b}_x$.

The non-constant portion of (4.126) involves the sub-matrices formed by the remaining columns of $\tilde{\mathbf{B}}$, here referred to as $\mathbf{F}$, and the remaining rows of $\mathbf{L}$, which are designated as

$\mathbf{L}_b$. The 6×12 sub-matrix $\mathbf{F}$ is given by

$$\mathbf{F} = [\mathbf{R}_{\xi\eta}, \mathbf{R}_{\zeta\eta}, \mathbf{R}_{\zeta\xi}, \mathbf{R}_{\xi\eta\zeta}] \tag{4.128}$$

and the 12×24 sub-matrix $\mathbf{L}_b = [\mathbf{L}_{b\,1}, \ldots, \mathbf{L}_{b\,I}, \ldots, \mathbf{L}_{b\,8}]$ has the form

$$\mathbf{L}_{b\,I} = \begin{bmatrix} \boldsymbol{\gamma}_{\xi\eta\,I} & 0 & 0 \\ 0 & \boldsymbol{\gamma}_{\xi\eta\,I} & 0 \\ 0 & 0 & \boldsymbol{\gamma}_{\xi\eta\,I} \\ \boldsymbol{\gamma}_{\zeta\eta\,I} & 0 & 0 \\ 0 & \boldsymbol{\gamma}_{\zeta\eta\,I} & 0 \\ 0 & 0 & \boldsymbol{\gamma}_{\zeta\eta\,I} \\ \boldsymbol{\gamma}_{\zeta\xi\,I} & 0 & 0 \\ 0 & \boldsymbol{\gamma}_{\zeta\xi\,I} & 0 \\ 0 & 0 & \boldsymbol{\gamma}_{\zeta\xi\,I} \\ \boldsymbol{\gamma}_{\xi\eta\zeta\,I} & 0 & 0 \\ 0 & \boldsymbol{\gamma}_{\xi\eta\zeta\,I} & 0 \\ 0 & 0 & \boldsymbol{\gamma}_{\xi\eta\zeta\,I} \end{bmatrix} \tag{4.129}$$

where, e.g., $\boldsymbol{\gamma}_{\xi\eta\,I}$ is component I of the 1×8 vector $\boldsymbol{\gamma}_{\xi\eta}$.

4.4.3 Assumed Strain Field

The kinematic relation presented in (4.126) facilitates efficiency in the element by allowing for separate evaluation of the constant and non-constant portions of the strain field, however, the locking phenomena associated with the non-constant portion must still be addressed for the purposes of accuracy. The non-constant portion of the strain field is modified based on the enhanced assumed strain concept (Simo and Armero, 1992; Simo et al., 1993) such that parasitic shear and volumetric locking are eliminated.

After Reese (2005), the enhanced strain field concept is reduced from a two-field formulation to an equivalent reduced-integration one-field formulation. The resulting modification to the element kinematic relation (4.126) is expressed as

$$\boldsymbol{\varepsilon} = \left[\mathbf{B}_0 + \left(\hat{\mathbf{F}} - \mathbf{F}_{\text{enh}}\mathbf{K}_{ww}^{-1}\mathbf{K}_{wu}\right)\mathbf{L}_b\right]\mathbf{d} \tag{4.130}$$

where

$$\mathbf{F}_{\text{enh}} = \begin{bmatrix} \xi_{,x}\,\xi & 0 & 0 & \eta_{,x}\,\eta & 0 & 0 & \zeta_{,x}\,\zeta & 0 & 0 \\ 0 & \xi_{,y}\,\xi & 0 & 0 & \eta_{,y}\,\eta & 0 & 0 & \zeta_{,y}\,\zeta & 0 \\ 0 & 0 & \xi_{,z}\,\xi & 0 & 0 & \eta_{,z}\,\eta & 0 & 0 & \zeta_{,z}\,\zeta \\ \xi_{,y}\,\xi & \xi_{,x}\,\xi & 0 & \eta_{,y}\,\eta & \eta_{,x}\,\eta & 0 & \zeta_{,y}\,\zeta & \zeta_{,x}\,\zeta & 0 \\ 0 & \xi_{,z}\,\xi & \xi_{,y}\,\xi & 0 & \eta_{,z}\,\eta & \eta_{,y}\,\eta & 0 & \zeta_{,z}\,\zeta & \zeta_{,y}\,\zeta \\ \xi_{,z}\,\xi & 0 & \xi_{,x}\,\xi & \eta_{,z}\,\eta & 0 & \eta_{,x}\,\eta & \zeta_{,z}\,\zeta & 0 & \zeta_{,x}\,\zeta \end{bmatrix} \tag{4.131}$$

In (4.130), the kinematic hourglass matrix (4.128) is modified to eliminate the volumetric locking associated with the trilinear terms in the volumetric portion of (4.108). The modified matrix is defined as

$$\hat{\mathbf{F}} = [\mathbf{R}_{\xi\eta}, \mathbf{R}_{\zeta\eta}, \mathbf{R}_{\zeta\xi}, \hat{\mathbf{R}}_{\xi\eta\zeta}] \tag{4.132}$$

with

$$\hat{\mathbf{R}}_{\xi\eta\zeta} = \begin{bmatrix} 0 & 0 & 0 \\ 0 & 0 & 0 \\ 0 & 0 & 0 \\ h_{\xi\eta\zeta,y} & h_{\xi\eta\zeta,x} & 0 \\ 0 & h_{\xi\eta\zeta,z} & h_{\xi\eta\zeta,y} \\ h_{\xi\eta\zeta,z} & 0 & h_{\xi\eta\zeta,x} \end{bmatrix} \tag{4.133}$$

The remaining terms of (4.130),

$$\mathbf{K}_{ww} = \int_{\Omega_E} \mathbf{F}_{\text{enh}}^T \hat{\mathbb{C}} \mathbf{F}_{\text{enh}} d\Omega_E \tag{4.134}$$

$$\mathbf{K}_{wu} = \int_{\Omega_E} \mathbf{F}_{\text{enh}}^T \hat{\mathbb{C}} \mathbf{F}^\star d\Omega_E \tag{4.135}$$

where $\hat{\mathbb{C}}$ is the initial material tangent operator, and

$$\mathbf{F}^\star = [\mathbf{R}_{\xi\eta}, \mathbf{R}_{\zeta\eta}, \mathbf{R}_{\zeta\xi}, \mathbf{0}] \tag{4.136}$$

where $\mathbf{0}$ is a 6×3 zero matrix, result from the addition of the internal degrees of freedom corresponding to the enhanced assumed strain formulation. The evaluation of $\mathbf{K}_{ww}$ and $\mathbf{K}_{wu}$ is described in the following section.

4.4.4 Element Stiffness

Using the kinematic basis given by (4.130), the element stiffness, $\mathbf{K}_E$, is decomposed into the sum

$$\mathbf{K}_E = \mathbf{K}_0 + \mathbf{K}_{\text{stab}} \tag{4.137}$$

where $\mathbf{K}_0$ and $\mathbf{K}_{\text{stab}}$ are the constant and stabilization portions, respectively. The constant part of the element stiffness is evaluated using single-point integration as

$$\mathbf{K}_0 = \int_{\Omega_E} \mathbf{B}_0^T \mathbb{C} \mathbf{B}_0 d\Omega_E = V \mathbf{B}_0^T \mathbb{C} \mathbf{B}_0 \tag{4.138}$$

where $\mathbb{C}$ is the current material tangent operator and V is the element volume as defined in (4.78). This portion of the element stiffness is updated during each step of the analysis.

The stabilization stiffness matrix for the element,

$$\mathbf{K}_{\text{stab}} = \mathbf{L}_b^T \left[\int_{\Omega_E} \mathbf{F}^T \hat{\mathbb{C}} \mathbf{F} d\Omega_E - \mathbf{K}_{wu}^T \mathbf{K}_{ww}^{-T} \left(\int_{\Omega_E} \mathbf{F}_{\text{enh}}^T \hat{\mathbb{C}} \mathbf{F}_{\text{enh}} d\Omega_E \right) \mathbf{K}_{ww}^{-1} \mathbf{K}_{wu} \right] \mathbf{L}_b \tag{4.139}$$

where $\hat{\mathbb{C}}$ is the initial material tangent operator, is evaluated through analytical integration using the polynomial expansion of the Jacobian determinant given in (4.76). The stabilization stiffness matrix is assembled only upon initialization of the element.

The evaluation of the first integral term in (4.139)

$$\int_{\Omega_E} \hat{\mathbf{F}}^T \hat{\mathbb{C}} \hat{\mathbf{F}} d\Omega_E = \int_{-1}^{1} \int_{-1}^{1} \int_{-1}^{1} \hat{\mathbf{F}}^T \hat{\mathbb{C}} \hat{\mathbf{F}} J d\xi d\eta d\zeta \tag{4.140}$$

involves multiplying the components of the matrix product $\hat{\mathbf{F}}^T \hat{\mathbb{C}} \hat{\mathbf{F}}$ with the expanded Jacobian determinant of (4.76). Integration of the resulting terms leads to the following definitions

$$H_{\xi\eta}^{\alpha\beta} = \int_{\Omega_E} h_{\xi\eta,\alpha} h_{\xi\eta,\beta} d\Omega_E = \mu_2 \xi_{,\alpha}\, \xi_{,\beta} + \mu_1 \eta_{,\alpha}\, \eta_{,\beta} + \mu_6 \left(\xi_{,\alpha}\, \eta_{,\beta} + \eta_{,\alpha}\, \xi_{,\beta} \right) \tag{4.141}$$

$$H_{\zeta\eta}^{\alpha\beta} = \int_{\Omega_E} h_{\zeta\eta,\alpha} h_{\zeta\eta,\beta} d\Omega_E = \mu_3 \eta_{,\alpha}\, \eta_{,\beta} + \mu_2 \zeta_{,\alpha}\, \zeta_{,\beta} + \mu_4 \left(\eta_{,\alpha}\, \zeta_{,\beta} + \zeta_{,\alpha}\, \eta_{,\beta} \right) \tag{4.142}$$

$$H_{\zeta\xi}^{\alpha\beta} = \int_{\Omega_E} h_{\zeta\xi,\alpha} h_{\zeta\xi,\beta} d\Omega_E = \mu_3 \xi_{,\alpha}\, \xi_{,\beta} + \mu_1 \zeta_{,\alpha}\, \zeta_{,\beta} + \mu_5 \left(\xi_{,\alpha}\, \zeta_{,\beta} + \zeta_{,\alpha}\, \xi_{,\beta} \right) \tag{4.143}$$

$$\begin{aligned} H_{\xi\eta\zeta}^{\alpha\beta} = \int_{\Omega_E} h_{\xi\eta\zeta,\alpha} h_{\xi\eta\zeta,\beta} d\Omega_E &= \mu_{14} \xi_{,\alpha}\, \xi_{,\beta} + \mu_{15} \eta_{,\alpha}\, \eta_{,\beta} + \mu_{13} \zeta_{,\alpha}\, \zeta_{,\beta} + \mu_{18} \left(\xi_{,\alpha}\, \eta_{,\beta} + \eta_{,\alpha}\, \xi_{,\beta} \right) \\ &\quad + \mu_{17} \left(\xi_{,\alpha}\, \zeta_{,\beta} + \zeta_{,\alpha}\, \xi_{,\beta} \right) + \mu_{16} \left(\eta_{,\alpha}\, \zeta_{,\beta} + \zeta_{,\alpha}\, \eta_{,\beta} \right) \end{aligned} \tag{4.144}$$

$$I_{\eta\eta}^{\alpha\beta} = \int_{\Omega_E} h_{\xi\eta,\alpha} h_{\zeta\eta,\beta} d\Omega_E = \mu_2 \xi_{,\alpha}\, \zeta_{,\beta} + \mu_4 \xi_{,\alpha}\, \eta_{,\beta} + \mu_5 \eta_{,\alpha}\, \eta_{,\beta} + \mu_6 \eta_{,\alpha}\, \zeta_{,\beta} \tag{4.145}$$

$$I_{\xi\xi}^{\alpha\beta} = \int_{\Omega_E} h_{\xi\eta,\alpha} h_{\zeta\xi,\beta} d\Omega_E = \mu_1 \eta_{,\alpha}\, \zeta_{,\beta} + \mu_4 \xi_{,\alpha}\, \xi_{,\beta} + \mu_5 \eta_{,\alpha}\, \xi_{,\beta} + \mu_6 \xi_{,\alpha}\, \zeta_{,\beta} \tag{4.146}$$

$$I_{\zeta\zeta}^{\alpha\beta} = \int_{\Omega_E} h_{\zeta\eta,\alpha} h_{\zeta\xi,\beta} d\Omega_E = \mu_3 \eta_{,\alpha}\, \xi_{,\beta} + \mu_4 \zeta_{,\alpha}\, \xi_{,\beta} + \mu_5 \eta_{,\alpha}\, \zeta_{,\beta} + \mu_6 \zeta_{,\alpha}\, \zeta_{,\beta} \tag{4.147}$$

$$\begin{aligned} I_{\xi\eta}^{\alpha\beta} = \int_{\Omega_E} h_{\xi\eta\zeta,\alpha} h_{\xi\eta,\beta} d\Omega_E &= \mu_{11} \xi_{,\alpha}\, \xi_{,\beta} + \mu_{12} \eta_{,\alpha}\, \eta_{,\beta} + \mu_{10} \zeta_{,\alpha}\, \eta_{,\beta} \\ &\quad + \mu_8 \zeta_{,\alpha}\, \xi_{,\beta} + \frac{8}{27} J_{16} \left(\xi_{,\alpha}\, \eta_{,\beta} + \eta_{,\alpha}\, \xi_{,\beta} \right) \end{aligned} \tag{4.148}$$

$$\begin{aligned} I_{\zeta\eta}^{\alpha\beta} = \int_{\Omega_E} h_{\xi\eta\zeta,\alpha} h_{\zeta\eta,\beta} d\Omega_E &= \mu_9 \xi_{,\alpha}\, \eta_{,\beta} + \mu_{11} \xi_{,\alpha}\, \zeta_{,\beta} + \mu_7 \eta_{,\alpha}\, \eta_{,\beta} \\ &\quad + \mu_8 \zeta_{,\alpha}\, \zeta_{,\beta} + \frac{8}{27} J_{16} \left(\eta_{,\alpha}\, \zeta_{,\beta} + \zeta_{,\alpha}\, \eta_{,\beta} \right) \end{aligned} \tag{4.149}$$

$$\begin{aligned} I_{\zeta\xi}^{\alpha\beta} = \int_{\Omega_E} h_{\xi\eta\zeta,\alpha} h_{\zeta\xi,\beta} d\Omega_E &= \mu_9 \xi_{,\alpha}\, \xi_{,\beta} + \mu_7 \eta_{,\alpha}\, \xi_{,\beta} + \mu_{12} \eta_{,\alpha}\, \zeta_{,\beta} \\ &\quad + \mu_{10} \zeta_{,\alpha}\, \zeta_{,\beta} + \frac{8}{27} J_{16} \left(\xi_{,\alpha}\, \zeta_{,\beta} + \zeta_{,\alpha}\, \xi_{,\beta} \right) \end{aligned} \tag{4.150}$$

for $\alpha, \beta = x, y, z$.

The H-terms in (4.141)-(4.144) are commutative in terms of x, y, and z, i.e., $H_{\xi\eta}^{\alpha\beta} = H_{\xi\eta}^{\beta\alpha}$, while the I-terms of (4.145)-(4.150) are not, i.e., $I_{\xi\zeta}^{\alpha\beta} \neq I_{\xi\zeta}^{\beta\alpha}$. The μ-coefficients in (4.141)-(4.150) are combinations of the J_n-coefficients of (4.76) and (4.77). These new terms are defined as

$$\mu_1 = 8 \left(\frac{1}{3} J_0 + \frac{1}{5} J_7 + \frac{1}{9} J_8 + \frac{1}{9} J_9 \right) \tag{4.151}$$

$$\mu_2 = 8 \left(\frac{1}{3} J_0 + \frac{1}{5} J_8 + \frac{1}{9} J_7 + \frac{1}{9} J_9 \right) \tag{4.152}$$

$$\mu_3 = 8 \left(\frac{1}{3} J_0 + \frac{1}{5} J_9 + \frac{1}{9} J_7 + \frac{1}{9} J_8 \right) \tag{4.153}$$

$$\mu_4 = 8 \left(\frac{1}{9} J_4 + \frac{1}{27} J_{17} \right) \tag{4.154}$$

$$\mu_5 = 8 \left(\frac{1}{9} J_5 + \frac{1}{27} J_{18} \right) \tag{4.155}$$

$$\mu_6 = 8\left(\frac{1}{9}J_6 + \frac{1}{27}J_{19}\right) \tag{4.156}$$

$$\mu_7 = 8\left(\frac{1}{9}J_1 + \frac{1}{15}J_{12} + \frac{1}{27}J_{15}\right) \tag{4.157}$$

$$\mu_8 = 8\left(\frac{1}{9}J_1 + \frac{1}{15}J_{15} + \frac{1}{27}J_{12}\right) \tag{4.158}$$

$$\mu_9 = 8\left(\frac{1}{9}J_2 + \frac{1}{15}J_{11} + \frac{1}{27}J_{14}\right) \tag{4.159}$$

$$\mu_{10} = 8\left(\frac{1}{9}J_2 + \frac{1}{15}J_{14} + \frac{1}{27}J_{11}\right) \tag{4.160}$$

$$\mu_{11} = 8\left(\frac{1}{9}J_3 + \frac{1}{15}J_{10} + \frac{1}{27}J_{13}\right) \tag{4.161}$$

$$\mu_{12} = 8\left(\frac{1}{9}J_3 + \frac{1}{15}J_{13} + \frac{1}{27}J_{10}\right) \tag{4.162}$$

$$\mu_{13} = 8\left(\frac{1}{9}J_0 + \frac{1}{15}J_7 + \frac{1}{15}J_8 + \frac{1}{27}J_9\right) \tag{4.163}$$

$$\mu_{14} = 8\left(\frac{1}{9}J_0 + \frac{1}{15}J_8 + \frac{1}{15}J_9 + \frac{1}{27}J_7\right) \tag{4.164}$$

$$\mu_{15} = 8\left(\frac{1}{9}J_0 + \frac{1}{15}J_7 + \frac{1}{15}J_9 + \frac{1}{27}J_8\right) \tag{4.165}$$

$$\mu_{16} = 8\left(\frac{1}{27}J_4 + \frac{64}{45}J_{17}\right) \tag{4.166}$$

$$\mu_{17} = 8\left(\frac{1}{27}J_5 + \frac{64}{45}J_{18}\right) \tag{4.167}$$

$$\mu_{18} = 8\left(\frac{1}{27}J_6 + \frac{64}{45}J_{19}\right) \tag{4.168}$$

The full evaluation of (4.140) yields a symmetric 12×12 matrix which can be expressed in terms of sixteen 3×3 sub-matrices as

$$\int_{\Omega_E} \mathbf{F}^T \hat{\mathbb{C}} \mathbf{F} d\Omega_E = \begin{bmatrix} \mathbf{K}_{11} & \mathbf{K}_{12} & \mathbf{K}_{13} & \mathbf{K}_{14} \\ \mathbf{K}_{21} & \mathbf{K}_{22} & \mathbf{K}_{23} & \mathbf{K}_{24} \\ \mathbf{K}_{31} & \mathbf{K}_{32} & \mathbf{K}_{33} & \mathbf{K}_{34} \\ \mathbf{K}_{41} & \mathbf{K}_{42} & \mathbf{K}_{43} & \mathbf{K}_{44} \end{bmatrix} \tag{4.169}$$

The sub-matrices in this array are defined as

$$\mathbf{K}_{11} = \begin{bmatrix} C_1 H^{xx}_{\xi\eta} + C_3(H^{yy}_{\xi\eta} + H^{zz}_{\xi\eta}) & C_4 H^{xy}_{\xi\eta} & C_4 H^{xz}_{\xi\eta} \\ C_4 H^{xy}_{\xi\eta} & C_1 H^{yy}_{\xi\eta} + C_3(H^{xx}_{\xi\eta} + H^{zz}_{\xi\eta}) & C_4 H^{yz}_{\xi\eta} \\ C_4 H^{xz}_{\xi\eta} & C_4 H^{yz}_{\xi\eta} & C_1 H^{zz}_{\xi\eta} + C_3(H^{xx}_{\xi\eta} + H^{yy}_{\xi\eta}) \end{bmatrix} \tag{4.170}$$

$$\mathbf{K}_{12} = \mathbf{K}^T_{21} = \begin{bmatrix} C_1 I^{xx}_{\eta\eta} + C_3(I^{yy}_{\eta\eta} + I^{zz}_{\eta\eta}) & C_2 I^{xy}_{\eta\eta} + C_3 I^{yx}_{\eta\eta} & C_2 I^{xz}_{\eta\eta} + C_3 I^{zx}_{\eta\eta} \\ C_2 I^{yx}_{\eta\eta} + C_3 I^{xy}_{\eta\eta} & C_1 I^{yy}_{\eta\eta} + C_3(I^{xx}_{\eta\eta} + I^{zz}_{\eta\eta}) & C_2 I^{yz}_{\eta\eta} + C_3 I^{zy}_{\eta\eta} \\ C_2 I^{zx}_{\eta\eta} + C_3 I^{xz}_{\eta\eta} & C_2 I^{zy}_{\eta\eta} + C_3 I^{yz}_{\eta\eta} & C_1 I^{zz}_{\eta\eta} + C_3(I^{xx}_{\eta\eta} + I^{yy}_{\eta\eta}) \end{bmatrix} \tag{4.171}$$

$$\mathbf{K}_{13} = \mathbf{K}^T_{31} = \begin{bmatrix} C_1 I^{xx}_{\xi\xi} + C_3(I^{yy}_{\xi\xi} + I^{zz}_{\xi\xi}) & C_2 I^{xy}_{\xi\xi} + C_3 I^{yx}_{\xi\xi} & C_2 I^{xz}_{\xi\xi} + C_3 I^{zx}_{\xi\xi} \\ C_2 I^{yx}_{\xi\xi} + C_3 I^{xy}_{\xi\xi} & C_1 I^{yy}_{\xi\xi} + C_3(I^{xx}_{\xi\xi} + I^{zz}_{\xi\xi}) & C_2 I^{yz}_{\xi\xi} + C_3 I^{zy}_{\xi\xi} \\ C_2 I^{zx}_{\xi\xi} + C_3 I^{xz}_{\xi\xi} & C_2 I^{zy}_{\xi\xi} + C_3 I^{yz}_{\xi\xi} & C_1 I^{zz}_{\xi\xi} + C_3(I^{xx}_{\xi\xi} + I^{yy}_{\xi\xi}) \end{bmatrix} \tag{4.172}$$

$$\mathbf{K}_{14} = \mathbf{K}^T_{41} = \begin{bmatrix} C_3(I^{yy}_{\xi\eta} + I^{zz}_{\xi\eta}) & C_3 I^{xy}_{\xi\eta} & C_3 I^{xz}_{\xi\eta} \\ C_3 I^{yx}_{\xi\eta} & C_3(I^{xx}_{\xi\eta} + I^{zz}_{\xi\eta}) & C_3 I^{yz}_{\xi\eta} \\ C_3 I^{zx}_{\xi\eta} & C_3 I^{zy}_{\xi\eta} & C_3(I^{xx}_{\xi\eta} + I^{yy}_{\xi\eta}) \end{bmatrix} \tag{4.173}$$

$$\mathbf{K}_{22} = \begin{bmatrix} C_1 H^{xx}_{\zeta\eta} + C_3(H^{yy}_{\zeta\eta} + H^{zz}_{\zeta\eta}) & C_4 H^{xy}_{\zeta\eta} & C_4 H^{xz}_{\zeta\eta} \\ C_4 H^{xy}_{\zeta\eta} & C_1 H^{yy}_{\zeta\eta} + C_3(H^{xx}_{\zeta\eta} + H^{zz}_{\zeta\eta}) & C_4 H^{yz}_{\zeta\eta} \\ C_4 H^{xz}_{\zeta\eta} & C_4 H^{yz}_{\zeta\eta} & C_1 H^{zz}_{\zeta\eta} + C_3(H^{xx}_{\zeta\eta} + H^{yy}_{\zeta\eta}) \end{bmatrix} \tag{4.174}$$

$$\mathbf{K}_{23} = \mathbf{K}^T_{32} = \begin{bmatrix} C_1 I^{xx}_{\zeta\zeta} + C_3(I^{yy}_{\zeta\zeta} + I^{zz}_{\zeta\zeta}) & C_2 I^{xy}_{\zeta\zeta} + C_3 I^{yx}_{\zeta\zeta} & C_2 I^{xz}_{\zeta\zeta} + C_3 I^{zx}_{\zeta\zeta} \\ C_2 I^{yx}_{\zeta\zeta} + C_3 I^{xy}_{\zeta\zeta} & C_1 I^{yy}_{\zeta\zeta} + C_3(I^{xx}_{\zeta\zeta} + I^{zz}_{\zeta\zeta}) & C_2 I^{yz}_{\zeta\zeta} + C_3 I^{zy}_{\zeta\zeta} \\ C_2 I^{zx}_{\zeta\zeta} + C_3 I^{xz}_{\zeta\zeta} & C_2 I^{zy}_{\zeta\zeta} + C_3 I^{yz}_{\zeta\zeta} & C_1 I^{zz}_{\zeta\zeta} + C_3(I^{xx}_{\zeta\zeta} + I^{yy}_{\zeta\zeta}) \end{bmatrix} \tag{4.175}$$

$$\mathbf{K}_{24} = \mathbf{K}^T_{42} = \begin{bmatrix} C_3(I^{yy}_{\zeta\eta} + I^{zz}_{\zeta\eta}) & C_3 I^{xy}_{\zeta\eta} & C_3 I^{xz}_{\zeta\eta} \\ C_3 I^{yx}_{\zeta\eta} & C_3(I^{xx}_{\zeta\eta} + I^{zz}_{\zeta\eta}) & C_3 I^{yz}_{\zeta\eta} \\ C_3 I^{zx}_{\zeta\eta} & C_3 I^{zy}_{\zeta\eta} & C_3(I^{xx}_{\zeta\eta} + I^{yy}_{\zeta\eta}) \end{bmatrix} \tag{4.176}$$

$$\mathbf{K}_{33} = \begin{bmatrix} C_1 H^{xx}_{\zeta\xi} + C_3(H^{yy}_{\zeta\xi} + H^{zz}_{\zeta\xi}) & C_4 H^{xy}_{\zeta\xi} & C_4 H^{xz}_{\zeta\xi} \\ C_4 H^{xy}_{\zeta\xi} & C_1 H^{yy}_{\zeta\xi} + C_3(H^{xx}_{\zeta\xi} + H^{zz}_{\zeta\xi}) & C_4 H^{yz}_{\zeta\xi} \\ C_4 H^{xz}_{\zeta\xi} & C_4 H^{yz}_{\zeta\xi} & C_1 H^{zz}_{\zeta\xi} + C_3(H^{xx}_{\zeta\xi} + H^{yy}_{\zeta\xi}) \end{bmatrix} \tag{4.177}$$

$$\mathbf{K}_{34} = \mathbf{K}^T_{43} = \begin{bmatrix} C_3(I^{yy}_{\zeta\xi} + I^{zz}_{\zeta\xi}) & C_3 I^{xy}_{\zeta\xi} & C_3 I^{xz}_{\zeta\xi} \\ C_3 I^{yx}_{\zeta\xi} & C_3(I^{xx}_{\zeta\xi} + I^{zz}_{\zeta\xi}) & C_3 I^{yz}_{\zeta\xi} \\ C_3 I^{zx}_{\zeta\xi} & C_3 I^{zy}_{\zeta\xi} & C_3(I^{xx}_{\zeta\xi} + I^{yy}_{\zeta\xi}) \end{bmatrix} \tag{4.178}$$

$$\mathbf{K}_{44} = \begin{bmatrix} C_3(H^{yy}_{\xi\eta\zeta} + H^{zz}_{\xi\eta\zeta}) & C_3 H^{xy}_{\xi\eta\zeta} & C_3 H^{xz}_{\xi\eta\zeta} \\ C_3 H^{xy}_{\xi\eta\zeta} & C_3(H^{xx}_{\xi\eta\zeta} + H^{zz}_{\xi\eta\zeta}) & C_3 H^{yz}_{\xi\eta\zeta} \\ C_3 H^{xz}_{\xi\eta\zeta} & C_3 H^{yz}_{\xi\eta\zeta} & C_3(H^{xx}_{\xi\eta\zeta} + H^{yy}_{\xi\eta}) \end{bmatrix} \tag{4.179}$$

In the sub-matrices above, the C-coefficients are defined as

$$C_1 = \kappa + \frac{4}{3}G \tag{4.180}$$

$$C_2 = \kappa - \frac{2}{3}G \tag{4.181}$$

$$C_3 = G \tag{4.182}$$

$$C_4 = C_2 + C_3 = \kappa + \frac{1}{3}G \tag{4.183}$$

where κ and G are the bulk and shear moduli of the solid phase, respectively.

The evaluation of the second integral term in (4.139)

$$\mathbf{K}^T_{wu}\mathbf{K}^{-T}_{ww}\left(\int_{\Omega_E} \mathbf{F}^T_{\text{enh}}\hat{\mathbb{C}}\mathbf{F}_{\text{enh}}d\Omega_E\right)\mathbf{K}^{-1}_{ww}\mathbf{K}_{wu} \tag{4.184}$$

is conducted in a similar manner. This evaluation is simplified by recognizing that the integral inside the parentheses is equal to $\mathbf{K}_{ww}$, see (4.134). Making this substitution, and noting that $\mathbf{K}_{ww}$ is symmetric, simplifies (4.184) to

$$\mathbf{K}^T_{wu}\mathbf{K}^{-T}_{ww}\mathbf{K}_{wu} \tag{4.185}$$

The array $\mathbf{K}_{ww}$ is a 9×9 matrix which can be expressed as

$$\mathbf{K}_{ww} = \begin{bmatrix} \mu_1 \begin{bmatrix} T^{xx}_{\xi\xi} & T^{xy}_{\xi\xi} & T^{xz}_{\xi\xi} \\ T^{xy}_{\xi\xi} & T^{yy}_{\xi\xi} & T^{yz}_{\xi\xi} \\ T^{xz}_{\xi\xi} & T^{yz}_{\xi\xi} & T^{zz}_{\xi\xi} \end{bmatrix} & \mu_6 \begin{bmatrix} T^{xx}_{\xi\eta} & T^{xy}_{\xi\eta} & T^{xz}_{\xi\eta} \\ T^{yx}_{\xi\eta} & T^{yy}_{\xi\eta} & T^{yz}_{\xi\eta} \\ T^{zx}_{\xi\eta} & T^{zy}_{\xi\eta} & T^{zz}_{\xi\eta} \end{bmatrix} & \mu_5 \begin{bmatrix} T^{xx}_{\xi\zeta} & T^{xy}_{\xi\zeta} & T^{xz}_{\xi\zeta} \\ T^{yx}_{\xi\zeta} & T^{yy}_{\xi\zeta} & T^{yz}_{\xi\zeta} \\ T^{zx}_{\xi\zeta} & T^{zy}_{\xi\zeta} & T^{zz}_{\xi\zeta} \end{bmatrix} \\ & \mu_2 \begin{bmatrix} T^{xx}_{\eta\eta} & T^{xy}_{\eta\eta} & T^{xz}_{\eta\eta} \\ T^{xy}_{\eta\eta} & T^{yy}_{\eta\eta} & T^{yz}_{\eta\eta} \\ T^{xz}_{\eta\eta} & T^{yz}_{\eta\eta} & T^{zz}_{\eta\eta} \end{bmatrix} & \mu_4 \begin{bmatrix} T^{xx}_{\eta\zeta} & T^{xy}_{\eta\zeta} & T^{xz}_{\eta\zeta} \\ T^{yx}_{\eta\zeta} & T^{yy}_{\eta\zeta} & T^{yz}_{\eta\zeta} \\ T^{zx}_{\eta\zeta} & T^{zy}_{\eta\zeta} & T^{zz}_{\eta\zeta} \end{bmatrix} \\ & & \mu_3 \begin{bmatrix} T^{xx}_{\zeta\zeta} & T^{xy}_{\zeta\zeta} & T^{xz}_{\zeta\zeta} \\ T^{xy}_{\zeta\zeta} & T^{yy}_{\zeta\zeta} & T^{yz}_{\zeta\zeta} \\ T^{xz}_{\zeta\zeta} & T^{yz}_{\zeta\zeta} & T^{zz}_{\zeta\zeta} \end{bmatrix} \\ \text{symm.} & & \end{bmatrix} \tag{4.186}$$

where

$$T^{xx}_{\xi\xi} = C_1 \xi_{,x}{}^2 + C_3(\xi_{,y}{}^2 + \xi_{,z}{}^2) \tag{4.187}$$
$$T^{xy}_{\xi\xi} = C_4 \xi_{,x}\, \xi_{,y} \tag{4.188}$$
$$T^{xz}_{\xi\xi} = C_4 \xi_{,x}\, \xi_{,z} \tag{4.189}$$
$$T^{yy}_{\xi\xi} = C_1 \xi_{,y}{}^2 + C_3(\xi_{,x}{}^2 + \xi_{,z}{}^2) \tag{4.190}$$
$$T^{yz}_{\xi\xi} = C_4 \xi_{,y}\, \xi_{,z} \tag{4.191}$$
$$T^{zz}_{\xi\xi} = C_1 \xi_{,z}{}^2 + C_3(\xi_{,x}{}^2 + \xi_{,y}{}^2) \tag{4.192}$$

with $T^{\alpha\beta}_{\eta\eta}$ and $T^{\alpha\beta}_{\zeta\zeta}$ similarly defined, and

$$T^{xx}_{\xi\eta} = C_1 \xi_{,x}\, \eta_{,x} + C_3(\xi_{,y}\, \eta_{,y} + \xi_{,z}\, \eta_{,z}) \tag{4.193}$$
$$T^{xy}_{\xi\eta} = C_2 \xi_{,x}\, \eta_{,y} + C_3 \xi_{,y}\, \eta_{,x} \tag{4.194}$$
$$T^{xz}_{\xi\eta} = C_2 \xi_{,x}\, \eta_{,z} + C_3 \xi_{,z}\, \eta_{,x} \tag{4.195}$$
$$T^{yx}_{\xi\eta} = C_2 \xi_{,y}\, \eta_{,x} + C_3 \xi_{,x}\, \eta_{,y} \tag{4.196}$$
$$T^{yy}_{\xi\eta} = C_1 \xi_{,y}\, \eta_{,y} + C_3(\xi_{,x}\, \eta_{,x} + \xi_{,z}\, \eta_{,z}) \tag{4.197}$$
$$T^{yz}_{\xi\eta} = C_2 \xi_{,y}\, \eta_{,z} + C_3 \xi_{,z}\, \eta_{,y} \tag{4.198}$$
$$T^{zx}_{\xi\eta} = C_2 \xi_{,z}\, \eta_{,x} + C_3 \xi_{,x}\, \eta_{,z} \tag{4.199}$$
$$T^{zy}_{\xi\eta} = C_2 \xi_{,z}\, \eta_{,y} + C_3 \xi_{,y}\, \eta_{,z} \tag{4.200}$$
$$T^{zz}_{\xi\eta} = C_1 \xi_{,z}\, \eta_{,z} + C_3(\xi_{,x}\, \eta_{,x} + \xi_{,y}\, \eta_{,y}) \tag{4.201}$$

with $T^{\alpha\beta}_{\xi\zeta}$ and $T^{\alpha\beta}_{\eta\zeta}$ similarly defined.

The array $\mathbf{K}_{wu}$ is a 9×12 matrix which can be expressed in terms of twelve 3×3 sub-matrices as

$$\mathbf{K}_{wu} = \begin{bmatrix} \hat{\mathbf{K}}_{11} & \hat{\mathbf{K}}_{12} & \hat{\mathbf{K}}_{13} & \mathbf{0} \\ \hat{\mathbf{K}}_{21} & \hat{\mathbf{K}}_{22} & \hat{\mathbf{K}}_{23} & \mathbf{0} \\ \hat{\mathbf{K}}_{31} & \hat{\mathbf{K}}_{32} & \hat{\mathbf{K}}_{33} & \mathbf{0} \end{bmatrix} \tag{4.202}$$

where $\mathbf{0}$ is a 3×3 zero matrix and

$$\hat{\mathbf{K}}_{11} = \begin{bmatrix} \mu_1 T^{xx}_{\xi\eta} + \mu_6 T^{xx}_{\xi\xi} & \mu_1 T^{xy}_{\xi\eta} + \mu_6 T^{xy}_{\xi\xi} & \mu_1 T^{xz}_{\xi\eta} + \mu_6 T^{xz}_{\xi\xi} \\ \mu_1 T^{yx}_{\xi\eta} + \mu_6 T^{xy}_{\xi\xi} & \mu_1 T^{yy}_{\xi\eta} + \mu_6 T^{yy}_{\xi\xi} & \mu_1 T^{yz}_{\xi\eta} + \mu_6 T^{yz}_{\xi\xi} \\ \mu_1 T^{zx}_{\xi\eta} + \mu_6 T^{xz}_{\xi\xi} & \mu_1 T^{zy}_{\xi\eta} + \mu_6 T^{yz}_{\xi\xi} & \mu_1 T^{zz}_{\xi\eta} + \mu_6 T^{zz}_{\xi\xi} \end{bmatrix} \tag{4.203}$$

$$\hat{\mathbf{K}}_{12} = \begin{bmatrix} \mu_6 T^{xx}_{\xi\zeta} + \mu_5 T^{xx}_{\xi\eta} & \mu_6 T^{xy}_{\xi\zeta} + \mu_5 T^{xy}_{\xi\eta} & \mu_6 T^{xz}_{\xi\zeta} + \mu_5 T^{xz}_{\xi\eta} \\ \mu_6 T^{yx}_{\xi\zeta} + \mu_5 T^{yx}_{\xi\eta} & \mu_6 T^{yy}_{\xi\zeta} + \mu_5 T^{yy}_{\xi\eta} & \mu_6 T^{yz}_{\xi\zeta} + \mu_5 T^{yz}_{\xi\eta} \\ \mu_6 T^{zx}_{\xi\zeta} + \mu_5 T^{zx}_{\xi\eta} & \mu_6 T^{zy}_{\xi\zeta} + \mu_5 T^{zy}_{\xi\eta} & \mu_6 T^{zz}_{\xi\zeta} + \mu_5 T^{zz}_{\xi\eta} \end{bmatrix} \tag{4.204}$$

$$\hat{\mathbf{K}}_{13} = \begin{bmatrix} \mu_1 T^{xx}_{\xi\zeta} + \mu_5 T^{xx}_{\xi\xi} & \mu_1 T^{xy}_{\xi\zeta} + \mu_5 T^{xy}_{\xi\xi} & \mu_1 T^{xz}_{\xi\zeta} + \mu_5 T^{xz}_{\xi\xi} \\ \mu_1 T^{yx}_{\xi\zeta} + \mu_5 T^{xy}_{\xi\xi} & \mu_1 T^{yy}_{\xi\zeta} + \mu_5 T^{yy}_{\xi\xi} & \mu_1 T^{yz}_{\xi\zeta} + \mu_5 T^{yz}_{\xi\xi} \\ \mu_1 T^{zx}_{\xi\zeta} + \mu_5 T^{xz}_{\xi\xi} & \mu_1 T^{zy}_{\xi\zeta} + \mu_5 T^{yz}_{\xi\xi} & \mu_1 T^{zz}_{\xi\zeta} + \mu_5 T^{zz}_{\xi\xi} \end{bmatrix} \tag{4.205}$$

$$\hat{\mathbf{K}}_{21} = \begin{bmatrix} \mu_2 T^{xx}_{\xi\eta} + \mu_6 T^{xx}_{\eta\eta} & \mu_2 T^{yx}_{\xi\eta} + \mu_6 T^{xy}_{\eta\eta} & \mu_2 T^{zx}_{\xi\eta} + \mu_6 T^{xz}_{\eta\eta} \\ \mu_2 T^{xy}_{\xi\eta} + \mu_6 T^{xy}_{\eta\eta} & \mu_2 T^{yy}_{\xi\eta} + \mu_6 T^{yy}_{\eta\eta} & \mu_2 T^{zy}_{\xi\eta} + \mu_6 T^{yz}_{\eta\eta} \\ \mu_2 T^{xz}_{\xi\eta} + \mu_6 T^{xz}_{\eta\eta} & \mu_2 T^{yz}_{\xi\eta} + \mu_6 T^{yz}_{\eta\eta} & \mu_2 T^{zz}_{\xi\eta} + \mu_6 T^{zz}_{\eta\eta} \end{bmatrix} \tag{4.206}$$

$$\hat{\mathbf{K}}_{22} = \begin{bmatrix} \mu_2 T^{xx}_{\eta\zeta} + \mu_4 T^{xx}_{\eta\eta} & \mu_2 T^{yx}_{\eta\zeta} + \mu_4 T^{xy}_{\eta\eta} & \mu_2 T^{zx}_{\eta\zeta} + \mu_4 T^{xz}_{\eta\eta} \\ \mu_2 T^{xy}_{\eta\zeta} + \mu_4 T^{xy}_{\eta\eta} & \mu_2 T^{yy}_{\eta\zeta} + \mu_4 T^{yy}_{\eta\eta} & \mu_2 T^{zy}_{\eta\zeta} + \mu_4 T^{yz}_{\eta\eta} \\ \mu_2 T^{xz}_{\eta\zeta} + \mu_4 T^{xz}_{\eta\eta} & \mu_2 T^{yz}_{\eta\zeta} + \mu_4 T^{yz}_{\eta\eta} & \mu_2 T^{zz}_{\eta\zeta} + \mu_4 T^{zz}_{\eta\eta} \end{bmatrix} \tag{4.207}$$

$$\hat{\mathbf{K}}_{23} = \begin{bmatrix} \mu_6 T^{xx}_{\eta\zeta} + \mu_4 T^{xx}_{\xi\eta} & \mu_6 T^{xy}_{\eta\zeta} + \mu_4 T^{yx}_{\xi\eta} & \mu_6 T^{xz}_{\eta\zeta} + \mu_4 T^{zx}_{\xi\eta} \\ \mu_6 T^{yx}_{\eta\zeta} + \mu_4 T^{xy}_{\xi\eta} & \mu_6 T^{yy}_{\eta\zeta} + \mu_4 T^{yy}_{\xi\eta} & \mu_6 T^{yz}_{\eta\zeta} + \mu_4 T^{zy}_{\xi\eta} \\ \mu_6 T^{zx}_{\eta\zeta} + \mu_4 T^{xz}_{\xi\eta} & \mu_6 T^{zy}_{\eta\zeta} + \mu_4 T^{yz}_{\xi\eta} & \mu_6 T^{zz}_{\eta\zeta} + \mu_4 T^{zz}_{\xi\eta} \end{bmatrix} \tag{4.208}$$

$$\hat{\mathbf{K}}_{31} = \begin{bmatrix} \mu_5 T^{xx}_{\eta\zeta} + \mu_4 T^{xx}_{\xi\zeta} & \mu_5 T^{yx}_{\eta\zeta} + \mu_4 T^{yx}_{\xi\zeta} & \mu_5 T^{zx}_{\eta\zeta} + \mu_4 T^{zx}_{\xi\zeta} \\ \mu_5 T^{xy}_{\eta\zeta} + \mu_4 T^{xy}_{\xi\zeta} & \mu_5 T^{yy}_{\eta\zeta} + \mu_4 T^{yy}_{\xi\zeta} & \mu_5 T^{zy}_{\eta\zeta} + \mu_4 T^{zy}_{\xi\zeta} \\ \mu_5 T^{xz}_{\eta\zeta} + \mu_4 T^{xz}_{\xi\zeta} & \mu_5 T^{yz}_{\eta\zeta} + \mu_4 T^{yz}_{\xi\zeta} & \mu_5 T^{zz}_{\eta\zeta} + \mu_4 T^{zz}_{\xi\zeta} \end{bmatrix} \tag{4.209}$$

$$\hat{\mathbf{K}}_{32} = \begin{bmatrix} \mu_3 T^{xx}_{\eta\zeta} + \mu_4 T^{xx}_{\zeta\zeta} & \mu_3 T^{yx}_{\eta\zeta} + \mu_4 T^{xy}_{\zeta\zeta} & \mu_3 T^{zx}_{\eta\zeta} + \mu_4 T^{xz}_{\zeta\zeta} \\ \mu_3 T^{xy}_{\eta\zeta} + \mu_4 T^{xy}_{\zeta\zeta} & \mu_3 T^{yy}_{\eta\zeta} + \mu_4 T^{yy}_{\zeta\zeta} & \mu_3 T^{zy}_{\eta\zeta} + \mu_4 T^{yz}_{\zeta\zeta} \\ \mu_3 T^{xz}_{\eta\zeta} + \mu_4 T^{xz}_{\zeta\zeta} & \mu_3 T^{yz}_{\eta\zeta} + \mu_4 T^{yz}_{\zeta\zeta} & \mu_3 T^{zz}_{\eta\zeta} + \mu_4 T^{zz}_{\zeta\zeta} \end{bmatrix} \tag{4.210}$$

$$\hat{\mathbf{K}}_{33} = \begin{bmatrix} \mu_3 T^{xx}_{\xi\zeta} + \mu_5 T^{xx}_{\zeta\zeta} & \mu_3 T^{yx}_{\eta\zeta} + \mu_5 T^{xy}_{\zeta\zeta} & \mu_3 T^{zx}_{\xi\zeta} + \mu_5 T^{xz}_{\zeta\zeta} \\ \mu_3 T^{xy}_{\xi\zeta} + \mu_5 T^{xy}_{\zeta\zeta} & \mu_3 T^{yy}_{\eta\zeta} + \mu_5 T^{yy}_{\zeta\zeta} & \mu_3 T^{zy}_{\xi\zeta} + \mu_5 T^{yz}_{\zeta\zeta} \\ \mu_3 T^{xz}_{\xi\zeta} + \mu_5 T^{xz}_{\zeta\zeta} & \mu_3 T^{yz}_{\eta\zeta} + \mu_5 T^{yz}_{\zeta\zeta} & \mu_3 T^{zz}_{\xi\zeta} + \mu_5 T^{zz}_{\zeta\zeta} \end{bmatrix} \tag{4.211}$$

4.4.5 Internal and External Forces

The internal force vector for the solid phase, $\mathbf{f}_u^{\text{int}}$, is evaluated using a decomposition into constant and stabilization portions

$$\mathbf{f}_u^{\text{int}} = \mathbf{f}_0^{\text{int}} + \mathbf{f}_{\text{stab}}^{\text{int}} \tag{4.212}$$

The constant portion of the internal force vector is evaluated using single-point integration as

$$\mathbf{f}_0^{\text{int}} = \int_{\Omega_E} \mathbf{B}_0^T \boldsymbol{\sigma}'(\boldsymbol{\varepsilon}) d\Omega_E = V \mathbf{B}_0^T \boldsymbol{\sigma}'(\boldsymbol{\varepsilon}) \tag{4.213}$$

The stabilization portion is computed directly from the stabilization stiffness matrix,

$$\mathbf{f}_{\text{stab}}^{\text{int}} = \mathbf{K}_{\text{stab}} \mathbf{d} \tag{4.214}$$

where $\mathbf{d}$ is the current nodal displacement vector for the element.

The external nodal forces for the solid phase resulting from an applied body force, $\mathbf{g}$, are evaluated analytically from (4.9) as

$$\begin{aligned} \mathbf{f}_I^{\text{ext}} = \mathbf{g} \Bigg[& J_0 + \frac{1}{3}\Big(J_1\xi_I + J_2\eta_I + J_3\zeta_I + J_7 + J_8 + J_9\Big) \\ & + \frac{1}{9}\Big(J_4 h_{\zeta\eta\, I} + J_5 h_{\zeta\xi\, I} + J_6 h_{\xi\eta\, I} + (J_{10} + J_{13})\zeta_I + (J_{11} + J_{14})\eta_I + (J_{12} + J_{15})\xi_I\Big) \\ & + \frac{1}{27}\Big(J_{16} h_{\xi\eta\zeta\, I} + J_{17} h_{\zeta\eta\, I} + J_{18} h_{\zeta\xi\, I} + J_{19} h_{\xi\eta\, I}\Big)\Bigg] \end{aligned} \tag{4.215}$$

using the expanded form of the Jacobian determinant given by (4.76). Surface force contributions from a traction, $\mathbf{t}$, are identical to a standard displacement element.

4.4.6 Mass Matrix for the Mixture

The mass matrix for the mixture, (4.5), is approximated as a lumped mass matrix. The nodal masses in this matrix are determined using the strategy used for nodal forces, thus,

$$\begin{aligned} M_{II} = \rho \Bigg[& J_0 + \frac{1}{3}\Big(J_1\xi_I + J_2\eta_I + J_3\zeta_I + J_7 + J_8 + J_9\Big) \\ & + \frac{1}{9}\Big(J_4 h_{\zeta\eta\, I} + J_5 h_{\zeta\xi\, I} + J_6 h_{\xi\eta\, I} + (J_{10} + J_{13})\zeta_I + (J_{11} + J_{14})\eta_I + (J_{12} + J_{15})\xi_I\Big) \\ & + \frac{1}{27}\Big(J_{16} h_{\xi\eta\zeta\, I} + J_{17} h_{\zeta\eta\, I} + J_{18} h_{\zeta\xi\, I} + J_{19} h_{\xi\eta\, I}\Big)\Bigg] \end{aligned} \tag{4.216}$$

where ρ is the mixture mass density.

4.5 Evaluation of Fluid Phase for Eight-Node Hexahedral Element

The pore fluid terms in the discretized field equations, (4.3) and (4.4), are evaluated using linear interpolation functions and a combination of single-point and full numerical integration. Because the pressure-field interpolation is of the same order as the displacement interpolation, a stabilization technique is used to enhance element stability in the incompressible-impermeable limit (see Section 4.6).

4.5.1 Coupling Matrix

The 24×8 coupling matrix, $\mathbf{Q}$, is approximated from (4.6) using single-point integration as

$$\mathbf{Q} = V\mathbf{B}_0^T\mathbf{1}\mathbf{N}_p(0,0,0) \tag{4.217}$$

where $\mathbf{1} = [1,1,1,0,0,0]^T$, and $\mathbf{N}_p(0,0,0)$ is a 1×8 vector of linear shape functions, (4.24), evaluated at $\xi = \eta = \zeta = 0$.

4.5.2 Compressibility Matrix

The compressibility matrix, $\mathbf{S}$, is evaluated from (4.7) using single-point integration as

$$\mathbf{S} = V\frac{n}{K_f}\mathbf{N}_p^T(0,0,0)\mathbf{N}_p(0,0,0) \tag{4.218}$$

The computation of the compressibility matrix can be further simplified by recognizing that $\mathbf{S}$ is a fully-populated 8×8 matrix with identical components, i.e.,

$$S_{ij} = V\frac{n}{64K_f} \tag{4.219}$$

4.5.3 Permeability Matrix

The 8×8 permeability matrix, $\mathbf{H}$, is evaluated from (4.8) using full numerical integration as

$$\mathbf{H} = \sum_{I=1}^{8} J\boldsymbol{\nabla}\mathbf{N}_{p\,I}^T\mathbf{k}\boldsymbol{\nabla}\mathbf{N}_{p\,I} \tag{4.220}$$

where $\boldsymbol{\nabla}\mathbf{N}_p$ is the 3×8 gradient of the shape function vector $\mathbf{N}_p$ and $\mathbf{k}$ is the 3×3 permeability matrix. For isotropic permeability conditions, $\mathbf{k}$ reduces to a single scalar value. This term is only evaluated upon initialization of the element or upon changes in permeability.

4.5.4 Internal and External Forces

The internal nodal force vector for the fluid phase, $\mathbf{f}_p^{\text{int}}$, is a combination of compressibility and permeability forces. This vector is computed as

$$\mathbf{f}_p^{\text{int}} = \mathbf{S}\dot{\mathbf{p}} + \mathbf{H}\mathbf{p} \tag{4.221}$$

The external nodal forces for the fluid phase resulting from an applied body force are evaluated from (4.10) using single-point integration as

$$\mathbf{f}_p^{\text{ext}} = V\rho_f \boldsymbol{\nabla}\mathbf{N}_p^T(0,0,0)\mathbf{k}\mathbf{g} \tag{4.222}$$

where ρ_f is the pore fluid mass density. The contributions from a surface flux, $\mathbf{q}$, are identical to those computed for a standard element formulation

4.6 Stabilization in the Incompressible-Impermeable Limit

As the pore fluid approaches incompressibility, $\mathbf{S} \to \mathbf{0}$, and as the mixture approaches impermeability, $\mathbf{H} \to \mathbf{0}$. The stability of the coupled fluid-solid elements must be addressed in this limiting state, as the use of equal-order interpolation functions for the displacement and pressure fields precludes satisfaction the *inf-sup* condition. A non-residual based stabilization scheme, modeled after the direct α-method (Huang et al., 2004; Zienkiewicz et al., 1994), is used to enhance stability in the incompressible-impermeable limit for both element types.

The direct α-method is a residual based stabilization scheme derived by adding the product of an arbitrary constant, α, with the divergence of the time derivative of the equation of motion for the system (4.1) to the combined equation of motion for the fluid and mixture (4.2). This process results in the addition of two stabilization terms to the discretized system, a pressure Laplacian term

$$\tilde{\mathbf{H}} = \int_V \boldsymbol{\nabla}\mathbf{N}_p^T \alpha \boldsymbol{\nabla}\mathbf{N}_p \, dV \tag{4.223}$$

and a stress-dependent term

$$-\int_{\Omega_E} \boldsymbol{\nabla}\mathbf{N}_p^T \alpha \mathbf{D}^T \dot{\boldsymbol{\sigma}}' d\Omega_E \tag{4.224}$$

where, for the 2D element

$$\mathbf{D} = \begin{bmatrix} \partial/\partial x & 0 \\ 0 & \partial/\partial y \\ \partial/\partial y & \partial/\partial x \end{bmatrix} \tag{4.225}$$

and for the 3D element

$$\mathbf{D} = \begin{bmatrix} \partial/\partial x & 0 & 0 \\ 0 & \partial/\partial y & 0 \\ 0 & 0 & \partial/\partial z \\ \partial/\partial y & \partial/\partial x & 0 \\ 0 & \partial/\partial z & \partial/\partial y \\ \partial/\partial z & 0 & \partial/\partial x \end{bmatrix} \tag{4.226}$$

Because the stabilization terms are computed from the residual of the equation of motion, stability is enhanced without affecting the consistency of the element.

The pressure Laplacian term of (4.223) is evaluated in the same manner as the permeability matrix for each element. For the 2D element, single-point integration is used as indicated in (4.65). For the 3D element, full integration is used as described with (4.220). The stress-dependent term of (4.224) may be evaluated using the stress recovery techniques of Wan (2002), however, this term is omitted from the current element formulations due to issues of computational efficiency. The term causes the system of equations to become unsymmetric, and the computational demand associated with its evaluation does not coincide with the goals of the elements.

With the omission of the stress-dependent term, the stabilization scheme corresponds to that originally developed by Brezzi and Pitäkaranta (1984) for the Stokes equations. Implementation of this scheme results in a modification to the discretized field equation of (4.4), which is now expressed as

$$\mathbf{Q}^T\dot{\mathbf{d}} + \left(\mathbf{S}+\tilde{\mathbf{H}}\right)\dot{\mathbf{p}} + \mathbf{H}\mathbf{p} = \mathbf{f}_p^{\text{ext}} \tag{4.227}$$

Similar non-residual stabilization approaches have been shown to produce comparable results to residual based methods with mixed elements (Truty and Zimmermann, 2006), and in the similarly constrained problem of incompressible elasticity (Commend et al., 2004). Other examples of non-residual based stabilization approaches are discussed in Bochev et al. (2006) and White and Borja (2008).

After the work of Huang et al. (2004) and Zienkiewicz et al. (1994), α is defined for the current elements as

$$\alpha = \frac{\alpha_0 h^2}{K_s + \frac{4}{3}G_s} \tag{4.228}$$

where K_s and G_s are the bulk and shear moduli of the solid phase, respectively, and α_0 falls in the range $0.1 \leq \alpha_0 \leq 0.5$. Because α is dependent on the element size, h, the stabilization remains consistent in the sense that as the mesh is refined, $\tilde{\mathbf{H}} \to \mathbf{0}$. Numerical analysis suggests that the resulting range of α values is acceptable for most problems. Alternative definitions for this stabilization parameter are given by Truty (2001) and Truty

and Zimmermann (2006).

4.7 Set-Up for Temporal Integration

The numerical solution to the discretized field equations (4.3) and (4.227) requires integration in time. There are many temporal integration schemes which can be used for this purpose (e.g., Newmark, 1959) but for all such schemes, the essential process is the same. The known values of $\mathbf{d}_n$, $\dot{\mathbf{d}}_n$, $\ddot{\mathbf{d}}_n$, $\mathbf{p}_n$, and $\dot{\mathbf{p}}_n$ at time t_n must in some manner be updated to the unknown values $\mathbf{d}_{n+1}$, $\dot{\mathbf{d}}_{n+1}$, $\ddot{\mathbf{d}}_{n+1}$, $\mathbf{p}_{n+1}$, and $\dot{\mathbf{p}}_{n+1}$ at time $t_{n+1} = t_n + \Delta t$.

A useful way to facilitate this process is to set up the system in the form

$$\bar{\mathbf{M}}\ddot{\mathbf{w}} + \bar{\mathbf{C}}\dot{\mathbf{w}} + \bar{\mathbf{K}}\mathbf{w} = \mathbf{f} \tag{4.229}$$

where $\bar{\mathbf{M}}$ is the generalized mass matrix,

$$\bar{\mathbf{M}} = \begin{bmatrix} \mathbf{M} & \mathbf{0} \\ \mathbf{0} & -\left(\mathbf{S} + \tilde{\mathbf{H}}\right) \end{bmatrix} \tag{4.230}$$

$\bar{\mathbf{C}}$ is the generalized damping matrix,

$$\bar{\mathbf{C}} = \begin{bmatrix} \mathbf{C} & -\mathbf{Q} \\ -\mathbf{Q}^T & -\mathbf{H} \end{bmatrix} \tag{4.231}$$

with $\mathbf{C}$ as an optional damping matrix for the solid phase, $\bar{\mathbf{K}}$ is the generalized stiffness matrix,

$$\bar{\mathbf{K}} = \begin{bmatrix} \mathbf{K} & \mathbf{0} \\ \mathbf{0} & \mathbf{0} \end{bmatrix} \tag{4.232}$$

and $\mathbf{f}$ is the generalized force vector,

$$\mathbf{f} = \begin{Bmatrix} \mathbf{f}_u^{\text{ext}} - \mathbf{f}_u^{\text{int}} \\ \mathbf{f}_p^{\text{int}} - \mathbf{f}_p^{\text{ext}} \end{Bmatrix} \tag{4.233}$$

The generalized degrees-of-freedom are defined as

$$\mathbf{w} = \begin{Bmatrix} \mathbf{d} \\ \int \mathbf{p} dt \end{Bmatrix} \tag{4.234}$$

with time derivatives

$$\dot{\mathbf{w}} = \begin{Bmatrix} \dot{\mathbf{d}} \\ \mathbf{p} \end{Bmatrix} \tag{4.235}$$

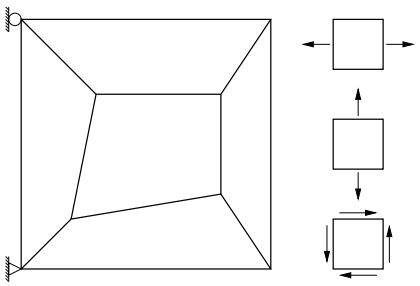

Figure 4.1: 2D element patch after Bathe (1996) with considered constant stress states.

$$\ddot{\mathbf{w}} = \begin{Bmatrix} \ddot{\mathbf{d}} \\ \dot{\mathbf{p}} \end{Bmatrix} \tag{4.236}$$

The time integral of the pressure in (4.234) is an ignored artifact of rearranging the terms related to (4.227). The terms of (4.227) have been multiplied by minus one to create symmetry in (4.229)

4.8 Numerical Examples for Four-Node Quadrilateral Elements

The 2D formulation is implemented in the finite element platform OpenSees as two separate elements; an efficient Q1 element, which uses the solid phase formulation only (Section 4.2), and an efficient coupled fluid-solid Q1-P1 element, which uses the solid and fluid phase formulations (Sections 4.2 and 4.3) with the pressure field stabilization and temporal integration schemes of Sections 4.6 and 4.7. To differentiate these new elements from standard Q1 and Q1-P1 elements, they are given the designations Q1ssp and Q1-P1ssp, where **ssp** is an abbreviation for hourglass **s**tabilized **s**ingle-**p**oint integration.

Several numerical test problems are analyzed with the OpenSees implementations of the Q1ssp and Q1-P1ssp elements (respectively referred to as SSPquad and SSPquadUP in the OpenSees interpreter). These tests are used to establish and analyze the convergence behavior of the solid phase formulation, to demonstrate the effectiveness of the implemented anti-locking procedures, to verify stability of the pressure field in the incompressible-impermeable limit, and to test the applicability of the elements to a complex constitutive model typical to geotechnical analysis.

4.8.1 Patch Test

The patch test is analyzed to establish the consistency, stability, and robustness of the Q1ssp element formulation using the element patch shown in Figure 4.1. Several iterations of consistent refinement are analyzed using three constant stress states. The conditions of the patch test are satisfied for all considered cases.

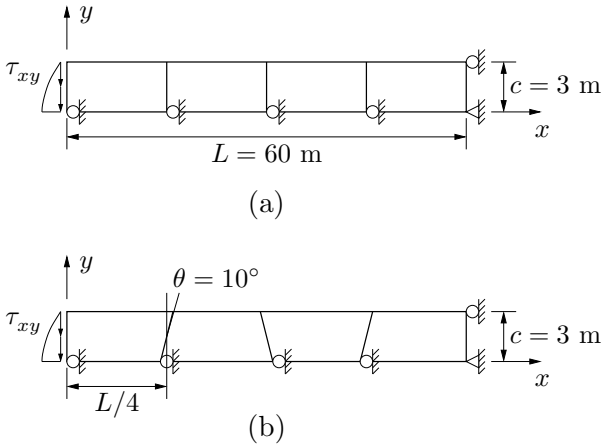

Figure 4.2: Cantilever beam meshes. (a) Rectangular mesh (coarsest mesh shown). (b) Skewed mesh.

4.8.2 Cantilever Beam Analysis

A cantilever beam model is used to assess the effectiveness of the anti-locking strategy and analyze the convergence behavior of the stabilized solid phase formulation. Two mesh configurations are analyzed: a mesh with rectangular elements, Figure 4.2(a), and a mesh with skewed elements, Figure 4.2(b). These models consider the anti-symmetry of the problem as shown.

A vertical load at $x = 0$ and the corresponding support reactions at $x = L$ are applied in accordance with the stress field solutions given by Timoshenko and Goodier (1951)

$$\sigma_x(x, y) = -\frac{Pxy}{I} \tag{4.237}$$

$$\sigma_y(x, y) = 0 \tag{4.238}$$

$$\tau_{xy}(x, y) = -\frac{P\left(c^2 - y^2\right)}{2I} \tag{4.239}$$

in which $I = D^3/12$ is the second moment of the area, with $D = 2c$ as the depth of the beam, and $P = 200$ kPa is the applied force at the free end.

The expected axial and vertical displacements, u and v, respectively, for a plane stress cantilever beam considering shear deformation (after Timoshenko and Goodier, 1951) are given by

$$u = \frac{P(L^2 - x^2)y}{2EI} - \frac{\nu P y^3}{6EI} + \frac{Py^3}{6IG} \tag{4.240}$$

$$v = \frac{\nu P x y^2}{2EI} + \frac{P(x^3 - L^3)}{6EI} - \frac{PL^2(x - L)}{2EI} - \frac{Pc^2(x - L)}{2IG} \tag{4.241}$$

in which L is the beam length, E is the elastic modulus, G the shear modulus, and ν is Poisson's ratio. Plane strain conditions are imposed by substituting $\bar{\nu} = \nu/(1 - \nu)$ and

Table 4.1: Centerline tip deflection ratio for coarse rectangular mesh.

	Plane Strain		Plane Stress	
Element	$\nu = 0.25$	$\nu = 0.499$	$\nu = 0.25$	$\nu = 0.499$
Q1	0.295	0.013	0.284	0.315
Q1ssp	1.162	1.202	1.154	1.176

Table 4.2: Centerline tip deflection ratio for coarse skewed mesh.

	Plane Strain		Plane Stress	
Element	$\nu = 0.25$	$\nu = 0.499$	$\nu = 0.25$	$\nu = 0.499$
Q1	0.271	0.013	0.262	0.283
Q1ssp	0.962	1.013	0.953	0.978

$\bar{E} = E/(1-\nu^2)$ for the elastic parameters in (4.240) and (4.241). In all cases, $E = 2000$ MPa.

Recorded deflections at $x = y = 0$ are compared to (4.241) in a ratio to assess the coarse-mesh accuracy of the Q1ssp element. This ratio, $v_{\text{approx}}/v_{\text{exact}}$, is computed for both mesh types, as well as for a standard Q1 element. Results are reported in Tables 4.1 and 4.2. The Q1ssp element is more accurate due to the included anti-locking procedures. The elastic response is somewhat too soft for the rectangular mesh due to the choice of $e_1 = 0.5$ and $e_2 = -0.5$ in (4.36), however, this choice of coefficients is superior for general analysis.

The rectangular mesh, Figure 4.2(a), is used to assess the rate of convergence for the Q1ssp element. The shown mesh, 1×4, is considered, along with three levels of refinement (2×8, 4×16, and 8×32) for two configurations: plane stress with $\nu = 0.25$ and plane strain with $\nu = 0.499$. Convergence is evaluated in terms of the displacement error norm

$$\frac{||\mathbf{u}_{\text{exact}} - \mathbf{u}_{\text{approx}}||}{||\mathbf{u}_{\text{exact}}||} \tag{4.242}$$

and energy error norm

$$\frac{||\boldsymbol{\sigma}_{\text{exact}} - \boldsymbol{\sigma}_{\text{approx}}||_E}{||\boldsymbol{\sigma}_{\text{exact}}||_E} \tag{4.243}$$

where

$$||\boldsymbol{\sigma}||_E = \sqrt{\int_\Omega \boldsymbol{\sigma}^T \mathbb{C}^{-1} \boldsymbol{\sigma} \, d\Omega} \tag{4.244}$$

Convergence plots are shown in Figures 4.3 and 4.4. In all cases, the accuracy and convergence rate for Q1ssp are at least an order greater than those for Q1. The Q1ssp element is largely unaffected by the transition to nearly incompressible conditions. These results confirm the success of the stabilized single-point scheme with anti-locking used in the Q1ssp element and the solid phase formulation of the Q1-P1ssp element.

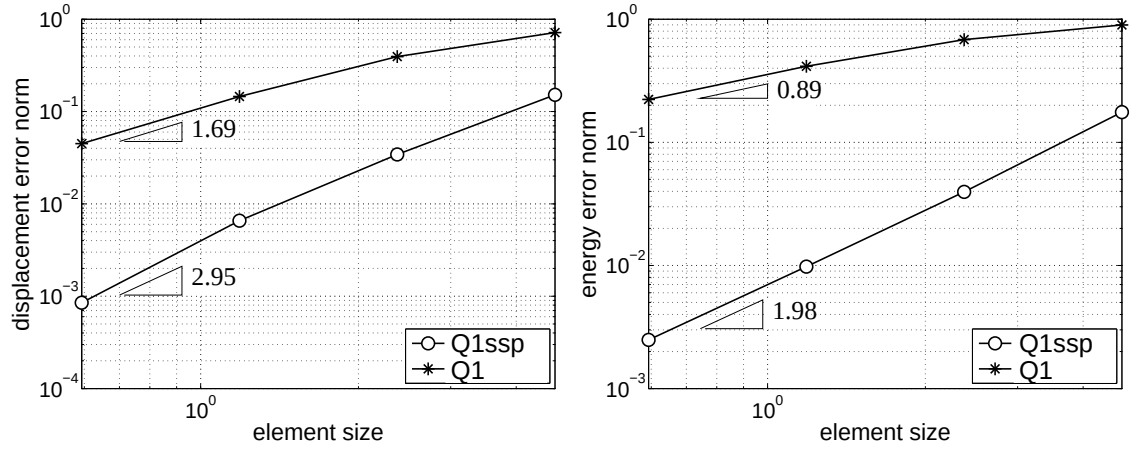

Figure 4.3: Displacement and energy error norms for rectangular cantilever beam mesh (plane stress, $\nu = 0.25$).

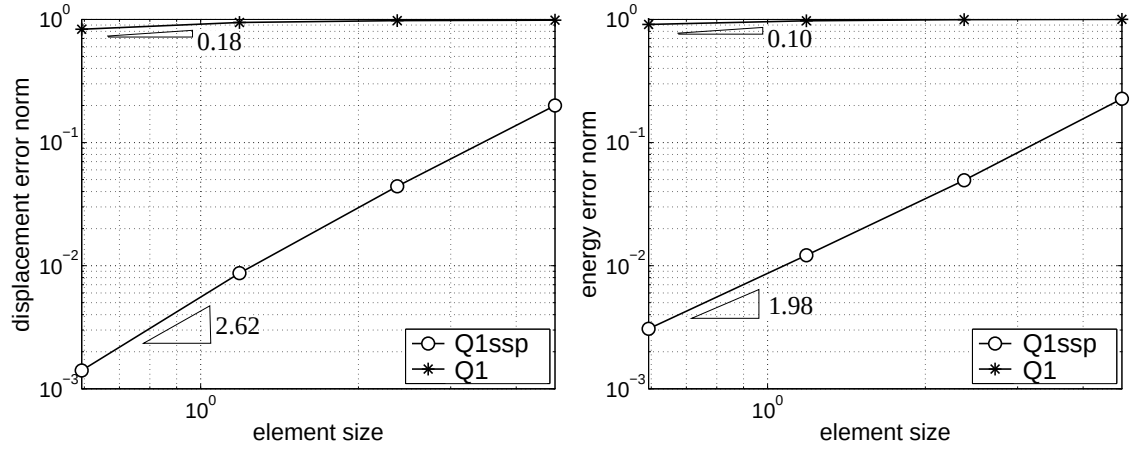

Figure 4.4: Displacement and energy error norms for rectangular cantilever beam mesh (plane strain, $\nu = 0.499$).

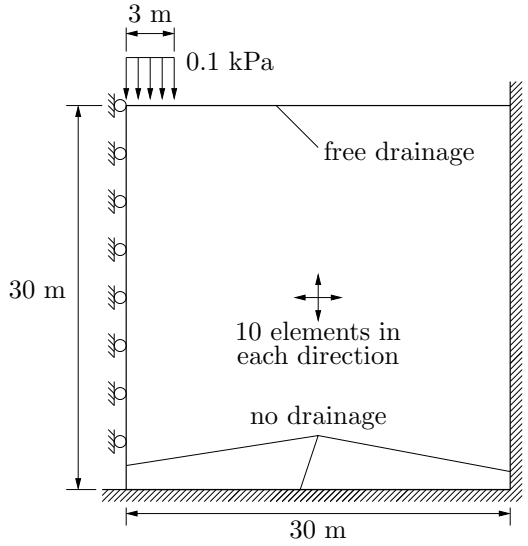

Figure 4.5: Flexible footing load test problem.

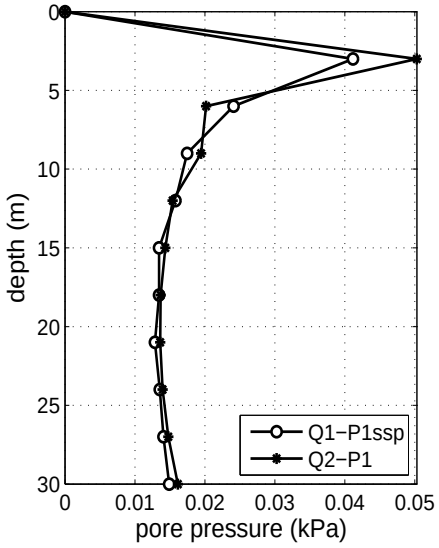

Figure 4.6: Pore pressure distributions below center of footing load at 1 second for Q1-P1ssp and Q2-P1 elements.

4.8.3 Flexible Footing Load Analysis

The stability of the pressure field for the Q1-P1ssp element is evaluated using a test problem in which a flexible footing load is applied to a saturated plane strain soil continuum. The general layout of this problem is provided in Figure 4.5. Zero drainage boundaries and symmetry conditions are enforced as shown. Cases are considered both with and without stabilization of the coupled system to highlight the effectiveness of the implemented stabilization scheme. The results are compared to a full-integration Q1-P1 element, which is not fully acceptable in the incompressible-impermeable limit, and a Q2-P1 element, which possesses inherent stability in the limiting case(quadUP and 9_4quadUP in the OpenSees interpreter, respectively).

In all cases, the applied load increases linearly from zero to 0.1 kPa over 0.1 seconds, then remains constant. The permeability is isotropic at 10^{-7} m/s, the fluid density is $\rho_f = 1.0$ Mg/m^3, and the fluid bulk modulus is set as $K_f = 2.2 \cdot 10^{12}$ kPa. The soil is linear elastic with elastic modulus $E_s = 25000$ kPa, Poisson's ratio $\nu = 0.3$, and saturated mass density $\rho = 2.67$ Mg/m^3. Rayleigh damping with $\mathbf{C} = 0.05\mathbf{M} + 0.02\mathbf{K}$ is assumed for the solid phase.

The variations of nodal pore pressure along the symmetry plane for the Q1-P1ssp and Q2-P1 elements are compared in Figure 4.6. The peak magnitude obtained using the Q1-P1ssp element is somewhat less than that for the Q2-P1 element, however, the Q1-P1ssp solution displays stability and the overall distribution is reasonably similar to the higher-order element solution.

Spatial pore pressure distributions at $t = 1$ second are used to provide further comparison

between the various element types. Figure 4.7(a) shows the pore pressure field for the Q1-P1ssp element with $\alpha = 0.0$ (stabilization inactive). The observed pressure instabilities are expected for this case. Figure 4.7(b) shows corresponding results for the same element, however, stabilization is active with $\alpha = 6.8 \cdot 10^{-5}$, the value obtained from (4.228). The eff

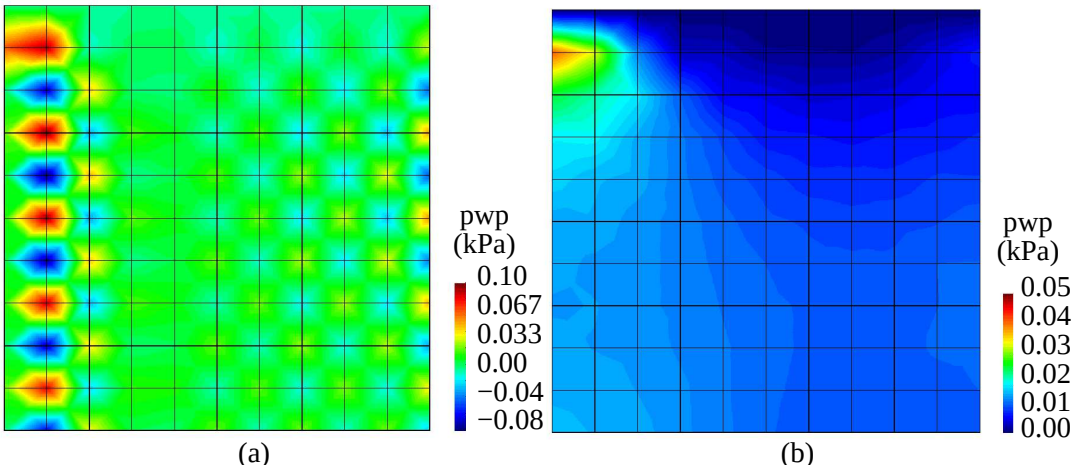

Figure 4.7: Pore pressure distributions in flexible footing analysis at 1 second for (a) Q1-P1ssp with $\alpha = 0.0$, and (b) Q1-P1ssp with $\alpha = 6.8 \cdot 10^{-5}$.

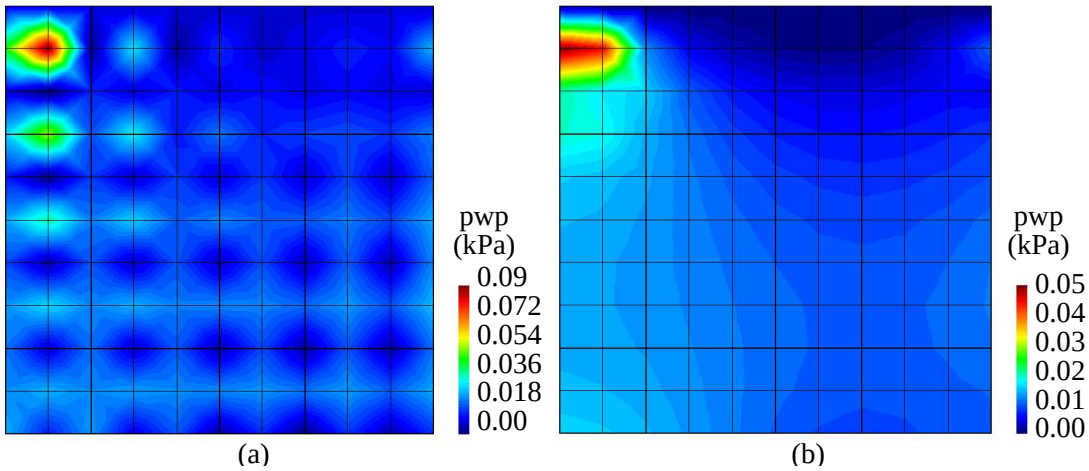

Figure 4.8: Pore pressure distributions in flexible footing analysis at 1 second for (a) Q1-P1, and (b) Q2-P1.

Figures 4.8(a) and 4.8(b) show the pressure fields for the Q1-P1 and Q2-P1 elements, respectively. The expected pressure instabilities for the Q1-P1 element are observed, though they are not as severe as for the Q1-P1ssp element with $\alpha = 0$, likely due to the differences between full and reduced integration for the pressure field. The pore pressure field obtained

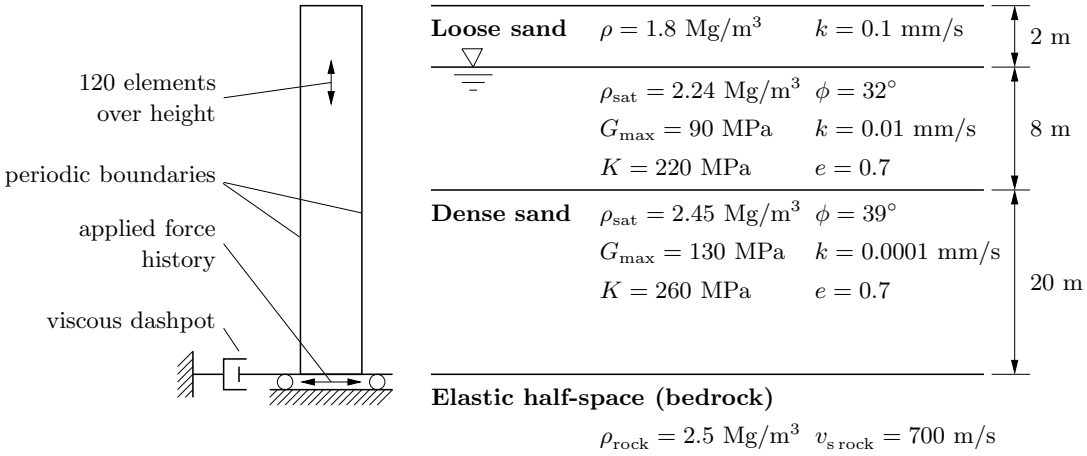

Figure 4.9: Model layout and soil profile for site-response analysis test problem.

using the Q1-P1ssp element, Figure 4.7(b), correlates well with that obtained for the Q2-P1 element, Figure 4.8(b). The ability of the Q1-P1ssp element to produce similar results to the higher-order element in this type of analysis is advantageous. In addition to the computational savings related to reduced integration, the Q1-P1ssp element reduces the degrees-of-freedom for the problem and simplifies mesh generation as compared to the nine-node Q2-P1 element while preserving similar accuracy, as confirmed by Figures 4.6, 4.7(b), and 4.8(b).

4.8.4 Site Response Analysis

The Q1-P1ssp element is evaluated in a dynamic, nonlinear context via a site-response analysis. The model, shown in Figure 4.9, consists of a single column of elements supported vertically at the base. Periodic boundary conditions are enforced in the horizontal direction to restrict element deformation to a pure shear mode. A viscous dashpot is used to represent the compliance of an underlying elastic layer after Lysmer and Kuhlemeyer (1969). The nodes at and above the groundwater table are free to drain. Zero drainage is enforced on the remaining boundaries.

The soil profile modeled by this test problem, also shown in Figure 4.9, consists of two layers of cohesionless soil underlain by bedrock. The groundwater table is 2 m below the surface and all material below the groundwater table is assumed to be saturated. A pressure-dependent nested yield surface constitutive model capable of capturing cyclic mobility (Elgamal et al., 2003; Prevost, 1985a) is used to approximate the behavior of the liquefiable cohesionless soil. The assumed material parameters are provided in Figure 4.9. The reported permeabilities are isotropic and chosen with relatively low values to assess stability near the incompressible-impermeable limit. Stabilization α-parameters are computed from (4.228), with values of $\alpha = 1.46 \cdot 10^{-6}$ and $\alpha = 1.17 \cdot 10^{-6}$ applying to the loose and dense sand layers, respectively.

The Gilroy Array No. 1 fault parallel record from the 1989 Loma Prieta event (NGA

Table 4.3: Execution times for site-response analyses.

Element	Q1-P1ssp	Q1-P1	Q2-P1
Execution time	4.2 min	17.7 min	15.3 min

#765) from the PEER ground motion database is used as the input motion. The ground motion is applied at the base of the soil column as an equivalent force time history obtained from the product of ρ_{rock} and $v_{s\,\text{rock}}$ with the velocity time history of the input motion after Joyner and Chen (1975). The Q1-P1 and Q2-P1 elements introduced in example 6.3 are considered in addition to the Q1-P1ssp element. In order to provide comparable degrees-of-freedom for a comparison of computational demand, a mesh with only 60 Q2-P1 elements over the height of the soil column is considered.

Table 4.3 shows the execution times (user CPU time) for each element type. As expected, the Q2-P1 element is significantly more computationally expensive than the Q1-P1ssp element. It is interesting to note that the Q1-P1 element had the longest runtime of the three elements. This is not due to some inherent computational inefficiency in this element formulation, instead, it is due to the smaller analysis time step which was necessary for convergence, likely due to lack of stability in the pressure field.

The efficiency of the Q1-P1ssp element is apparent from the results of Table 4.4, however, efficiency alone does not verify the effectiveness of the element formulation. Figure 4.10 shows the acceleration, velocity, and displacement response spectra at the top of the soil column for each element type. In this comparison, a more refined mesh of 120 Q2-P1 elements is considered. All three analyses produced reasonably similar results, though it is somewhat difficult to gauge relative similarities and differences in this plot. There is no analytical solution to which the results can be compared, however, the refined Q2-P1 mesh provides an acceptable baseline for comparison. Figure 4.11 shows the ratios of the spectral accelerations returned by the Q1-P1ssp and Q1-P1 elements to that for the Q2-P1 element. There is better overall similarity for the Q1-P1ssp element, though there is greater discrepancy at longer periods.

To further evaluate the Q1-P1ssp element, the stress, strain, and pore pressure responses are compared to corresponding results for the Q2-P1 element. Figures 4.12 and 4.13 show a summary of the constitutive response at three depths (3, 7, and 17 m). The stress and strain values shown for the Q2-P1 element are from the central integration point. In these figures, the left column of plots shows the shear stress-strain response (τ-γ), the central column of plots shows the stress path in shear-normal stress space with the failure (solid line) and phase transformation (dashed line) surfaces, and the right column of plots shows the evolution of the pore pressure ratio with time. The pore pressure ratio, $r_u(t)$, is computed

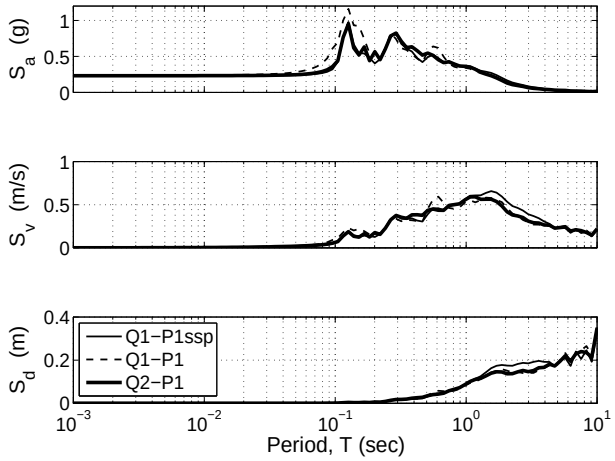

Figure 4.10: Acceleration, velocity, and displacement response spectra at the surface of the soil column in site-response analysis.

as

$$r_u(t) = \frac{u(t) - u_0}{\sigma'_{v0}} \tag{4.245}$$

where $u(t)$ is the pore pressure at time t, u_0 is the initial pore pressure at $t = 0$, and σ'_{v0} is the initial vertical effective stress. Stress recovery is used to determine nodal stress values for use in this computation.

As shown in Figures 4.12 and 4.13, the responses returned by each element formulation are similar. Both are able to capture the liquefaction and subsequent cyclic mobility of the material at a depth of 7 m. The results obtained in this test problem verify that the Q1-P1ssp element is robust enough to be used in dynamic analysis with a sophisticated constitutive model, producing results which are comparable to higher-order elements at a fraction of the computational cost.

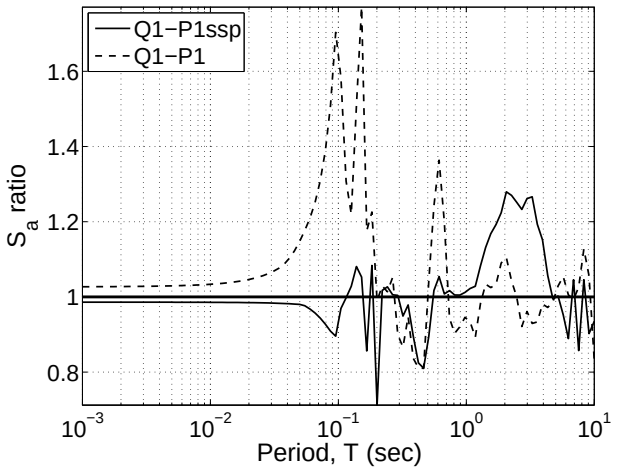

Figure 4.11: Spectral acceleration ratios for Q1-P1ssp and Q1-P1 elements in site-response analysis.

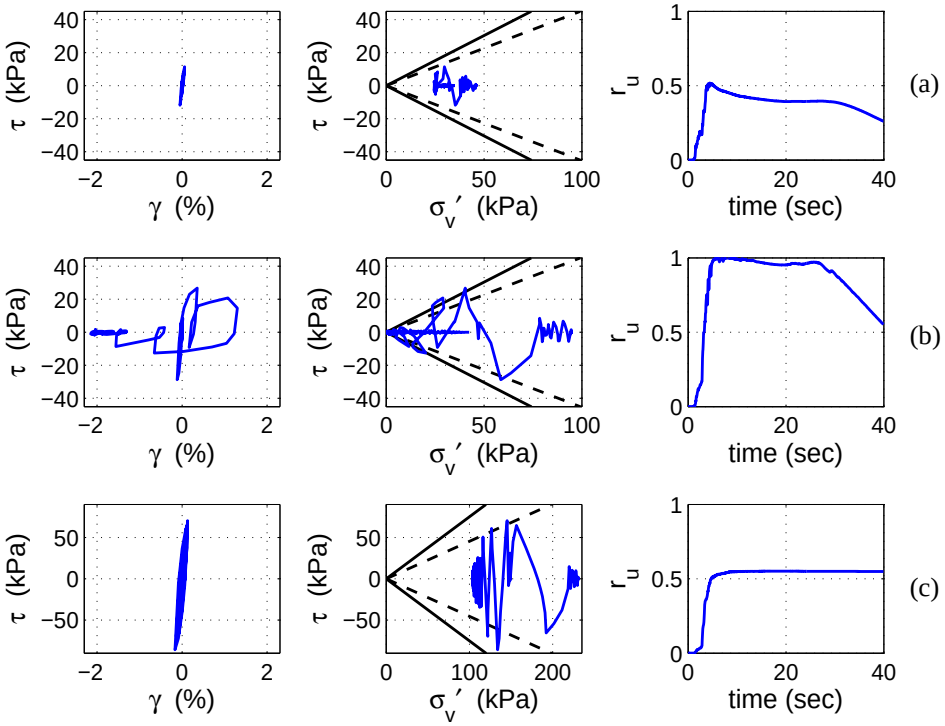

Figure 4.12: Summary of stress, strain, and pore pressure ratio response for Q1-P1ssp element; (a) 3 m, (b) 7 m, and (c) 17 m below surface.

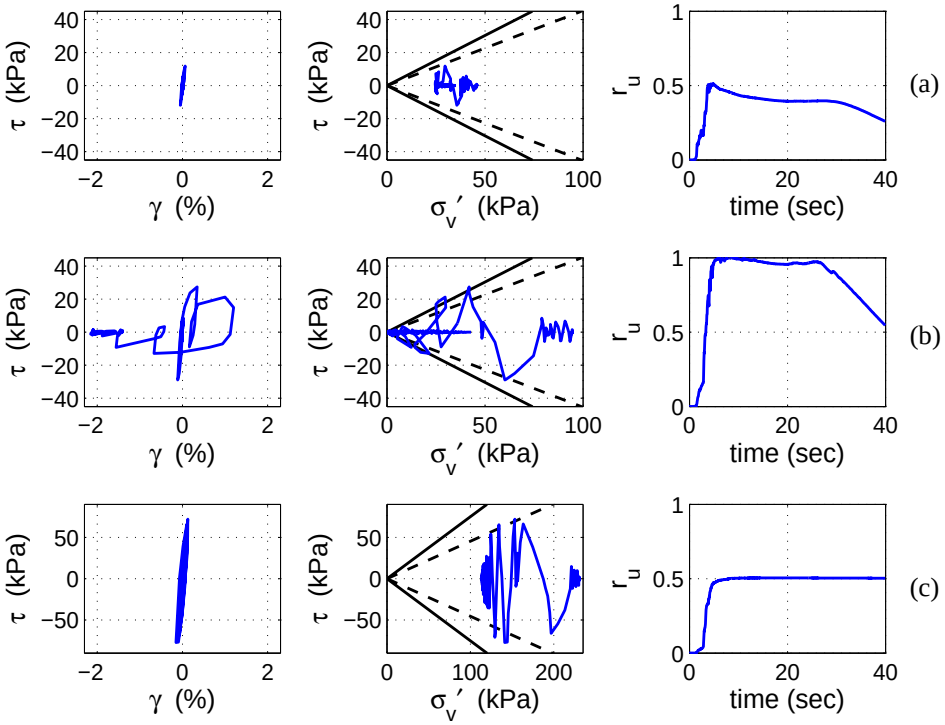

Figure 4.13: Summary of stress, strain, and pore pressure ratio response for Q2-P1 element; (a) 3 m, (b) 7 m, and (c) 17 m below surface.

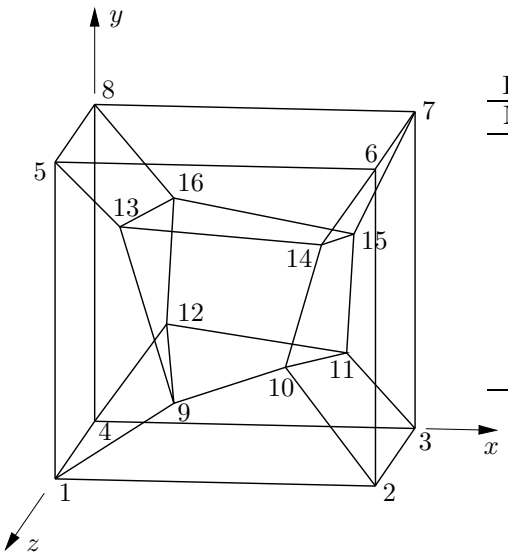

Interior Nodal Locations

Node	x	y	z
9	0.320	0.186	0.643
10	0.677	0.305	0.683
11	0.826	0.288	0.288
12	0.249	0.342	0.192
13	0.165	0.745	0.702
14	0.788	0.693	0.644
15	0.850	0.649	0.263
16	0.273	0.750	0.230

Figure 4.14: 3D element patch after MacNeal and Harder (1985). Exterior nodal locations are for unit cube.

4.9 Numerical Examples for Eight-Node Hexahedral Elements

As with the 2D elements, the 3D formulation is implemented in OpenSees as two separate elements; H1ssp, a displacement element using the solid phase formulation of Section 4.4, and H1-P1ssp, a coupled fluid-solid element using the solid and fluid phase formulations (Sections 4.4 and 4.5) with the pressure field stabilization and temporal integration schemes of Sections 4.6 and 4.7. The OpenSees implementations of these two new elements (respectively SSPbrick and SSPbrickUP in the OpenSees interpreter) are analyzed using a set of numerical test problems similar to those used for the 2D elements to test the effectiveness of the formulations and to quantify the computational savings gained through their use.

4.9.1 Patch Test

The consistency, stability, and robustness of the H1-P1ssp solid phase formulation is established using the solid element patch test of MacNeal and Harder (1985). With only the minimum essential boundary conditions enforced, natural boundary conditions are applied for the base mesh shown in Figure 4.14 as well as several iterations of consistent refinement. For all considered element patches, the conditions of the patch test are satisfied.

4.9.2 Cantilever Beam Analysis

A cantilever beam model is used to assess the convergence rate and accuracy of the H1ssp formulation. The model beam has a length $L = 16$ m and a depth $D = 1$ m. The analysis is performed under plane strain conditions with an element thickness of 1 m in the z-direction (normal to the plane of bending). A vertical load at $x = 0$ and the corresponding reactions

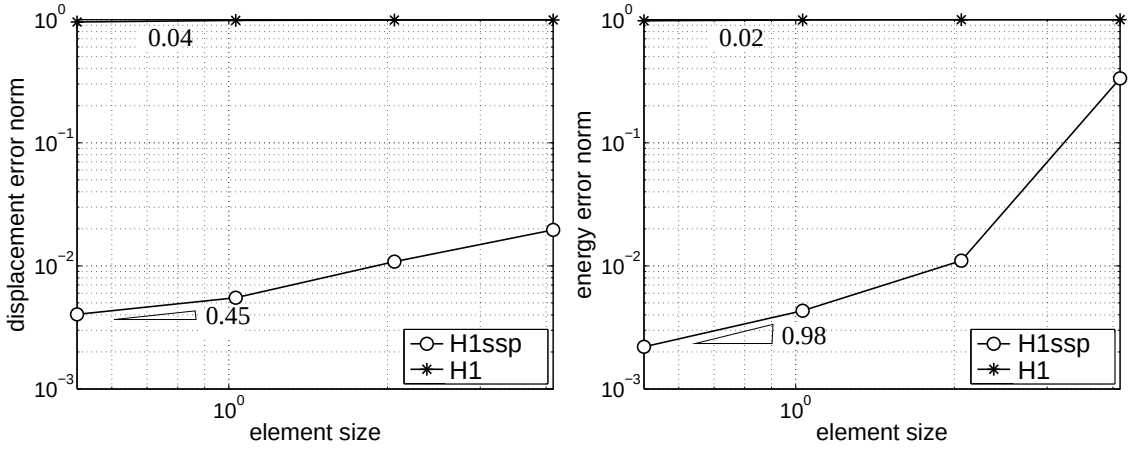

Figure 4.15: Displacement and energy error norms for plane strain cantilever beam.

at $x = L$ are applied in accordance with the stress field solutions given in (4.237)-(4.239). The expected axial and vertical displacements, u and v, respectively, for a plane strain cantilever beam considering shear deformation (after Timoshenko and Goodier, 1951) are given by

$$u = \frac{P(L^2 - x^2)y}{2\bar{E}I} - \frac{\bar{\nu}Py^3}{6\bar{E}I} + \frac{Py^3}{6IG} \tag{4.246}$$

$$v = \frac{\bar{\nu}Pxy^2}{2\bar{E}I} + \frac{P(x^3 - L^3)}{6\bar{E}I} - \frac{PL^2(x - L)}{2\bar{E}I} - \frac{Pc^2(x - L)}{2IG} \tag{4.247}$$

in which L is the beam length, G is the shear modulus, and

$$\bar{E} = E/(1 - \nu^2); \qquad \bar{\nu} = \nu/(1 - \nu) \tag{4.248}$$

where $E = 2000$ MPa is the elastic modulus and $\nu = 0.4999$ is Poisson's ratio.

Coarse mesh accuracy is evaluated using a tip deflection ratio, computed as the ratio of the average recorded deflection at $x = 0$ to the $v(0, 0)$ solution of (4.247) for a 1×4 mesh (one element over D, four elements over L). The tip deflection ratio for H1ssp is 0.983, demonstrating a considerable increase in coarse mesh accuracy over the 0.005 ratio for an H1 element with the same mesh and material properties.

The convergence rates of the H1ssp and H1 elements are evaluated in terms of the displacement error norm and energy error norm defined in (4.242)-(4.244) for four levels of consistent refinement (1×4, 2×8, 4×16, and 8×32). Convergence plots are shown for each error norm in Figure 4.15. The accuracy and convergence rates for H1ssp far exceed those of H1 for this nearly incompressible case, thus confirming the success of the anti-locking scheme used in the stabilized single-point H1ssp element and H1-P1ssp solid phase formulation.

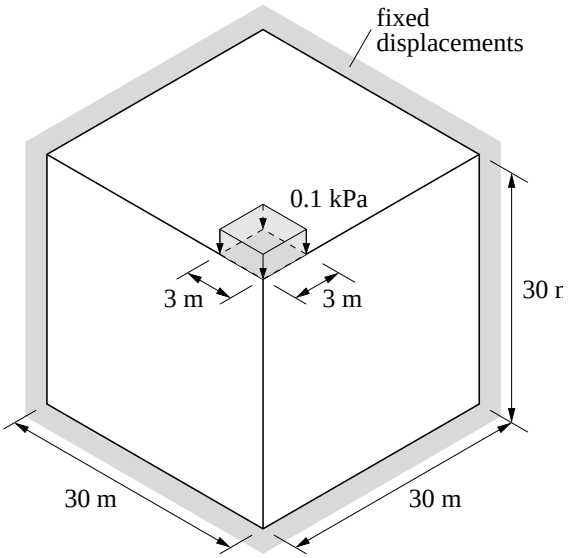

Figure 4.16: Model layout for flexible footing load test problem.

4.9.3 Flexible Footing Load Analysis

Stability in the incompressible-impermeable limit is evaluated using a test problem in which a footing load is applied to a saturated continuum of soil with a low permeability and a pore fluid with a large bulk modulus. The general layout of this test problem is shown in Figure 4.16. Zero drainage boundaries are enforced on all faces except that with the applied loading, displacements are fixed on the surfaces indicated, and symmetry conditions are used as shown. The mesh has 12 elements in each direction and is selectively refined near the loading with the elements gradually increasing in size away from this zone.

The loading is applied as linearly increasing from zero to 0.1 kPa over 0.1 s, then held constant for the remainder of the analysis. Permeability is isotropic at 10^{-7} m/s, fluid density is set at 1.0 Mg/m^3, the fluid build modulus is $2.2 \cdot 10^{12}$ kPa, the void ratio is 0.7, and the mixture mass density is 2.67 Mg/m^3. The soil is modeled as linear elastic with elastic modulus $E_s = 25,000$ kPa and Poisson's ratio $\nu = 0.3$. Rayleigh damping with $\mathbf{C} = 0.05\mathbf{M} + 0.0003\mathbf{K}$ is assumed for the solid phase.

Cases are considered both with and without the non-residual stabilization implemented in the H1-P1ssp element to assess the effectiveness of the stabilization scheme. The results are compared to full-integration H1-P1 (8 nodes, 32 degrees-of-freedom) and H2-P1 (20 nodes, 68 degrees-of-freedom) elements with similarly implemented $\mathbf{u}$-p formulations to provide an independent assessment of element performance. In the OpenSees interpreter, these elements are referred to as brickUP and Twenty_Eight_Node_BrickUP, respectively.

The variation of nodal pore pressure with depth directly below the center of the applied load at $t = 0.95$ s is shown in Figure 4.17 for the H1-P1ssp and H2-P1 elements. Stabilization for the H1-P1ssp element is active with α ranging from $2.97 \cdot 10^{-6}$ to $1.44 \cdot 10^{-5}$ depending on the element size. As shown in Figure 4.17, the pressure distribution for the H1-P1ssp

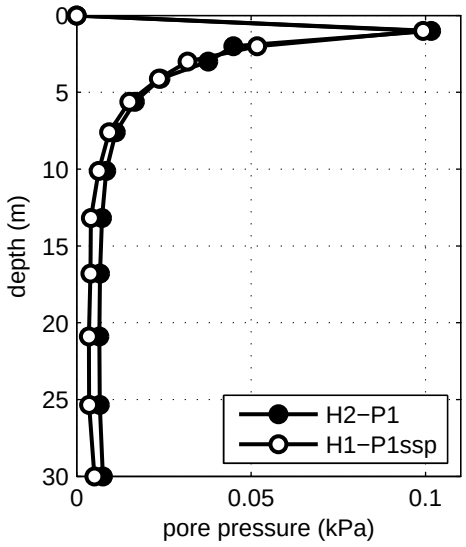

Figure 4.17: Variation of pore pressure with depth below center of footing load at 0.95 s for H1-P1ssp and H2-P1 elements.

element compares favorably with the higher-order , thus inherently stable, H2-P1 solution.

Spatial pore pressure distributions at $t = 0.95$ s are used compare the considered element types. Figure 4.18(a) shows the pore pressure field for the H1-P1ssp element with stabilization inactive ($\alpha = 0$). The observed instability is expected for this case. The corresponding result for the H1-P1ssp element with stabilization active ($2.97 \cdot 10^{-6} \leq \alpha \leq 1.44 \cdot 10^{-5}$ according to element size) is shown in Figure 4.18(b). The effect of stabilization on the solution is dramatic.

The pore pressure fields for the H1-P1 and H2-P1 elements are shown in Figures 4.18(c) and (d), respectively. The expected pressure instability for the H1-P1 element is observed, though the effect is not as severe as for the H1-P1ssp element, likely due to the difference in integration schemes. The H2-P1 element provides a stable basis of comparison for the H1-P1ssp element, and as shown in Figure 4.18, the two cases produce reasonably similar results, thus verifying the effectiveness of the non-residual stabilization scheme implemented in the H1-P1ssp element

The advantages of the H1-P1ssp element for the analysis of saturated porous media are evident from the results presented here. The H1-P1ssp and H1-P1 elements are identical with respect to degrees-of-freedom, however, not only is the H1-P1ssp element more efficient computationally due to the use of reduced integration, the stability of the pressure field is superior. Compared to the H2-P1 element, the H1-P1ssp element greatly reduces the number of degrees-of-freedom for the problem, simplifies mesh generation, and offers increased computational efficiency while preserving similar accuracy. The reduction in computational effort for the H1-P1ssp element is further analyzed and quantified in the following example analysis.

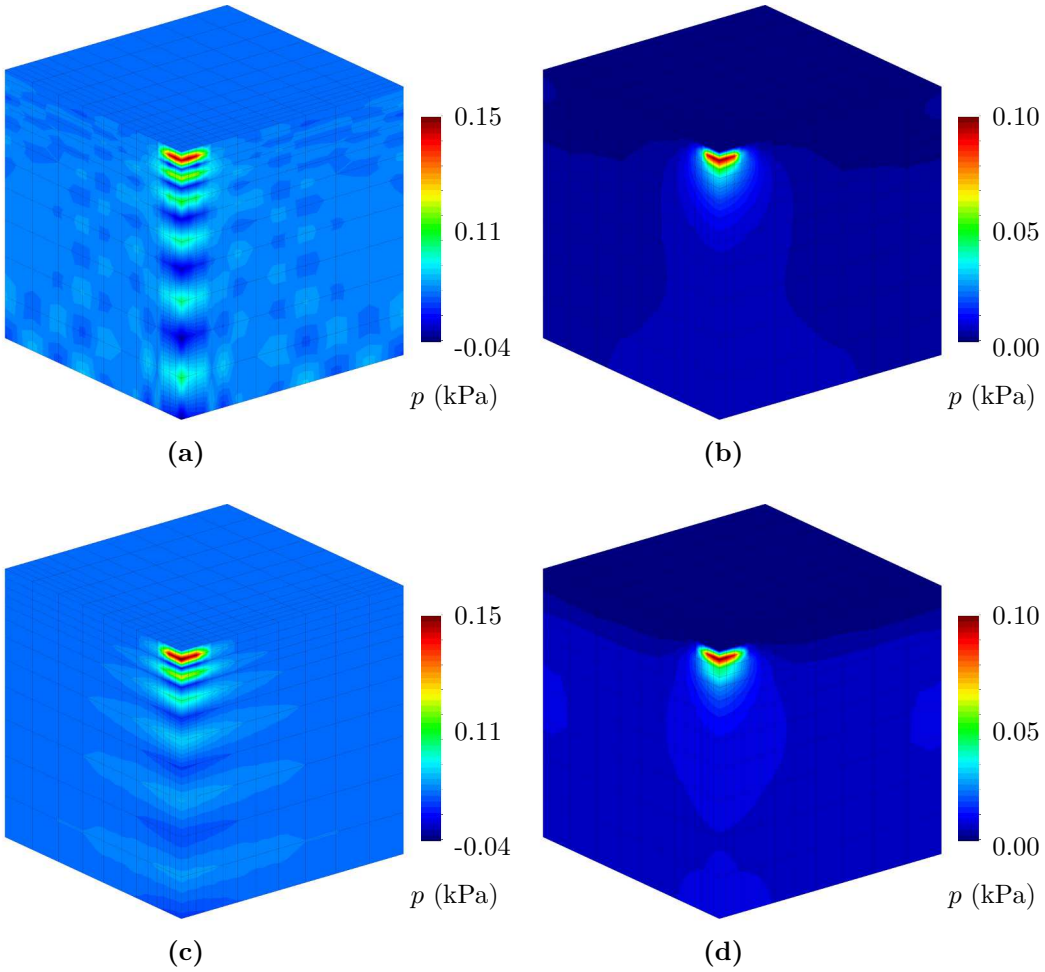

Figure 4.18: Pore pressure distributions at 0.95 s. (a) H1-P1ssp element without stabilization ($\alpha = 0$). (b) H1-P1ssp element with stabilization active. (c) H1-P1 element. (d) H2-P1 element.

4.9.4 Site Response Analysis

The applicability of the H1-P1ssp element to a general dynamic, nonlinear problem is evaluated, and the relative computational efficiency of the new element is assessed, using a site response analysis. Typically, a site response analysis considers only 1D wave propagation (see Section 4.8.4 for a more traditional approach), in this case the 3D H1-P1ssp element is used to model an infinite slope subject to an earthquake in the transverse (across slope) direction. The intention of this model is to capture the down slope displacements which occur due to pore pressure build up from the shaking in the across slope direction.

The model consists of a single column of elements supported vertically at the base. Schematically, the x-y plane of the 3D site response model is identical to that used to test the 2D element and shown in Figure 4.9. Periodic boundary conditions are enforced in the two horizontal directions to restrict element deformation to a pure shear mode. In the

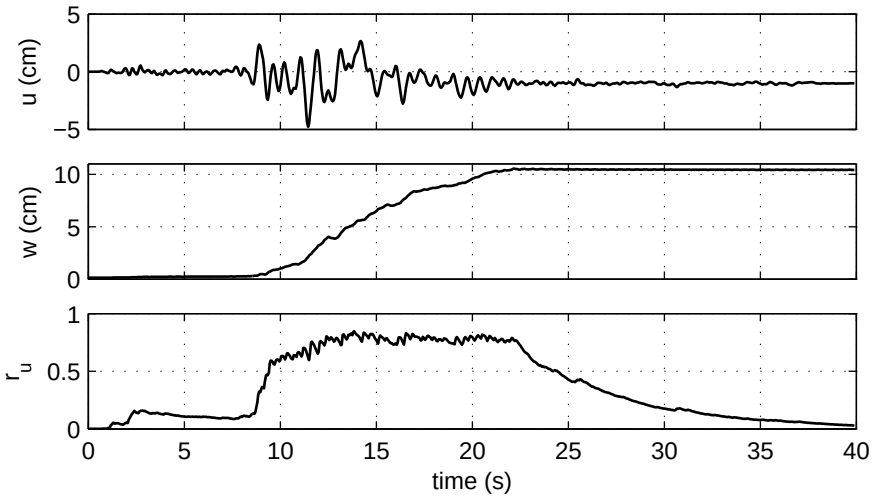

Figure 4.19: Across slope (u) and down slope (w) displacements at ground surface with pore pressure ratio (r_u) in center of saturated loose sand layer for H1-P1ssp element.

direction of loading (x-direction), a viscous dashpot is used to represent the compliance of an underlying bedrock layer, modeled as linear elastic, after Lysmer and Kuhlemeyer (1969). Displacements are fixed at the base in the down slope direction (z-direction). The nodes at and above the groundwater table are free to drain. Zero drainage is enforced on all remaining boundaries.

The soil profile modeled in this test problem, also shown in Figure 4.9, consists of two layers of cohesionless soil underlain by bedrock. The groundwater table is 2 m below the surface and all material below the groundwater table is assumed to be saturated. The slope is assigned a 2% grade and is incorporated into the model using appropriate body force vectors. A pressure-dependent nested yield surface constitutive model capable of capturing cyclic mobility (Elgamal et al., 2003; Prevost, 1985a) is used to approximate the behavior of the cohesionless soil. The assumed material parameters are provided in Figure 4.9. The reported permeability values are isotropic. Stabilization is active for the H1-P1ssp element with $\alpha = 2.4 \cdot 10^{-6}$. The Yerba Buena Island record from the 1989 Loma Prieta event (NGA #813) from the PEER ground motion database is used as the input motion. This motion is scaled to a PGA of 0.2 g and is applied at the base of the soil column in the across slope direction as an equivalent force time history obtained from the product of ρ_{rock} and $v_{s\,\text{rock}}$ with the velocity time history of the scaled motion after Joyner and Chen (1975).

Figure 4.19 presents a summary of the behavior of this 3D site response model, providing the recorded displacements for the H1-P1ssp element at the top of the soil column in the x- and z-directions, u and w respectively, as well as the pore pressure ratio in the center of the saturated loose sand layer (6 m below the surface). The pore pressure ratio is computed from (4.245). Initially, the applied shaking causes periodic displacements in the x-direction only. As the shaking intensifies, pore pressure increases in the saturated loose sand layer,

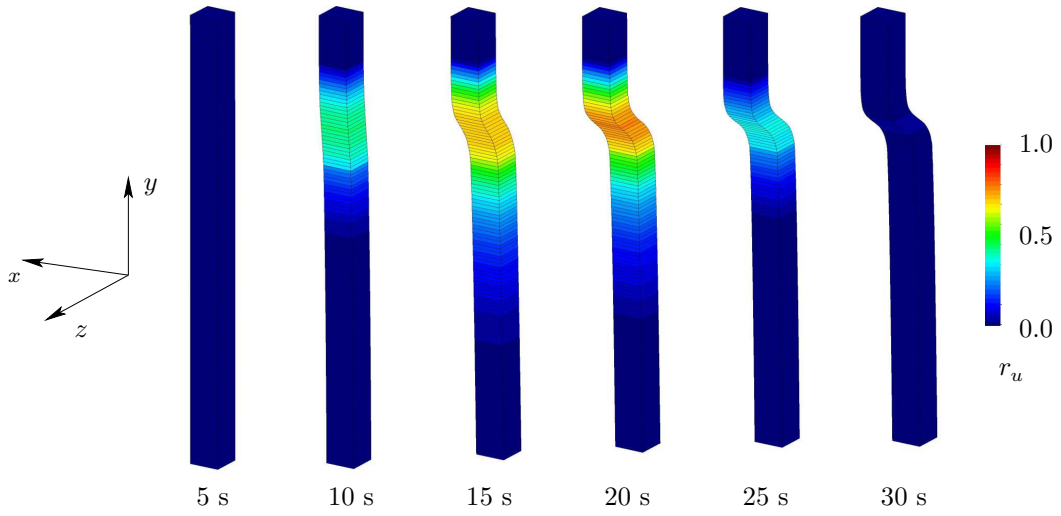

Figure 4.20: Progression of down slope (z-direction) displacement with contours of pore pressure ratio r_u for H1-P1ssp element. Displacements are magnified 25 times.

Table 4.4: Execution times for site response analysis.

Element	H1-P1ssp	H1-P1	H2-P1
Execution time	2.60 min	7.06 min	43.03 min

indicated in Figure 4.19 as an increase in pore pressure ratio. Once the pore pressure has increased to the point where the effective strength of the soil is less than the static shear stress induced by the slope, the soil begins to displace in the z-direction. After the strong shaking in the applied motion has completed, the pore pressure in the loose sand layer begins to dissipate, and no further down slope displacement occurs. This effect is also shown in Figure 4.20, which provides the displaced shape of the soil column (exaggerated) with contours of pore pressure ratio at several indicated times during the analysis.

To further evaluate the H1-P1ssp element, the constitutive behavior is examined at several depths within the soil column (4, 8, and 12m). Figure 4.21 shows the constitutive response in the x-y plane, with the shear stress-strain response (τ_{xy}-γ_{xy}) at left and the stress path in shear-mean effective stress space (τ_{xy}-p') at right, with failure and phase transformation surfaces indicated as solid and dashed lines, respectively. At all depths, the mean effective stress initially decreases, then increases as the pore pressures dissipate. The soil remains nearly elastic at the 4 m and 12 m locations, while exhibiting a nonlinear stress-strain response at the 8 m location and a stress path that is indicative of cyclic mobility. Figure 4.22 shows the corresponding constitutive responses for the z-y plane. As shown, the shear stresses are significantly smaller than in the plane of applied shaking. The reduction in mean effective stress at the 8 m depth is large enough to cause failure, leading to very large shear strains, manifested as the large down slope displacement of the upper portion of the soil column indicated in Figures 4.19 and 4.20.

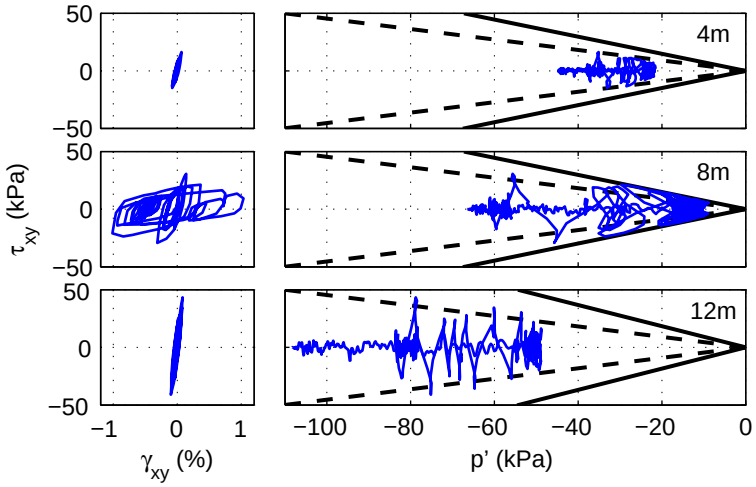

Figure 4.21: Constitutive response in the x-y plane at three depths in soil column (4 m, 8 m, 12 m) during site response analysis for H1-P1ssp element.

To evaluate the relative efficiency of the H1-P1ssp element, the H1-P1 and H2-P1 elements introduced in the footing load example are also considered in the site response model. Table 4.4 shows the user CPU time for each element type. All three cases were run with the same solution algorithms and analysis time steps on the same computer. In order to provide a comparable number of degrees-of-freedom, the mesh for the H2-P1 element has only 60 elements over the height of the soil column. As expected, the H1-P1ssp element is the most computationally efficient of the three. The higher-order H2-P1 element is significantly more expensive computationally than either of the linear elements, taking approximately 6 times longer than the H1-P1 element and about 16.5 times longer than the H1-P1ssp element. It should be noted that due to the peculiarities of the 20 node H2-P1 element, there are a greater number of degrees-of-freedom for the H2-P1 case, even with half the number of elements, however, it is likely that the large difference in computational effort is primarily due to the larger number of integration points used by this element rather than the increased size of the problem.

The efficiency of the H1-P1ssp element is apparent from the results of Table 4.4, however, efficiency alone does not verify the effectiveness of the element formulation. Figure 4.23 shows the acceleration, velocity, and displacement response spectra in the loading direction at the top of the soil column for each element type. All three cases produced reasonably similar results, though there are large differences at lower periods. To better assess the relative similarities and differences across the three cases, Figure 4.24 shows the ratios of the spectral acceleration for the H1-P1 and H1-P1ssp elements to that for the H2-P1 element. The discrepancies in the results at lower periods for both of the lower-order elements are clearly shown here, with the H1-P1ssp element providing a better correlation in PGA.

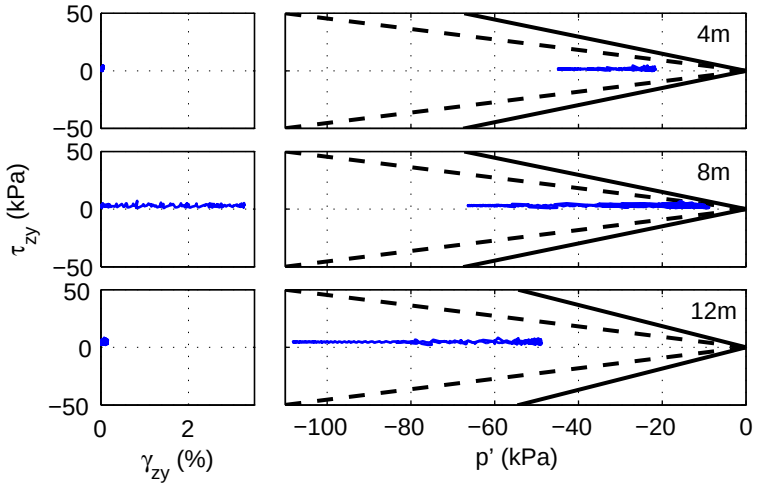

Figure 4.22: Constitutive response in the z-y plane at three depths in soil column (4 m, 8 m, 12 m) during site response analysis for H1-P1ssp element.

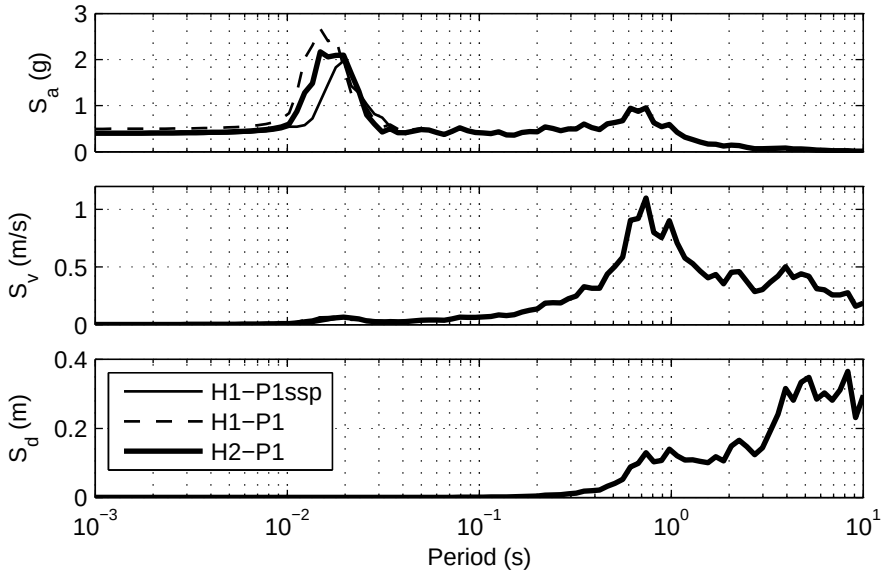

Figure 4.23: Acceleration, velocity, and displacement response spectra in loading direction at ground surface.

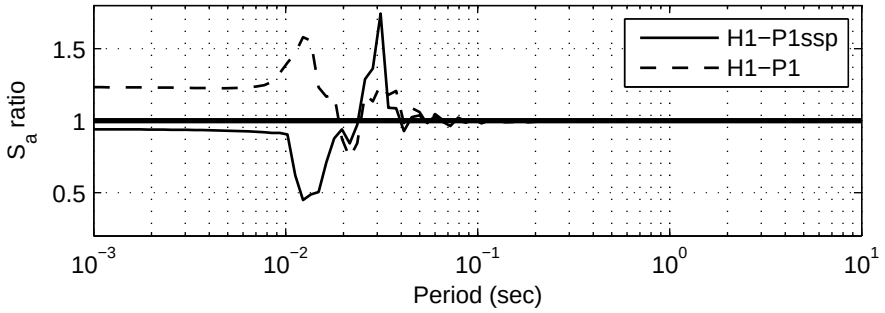

Figure 4.24: Spectral acceleration ratios for H1-P1ssp and H1-P1 elements.

4.10 Summary

Low-order single-point quadrature **u**-p elements for dynamic analysis of saturated porous media in two- and three-dimensions have been developed and studied. The new elements, Q1-P1ssp and H1-P1ssp, use hourglass stabilization of the solid phase to eliminate the spurious modes associated with reduced integration. Assumed strain fields are used to eliminate shear and volumetric locking from the solid phase. The fluid phase is stabilized in the incompressible-impermeable limit using a non-residual stabilization scheme, facilitating the use of equal-order interpolation for the displacement and pressure fields.

The solid phases of the elements were implemented as distinct elements, Q1ssp and H1ssp. These displacement elements were evaluated using the standard patch test, and the anti-locking strategies were verified in pure bending analyses with various configurations, including nearly incompressible cases. The adopted hourglass-stabilization techniques were shown to successfully stabilize the implemented single-point integration schemes, and the anti-locking strategies were found to effectively remove both parasitic shear and volumetric locking phenomena from the new elements.

The stability of the coupled fluid-solid elements in the limiting case of incompressibility and impermeability was evaluated, and the effectiveness of the implemented stabilization technique was demonstrated. Comparisons to higher order elements and full-integration low-order elements highlighted the advantages of the new elements. The Q1ssp, Q1-P1ssp, H1ssp, and H1-P1ssp elements are more stable, accurate, and efficient than the standard low-order elements while producing comparable results to the higher-order elements with greater computational efficiency.

Chapter 5

REVIEW OF DESIGN PROCEDURES FOR BRIDGE FOUNDATIONS SUBJECT TO LIQUEFACTION-INDUCED LATERAL SPREADING

In a typical bridge analysis or design procedure, the individual component systems are analyzed individually to determine appropriate demands for various load cases. The results of the component analyses are then synthesized into a global bridge analysis to assess the suitability of the entire structure. A balance between engineering rigor and economic efficiency is sought, and the treatment of foundation behavior in the component and global analysis phases is generally simplified. The analytical approaches adopted in practice typically assume the applicability of 1D or 2D descriptions, or incorporate 3D effects in a simplified manner. Fully 3D analysis may be conducted for sites with high levels of importance or certain types of topography, however, widespread use of 3D analysis in practice is limited.

Two example design approaches for bridge foundations subject to liquefaction-induced lateral spreading are discussed in the following sections: the California Department of Transportation (Caltrans) procedure and the Washington State Department of Transportation (WSDOT) procedure. Each design procedure is based off of the applicable American Association of State Highway and Transportation Officials bridge design specifications (AASHTO, 2010a,b), and each approach considers many of the same analysis components, but the two procedures lead to different results due to key differences in the assumptions made.

5.1 Summary of Caltrans Design Guidelines for Lateral Spreading

The current bridge foundation design guidelines for liquefaction-induced lateral spreading used by the California Department of Transportation are contained in an internal policy proposal (Caltrans, 2011). These guidelines are based off of the NCHRP (2002) design recommendations which effectively separate the design problem into two distinct cases: (1) an unrestrained ground displacement case, and (2) a restrained ground displacement case. The unrestrained ground displacement case assumes that the foundation is subject to a broad failure mass and will not provide significant resistance to lateral soil movement. The restrained ground displacement case assumes the failure mass has a limited width and that the foundation provides resistance to soil deformation during lateral spreading. The design processes for the restrained and unrestrained ground displacement cases, per Caltrans (2011), are described in the following discussion.

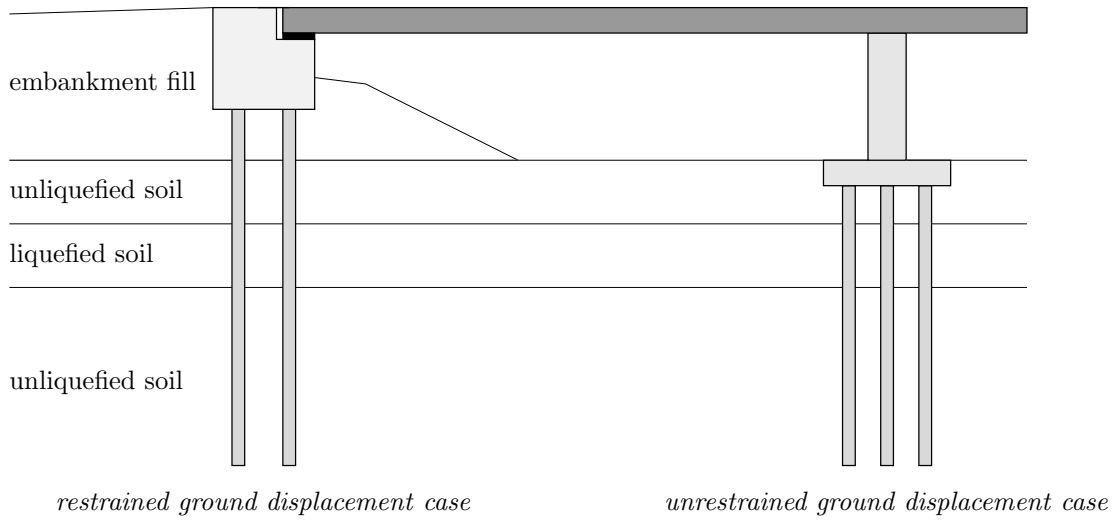

Figure 5.1: Prototype examples for restrained and unrestrained ground displacement cases.

5.1.1 Restrained Ground Displacement Case

The restrained design case applies to foundations which are assumed to provide partial restraint to soil flow during lateral spreading. The prototype for this case is an approach embankment acting on a pile-supported abutment, see Figure 5.1. Due to the limited width of the embankment, it is assumed that the lateral stiffness of the abutment foundation will provide resistance to soil movement. The procedure recommended for this design case is based on the pile pinning analysis concept (Martin et al., 2002) as refined and expanded upon by later works (Zha, 2004; Boulanger et al., 2006; Ashford et al., 2011). In the pile pinning approach, a beam on nonlinear Winkler foundation (BNWF) model of the foundation is combined with a limit equilibrium slope stability analysis of the embankment to determine the force-displacement state at which the resistance of the foundation is compatible with the deformation of the lateral spreading mass. The method consists of 7 basic steps:

1. **Assess Liquefaction Potential**

   The liquefaction potential of the site soils is characterized for a peak ground acceleration (PGA) corresponding to a 5% in 50 years hazard. This is typically accomplished using a simplified approach (e.g., Youd et al., 2001). Per AASHTO (2010b), the assumption of reduced strength due to pore pressure build-up or full liquefaction is required for soils with a factor of safety against liquefaction less than 1.2.

2. **Estimate Residual Strength of Liquefied Soils**

   There are two options which can be used to account for the residual strength of the *p-y* curves representing liquefied layers in the BNWF model of the soil-foundation system. No explicit preference of method is stated in Caltrans (2011).

(a) The p-multiplier (m_p) approach (e.g., Brandenberg et al., 2007b) may be used to obtain scaled p-y curves for liquefied soils based on a sand-type backbone curve.

(b) The residual strength of the liquefied soil may be estimated using an empirically-based method (e.g., Wang, 2003), and used as the ultimate resistance in the definition of p-y curves for liquefied soils based on a clay-type backbone curve.

3. **Develop Foundation Model**

The numerical BNWF model used to analyze the foundation requires definitions for the equivalent beam representing the foundation, the p-y curves for soil-pile interaction, and a force-displacement curve to capture abutment-embankment interaction. The commercial software LPILE is typically used for this purpose.

(a) ***Definition of equivalent beam:*** The equivalent beam used to model the foundation (piles and cap/abutment) may be defined assuming linear elastic or nonlinear elastoplastic behavior. In both cases, the spatial arrangement of the piles is largely ignored and the equivalent beam is developed in a simplified manner. For linear elastic behavior, the equivalent beam model is obtained by multiplying the bending stiffness, EI, of a single pile by the number of piles in the group. For nonlinear behavior, the moment-curvature response of a single pile is scaled by the number of piles in the group.

The pile cap/abutment is incorporated into the equivalent beam using a large linear elastic bending stiffness which approximates its rigidity relative to the piles. The rotational stiffness of the pile group is modeled using a rotational restraint located at the connection of the piles to the cap/abutment. This restraint is assigned a stiffness equivalent to the estimated rotational stiffness of the pile group after Mokwa and Duncan (2003).

(b) ***Definition of p-y curves for piles:*** The p-y curves used for soil-pile interaction are based on the work of Matlock (1970) for soft clay, Reese and Welch (1975) for stiff clay, and Reese et al. (1974) for sand. The base p-y curves determined for the site using these methods are modified to account for pile group effects and the effects of liquefaction.

- Group effects are considered using a composite group efficiency factor computed as the average of the reduction factors for each row in the pile group as recommended by Mokwa and Duncan (2001).
- The p-y curves of liquefied soils are defined as discussed in step 2. The influence of the weaker layer of liquefied soil on the surrounding material is accounted for using a linearly smeared ultimate lateral resistance profile as shown in Figure 5.2.

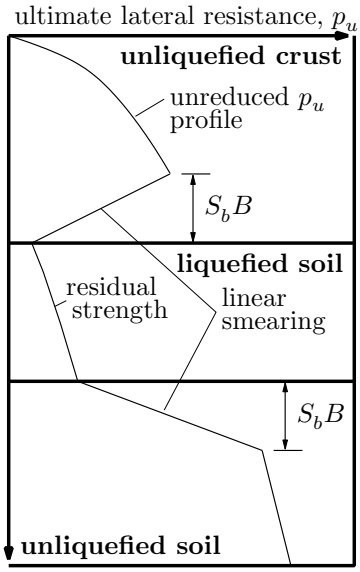

$$S_b = \begin{cases} 2, & B < 1 \text{ ft} \\ 2 - (B-1)/2, & 1 \text{ ft} \le B \le 3 \text{ ft} \\ 1, & B > 3 \text{ ft} \end{cases}$$

where B is the pile diameter (units of ft)

Figure 5.2: Smeared profile of ultimate lateral resistance to account for presence of liquefied layer on strength of surrounding soil (after Caltrans, 2011).

(c) ***Definition of cap/abutment-soil interaction curve:*** A tri-linear force-displacement curve describing the interaction of the cap/abutment with the surrounding soil is defined using the maximum passive load of the soil on the foundation, F_{ult}, and the displacement, Δ_{max}, required to mobilize this force. This curve is shown in Figure 5.3. Two failure cases are considered to determine F_{ult}, with the lesser force controlling the design. The two cases are as follows:

- A log-spiral passive wedge acting on the cap/abutment combined with the lateral resistance provided by the portions of the piles extending through the crust (i.e., soil above the liquefied layer).
- A Rankine passive wedge acting on foundation elements above the liquefied layer assuming that the cap/abutment, crust soil beneath the cap/abutment, and piles within the crust all act as a composite block.

The displacement, Δ_{max}, corresponding to the ultimate passive force is taken as the sum of 5% of the cap/abutment height with an adjustment factor which accounts for the effects of the depth of the liquefied material and the transverse thickness of the cap/abutment after Brandenberg et al. (2007a).

4. **Displacement Analysis of Foundation Model**

Once the foundation model has been completed, a series of pushover analyses are conducted in which increasing crustal displacements are considered. Displacements are applied to the soil end of the *p-y* springs using the displacement profile shown in Figure 5.4 to simulate the effects of lateral spreading. For a series of increasing surface displacements, the pile cap displacement and a running average of the shear force at

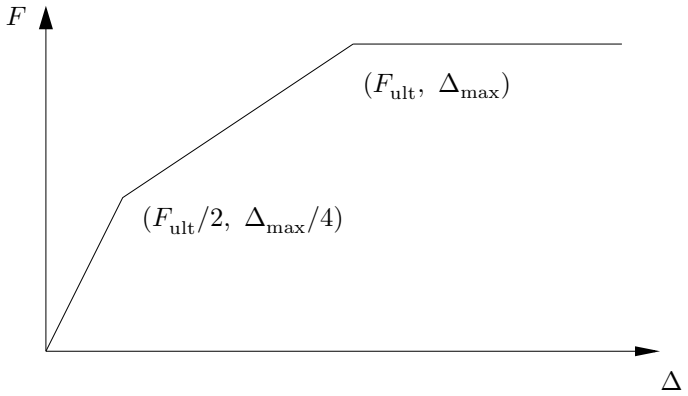

Figure 5.3: Tri-linear force-displacement curve for pile cap/abutment-soil interaction in foundation model (after Caltrans, 2011).

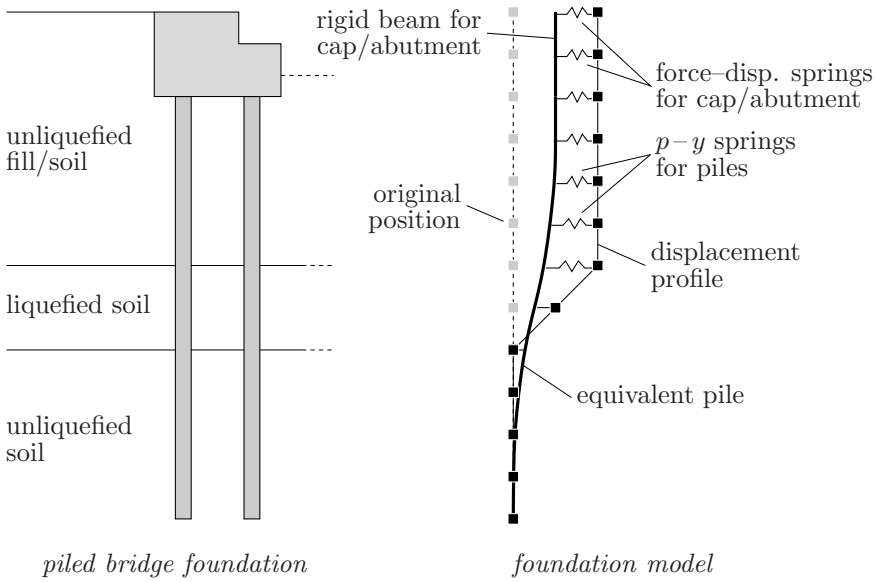

Figure 5.4: Transition from physical bridge foundation to foundation model showing the applied displacement profile for lateral spreading pushover analysis.

the center of the liquefied layer are recorded to obtain a lateral spreading pushover curve for the foundation.

The running average shear force for each displacement increment is computed as the sum of the current and all previous shear force values divided by the number of terms in the sum. This running average is made in an attempt to account for the discrepancy between the pushover analysis of this design step, in which the shear force increases with increasing ground displacement, and the slope deformation analyses of the next step, in which only constant foundation resisting forces are considered.

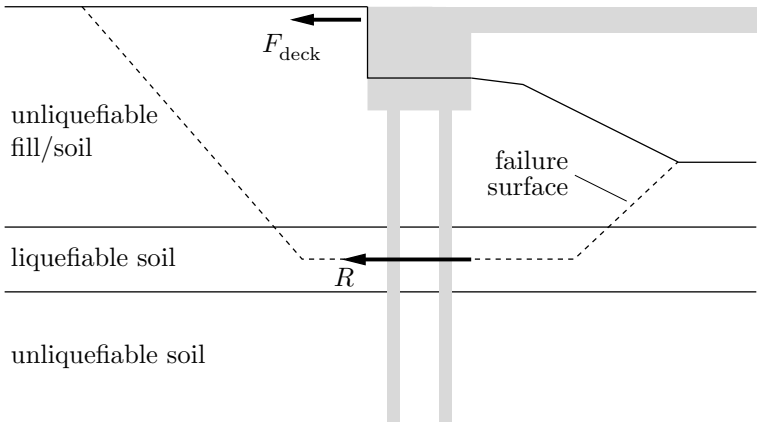

Figure 5.5: Schematic of slope stability analysis considering a deck resisting force, F_{deck}, and foundation resisting force, R.

5. **Slope Stability and Deformation Analysis of Approach Embankment**

   A pseudo-static slope stability model is used to determine foundation resisting forces, R, at the center of the liquefied layer for a series of horizontal accelerations, k_h, applied in the model as a constant inertial force

   $$F_h = k_h W \tag{5.1}$$

   where W is the weight of the failure mass. For each considered acceleration value, the resisting force for which the slope factor of safety reaches 1.0 is recorded.

   In these analyses, the restraining forces are applied on the lower edge of the failure surface, and the failure surface is constrained to the center of the liquefied layer, as depicted in Figure 5.5. It is also recommended that the failure surface be limited to extending ≤ 4 times the height of the embankment away from the bridge abutment. If it is assumed that the bridge deck will provide longitudinal resistance to abutment movement, a deck resisting force, F_{deck}, is computed based on the full passive resistance of the soil acting on the deck and applied during the slope stability analysis.

   Newmark rigid sliding block analysis is used to compute the slope displacements corresponding to the k_h coefficients used to determine resisting forces in the slope stability analyses. Typically, a simplified procedure (e.g., Bray and Travasarou, 2007) is used in lieu of site-specific sliding block analysis.

6. **Determine Force-Displacement Compatibility**

   The results of the pushover and slope stability/deformation analyses are used to determine a compatible force-displacement state which considers the restraining effects

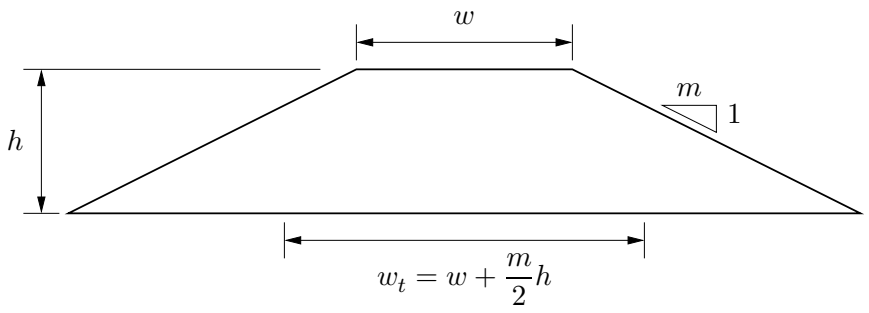

Figure 5.6: Tributary width of embankment, w_t (after Boulanger et al., 2006).

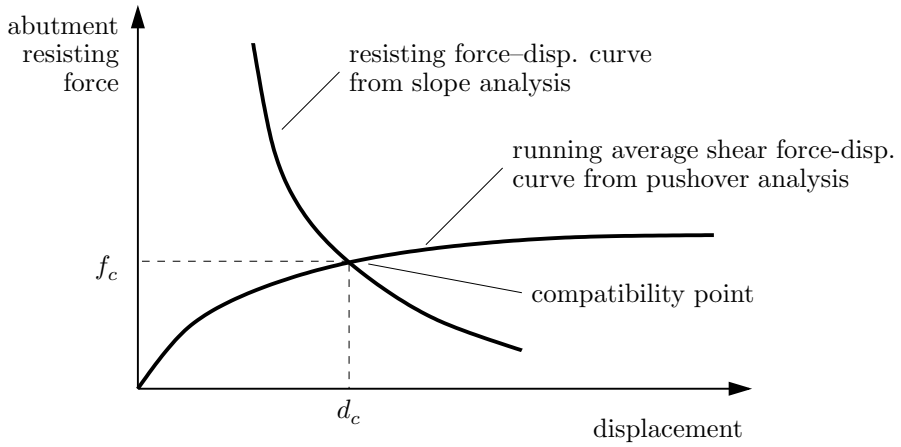

Figure 5.7: Determination of compatible force-displacement state.

of the bridge foundation on the deformation of the soil-foundation system during lateral spreading. This is accomplished by plotting the slope force-displacement curve determined from the slope stability/deformation analyses (step 5) with the foundation running average shear force-displacement curve determined in the pushover analyses (step 4) in the manner shown in Figure 5.7.

The running average forces are used for the foundation force-displacement curve to account for the differences in how the resisting force is handled in the two curves (constant in the slope deformation curve, non-constant in the pushover curve). Because the resisting forces obtained in the slope stability phase represent a force per unit thickness of soil, the lateral spreading pushover curve must be scaled by an appropriate width. For this purpose, the finite transverse thickness of an approach embankment is considered in the scaling factor, as the pushover curve forces are divided by the tributary width of the embankment determined as shown in Figure 5.6.

7. **Assess Foundation Performance**

The final performance evaluation for the foundation is conducted using a lateral spreading pushover analysis which considers the combined effects of kinematic and inertial loads. A kinematic loading is applied using the displacement profile shown in Figure 5.4 with an applied surface displacement set as the compatible displacement, d_c, determined in step 6. Consideration for inertial effects is made during this analysis by applying 50% of the inertial loads from any associated superstructure or pile caps, as it is unlikely that lateral spreading occurs during peak shaking.

The inertial effects of superstructure elements for typical bridge bents are considered using an applied moment and shear force pair, which are determined based on the design of the bridge columns. There are two possibilities:

(a) In most cases, the bridge columns are designed to yield and develop plastic hinges prior to the onset of yield in the foundation elements. For this type of design, the inertial moment is set at 1.2 times the plastic moment capacity of the column. For columns which have a pinned connection at the top and a fixed connection at the bottom (free-fixed configuration), the inertial shear force is determined by dividing this inertial moment by the height of the bridge column. For columns with a fixed-fixed configuration, the inertial shear force is set as the inertial moment divided by one-half the column height.

(b) If the column is not expected to yield for the design event, then the inertial shear force is estimated as the product of the tributary mass carried by the bridge column with the spectral acceleration corresponding to the first mode of the column. The inertial moment is set as the product of the inertial shear force with the column height for a free-fixed configuration, or one-half of the same product for a fixed-fixed configuration.

For seat-type abutment foundations, the superstructure is supported by bearings which can freely rotate, and the only means of transferring inertial shear from the superstructure is through a backwall, typically designed as a weak fuse with limited capacity to transfer load. For these reasons, it is assumed that no inertial loads are transferred from the superstructure for seat-type abutments. To account for the inertial effects of relatively massive foundation bodies, such as a pile cap, an inertial force is computed as

$$f_{\text{cap}} = 0.65 m_{\text{cap}} a_{\text{no liq}} \tag{5.2}$$

where $a_{\text{no liq}}$ is the design PGA without consideration for liquefaction, m_{cap} is the pile cap mass, and the 0.65 factor is used to represent a reduction in PGA due to the onset of liquefaction.

The combined kinematic-inertial pushover analysis is used to determine if the foundation has sufficient capacity under an assumed peak demand case. This analysis is used to evaluate the resulting shear force and bending moment demands for the deep foundations and to assess whether the displacement at the pile cap/abutment is acceptable for the overall bridge structure.

5.1.2 Unrestrained Ground Displacement Case

The unrestrained design case applies to foundations that are assumed to be unable to significantly restrain the flow of soil associated with lateral spreading. An example case is an interior bridge bent foundation embedded in a site with broad transverse continuity as shown in Figure 5.1. In this case, the lateral stiffness of the foundation is insignificant relative to the loads applied by the lateral soil flow. For design purposes, it is assumed that soil movement will be unaffected by the presence of the foundation, though evidence from previous earthquakes shows that this is not true at the local level.

The design process for the unrestrained ground displacement case begins in the same manner as the restrained ground displacement case, with the assessment of liquefaction potential (step 1), estimation of residual strength for liquefied soils (step 2), and the definition of a foundation model (step 3) corresponding exactly. After the completion of these steps, the remaining steps for the unrestrained case differ from those previously discussed.

Estimation of the design ground displacement for the unrestrained case is initiated by evaluating the slope stability factor of safety (FS) assuming the absence of the foundation. If FS $\leq$ 1.05, a flow-type failure is assumed. Typically, an assumption of 5 ft of displacement is made, as this is considered sufficient to mobilize the full passive force of the crust on the foundation, and it is stated in Caltrans (2011) that as long as the passive force is mobilized, the remaining analysis is insensitive to the specific displacement value. For cases where FS $>$ 1.05, the crustal displacement is estimated using one of two simplified techniques. When the slope has a predictable failure surface, a Newmark sliding block-based approach (e.g., Bray and Travasarou, 2007) is used with an input acceleration set equal to the design PGA. For gentle slopes, where there is greater uncertainty in the failure surface, crustal displacements are estimated using the strain potential procedure of Faris et al. (2006).

The foundation is evaluated using a lateral spreading pushover analysis, with an applied displacement profile as shown in Figure 5.4. The imposed surface displacement in this analysis is set equal to that required to mobilize the full passive soil resistance for the FS $\leq$ 1.05 case, or to the estimated crustal displacement for the FS $>$ 1.05 case. Inertial loads from the bridge superstructure (if any) are included in this analysis in the manner described in step 7 for the restrained ground deformation case. The bending moment, shear force, and displacement demands computed using the pushover analysis are compared to the allowable foundation performance criteria.

5.2 Washington State Department of Transportation Design Procedure

The Washington State Department of Transportation design guidelines for bridge foundations subject to liquefaction-induced lateral ground deformation are contained in the WSDOT geotechnical design manual, WSDOT (2011b), and WSDOT bridge design manual, WSDOT (2011a). For most scenarios, several alternative analysis procedures are made available, allowing the designer to choose the method most applicable to the particular site, foundation, and structure.

Overall, the WSDOT design procedure for liquefaction-induced lateral ground deformation is similar to the unrestrained ground displacement case presented in Caltrans (2011). The restrained ground displacement case addressed in the Caltrans guidelines, in which a compatible force-displacement state is sought for situations in which there is a limited transverse soil domain, is not explicitly included in the WSDOT procedure. Structural pinning effects are addressed, however, they are not handled using the pile pinning analysis procedure discussed in the previous section.

The WSDOT design procedure for liquefaction-induced lateral ground deformation is summarized in the following discussion. There are two potential outcomes in this procedure: (1) design for a flow-type failure, or (2) design for a lateral spreading type failure. The particular outcome is determined in the fourth step of the procedure using limit equilibrium slope stability analysis. The separate procedures for the two design outcomes are discussed following a summary of the first four steps in the design process.

1. **Assess Liquefaction Potential**

   Susceptibility to liquefaction is assessed for the PGA corresponding to the site-specific hazard (typically 7% in 75 years). Liquefaction potential may be assessed using a simplified approach (e.g., Youd et al., 2001; Cetin et al., 2004; Moss et al., 2006; Boulanger et al., 2006; Idriss and Boulanger, 2008), or the performance-based approach of Kramer and Mayfield (2007). For sites which are not well characterized by the simplified methods, nonlinear effective stress site response analysis or laboratory cyclic simple shear or cyclic triaxial shear testing may be used.

2. **Estimate Residual Strength of Liquefied Soils**

   Residual undrained shear strength parameters for liquefied soils are obtained from empirically-based relationships (e.g., Idriss and Boulanger, 2007; Olson and Stark, 2002; Wang, 2003). Residual strength conditions are assumed for all soils for which $FS_{liq} < 1.2$, or which are determined to be liquefiable for the return period of interest using the method of Kramer and Mayfield (2007). If a more refined characterization of residual strength is needed, cyclic triaxial shear or cyclic simple shear tests may

be used instead of the empirical relationships. The p-multiplier (m_p) approach (e.g., Brandenberg et al., 2007b) may also be used to obtained scaled p-y curves if a BNWF approach is used in the foundation analysis.

3. **Develop Foundation Model**

A numerical model of the soil-foundation system is the primary means of analysis for the effects of liquefaction-induced lateral ground deformation. There are two software options available for use, DFSAP, based on strain wedge theory, and LPILE, based on BNWF analysis using p-y curves.

(a) ***DFSAP Analysis Option:*** The DFSAP program uses strain wedge theory (e.g., Ashour et al., 1998, 2002) for lateral and axial analysis of single and grouped piles or drilled shafts. This software is particularly attractive for drilled shaft foundations for which the length is small relative to the diameter, as such foundations are outside of the scope of most p-y curve-based analysis methods.

The built-in liquefaction option in DFSAP is not used to account for liquefied soils in the analysis. Instead, the soil properties for liquefied soils are modified using a reduced friction angle

$$\phi_{\text{reduced}} = \arctan\left(\frac{S_r}{\sigma'_{vo}}\right) \tag{5.3}$$

where S_r is the estimated residual strength for the liquefied soil and σ'_{vo} is the effective overburden stress at the depth of the liquefied soil layer. The initial stiffness is reduced in a similar, unspecified, manner, and the soil unit weight is not adjusted for liquefied conditions.

Group efficiency effects are handled internally by the DFSAP program. The passive resistance of footings and pile caps below ground can also be accounted for internally by the DFSAP program, though this resistance should be neglected for areas prone to lateral spreading.

(b) ***LPILE Analysis Option:*** The LPILE program analyzes the laterally loaded deep foundation using a BNWF approach in which the soil is represented using p-y curves developed for various soil types (Matlock, 1970; Reese et al., 1974; Reese and Welch, 1975). This software is most applicable to relatively long and slender foundations.

When using LPILE, pile group efficiency effects are accounted for using p-multipliers as recommended in AASHTO (2010b). The effects of liquefaction on the p-y curves representing liquefied soil are considered using one of two approaches: (1) curves are scaled using the p-multiplier (m_p) approach (e.g., Bran-

denberg et al., 2007b), or (2) curves are computed using reduced soil properties based on the residual strength of the liquefied soil as is done when using DFSAP.

4. **Determine Potential for Lateral Soil Movement**

   The potential for liquefaction-induced lateral soil movement is initially assessed using limit equilibrium slope stability analysis. The analysis is decoupled from all seismic inertial forces, the resistance from any foundation elements in the slope is ignored, and liquefied soils are assigned residual strength values. If the limit equilibrium FS ≤ 1.0, it is assumed that a flow-type failure will occur. If FS > 1.0, it is assumed that flow failure is unlikely, and the effects of lateral spreading on the foundation are assessed instead.

5.2.1 Analysis for Flow-Type Failure: FS ≤ 1.0

The deformations associated with liquefaction-induced flow failure are typically too large to be acceptable for bridge foundation design if it is assumed that all of the deformation is transferred to the foundation. Due to the involved design assumptions, stabilization of the slope via structural pinning or ground improvement is typically required for the flow-type failure case. In some situations, the lateral capacities of the foundation and soil are such that the liquefied soil and any overlying crust will flow around the foundation, imparting only minimal deformations to the structure. The potential for this flow-around type of behavior is assessed by evaluating the full passive pressure of the soil acting on the foundation.

The lateral force which must be resisted by a foundation providing structural pinning for slope stabilization is estimated by computing the stabilizing force necessary to achieve a target slope stability FS of approximately 1.1. Seismic inertial forces are neglected unless the primary design earthquake is a long duration subduction zone event, in which case an inertial force is considered as

$$f_{\text{inertia}} = 0.25 a_g m \tag{5.4}$$

where a_g is the peak ground acceleration and m is the unstable soil mass.

The force required to bring FS ≥ 1.1 may exceed the force which the soil can apply to the foundation. To prevent this situation, it is recommended to check the stabilizing force against a limiting force determined from the full passive pressure of the unstable soil acting on the foundation using one of two approximations:

1. The passive pressure may be multiplied by the gross surface area of the foundation (i.e., width $\times$ height) over which it acts.

2. The normal component of the passive pressure acting on incremental segments along the foundation circumference may be multiplied by the individual lengths of the seg-

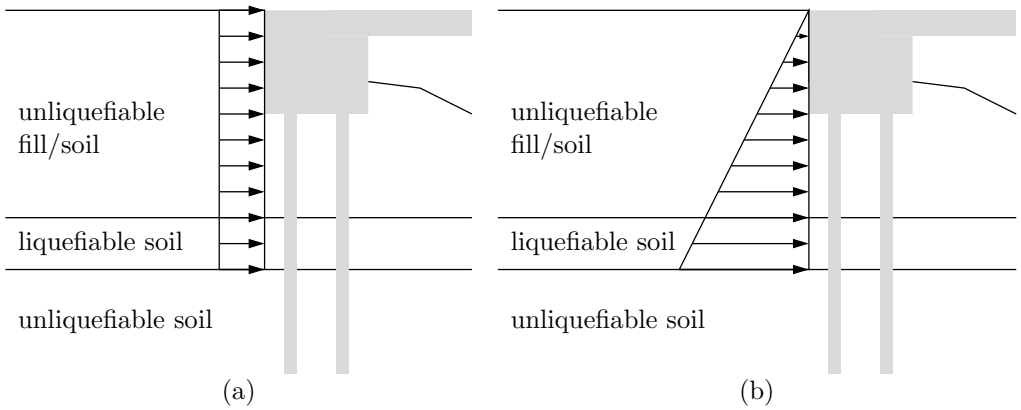

Figure 5.8: Load distributions for shallow liquefied layer in flow-type failure case. (a) Uniform for stabilizing force. (b) Linearly-increasing for passive force.

ments and the interface friction angle. If done in this way, it is recommended that the limiting force be multiplied by a factor of 1.1 to be approximately consistent with how the slope failure force is calculated.

The design load case is determined through a comparison of the estimated stabilizing (from limit equilibrium analysis) and limiting (from passive pressure) forces. The way in which these forces are applied and the manner in which their effects are compared is dependent on certain aspects of the soil profile. If it is determined that the design load case for flow-type failure is not structurally or economically feasible, then stabilizing ground improvement techniques must be explored.

1. For relatively shallow liquefiable layers, the stabilizing force should be applied as a uniform distributed load acting from the bottom of the liquefiable layer to the top of the foundation, as shown in Figure 5.8(a). The passive force should be applied as a linearly-increasing distributed load (passive wedge) acting from the bottom of the liquefiable layer to the top of the foundation, as shown in Figure 5.8(b). The load case which produces the smallest stress in the foundation controls the design.

2. For conditions where the flow failure surface does not extend to the bottom of a deep and/or thick liquefiable layer, multiple failure surfaces for which FS $\leq$ 1.0 are considered. The corresponding stabilizing forces are applied as uniformly distributed loads extending from each failure surface to the top of the foundation. These are compared to the limiting passive force, applied as a wedge distribution from the failure surface to the top of the foundation. An example of each distribution is shown in Figure 5.9 for a single failure surface. For the smaller of the two forces determined at each failure surface, the moment and shear at the estimated point of fixity of the foundation are computed. The lateral load distributions which result in the largest bending moment and shear force demands are used as design load cases.

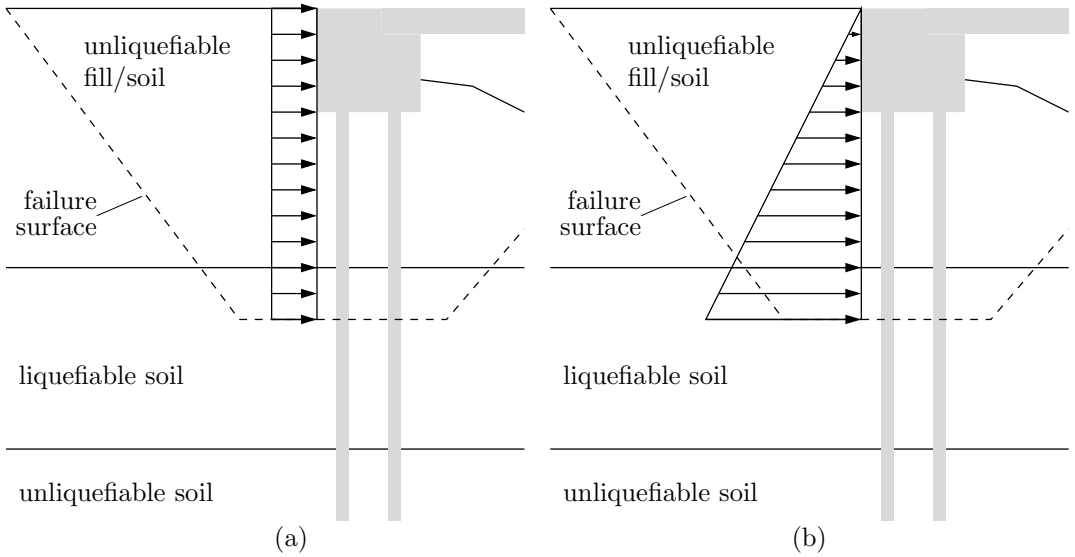

Figure 5.9: Load distributions for flow-type failure case where failure surface does not extend to the bottom of the liquefied layer. (a) Uniform for stabilizing force. (b) Linearly-increasing for passive force.

5.2.2 Lateral Spreading Analysis: FS > 1.0

The effects of lateral spreading on embedded foundations are assessed using a pushover analysis in which an estimated free-field displacement profile is applied to the free end of the soil-foundation interaction curves used in the soil-foundation model.

A lateral spreading deformation analysis is used to estimate potential ground deformation. This is accomplished using an empirically-derived relationship (e.g., Youd et al., 2002; Kramer, 2008), a Newmark sliding block analysis (e.g., Bray and Travasarou, 2007), or dynamic nonlinear effective stress numerical analysis. The estimated lateral deformation is treated as the free-field displacement of the ground surface in subsequent analyses.

The displacement profile used in the pushover analysis represents the free-field distribution of lateral spreading deformation with depth, and is dependent on the estimated free-field surface deformation. Three methods are available for defining a displacement profile:

1. An empirically-based shear strain profile approach (e.g., Zhang et al., 2004; Idriss and Boulanger, 2008).

2. A set of dynamic nonlinear effective stress analyses using several input motions.

3. Assuming a simplified profile which has a constant displacement in a unliquefied crust and a linearly varying displacement across the liquefied layer as shown in Figure 5.4.

The ultimate lateral resistance and stiffness of the soil-foundation interaction curves representing liquefied soil are reduced to account for residual strength using the methods

discussed in step 2. The resistance and stiffness of the unliquefied soil are based on the site soil properties as determined from field exploration and laboratory testing. Group effects are neglected for curves in fully liquefied soil after Rollins et al. (2005). The passive pressure and side friction generated on the pile cap must also be considered in the analysis.

As with the flow failure case, lateral forces are checked against a limiting case corresponding to the passive force of the unstable soil acting on the foundation. If the force applied to the foundation in the pushover analysis exceeds the passive capacity of the soil, it is assumed that the crustal soil will fail during lateral spreading, flowing around or piling-up behind the foundation, and the passive force is used for design. This force is applied as a passive wedge which extends from the ground surface to the lesser of the following depths:

1. The bottom of the liquefied layer.

2. The depth of the failure surface at its intersection with the foundation.

3. The assumed limiting depth for lateral spreading of 50 ft.

For the design load case, the induced loads are checked against the available resistance of the foundation and general bridge system, and the estimated displacements are checked against tolerable values. Mitigation of foundation subsoils may be required if the predicted forces or deformations are large enough to be structurally or economically infeasible.

5.3 Summary

The California Department of Transportation and Washington State Department of Transportation design procedures for bridge foundations subject to liquefaction-induced lateral spreading were presented. Each approach primarily involves the use of simplified analysis methods to determine the design demands for pile and drilled shaft foundations, however, there are differences in how these simplified methods are applied and in how the three-dimensional geometry of the site is incorporated into each procedure.

The Caltrans approach makes an initial distinction between restrained and unrestrained ground displacement based on a qualitative assessment of the geometry of the soil surrounding the foundations. For the restrained ground displacement case, it is assumed that the existence of the foundation will limit the demands that the soil can impose on the bridge structure during lateral spreading. Three-dimensional effects are considered and a compatible force-displacement state is determined and used for the design of the bridge foundations. The unrestrained ground displacement case assumes that the soil displacement will be largely unaffected by the presence of the foundations and the structure is typically designed to withstand the full passive force of the crust.

The WSDOT procedure is similar to the unrestrained ground displacement case from the Caltrans procedure in that the bridge structure is be designed to withstand the soil displacement, and corresponding lateral forces, that would occur in the absence of the embedded foundations. No direct consideration for 3D effects is made in this procedure, leading to potentially overconservative design solutions for cases which would be considered restrained ground displacement under the Caltrans approach.

Chapter 6

IDENTIFICATION AND SELECTION OF REPRESENTATIVE CASE STUDIES FROM CHILE

The geologic and seismic similarity between Chile and western Washington provides a unique opportunity to learn from the performance of bridges subject to liquefaction-induced lateral spreading. Reconnaissance efforts following the M_w8.8 February 27, 2010 offshore Maule earthquake identified multiple bridge sites subject to liquefaction and lateral spreading. These bridges are listed in Table 6.1, with a brief summary of reported performance. At most of the considered sites, there was a tendency for the crustal soil and approach fill to flow around embedded foundations, inducing only minor damage or lateral movement in the abutments and piers. These effects are manifested as settlement and longitudinal cracking in the approaches and a difference in the flow pattern of near-field and far-field soils.

To aid in an assessment of how the three-dimensional deformation of approach embankments and crustal soil may affect the lateral loads imposed on bridge foundations during lateral spreading, and how the imposed demands may differ from those estimated using current simplified design procedures, several Chilean bridge sites are evaluated for use as case studies. A survey of the information for the bridge sites identified in Table 6.1 indicates that the available structural data consists primarily of construction drawings, and the available geotechnical data consists primarily of standard penetration test (SPT) resistance data. This available data is summarized in Table 6.2. In several cases, the GEER (2010a) reconnaissance team performed site-specific investigations, including light detection and ranging (LIDAR) scans, dynamic cone penetration tests (DCPT), and spectral analysis of surface wave (SASW) evaluations.

6.1 Evaluation of Case Study Sites

Potential case study sites are evaluated with consideration for: (1) the sufficiency of the available data for characterizing the site soil profile and bridge foundations, (2) the presence of 3D deformation effects in the crustal soil and/or approach fill, and (3) the similarity of the bridge site to conditions typical in Washington state. The relative merits of each bridge listed in Tables 6.1 and 6.2 are evaluated using these criteria and summarized in the following discussion. The primary case study site for the investigation of the effects of 3D soil deformation on the lateral loads imposed on bridge foundations during liquefaction-induced lateral spreading is selected and several candidates for future study are identified.

Table 6.1: Summary of Chilean bridge sites affected by liquefaction-induced lateral spreading with target behavior at approaches (FHWA, 2011; GEER, 2010a).

Site Name	Reported Performance
Puente Mataquito (built 2006)	< 0.02 m lateral movement with minor crushing at NE abutment, 0.7–1.0 m settlement of approach fill at NE abutment, movement of approach fill perpendicular to bridge axis at NE abutment, no movement at SW abutment
Puente Llacolén (built 2000)	no lateral movement or significant damage at SW abutment, 0.25–0.3 m lateral movement of support pier at NE approach, approach span became unseated
Puente Juan Pablo II (built 1973)	significant displacement/rotation and shear failure of NE approach bent, vertical settlement of piers along length of bridge, minor damage to SW approach
Puente Raqui I (built 1992)	no lateral movement or significant damage at SE abutment, movement of approach fill perpendicular to bridge axis at SE abutment, twisting and 0.075–0.1 m lateral movement at NW abutment, 1 m settlement of approach fill at each abutment
Puente Raqui II (built 1992)	no lateral movement with minor damage at abutments, approach fill settlement < 1.5 m, movement of approach fills perpendicular to bridge axis, interior piers tilted laterally with span collapse
Puente Tubul (built 1992)	0.15 m lateral movement at N abutment with interior pier collapse, > 0.1 m lateral movement at S abutment with interior span collapse, 1.0–1.5 m settlement of approach fill at each abutment
Puente La Mochita (built 2004)	no lateral movement or significant damage at either abutment, 0.3–0.8 m settlement of approach fill at each abutment, movement of approach fills perpendicular to bridge axis

6.1.1 Puente Mataquito

Among the considered Chilean bridge sites, the Mataquito River Bridge (Puente Mataquito) is the most attractive site for use as a case study of three-dimensional lateral spreading effects. Clear evidence of liquefaction-induced lateral spreading was observed at this site, including the type of three-dimensional approach embankment deformation which is of interest in this research, Figures 6.1 and 6.2, and the available structural and geotechnical data is sufficient to create numerical models that are representative of site conditions. Puente Mataquito is a recently constructed bridge founded on grouped drilled shafts, a commonly-used foundation type in Washington state bridges, and the abutments reported performed well during the lateral spreading event.

6.1.2 Puente Llacolén

The northeast approach to Puente Llacolén was significantly affected by lateral spreading, however, the layout of this approach is not representative of the typical conditions where three-dimensional ground deformation effects have been observed during liquefaction-induced ground failure. As shown in Figure 6.3, the portion of the bridge affected by the lateral ground deformation involves a series of elevated approach spans supported by piers. The abutment and any associated approach fill are located well away from the river and the zone of ground failure. The available geotechnical data for the northeast approach site

Table 6.2: Summary of available structural, geotechnical, and miscellaneous data for considered Chilean bridge sites.

Site Name	Available Data
Puente Mataquito	original construction drawings, boring logs from original construction, geotechnical, hydraulic, and structural reports, SASW data
Puente Llacolén	original construction drawings, post-earthquake repair construction drawings, boring logs from post-earthquake repairs, LIDAR, DCPT, and SASW data near NE approach
Puente Juan Pablo II	post-earthquake repair construction drawings, boring logs from post-earthquake repairs, post-earthquake surveying data, LIDAR, DCPT, and SASW data near NE approach
Puente Raqui I	original construction drawings, no geotechnical data
Puente Raqui II	original construction drawings, post-earthquake repair construction drawings, boring logs from post-earthquake repair work
Puente Tubul	original construction drawings, geotechnical report from post-earthquake repairs,
Puente La Mochita	original construction drawings, boring logs from original construction, post-earthquake repair construction drawings, LIDAR scans

Figure 6.1: Lateral spreading on northern river bank at Puente Mataquito as seen from ground surface (GEER, 2010a).

Figure 6.2: Longitudinal crack in northern approach to Puente Mataquito (GEER, 2010a).

is limited, but is likely sufficient to characterize the soil conditions in a simplified manner. This site may be useful as a representative case where three-dimensional effects are not applicable. The southwest approach to Puente Llacolén is more representative of the idealized conditions for this study, with a small approach fill and an abutment which performed well during lateral spreading of the surrounding ground, however, there is no available geotechnical information for this side of the bridge and only limited observational data.

6.1.3 Puente Juan Pablo II

As with Puente Llacolén, the layout of Puente Juan Pablo II is such that three-dimensional ground deformation effects do not appear to have been an important factor during the liquefaction-induced lateral spreading which occurred near the northeast approach. In this area, the bridge approach consists primarily of elevated approach spans supported by piers. There is sufficient information for a geotechnical and structural characterization of the site, so Puente Juan Pablo II may be informative as a case study representing conditions where three-dimensional effects do not apply.

6.1.4 Puente Raqui I

Observations at Puente Raqui I suggest that liquefaction-induced lateral spreading occurred, triggering the target 3D deformation pattern in the approach fill at both ends of the bridge, however, there is no available geotechnical data with which to characterize the soil profile at this site. In addition, the available structural information is limited, and suggests that grouped timber piles were used as foundations for the abutments and piers. This combination of limited structural information and non-existent geotechnical data indicates that

Figure 6.3: Portion of northeast approach to Puente Llacolén affected by liquefaction-induced ground deformation (FHWA, 2011).

Puente Raqui I is not a strong candidate for further study.

6.1.5 Puente Raqui II

During lateral spreading at both ends of Puente Raqui II, the approach fill settled and deformed perpendicularly to the bridge axis, inducing little or no lateral movement in the abutments, though the lateral movement of some interior piers caused the collapse of the bridge spans. Due to post-earthquake reconstruction efforts, there is ample geotechnical data available for the bridge site, however, structural information for the original bridge is limited. As with Raqui I, it appears that the abutments and piers for Puente Raqui II were supported on grouped timber piles of unknown number and configuration. Since timber piles are not often used in new bridges, Puente Raqui II is not a preferred case, however, this bridge may be useful as a case study site if no other sites prove to be more promising.

6.1.6 Puente Tubul

The performance of Puente Tubul during the earthquake and subsequent liquefaction-induced phenomena was somewhat worse than that observed for Puente Raqui II, though the overall behavior was similar between the two sites. There is a wealth of available geotechnical data for Puente Tubul, but there is only limited available structural data, though it is likely sufficient for a simplified characterization of the site. As with Puente Raqui II, it appears that the original bridge at this site was supported on grouped timber piles, therefore, this bridge is not a strong candidate for future study.

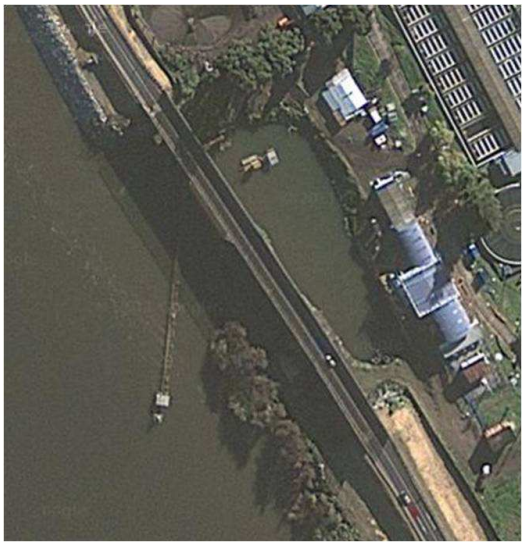

Figure 6.4: Aerial view of Puente La Mochita and surrounding site.

6.1.7 Puente La Mochita

The Puente La Mochita site meets the specified criteria for selection as a case study, but there are some problematic aspects to this site which reduce its viability for this purpose. As shown in Figure 6.4, the bridge runs parallel to Rio Bío-Bío, spanning a small inlet on the eastern bank. This geometry, combined with the deformation observations made by the FHWA (2011) and GEER (2010a) reconnaissance teams, suggest that the ground deformation mechanism at this site is outside of the scope of the research. Due to this uncertainty in the driving mechanism, Puente La Mochita is not strong selection for use as a case study.

6.2 Overview of Selected Case Study Site: Puente Mataquito

Based on the evaluation of the case studies discussed above, Puente Mataquito is chosen as a first candidate for further analysis. Puente Mataquito is a 320 m long two-lane highway bridge over the Mataquito river on the coastal route between Iloca and Quivolgo in the Maule region of Chile. Figure 6.5 provides a view of the bridge from the southern river bank near the approach embankment. Puente Mataquito is located near the city of Constitución, as shown in Figure 6.6, about 100 km NNW of the 2010 Maule earthquake epicenter at the approximate coordinates: 35.052°W, 72.163°S. The bridge is supported by precast prestressed concrete I-girders over eight 40 m long interior spans. There are two seat-type reinforced concrete abutments with wingwalls, founded on 4×2 groups of 1.5 m diameter reinforced concrete drilled shafts. The seven interior piers consist of 3×1 groups of the same 1.5 m diameter shafts, capped at the connection to the bridge girders in the manner visible in Figures 6.5 and 6.7.

Figure 6.5: Puente Mataquito looking northeast from the southwest approach. Photo retrieved January 14 2013, `www.panoramio.com/photo/8172577`.

Figure 6.6: Location of Puente Mataquito relative to Maule earthquake epicenter and several Chilean cities. Map retrieved January 15 2013, `maps.google.com`.

Extensive liquefaction and lateral spreading occurred on both river banks at the Puente Mataquito site due to the Maule earthquake. On the northern bank, the observed surface manifestation of lateral spreading extended approximately 270 m from the river's edge, involving a large portion of the surrounding fields. The estimated lateral spreading deformation on the ground surface was about 1.8 m over the approximately 65 m distance from the NE abutment wall to the river's edge (see Figure 6.1). The NE approach embankment settled about 0.7–1.0 m relative to the bridge deck and expanded about 0.6 m away from the road centerline. Reconnaissance teams noted the presence of lateral spreading at the southwest approach, however, there is little available discussion beyond a brief statement that

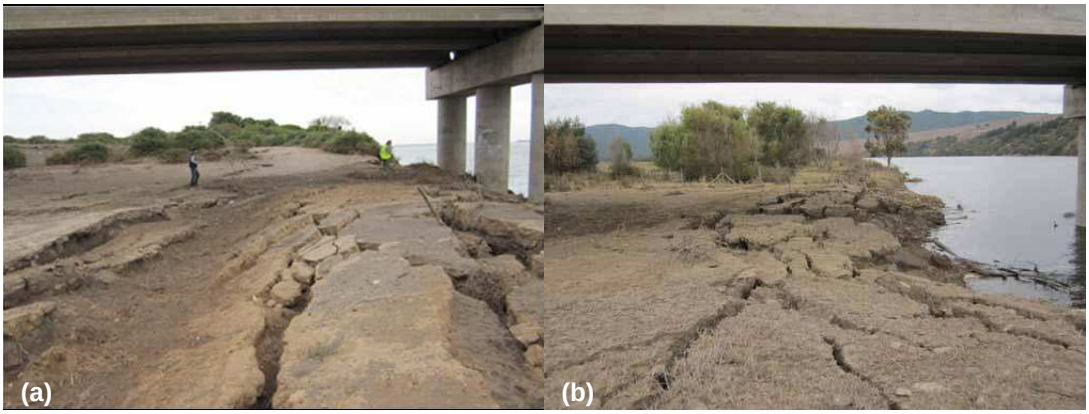

Figure 6.7: Surface manifestation of lateral spreading at Puente Mataquito. (a) Southwest approach (GEER, 2010a). (b) Northeast approach (MAE, 2010).

the scope of the spreading appeared to be constrained due to topographic effects (FHWA, 2011; GEER, 2010a; MAE, 2010). Figure 6.7 provides close-up images of the surface manifestation of the lateral spreading at each approach. No ground motion information was recorded for this site, however, the quantity and quality of the available information offsets this omission from the data set. Due to this lack of information on the specific ground motion experienced at the site, an alternative ground motion record is used during dynamic simulations (see Section 8.1.5 for more information).

Though liquefiable soils were identified in the geotechnical report (Petrus, 2006), there is no evidence that lateral spreading was explicitly considered during the design process. The design scour conditions at the site are particularly extreme, and it appears that scour was the controlling lateral load case for the foundations. Regardless of the particular load case that drove the design, and despite the evidence of liquefaction and lateral spreading near each approach, the overall performance of the bridge was favorable. Bridge operation was not affected beyond the easily repairable settlement and roadway cracking in the northeast approach embankment (FHWA, 2011; GEER, 2010a).

Only minor structural damage was reported, with some typical instances shown in Figure 6.8, however, based on photographs of the bridge, it seems that the movement of the abutment was underreported. Per Figure 6.9, which is taken from the construction drawings for Puente Mataquito, a 20 cm expansion gap is included at the connection of the bridge deck with the abutments. This gap is visible in Figure 6.5, which was taken prior to the Maule earthquake. As shown in Figure 6.8(a), the expansion gap has closed, placing the abutment and deck in direct contact. This observation suggests that the abutment potentially moved ≥ 20 cm towards the river, rather than the reported value of ≤ 2 cm.

Figure 6.8: Minor structural damage caused by lateral spreading (GEER, 2010a). (a) Crushing of NE abutment. (b) Shearing of bridge girder above interior piers.

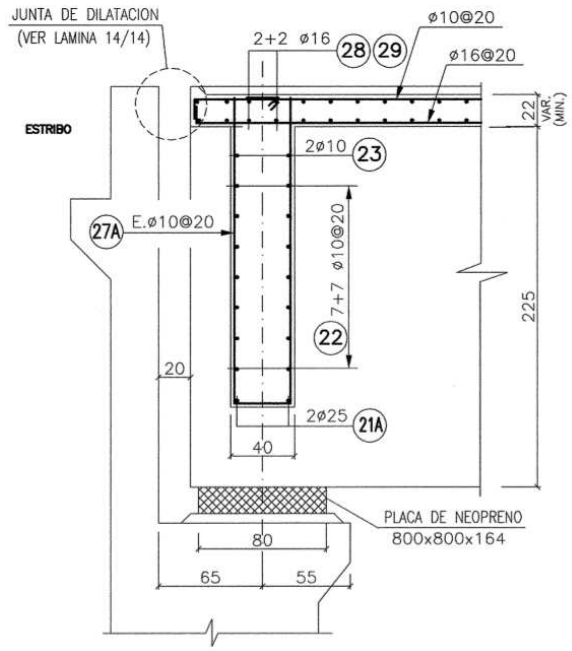

Figure 6.9: Construction detail for abutment to deck connection (courtesy Ministerio de Obras Públicas, Chile).

6.3 Summary

To gain a better understanding of the ways in which three-dimensional soil deformation affects the lateral loads imposed on piled bridge foundations during lateral spreading, a case study bridge site was selected for further analysis. The recent M_w8.8 Maule earthquake off the coast of Chile caused multiple observed cases of lateral spreading at bridge approaches, many of which displayed the target 3D behavior. After a review of the site observations and data available for a series of bridge sites, Puente Mataquito was selected as the primary case study for this research. The bridge sites that are most promising for future studies of this nature are also identified.

Chapter 7

GENERAL MODEL DEVELOPMENT: PUENTE MATAQUITO

Site observations following the M_w8.8 February 27, 2010 offshore Maule earthquake identified widespread lateral spreading at the site of Puente Mataquito, however, the structural damage to the bridge was insignificant in comparison. Numerical models are developed to identify the mechanisms for the reduction in lateral foundation loads implied by the minimal structural damage at this site. These models include beam on nonlinear Winkler foundation (BNWF) models used to test and compare simplified analysis procedures, dynamic effective stress models of the bridge-foundation-soil system in plane strain used to analyze the liquefaction susceptibility and response of the bridge system, and 3D models of the southern bridge abutment, approach embankment, and surrounding soil used to analyze the local effects of lateral spreading on the abutment and foundations and to identify three-dimensional mechanisms that may lead to reductions in estimated lateral loads. Since these models all represent the same structure and site, there are certain shared aspects that appear in all of the models. The development of these general model features is discussed in the following sections. Specific development details for the different modeling approaches are discussed in subsequent chapters dedicated to each aspect of the modeling effort.

7.1 Development of Idealized Soil Profile

The soil profile used for numerical models of the Puente Mataquito site is based on the subsurface explorations (sondajes) made at the site and the soil characterization profile reported by (Petrus, 2006). Initially, only three subsurface explorations were made (Sondajes 1-3), with one near each abutment and one near the center of the bridge. At a later date, three deeper explorations (Sondajes 1a-3a) were made adjacent to each of the originals. Figure 7.1 shows the locations of the six subsurface explorations relative to the bridge abutments and piers. The corresponding SPT resistance profiles are shown in Figure 7.2.

Boring logs for the subsurface explorations reveal a predominantly cohesionless soil profile. Small clay lenses or veins are present, the lower blow counts at depth for Sondajes 2a being one example. For the purposes of the numerical work, minor variations in the soil profile are ignored and all materials are assumed to be cohesionless. The groundwater table is assumed to be at a constant elevation of -0.251 m based on average findings during the site characterization, and all of the soil below the groundwater table is assumed to be saturated.

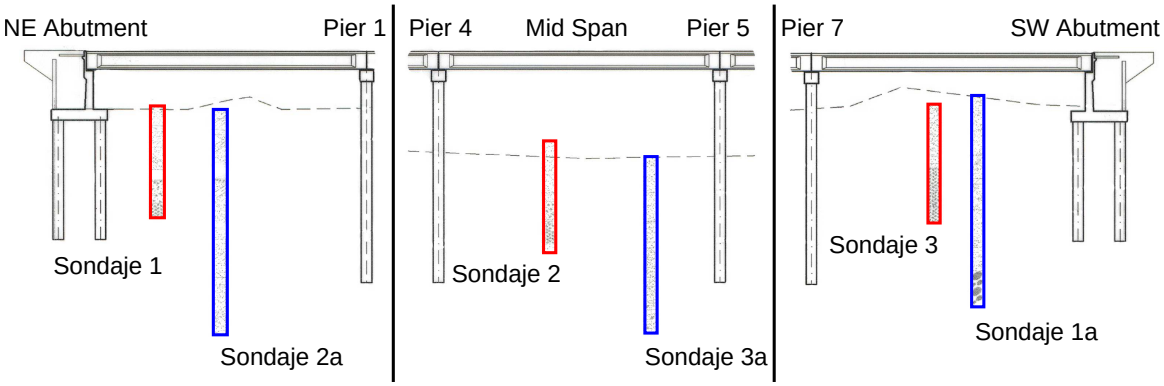

Figure 7.1: Locations of subsurface explorations relative to Puente Mataquito foundations (after Ministerio de Obras Públicas, Chile).

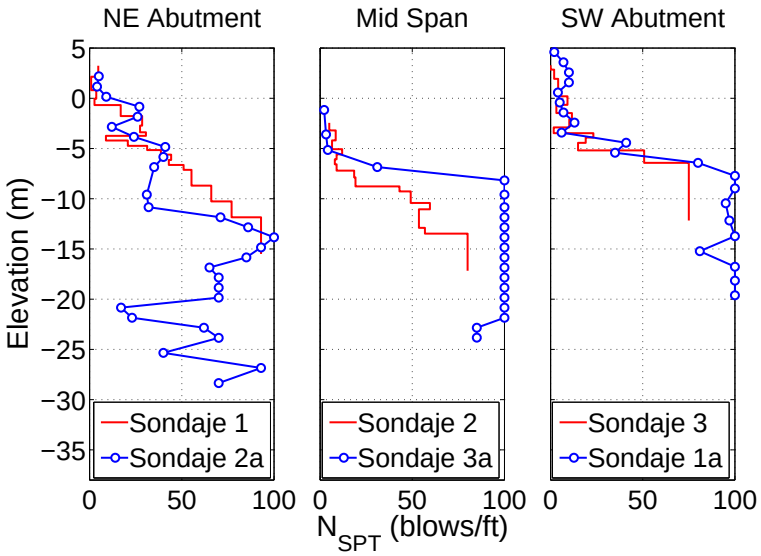

Figure 7.2: SPT resistance profiles for subsurface explorations at Puente Mataquito after Petrus (2006).

The geotechnical report for the project (Petrus, 2006) roughly divides the site into three layers, an upper loose sand layer, a middle layer of denser sand, and an underlying dense gravel layer. The spatial layout of the assumed soil profile is shown in Figure 7.3 with relevant model properties summarized in Table 7.1. For each layer, a weighted average SPT resistance value is computed from the data presented in Figure 7.2. Representative friction angles, ϕ, for each layer are estimated from these average SPT values using a combination of the correlations proposed by Meyerhof (1956) and Peck et al. (1974). Small strain shear and bulk moduli, $G_{\max}$ and $K_{\max}$, are estimated by correlating the assumed friction angle values to relative densities using the relation proposed in FHWA (1978). Void ratios, e, and phase transformation angles, ϕ_{pt}, are assumed based on the estimated relative densities.

Table 7.1: Model properties for soil layers in idealized soil profile.

Soil Type	ρ (Mg/m^3)	ρ_{sat} (Mg/m^3)	ϕ (°)	G_{max} (MPa)	K_{max} (MPa)	e	ϕ_{pt} (°)
loose sand	1.7	2.16	31	60	175	0.85	29
dense sand	1.7	2.11	36	90	230	0.77	27
gravel	1.7	2.08	42	130	250	0.55	32
fill	1.8	–	42	130	250	0.55	32

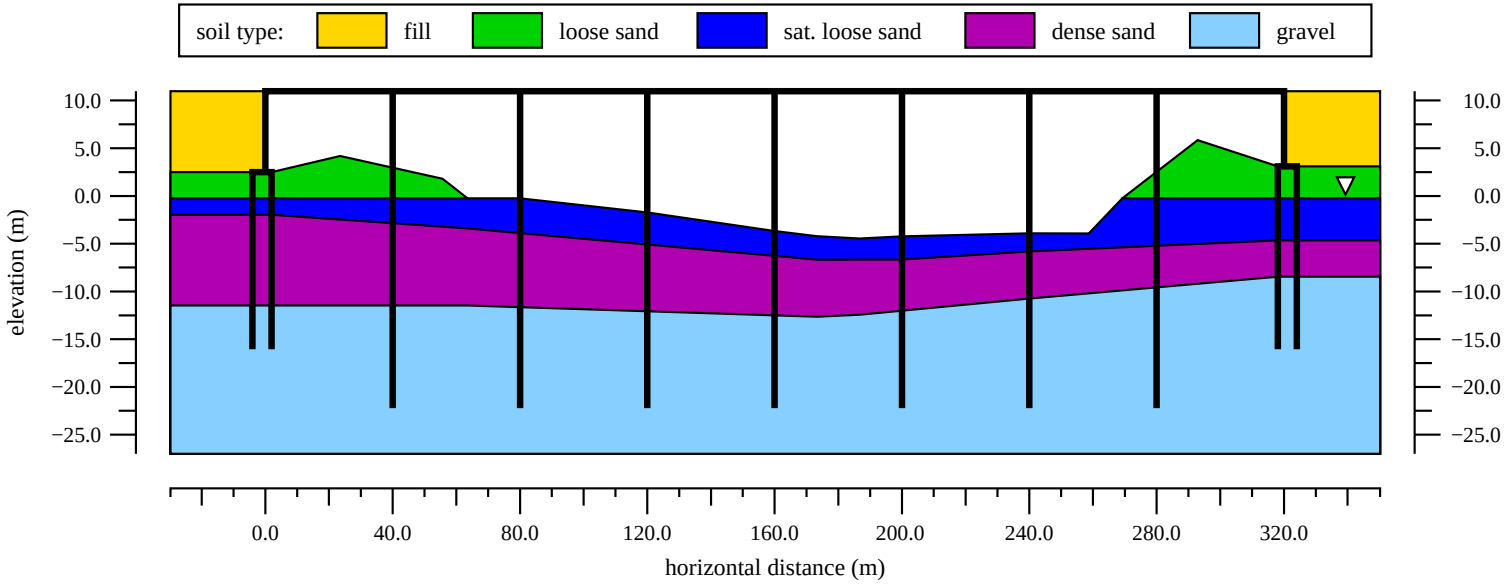

Figure 7.3: Elevation view of bridge and idealized soil profile (vertical scale increased). Horizontal datum is at the northeast bridge abutment.

The properties of the embankment fill are unspecified in the available documentation. The fill is assigned the properties of the gravel layer with a slightly larger mass density to reflect a compacted state. Specific information on the geometry of the approach embankments is similarly unavailable, therefore, a 3H:2V side slope is assumed based on the Chilean Ministry of Public Works (MOP, 2002) recommendations for typical bridge approach embankments. The northeast and southwest approach embankments are assumed to have identical geometries.

7.1.1 Assessment of Liquefaction Potential

The liquefaction susceptibility of the soil at the Puente Mataquito site is assessed using the sand liquefaction triggering relationship of Youd et al. (2001). Assuming a peak ground acceleration (PGA) of 0.4 g based on the recorded PGA in downtown Concepción (Boroschek et al., 2010), a fines content in the range of 5% to 15%, an average reduction coefficient of 0.9, a magnitude scaling factor of 0.75, and a total-to-effective vertical stress ratio of 2, Ledezma (2012) estimated that sands with a normalized SPT value below 28 blows/ft are likely to liquefy in an event similar to the Maule earthquake.

For the SPT blowcount and idealized soil profiles shown in Figures 7.2 and 7.3, this blow count limit indicates that the loose sand layer is highly susceptible to liquefaction and the boundaries of this layer represent the likely scope of liquefaction at the site. The underlying dense sand and gravel layers are much less likely to liquefy for the considered event. Unless otherwise noted, it is assumed in all analyses that liquefaction is confined to the saturated portion of the loose sand layer.

7.1.2 Constitutive Modeling of Site Soils

The constitutive models of Elgamal et al. (2003) are used to simulate the response of each soil material in the 2D and 3D continuum models. These constitutive models use a nested yield surface approach and are available in pressure independent (J2 type) and pressure dependent (Drucker-Prager type) yield surfaces in OpenSees. The pressure dependent version of this constitutive model is capable of capturing contraction, dilation, and cyclic mobility for cohesionless soils. Figures 7.4, 7.5, and 7.6 demonstrate the constitutive response of the material models used for each soil layer, showing the relationships between the norm of the deviatoric stress, $\|\mathbf{s}\|$, mean stress, $p = \operatorname{tr}\boldsymbol{\sigma}$, volumetric strain, $\operatorname{tr}\boldsymbol{\varepsilon}$, norm of the deviatoric strain, $\|\mathbf{e}\|$, and excess pore pressure, u_e. These figures are developed using single element models of a conventional triaxial compression (CTC) test and a direct simple shear (DSS) test. The CTC test simulates drained conditions and is performed in a monotonic configuration only. The DSS test is simulated under undrained conditions and is performed in monotonic and cyclic configurations.

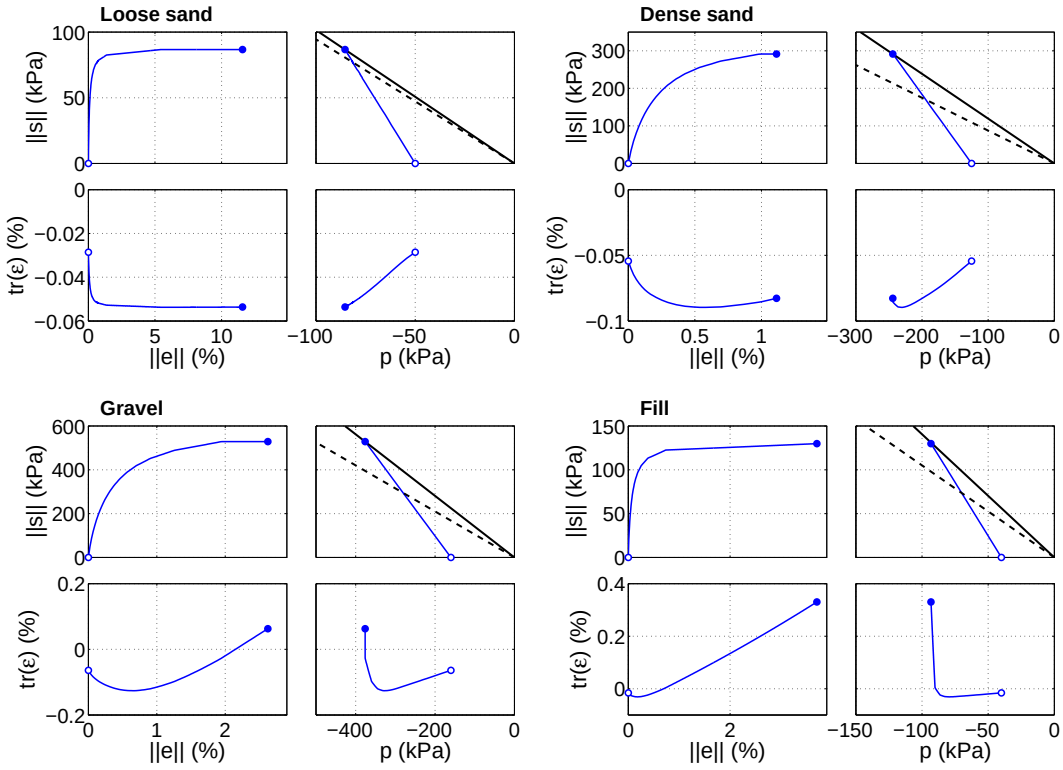

Figure 7.4: Constitutive response of model soils in simulated monotonic drained CTC test.

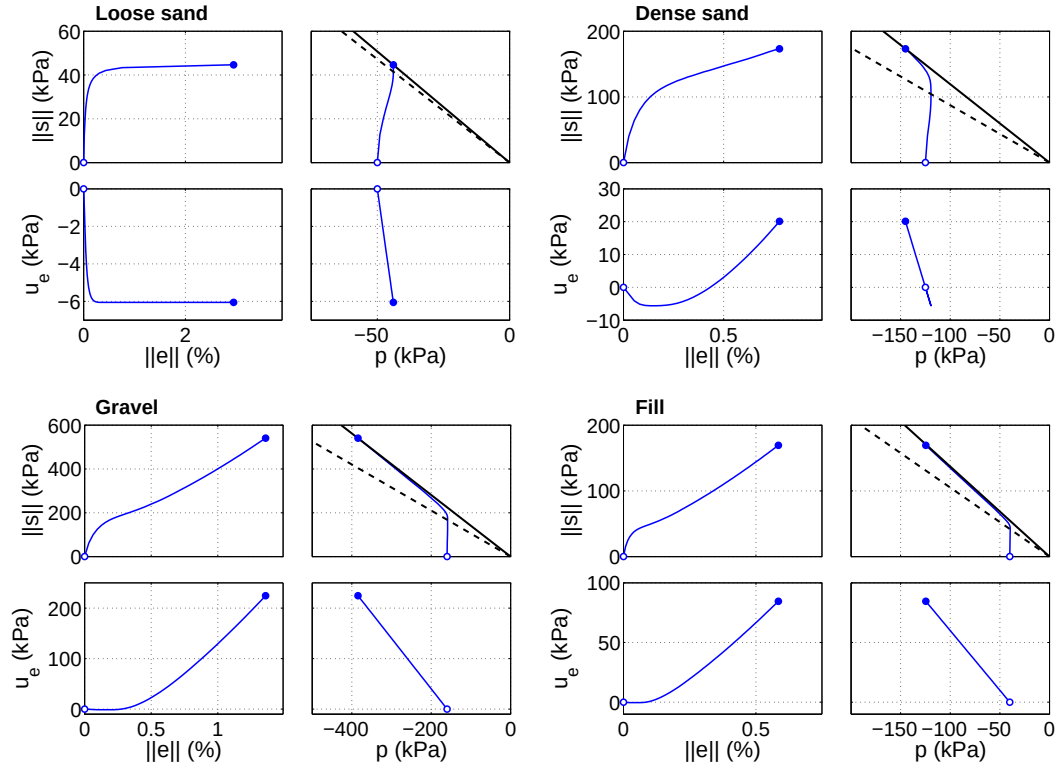

Figure 7.5: Constitutive response of model soils in simulated monotonic undrained DSS test.

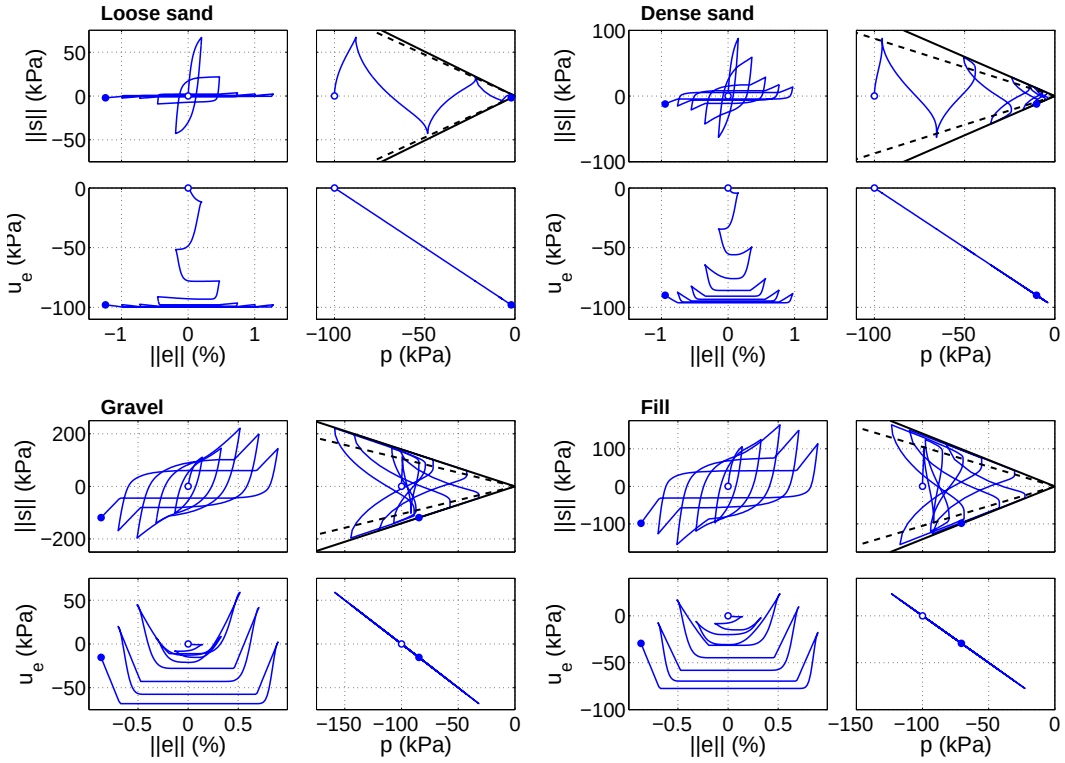

Figure 7.6: Constitutive response of model soils in simulated cyclic undrained DSS test.

Table 7.2: Contraction and dilation input parameters used in constitutive model for each soil type.

Soil Type	c_1	c_2	c_3	d_1	d_2	d_3
loose sand	0.087	5.0	0.18	0.0	0.0	3.0
dense sand	0.067	5.0	0.23	0.06	0.27	3.0
gravel	0.013	5.0	0.0	0.3	0.0	3.0
fill	0.013	5.0	0.0	0.3	0.0	3.0

The amount of contraction and dilation demonstrated in Figures 7.4, 7.5, and 7.6 are controlled by a series of input parameters that are related to the relative density of the model soils. The input parameters used for each soil type are summarized in Table 7.2. As would be expected, looser materials have larger contraction parameters and smaller dilation parameters, and these values get smaller and larger, respectively, with increasing relative density. The input parameters for the model soils beyond those referenced in Tables 7.1 and 7.2 are left as the default initialization values in all analyses.

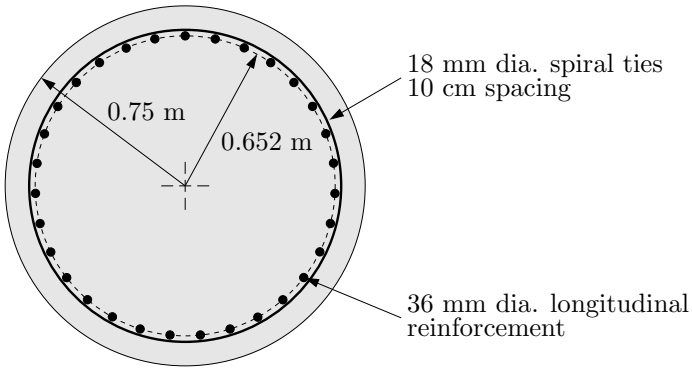

Figure 7.7: Dimensions and details of the model drilled shaft cross-section.

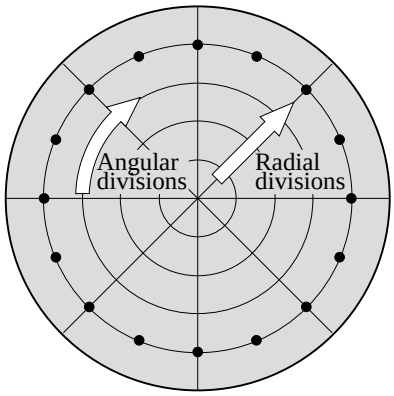

Figure 7.8: Typical discretization scheme for circular fiber section model.

7.2 Foundation Modeling Approach

The abutments and pier foundations for Puente Mataquito are 1.5 m diameter reinforced concrete shafts. For modeling purposes, an idealized template cross-section, Figure 7.7, is assumed based on the typical reinforcement configuration used in the shaft foundations. There are 31 longitudinal bars, all 36 mm in diameter, and the central core of the shaft is confined with 18 mm diameter spiral ties spaced 10 cm apart.

A fiber section approach is used to incorporate the cross-sectional behavior of the foundations into the finite element models. The fiber section model is discretized into subregions, Figure 7.8, which are assigned uniaxial constitutive behavior corresponding to the type of material they represent. The uniaxial constitutive models used for the concrete and steel portions of the fiber section model are shown in Figure 7.9, with the corresponding model input parameters listed in Table 7.3.

The uniaxial constitutive model assumed for the reinforcing steel, Figure 7.9(b), is a bilinear plasticity model. The parameters defining the constitutive response of this model

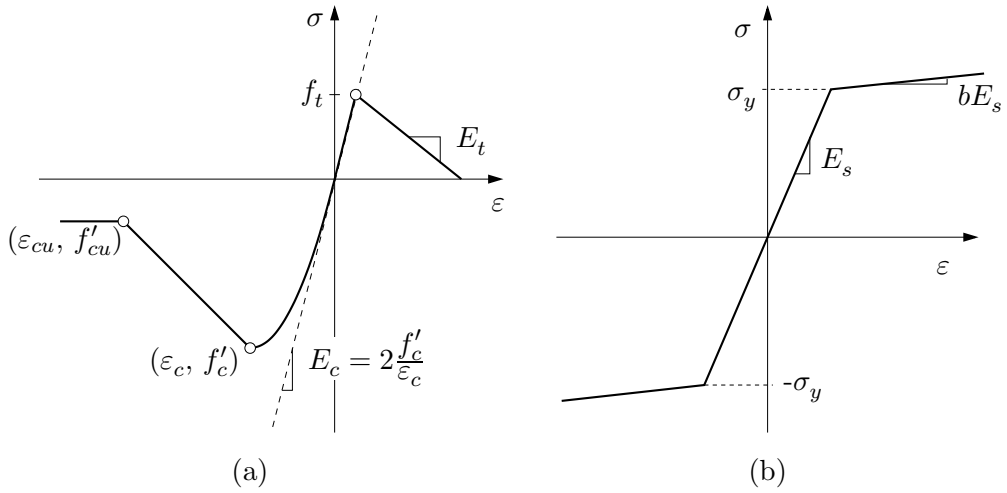

Figure 7.9: Uniaxial constitutive relations used in fiber section model for drilled shaft. (a) Concrete model. (b) Steel model. Refer to Table 7.3 for values used in the models.

Table 7.3: Concrete and steel material properties in drilled shaft fiber section model. Refer to Figure 7.9 for definitions of terms.

Concrete Properties						Steel Properties		
f'_c (kPa)	ε_c	f'_{cu} (kPa)	ε_{cu}	f_t (kPa)	E_t (MPa)	σ_y (MPa)	E_s (GPa)	b
24525	0.003	4905	0.0368	3070	-2039	412	200	0.001

are the steel yield stress, σ_y, elastic modulus, E_s, and strain hardening ratio, b. The design steel yield stress (Ingeniería Cuatro Ltda., 2006) is used in the model, and the elastic modulus and strain hardening ratio are assumed based on typical steel behavior.

The concrete constitutive model, Figure 7.9(a), has compressive behavior based on the work of Kent and Park (1971). The maximum compressive strength, f'_c, used in the model is the design compressive strength of the concrete used at Puente Mataquito (Ingeniería Cuatro Ltda., 2006). A strain at peak compressive stress, $\varepsilon_c = 0.003$, is assumed per ACI (2011) recommendations. The post-crushing behavior is defined after Park and Paulay (1975), where ε_{cu}, the strain at which the concrete is considered completely crushed, is based on the geometry of the core and amount of spiral confinement, and the residual compressive strength $f'_{cu} = 0.2f'_c$.

The tensile behavior for the concrete constitutive model is simplified, with a limited linear elastic capacity followed by linear softening. The tensile strength of the model, f_t, is defined based on the ACI (2011) recommended modulus of rupture for concrete in bending

$$f_r = 0.62\sqrt{f'_c} \tag{7.1}$$

where f_r and f'_c are in units of MPa. The tension softening stiffness, E_t, is determined from

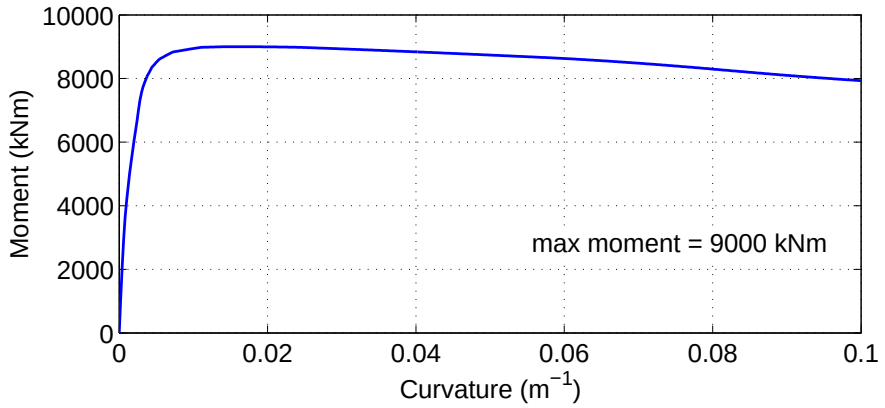

Figure 7.10: Model moment-curvature response for single drilled shaft foundation at design axial force.

the fracture energy of the concrete using the technique discussed by McGann et al. (2012).

A moment-curvature analysis is conducted to verify proper implementation of the fiber section model and establish the capacity of the model shaft foundation. Figure 7.10 shows the moment-curvature response of a single model shaft foundation. The maximum bending moment of 9000 kN·m compares favorably with the nominal design moment capacity for the shaft foundations used in the construction of Puente Mataquito. In some of the models used in this research, the shafts are modeled using linear elastic section behavior. This linear elastic response is defined using the initial tangent to the nonlinear moment-curvature response presented in Figure 7.10.

At the abutments, the shafts are grouped in a 4×2 layout with the dimensions and orientation shown in Figure 7.11. The short dimension of the pile cap corresponds to the longitudinal axis of the bridge. The shafts at the abutments are 17 m long, and extend from the pile cap down into the gravel soil layer, ending at a vertical elevation of -16.06 m (see Figure 7.3). The shafts are grouped in a 3×1 configuration at the seven interior piers with the layout and dimensions shown in Figure 7.12. The interior pier shafts are 28.6 m long and extend from a concrete cap just below the bridge girders into the gravel layer, ending at an elevation of -22.22 m.

The different types of numerical models used in this research vary in their treatment of the foundations. For the BNWF models, the grouped shafts at the bridge abutments are consolidated into a single equivalent shaft model following the procedure recommended by Caltrans (2011) and discussed in Section 5.1. The plane strain models consider a grouped pair of equivalent shaft models at the abutment which have the bending stiffness of a row of four shafts, and single equivalent shaft models at the interior piers with the stiffness of a row of three shafts. The 3D models consider the full geometry of the shaft group at the southern abutment, using beam-to-solid contact elements to model the soil-shaft interaction. Each

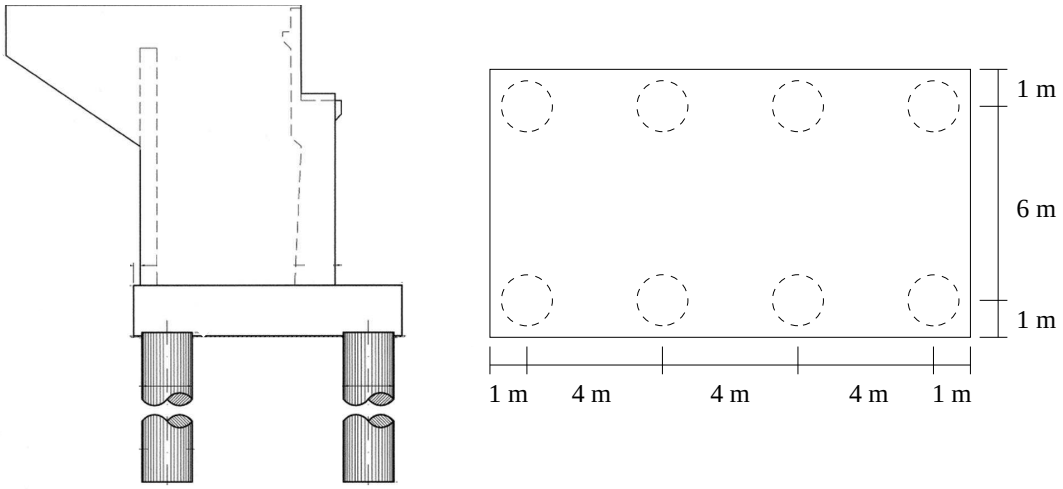

Figure 7.11: Elevation and plan views of typical abutment for Puente Mataquito (courtesy Ministerio de Obras Públicas, Chile).

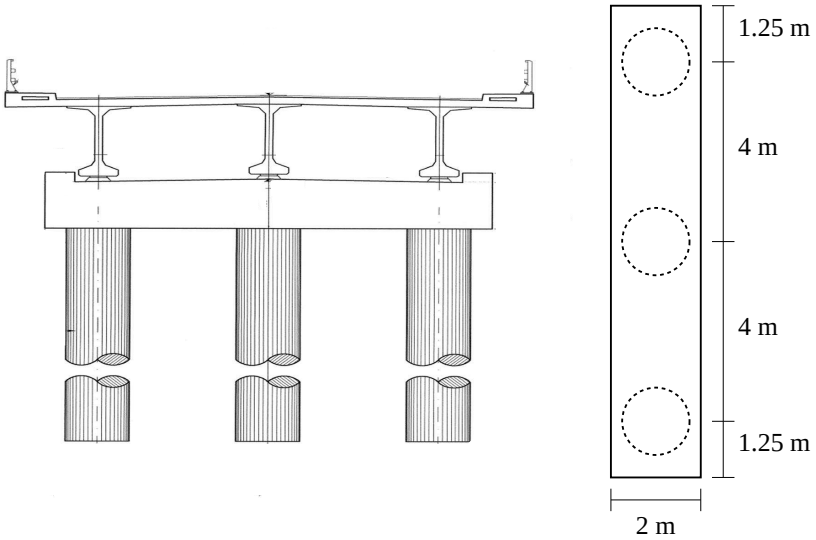

Figure 7.12: Elevation and plan views of typical interior pier shaft cap for Puente Mataquito (courtesy Ministerio de Obras Públicas, Chile).

of these specialized techniques are discussed further in the following sections.

7.3 Summary

To support the numerical modeling effort for the Puente Mataquito case study, an idealized soil profile is defined and a template section model of an individual shaft foundation is created. The idealized soil profile is used to inform the definition of the soil portion of the necessary models, and the template section model is the basis for all of the foundations

considered in this work.

Chapter 8

DYNAMIC PLANE STRAIN MODELS: PUENTE MATAQUITO

A dynamic effective stress plane strain finite element model of the Puente Mataquito site is created to analyze the dynamic response of the bridge and underlying soils using two ground motion records. This model uses the idealized soil profile and shaft foundation models introduced in Chapter 7, and makes use of the efficient element formulations discussed in Chapter 4. This model is developed to gain a better understanding of the response of the bridge site to seismic excitation and to inform further modeling efforts.

Initially, two small parameter studies are performed to establish an appropriate soil domain thickness for use in subsequent models, and to assess the effects of variations in the assumed liquefiable layer configuration on the response of the site. This is done to verify that the assumptions made during development of the idealized site soil profile are reasonable. After the completion of this initial assessment and model verification, further analysis is performed using the Convento Viejo ground motion record from the 2010 Maule event. This final dynamic study provides insight into the response of the bridge and surrounding soils during seismic excitation, allowing for comparison with physical observations made following the earthquake, and for assessment of the structural demands resulting from any liquefaction and subsequent lateral spreading simulated by the model.

8.1 Plane Strain Model Development

The plane strain finite element model uses the **u**-p formulation of the Q1-P1ssp element to represent the soil continuum, displacement-based beam elements to model the bridge foundations and superstructure, and uniaxial nonlinear force-displacement curves (p-y, t-z, Q-z springs) to consider soil-structure interaction effects. The commercial software GiD (CIMNE, 2008) is used as a pre- and post-processor for OpenSees to facilitate mesh creation and result visualization.

Figure 8.1 shows the finite element mesh for the plane strain model. Since the width of the model is far larger than the height, the central portion of the mesh is shown with increased resolution below a depiction of the full mesh. The colors in the soil domain represent separate layers within the soil profile. The boundaries and soil properties of these layers correspond with the idealized soil profile discussed in Section 7.1. Overall, the mesh is 795 m wide, with 237.5 m of soil on either side of the bridge. The gravel layer is extended 4.78 m below the lower extremity of the interior pier shafts, ending at a vertical elevation of

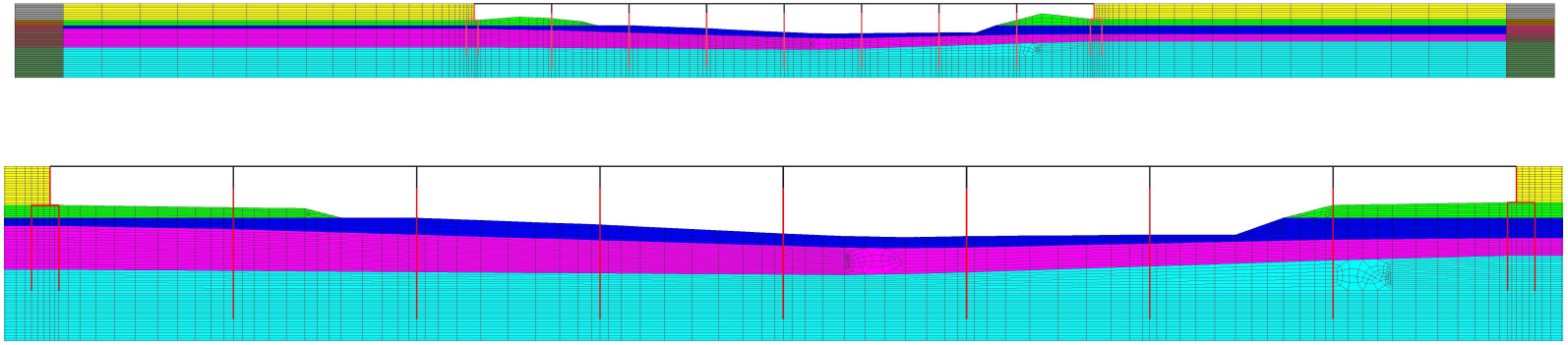

Figure 8.1: Finite element mesh for plane strain analysis of Puente Mataquito site.

-27 m. Two levels of mesh refinement are considered for the plane strain model. The more refined version has 8031 solid elements and the less refined mesh has 3990 solid elements. Each mesh includes 360 beam elements and 252 soil-structure interaction elements. The less refined version of the mesh is used primarily for testing and comparative studies for which this level of refinement is adequate, while the refined mesh is used for more detailed analysis of the site.

8.1.1 Boundary and Loading Conditions

The mesh shown in Figure 8.1 represents only a portion of a large soil domain that extends far beyond practical limitations for the model. The boundary and loading conditions are implemented to reduce the error associated with this limited model domain as much as possible. In the vertical direction, the primary goal is to achieve an initial state of stress representative of the conditions at the site. In the horizontal direction, the emphasis is on applying the ground motions to the model in a way that is the most consistent with site conditions and in ensuring that free-field conditions exist at the extents of the model.

To achieve an appropriate initial state of stress in the model, the nodes along the base of the soil mesh are fixed against vertical translation, and elemental body forces are used to simulate the effect of gravity on the soil. For the beam elements representing the shaft foundations, *t-z* and *Q-z* springs provide vertical restraint through simulated skin friction and end bearing, respectively. A distributed loading equivalent to the self-weight of the bridge is applied to the beams representing the bridge deck.

The base of the model is not a physical boundary between the gravel and an underlying layer of bedrock, therefore, a rigid base approach to dynamic loading is not ideal. Instead, ground motions are applied to the model as equivalent force histories using the method of Joyner and Chen (1975), which considers the compliance of an underlying elastic half-space, preventing all of the applied energy from becoming trapped inside the considered domain. To implement the Joyner and Chen (1975) approach, the nodes at the base of the mesh are constrained to have equal degrees-of-freedom in the horizontal direction with a control node at the lower left corner of the mesh. This control node is attached to a rate-dependent viscous damper element set with a dashpot coefficient

$$c = \rho_{\text{half}} v_{s\,\text{half}} A \tag{8.1}$$

where ρ_{half} and $v_{s\,\text{half}}$ are the mass density and shear wave velocity, respectively, of an assumed underlying elastic halfspace, and A is the base area of the model, accounting for the length of the model and the assigned thickness of the elements. The halfspace parameters are set as $\rho_{\text{half}} = 2.5$ Mg/m^3 and $v_{s\,\text{half}} = 750$ m/s for all analysis cases. A force history is

obtained as

$$F_{\text{equiv}}(t) = \rho_{\text{half}} v_{s\,\text{half}} A v_{\text{record}}(t) \tag{8.2}$$

where $v_{\text{record}}(t)$ is the velocity time history of the recorded motion at that depth, and is applied dynamically at the control node. This approach for ground motion application considers the compliance of the soil and rock which exists below the extents of the model, and prevents energy from becoming trapped in the model domain.

The columns of elements at the horizontal extents of the soil mesh, depicted in distinct colors in Figure 8.1, are used to apply a free-field soil response to the interior of the model. The elements in these columns are assigned a thickness 100 times larger than that assigned to the interior elements to ensure that they are significantly more massive. When the ground motion is applied to the base of the model, these columns of elements respond in the manner of the free-field soils at the site, while simultaneously transmitting this response into the interior of the model. The horizontal extents of the mesh are defined such that these free-field columns are sufficiently removed from the areas of interest. This technique has been applied to dynamic plane strain analysis by Shin (2007), among others.

8.1.2 Additional Soil Properties for Effective Stress Analysis

The soil properties and constitutive models discussed in Section 7.1 are used in the plane strain model, however, several additional material properties must be defined for an effective stress analysis of the site soils. A fluid bulk modulus $K_{\text{fluid}} = 2.2$ GPa and fluid mass density $\rho_{\text{fluid}} = 1.0$ Mg/m^3 are used for all soil layers below the groundwater table. Isotropic permeabilities are assigned to each submerged soil layer, with values of 8.5×10^{-6} m/s, 5.0×10^{-3} m/s, and 1×10^{-2} m/s corresponding to the loose sand, dense sand, and gravel layers, respectively. The permeability values are selected to be as similar as possible to the expected values for each soil type, while producing the desired response in the numerical model.

8.1.3 Bridge Superstructure and Foundations

Displacement based beam-column elements are used to model the bridge superstructure, abutments, and shaft foundations. The beam elements representing the shaft foundations are assigned a section response based on the model drilled-shaft cross-section discussed in Section 7.2, and both elastic and elastoplastic section responses are considered. For the interior piers, the section properties of the shaft model are scaled by three to capture the bending stiffness of a 3×1 row of shafts. The beam elements in the piers transition from this foundation section model to an elastic girder section model at the base of the pier cap shown in Figure 7.12. The 4×2 grouped shaft foundations at the abutments are modeled with two columns of vertical beam elements, assigned the model shaft section properties

scaled by four, connected at the top by a rigid horizontal beam representing the shaft cap. This configuration is shown in Figures 7.3 and 8.1.

The beam elements representing the bridge deck, interior piers above the pier caps, shaft caps, and abutment walls are assigned an elastic section response based on a composite cross-section defined by the bridge deck and girders. The second moment of area for this composite deck section is $I_{\text{deck}} = 4.58$ m^4 and the cross-sectional area is $A_{\text{deck}} = 7.25$ m^2. A modulus of elasticity $E_{\text{deck}} = 63.2$ GPa is chosen to represent a smearing of the reinforcement and concrete in the cross-section. The vertical location of the beam elements representing the bridge deck is the centroid of the composite deck girder cross-section.

8.1.4 Soil-Foundation Interaction Curves

The beam elements used to model the bridge foundations must be linked to the soil mesh in a manner that accounts for the disparity in what each element type represents in plane strain. Defining a direct link between the beam and soil nodes implies that the beam elements represent a wall with an infinitesimally small width in the plane and infinite thickness out of the plane. An appropriate link between the two element types is developed using interface elements assigned the constitutive response of commonly used soil-structure interaction curves that account for the three-dimensionality of the shaft foundations.

Zero-length elements are used for this purpose, with *p*-*y* curves defining the horizontal constitutive response and *t*-*z* and *Q*-*z* curves applied in the vertical direction. The use of zero-length elements allows for the beam and solid element nodes to share the same location within the mesh, thus simplifying mesh generation during pre-processing. Using this technique, the compatibility of displacements between the foundations and surrounding soil that occurred at the Puente Mataquito site cannot be directly captured, however, the mechanisms can still be identified. The modeled soil will displace approximately in the manner expected for the embedded foundations, and the structural demands in the foundation elements will approximate those in the actual shaft foundations. Another potential issue with this modeling technique is that the soil response is effectively modeled twice. The interpretation of the *p*-*y*, *t*-*z*, and *Q*-*z* curves as the near-field soil response, and the continuum elements as more of a far-field response removes some of this concern, however, it is important to note the potential for error associated with this doubled soil response.

The *p*-*y*, *t*-*z*, and *Q*-*z* curves in the plane strain model are defined based on existing relations and previous experience. For the *p*-*y* curves, p_u values are defined using the method of Brinch Hansen (1961) and k_T values are defined using the API (2007) procedure corrected for overburden after Boulanger et al. (2003). The *t*-*z* curves are defined after the work of Mosher (1984) and Kulhawy (1991), and the *Q*-*z* curves are defined based on the work of Meyerhof (1976) and Vijayvergiya (1977). Since the beam elements in the model represent a row of shaft foundations, group effects are considered for the soil-foundation

Figure 8.2: Location of the Convento Viejo recording site relative to Puente Mataquito.

interaction curves using the p-multipliers of Mokwa and Duncan (2001).

The interface elements connecting the beam elements representing the abutment walls with the solid elements representing the embankment fill are assigned an elastic-perfectly plastic constitutive response in compression with zero tensile strength or stiffness. The ultimate capacity of these constitutive models is determined from the Rankine passive capacity of the soil in the embankments. The elastic stiffness values are set in a similar manner to the tri-linear curves discussed in Section 5.1.1, with $\Delta_{\max}$ set equal to 5% of the nodal depth. At the surface nodes, small non-zero ultimate force and displacement values are assigned for numerical purposes.

8.1.5 Ground Motions

Two ground motions are used during analysis of the plane strain model, the Convento Viejo record from the 2010 Maule event and the Gilroy No. 1 record from the Loma Prieta event. The Convento Viejo recording was made by a triaxial accelerograph located on rock inside a diversion tunnel for the Convento Viejo embankment dam (ARCADIS, 2010), which is approximately 100 km inland from Puente Mataquito. Figure 8.2 shows the location of the recording site in relation to Puente Mataquito and several cities. The horizontal acceleration, a, velocity, v, and displacement, u, time histories for the Convento Viejo motion are shown in Figure 8.3. The Convento Viejo ground motion record was obtained via personal correspondence with Christian Ledezma from Pontifica Universidad Católica de Chile. At the time of the analyses, the Convento Viejo dam was the nearest available recording site to Puente Mataquito with a rock ground motion record.

The Gilroy Array No. 1 fault parallel record from the 1989 Loma Prieta event (NGA

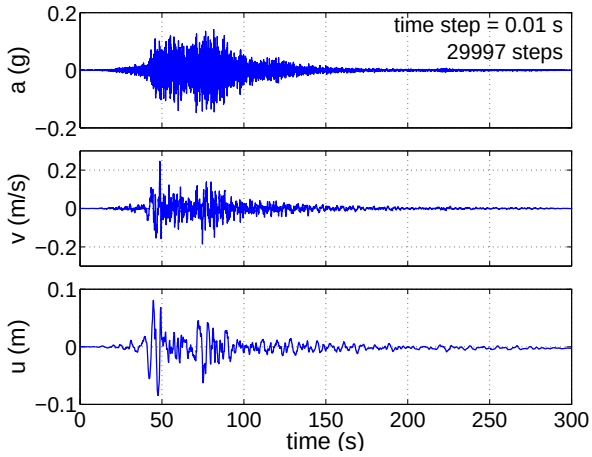

Figure 8.3: Acceleration, velocity, and displacement time histories for Convento Viejo ground motion record.

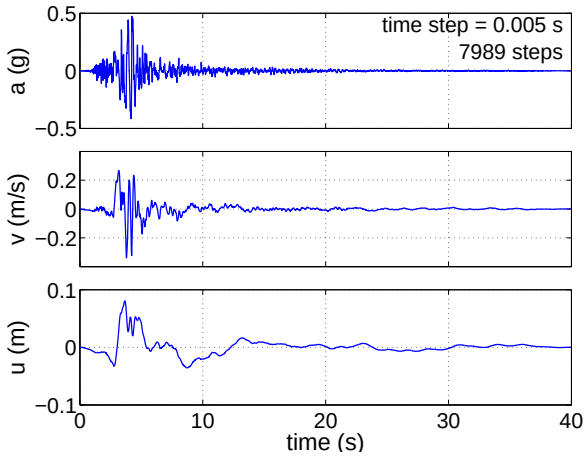

Figure 8.4: Acceleration, velocity, and displacement time histories for Gilroy No. 1 ground motion record.

#765) from the PEER strong ground motion database (PEER, 2010) is used as an alternative ground motion. While this record does not possess the long duration and high frequency content characteristic to recorded motions from the Maule event, it is a significantly shorter motion with fewer recorded time steps, thus facilitating shorter analysis times more suitable for testing the model and producing comparative studies for different modeling decisions. The time histories for the Gilroy No. 1 record are shown in Figure 8.4.

Table 8.1 provides the maximum acceleration, velocity, and displacement along with the Arias intensity, I_a, for each ground motion record. The peak acceleration for the Gilroy record is significantly larger, however, the peak velocities, peak displacements and Arias intensities are similar for the two records. As shown in Figure 8.5, the Arias intensities develop differently for each motion. For the Gilroy record, there are several large amplitude

Table 8.1: Maximum acceleration, velocity, displacement, and Arias intensity for Convento Viejo and Gilroy No. 1 ground motion records.

Record	$a_{\max}$ (g)	$v_{\max}$ (m/s)	$u_{\max}$ (m)	I_a (m/s)	duration (s)
Convento Viejo	0.147	0.246	0.081	1.74	299.97
Gilroy No. 1	0.473	0.267	0.081	1.68	39.945

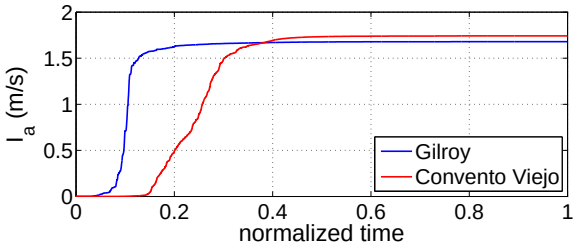

Figure 8.5: Arias intensity values over normalized motion duration for Convento Viejo and Gilroy No. 1 ground motion records.

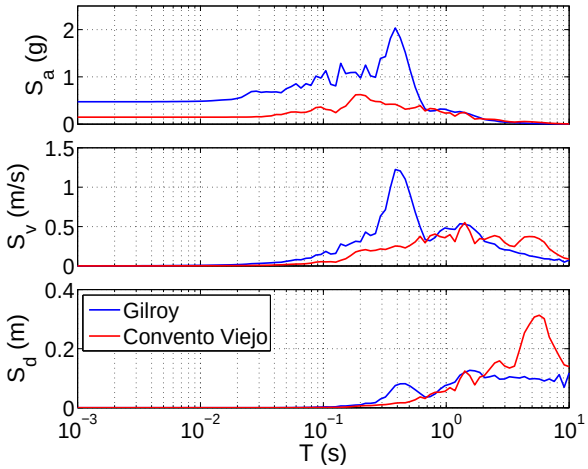

Figure 8.6: Response spectra (5% damping) for Convento Viejo and Gilroy No. 1 ground motion records.

waves early in the motion and these waves are the primary contribution to the Arias intensity for the record. The amplitudes for the Convento Viejo record are smaller in comparison, however, the high amplitude portion of this record lasts over a longer duration, leading to a slower rate of increase in the Arias intensity. For further comparison of the two ground

motion records, the response spectra at 5% damping are shown in Figure 8.6. As expected, the two ground motion records produce very different response spectra.

8.2 Dynamic Plane Strain Analysis: Gilroy No. 1 Ground Motion Record

In order to determine a set of appropriate modeling parameters for use in subsequent models of the Puente Mataquito site, a series of initial simulations are performed using the Gilroy No. 1 ground motion record from the 1989 Loma Preita event. This record is shorter and more forgiving numerically than the Convento Viejo motion (see Section 8.1 for details), thus enabling a series of analyses to be performed efficiently. The results from these analyses are compared to each other to gain valid insights into the behavior of the Puente Mataquito site and to gauge the effect of various modeling choices on the results of the simulations. Two primary modeling choices are considered in this study: the effect of soil element domain thickness, and the effect of different liquefiable layer configurations.

8.2.1 Alternative Model Configurations

Several different configurations of the plane strain model are considered in order to assess the sensitivity of the results to different modeling choices. One set of alternative model configurations is chosen to evaluate the effects of solid element thickness. The incompatibility between the plane strain continuum elements used to model the soil and the beam-column elements used to model the bridge foundations necessitates care in the treatment of this thickness in order to gain appropriate results. This is especially true where the beam elements represent a row of grouped piles or shafts, as is the case for the Puente Mataquito model. Typically, plane strain continuum elements are assigned a unit thickness in the out-of-plane direction. It is likely that this definition does not achieve a realistic soil mass to foundation stiffness ratio, and as a result, the soil deformation and structural demands returned from the simulation may be underpredicted. To examine the effect of solid element thickness on the results, models are created that consider three element thickness values: 20 m, 90 m, and 1 km.

The 20 m thickness is based on the equivalent embankment width, w_t, proposed by Boulanger et al. (2006) for simplified analysis of piled bridge abutments subject to lateral spreading (see Section 5.1.1, step 5). This equivalent width is computed as the sum of the crest width with one-half of the width of the sloped sides as shown in Figure 8.7. The 90 m thickness is based on the surface width of a soil wedge developed over the full length of the abutment shafts as predicted using strain wedge theory (Ashour et al., 1998). The 1 km thickness is chosen as a maximum credible value.

Another set of model configurations is used to analyze the liquefaction behavior of the Puente Mataquito site, primarily with regards to uncertainty in the definition of the lique-

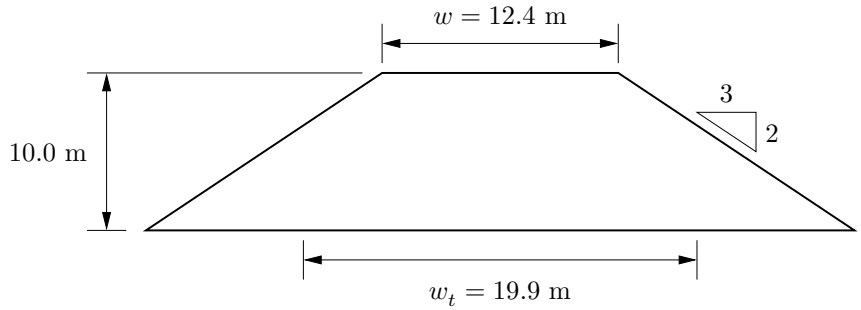

Figure 8.7: Idealized approach embankment dimensions for Puente Mataquito.

fiable layer for the idealized soil profile. To this purpose, three liquefaction configurations are considered for the plane strain model: no liquefaction, existing (idealized) liquefaction conditions, and thick liquefaction conditions. A 90 m soil domain thickness is assumed for these models. In the case without liquefaction, the permeabilities of the soil elements are set at 1.0 m/s, such that excess pore pressure will not develop. The existing liquefaction case considers the idealized soil profile discussed in Section 7.1, and the thick liquefaction case considers a soil profile in which the loose sand layer expands to replace the dense sand layer, resulting in a larger zone of liquefiable material. The results of these three cases are compared to each other and to observations made at the site to determine which liquefaction configuration is most representative of the Puente Mataquito site.

8.2.2 Effects of Soil Domain Thickness

Figure 8.8 demonstrates the effect of soil domain thickness on the residual horizontal displacement field returned by the model. Larger element thickness results in larger soil deformation, as the foundation stiffness is no longer sufficient to resist the movement of the increased soil masses. Figures 8.9, 8.10, and 8.11 show the progression of pore pressure ratio fields in the soil for for the 20 m, 90 m, and 1 km thick domains, respectively. As shown, there is little variation in pore pressure ratio with soil element thickness. The primary difference is in how long it takes for the large excess pore pressures to dissipate, and, as shown in Figure 8.8, how the build up of excess pore pressure is manifested in lateral soil deformation.

Figures 8.12 and 8.13 show the variation in pore pressure ratio with depth in the soil behind the two bridge abutments over the first half of the Gilroy ground motion. Significant excess pore pressures begin to develop at roughly the same point in the motion, and the dissipation of the express pore pressure tends to take longer as the soil domain thickness is increased. This is likely due to the lateral deformation of the soil above the liquefiable layer increasing the shear strain for the larger thickness values. Figures 8.14 and 8.15 verify this hypothesis, as significantly larger shear strains develop in the soil behind the abutments for the larger domain thickness values, especially on the southwest side.

The global response of the bridge is also affected by changing the thickness of the soil

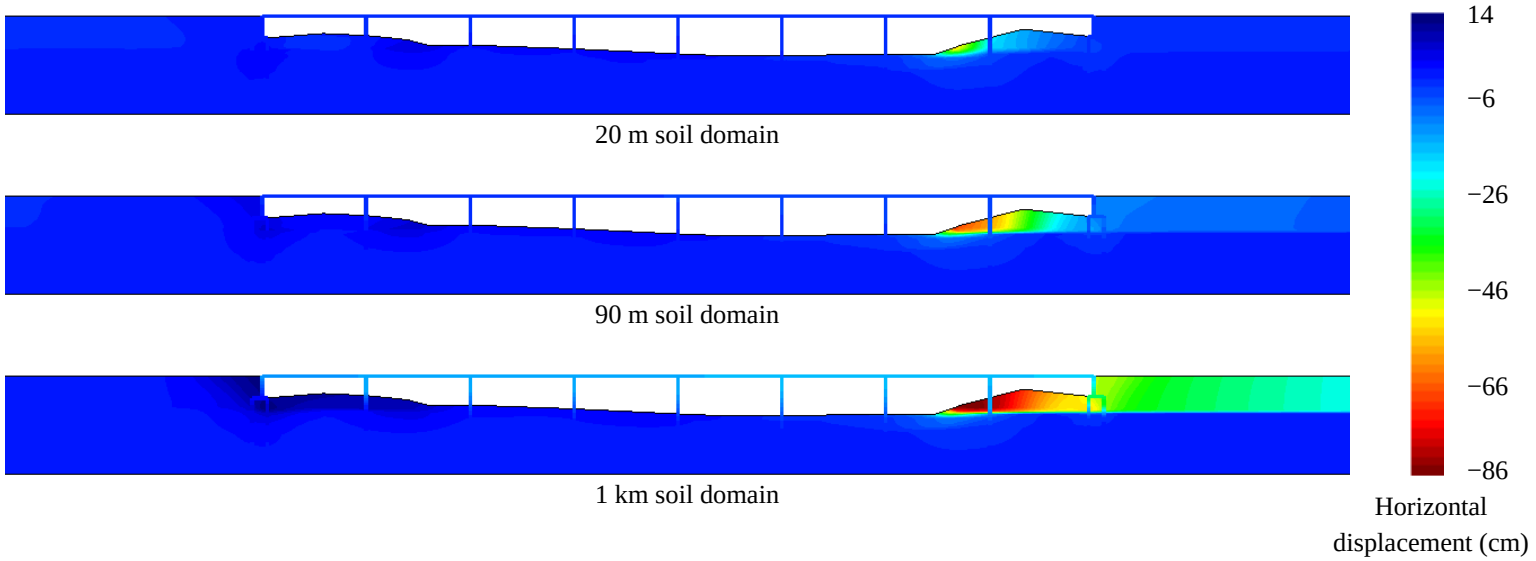

Figure 8.8: Residual displacement field for three soil domain thicknesses.

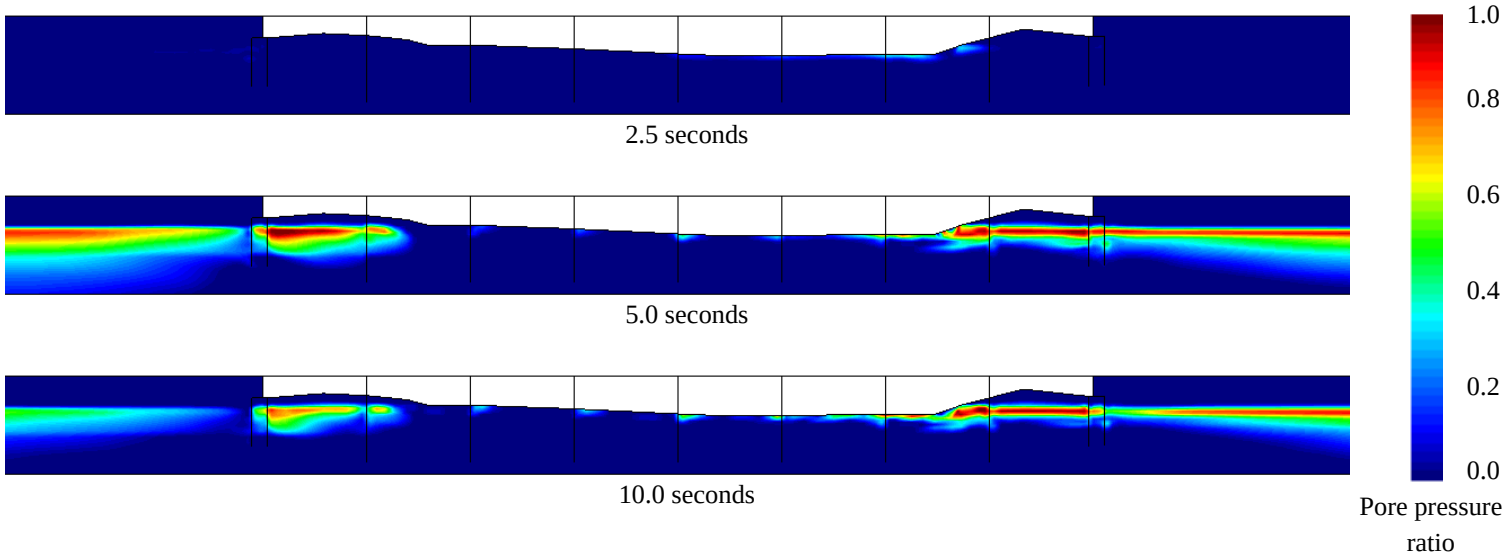

Figure 8.9: Progression of pore pressure ratio during analysis with Gilroy No. 1 motion and 20 m thick soil domain.

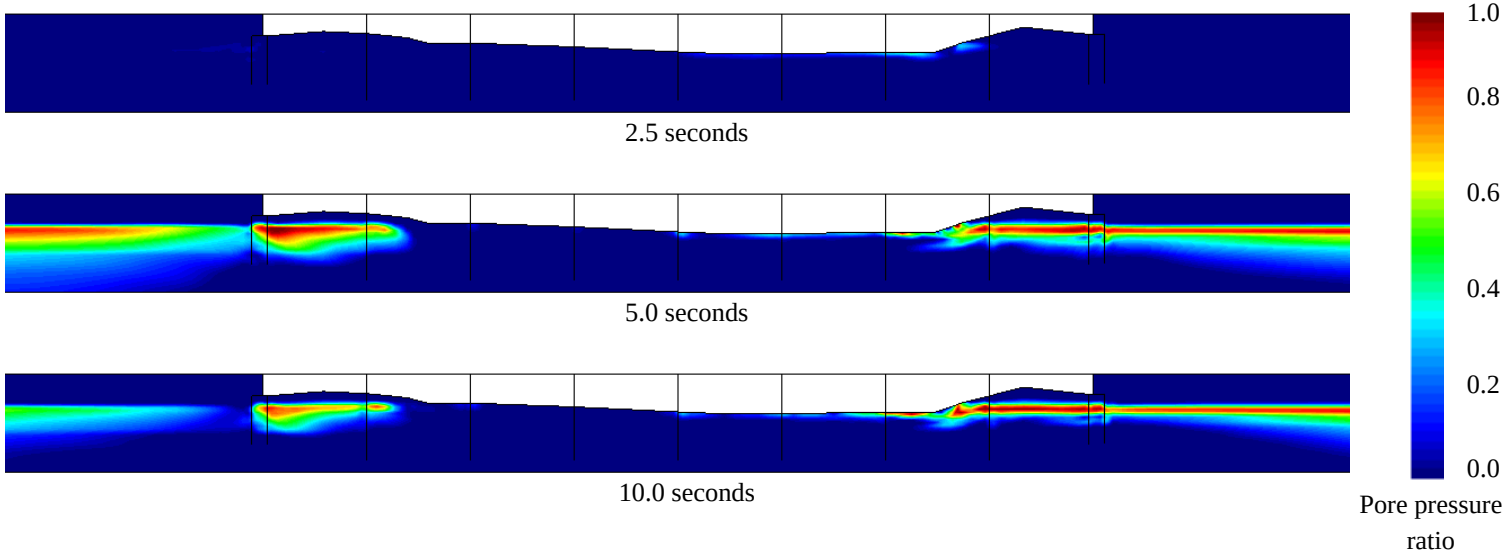

Figure 8.10: Progression of pore pressure ratio during analysis with Gilroy No. 1 motion and 90 m thick soil domain.

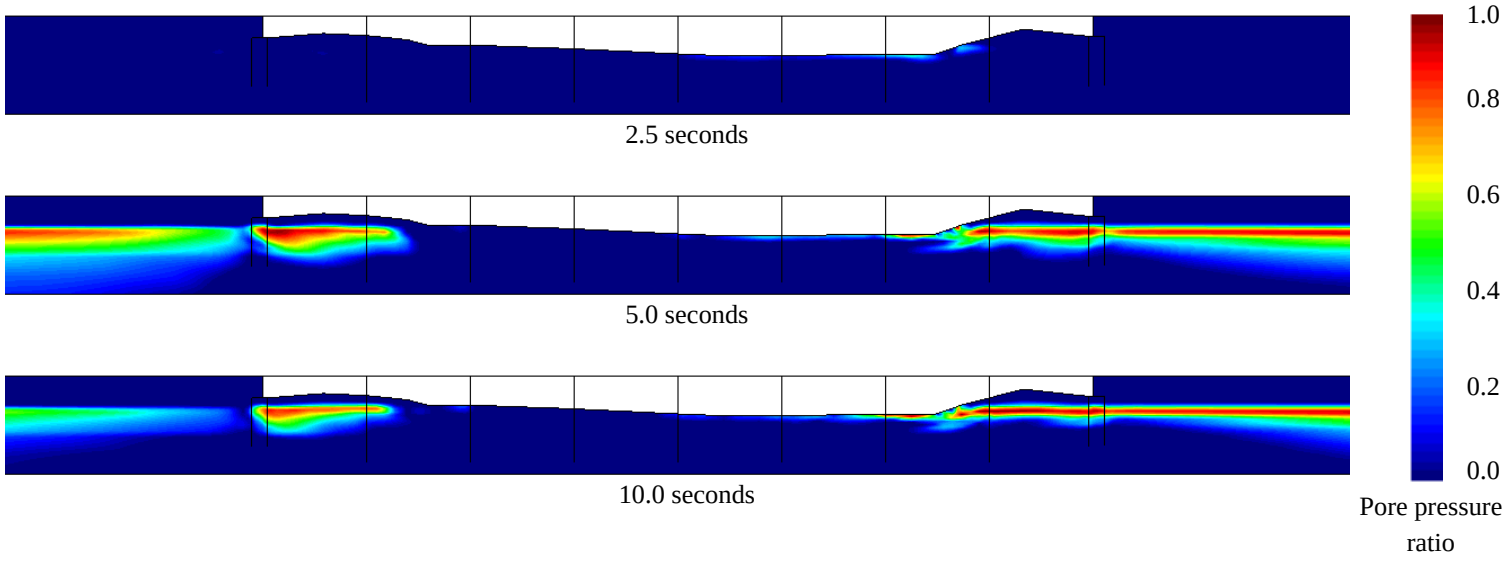

Figure 8.11: Progression of pore pressure ratio during analysis with Gilroy No. 1 motion and 1 km thick soil domain.

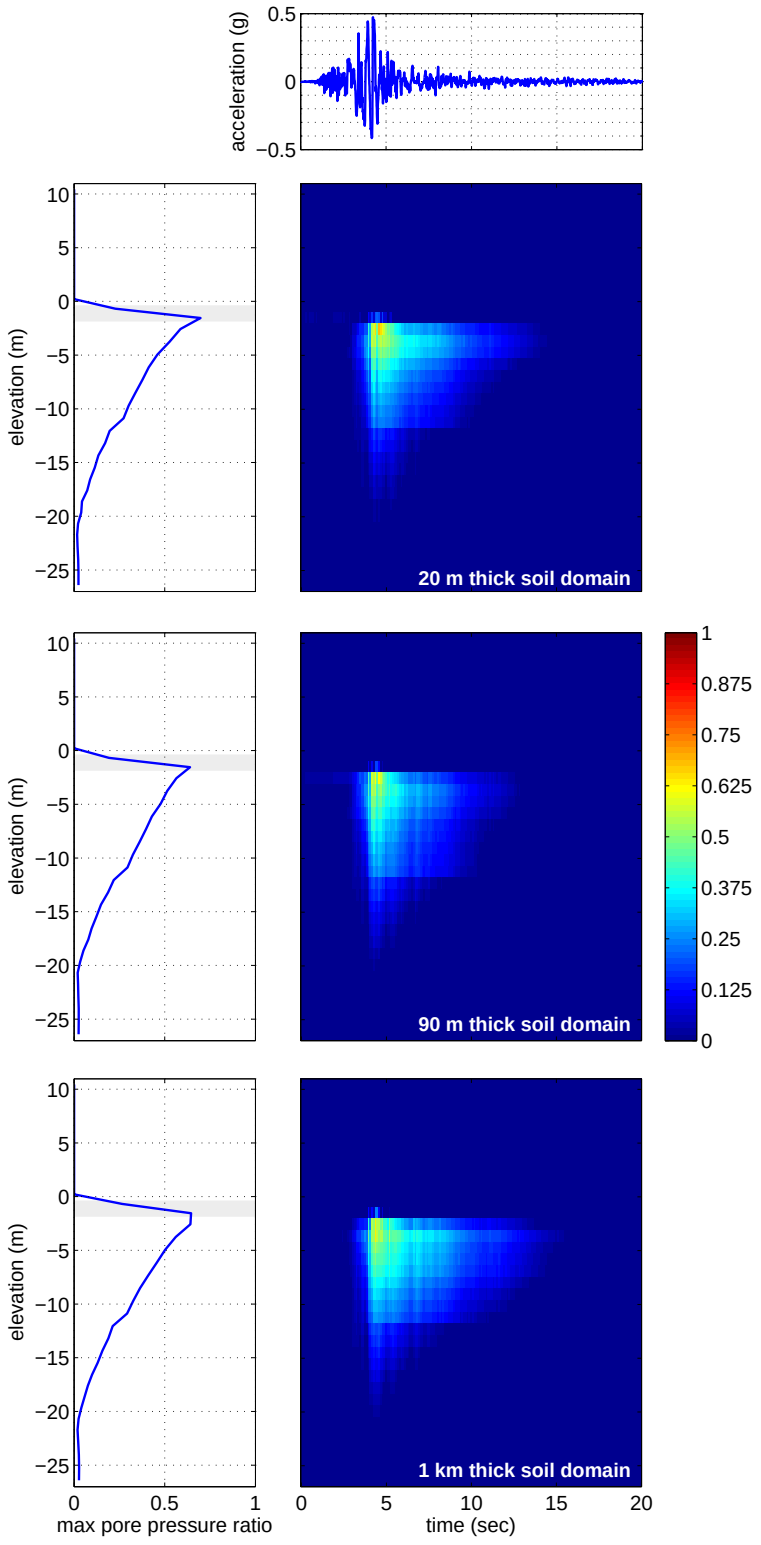

Figure 8.12: Spatial and temporal variation of pore pressure ratio in soil behind northeast abutment for three soil domain thicknesses.

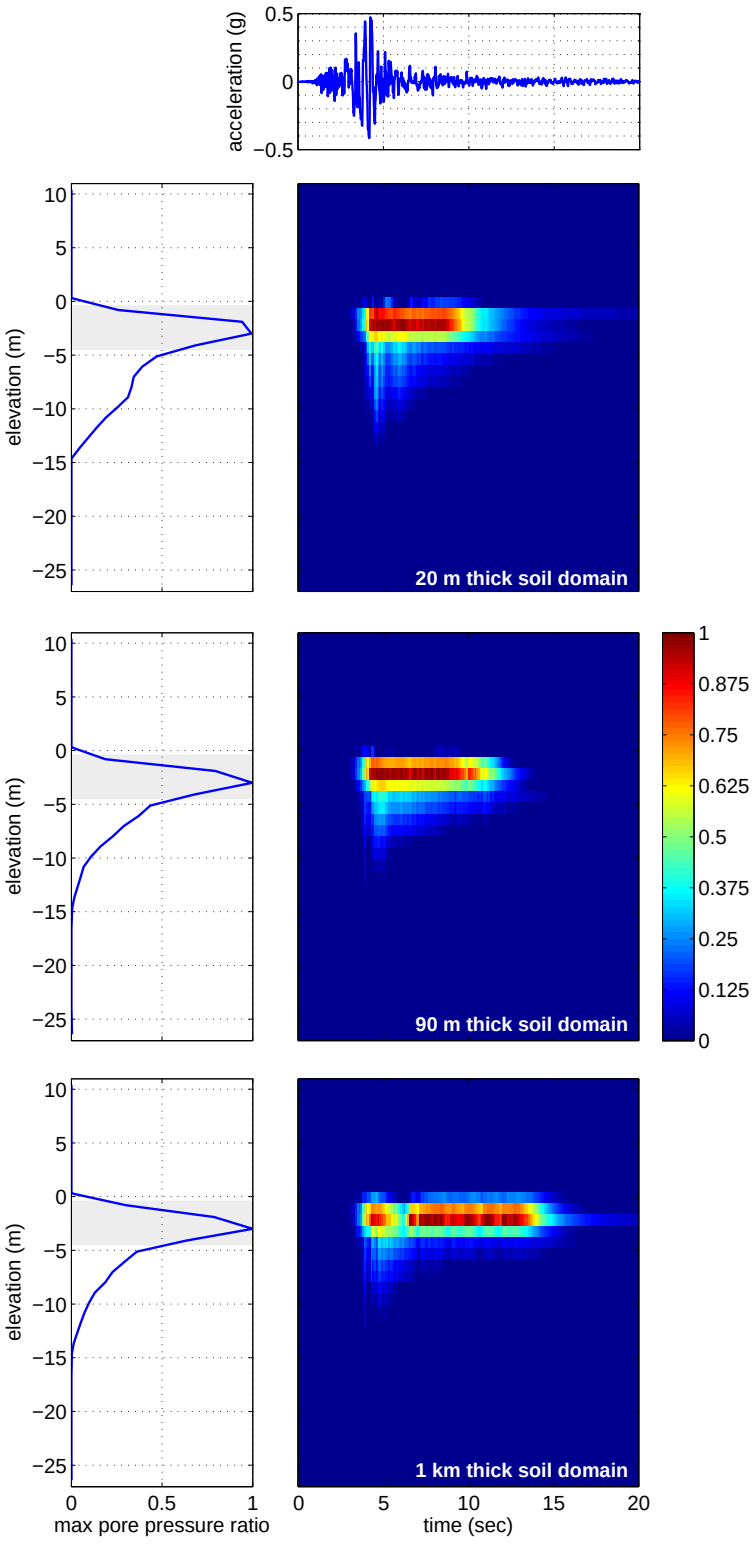

Figure 8.13: Spatial and temporal variation of pore pressure ratio in soil behind southwest abutment for three soil domain thicknesses.

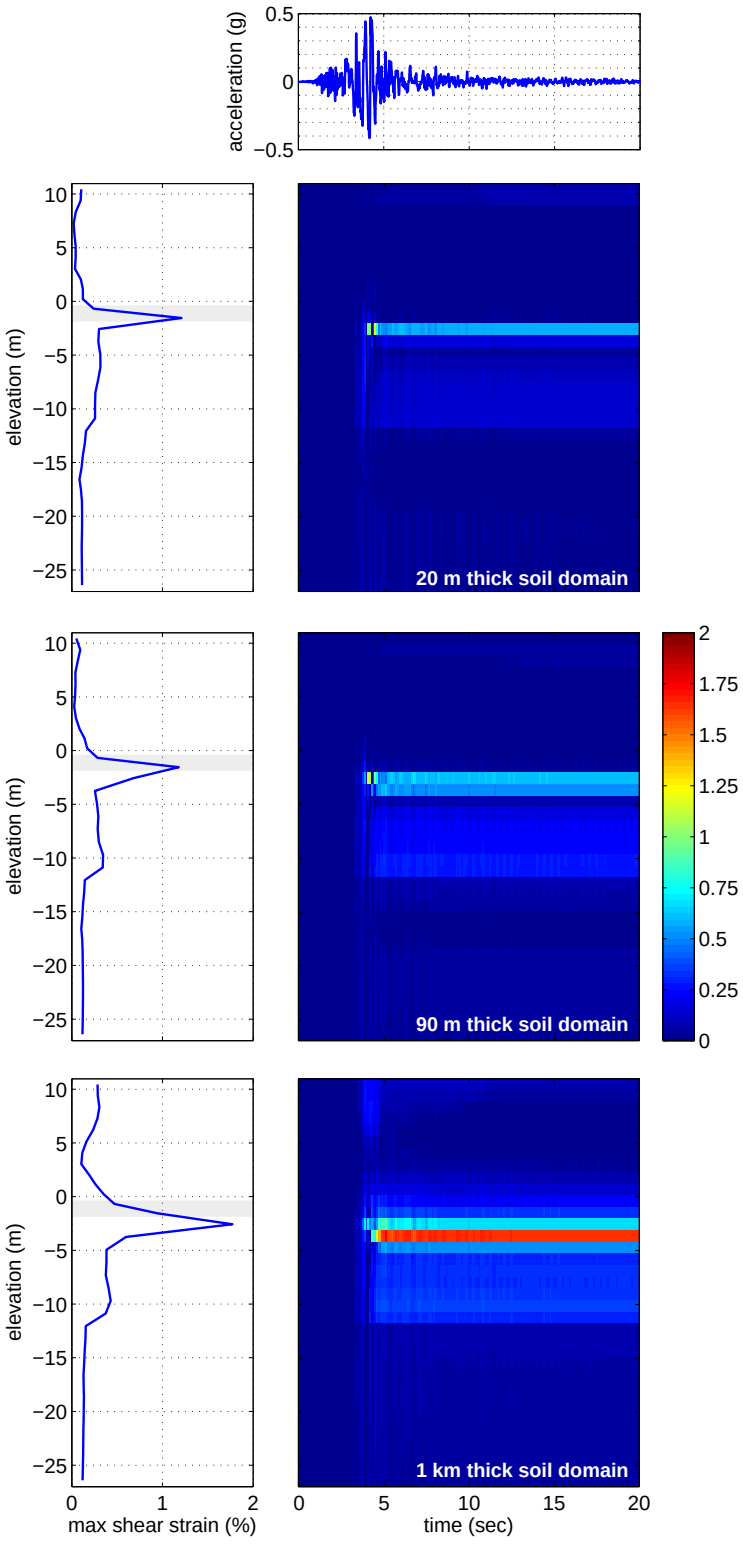

Figure 8.14: Spatial and temporal variation of shear strain in soil behind northeast abutment for three soil domain thicknesses.

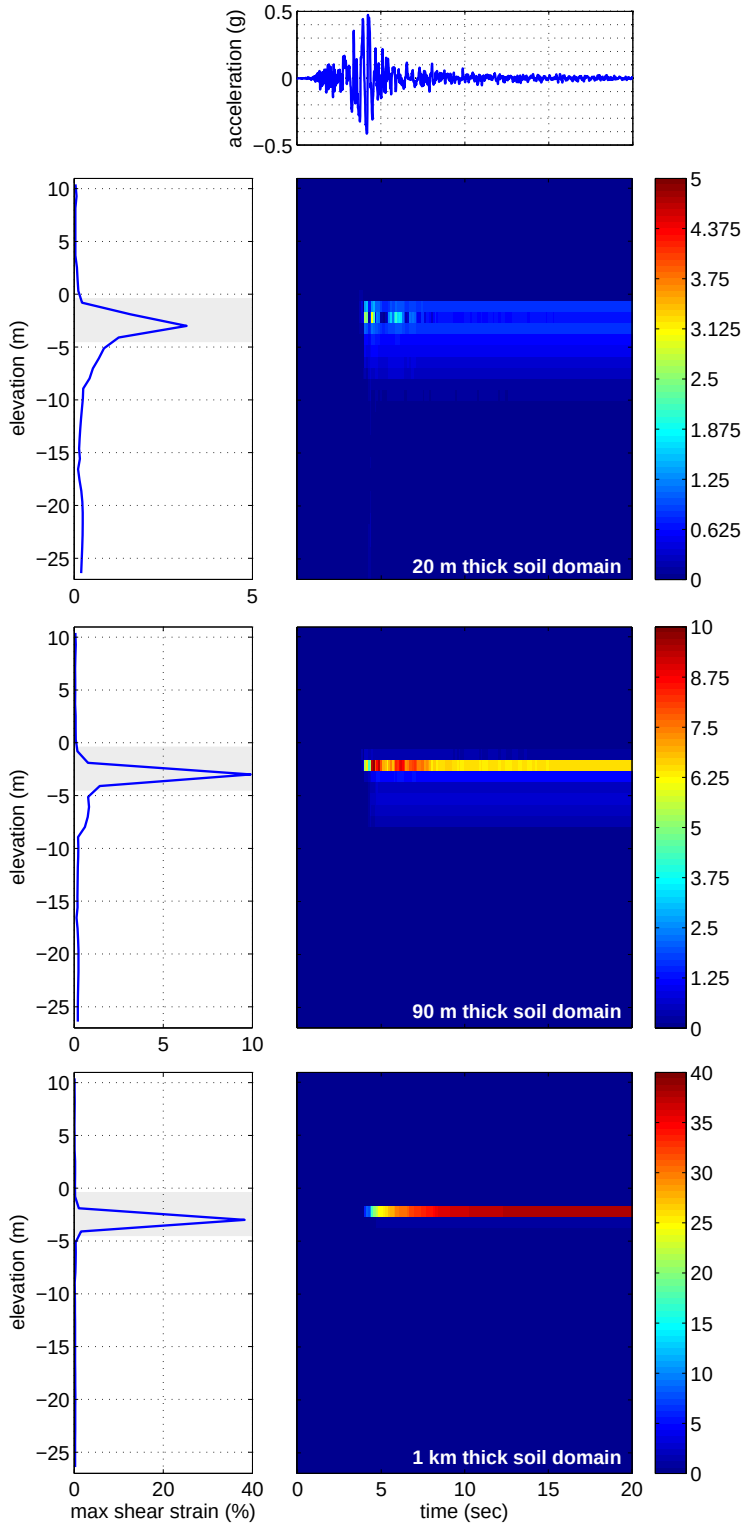

Figure 8.15: Spatial and temporal variation of shear strain in soil behind southwest abutment for three soil domain thicknesses.

elements. Figures 8.16, 8.17, and 8.18 show the residual displaced shapes of the shaft foundations for the bridge, arranged in the same orientation used in previous plots of the bridge model. The general deformation patterns for the 20 and 90 m thick domains are similar, though the 90 m case sees larger shaft displacements, especially in the southwest abutment shafts and adjacent interior piers. The shaft displacements for the 1 km thick case are significantly larger than the other cases, and Pier 7 displays a different bending mechanism that corresponds to the increased soil deformation in the vicinity of this foundation. For all three cases, the bridge deck moves towards the northeast side of the river. The shafts at the northeast abutment are subjected to a combined loading from the liquefaction-induced soil deformation and the bridge deck, resulting in relatively little displacement of the shaft cap.

Figure 8.19 shows the bending moment demands in each shaft foundation for all three soil domain thickness values. These moment diagrams agree with all previous observations, as the larger deformations resulting from increasing the mass of moving soil result in larger bending moments in the foundations. For the Gilroy motion, the model suggests that Pier 7 is likely to fail at the connection to the shaft cap for all three thicknesses, as the bending moment at this location is in excess of the 9 MN·m capacity of the shafts. Failure does not appear to be likely in any of the other foundations for the 20 and 90 m thick soil domains, while it appears that most of the foundations have failed for the 1 km thickness value.

For the geometry of the Puente Mataquito site, the 90 m thick soil domain appears to be the most appropriate choice of the three considered thickness values. Based on the results obtained from this small parameter study, it seems clear that a 1 km thick soil element domain is too large. The embankment and foundation deformations for this case far exceed the observations made at the site, and while this thickness may seem appropriate for the native portion of the soil profile, it is much to large for the embankment. The 20 m and 90 m thick element domains produce similar global results, and it is not immediately apparent from these results which is a better choice for this particular site. While the 20 m thickness accurately portrays the mass of the embankment fill, it may consider an insufficient mass of native soil in comparison to the foundation stiffness given the thickness of the grouped shafts, therefore, the 90 m thickness is selected for use in subsequent analyses.

8.2.3 Effects of Liquefiable Layer Thickness

The residual horizontal soil deformation fields for each liquefiable layer configuration are shown in Figure 8.20. There is a dramatic difference in the displacement magnitude between the three cases, with the larger liquefiable zone leading to significantly larger deformation. Figure 8.21 shows the progression of the pore pressure ratio field in the soil for the thick liquefiable layer configuration. As expected, increasing the scope of the liquefiable zone results in increased liquefaction throughout the soil profile.

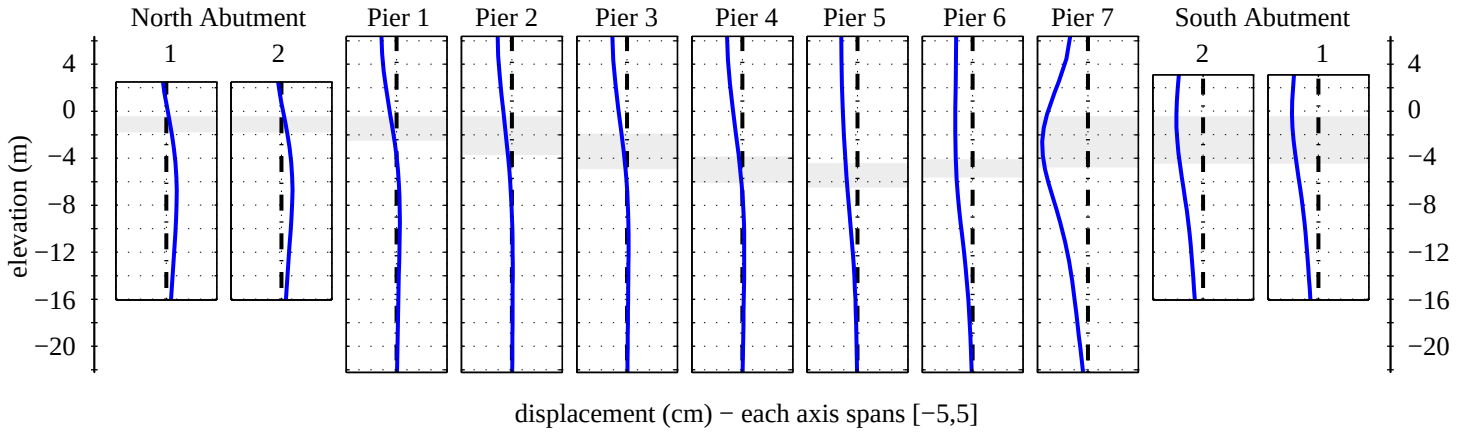

Figure 8.16: Residual shaft displacement profiles for 20 m thick domain.

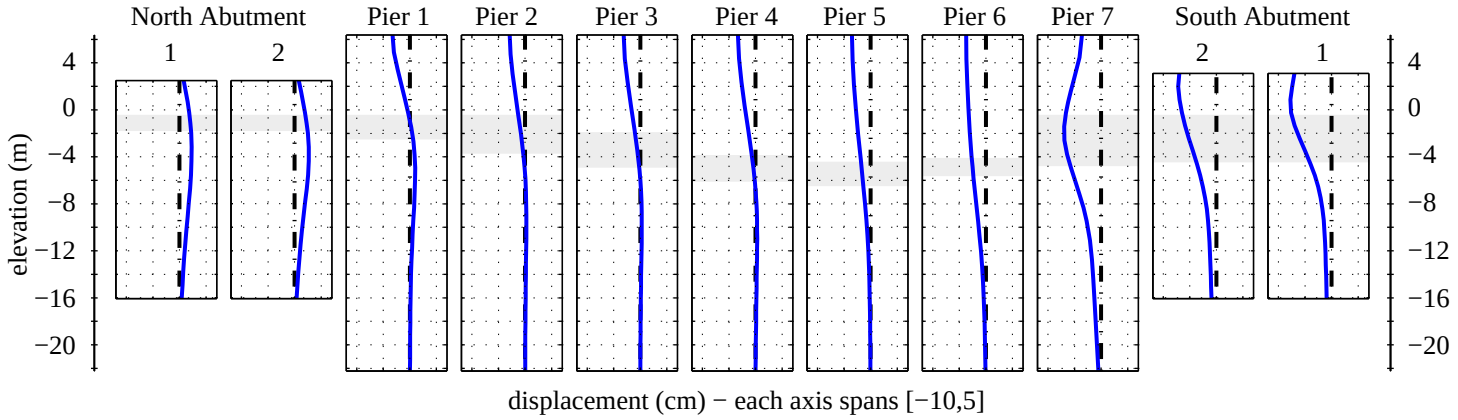

Figure 8.17: Residual shaft displacement profiles for 90 m thick domain.

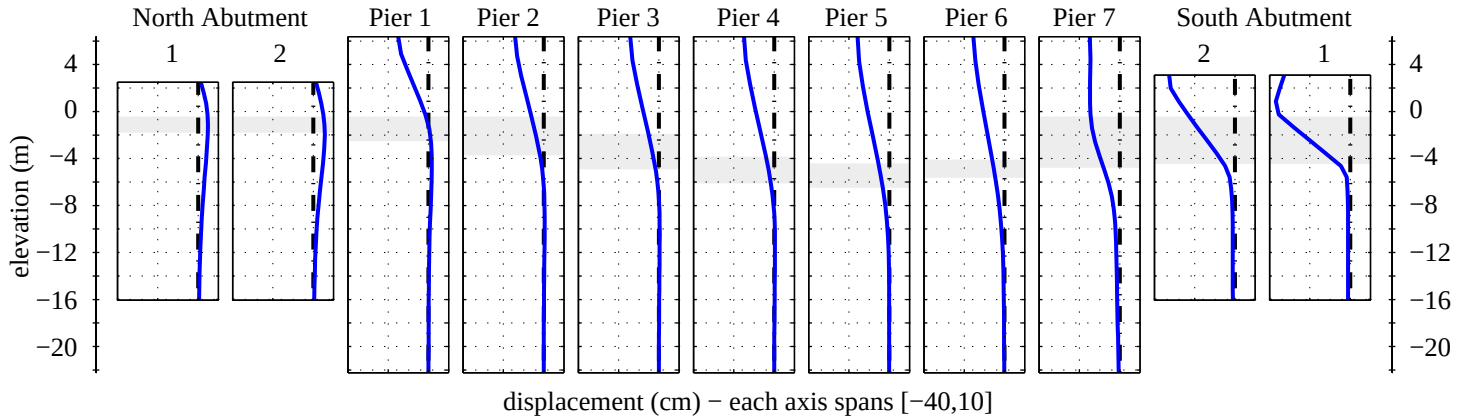

Figure 8.18: Residual shaft displacement profiles for 1 km thick domain.

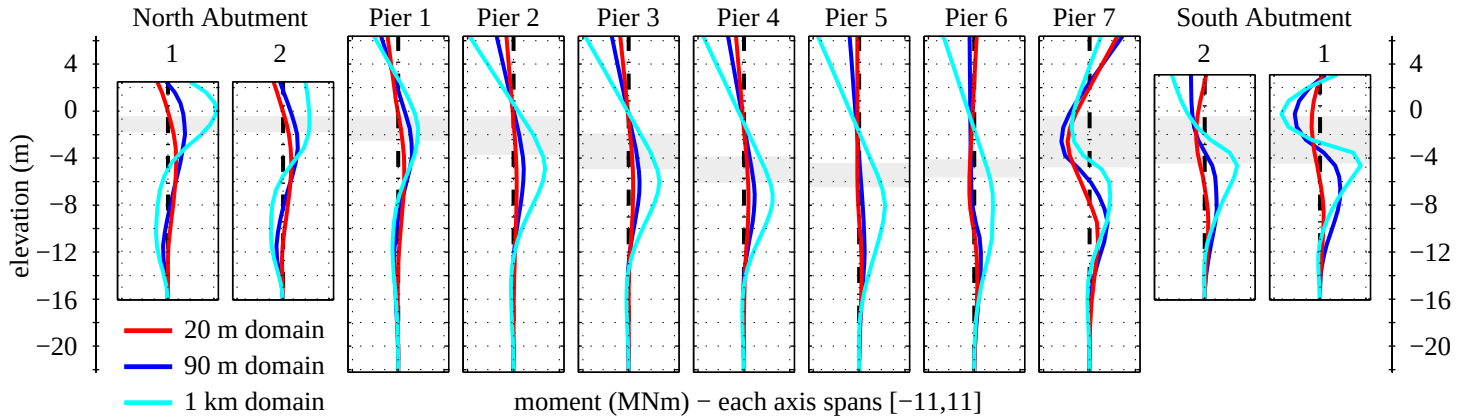

Figure 8.19: Residual bending moment profiles for three domain thicknesses.

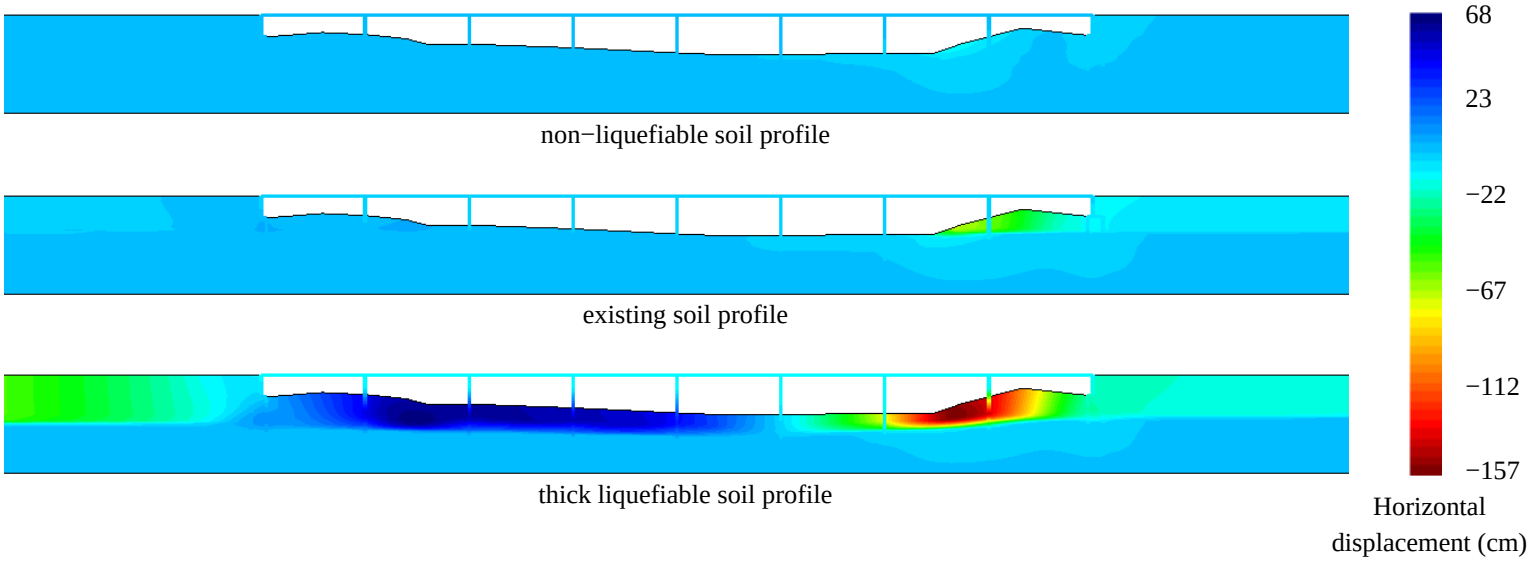

Figure 8.20: Residual displacement field for three liquefaction conditions.

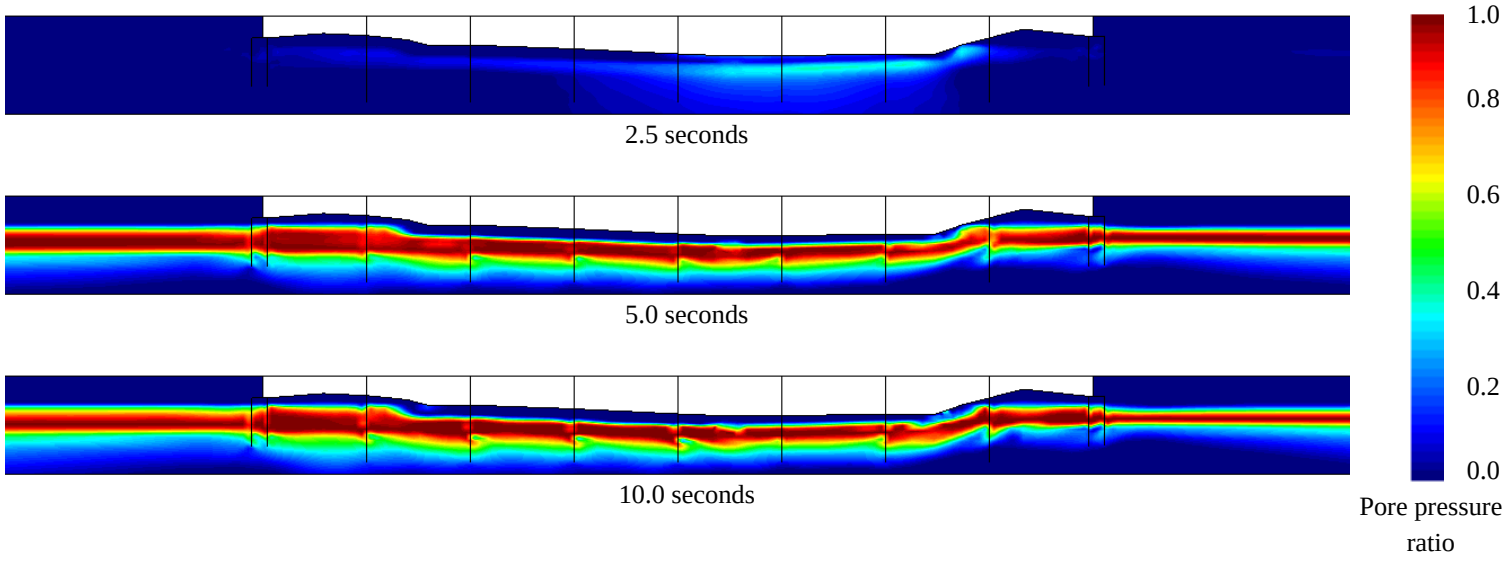

Figure 8.21: Pore pressure ratio field at three time steps during analysis for thick liquefiable soil profile.

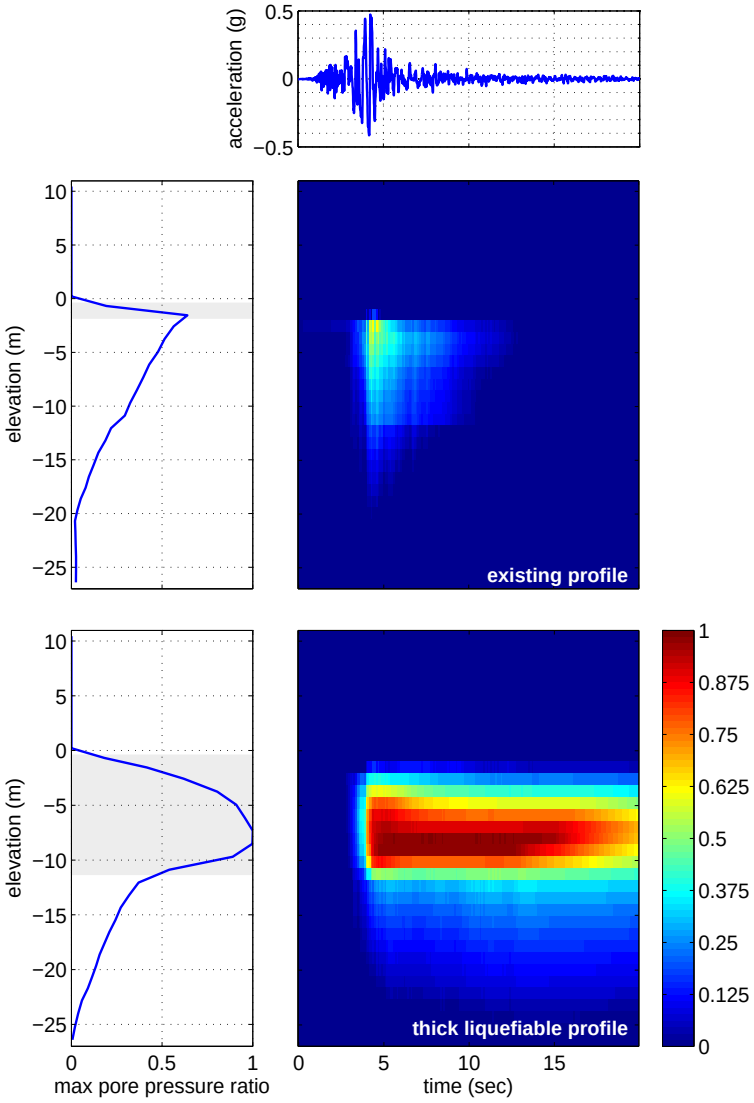

Figure 8.22: Spatial and temporal variation of pore pressure ratio in soil behind northeast abutment for two liquefaction configurations.

The effects of the increased liquefiable zone are also clear in Figures 8.22 and 8.23, which show the variation of pore pressure ratio with depth and time in the soil behind the northeast and southwest abutments, respectively, for the existing and thick liquefiable layer configurations. For the thick liquefaction configuration, the build up of significant excess pore pressure affects a larger amount of the soil profile, especially for the northeast side, and these excess pore pressures take much longer to dissipate. Figures 8.24 and 8.25 show the spatial and temporal variation of shear strain in the same locations behind the abutments for all three liquefiable layer configurations. For both sides, the maximum shear strains increase as the scope of liquefaction is increased. The shear strains on the southwest side are larger than those on the opposite bank, corresponding to the soil deformation fields shown in Figure 8.20.

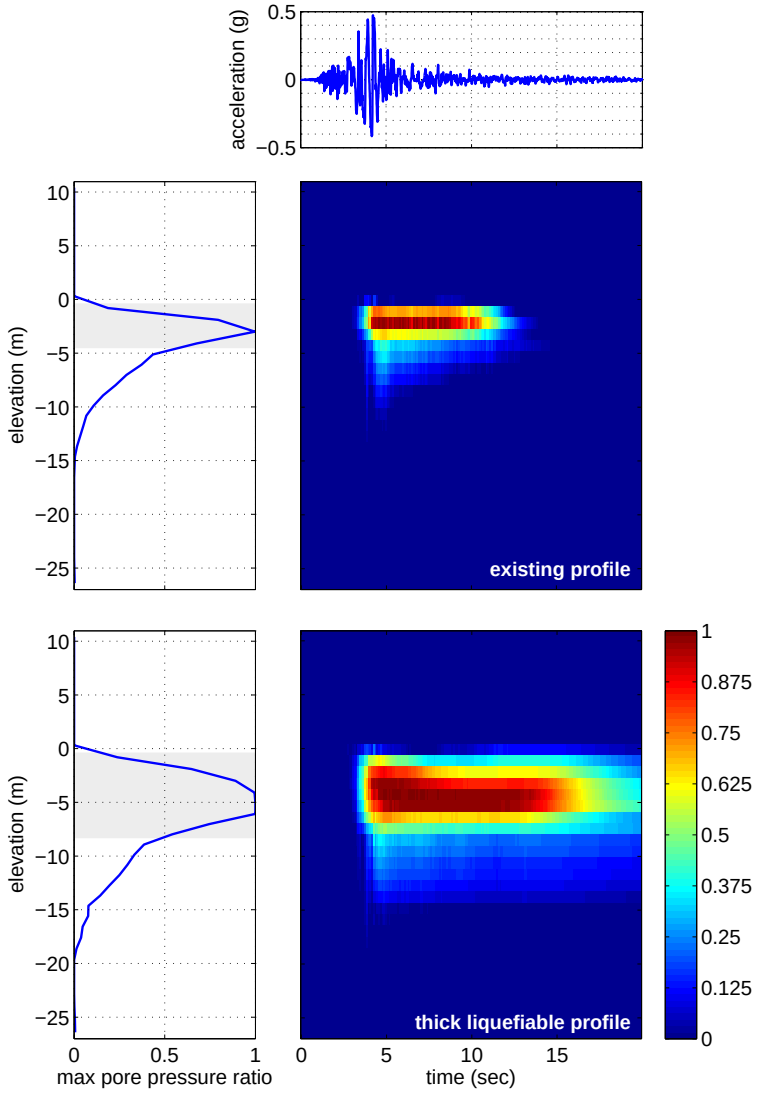

Figure 8.23: Spatial and temporal variation of pore pressure ratio in soil behind southwest bridge abutment for two liquefaction configurations.

Figures 8.26, 8.27, show the residual displaced shapes of the shaft foundations for the non-liquefiable and thick liquefiable layer configurations. Figure 8.17 shows the corresponding results for the existing liquefiable layer configuration. In the absence of liquefaction, the shaft deformations are relatively small, with a maximum value of 2.6 cm in Pier 7 and shaft cap displacements of approximately 2.0 cm at each abutment. Very large shaft deformations are returned for the thickened liquefiable layer configuration. For this case, the southwest abutment shaft cap translates 19 cm towards the river, pushing the bridge deck in the same direction and causing the northeast shaft cap to move 5.5 cm away from the river. The interior piers are severely deformed with the thick configuration, and as shown in Figure 8.28, based on the bending moment demands in the shafts, failure or near-failure is predicted for all of the bridge foundations.

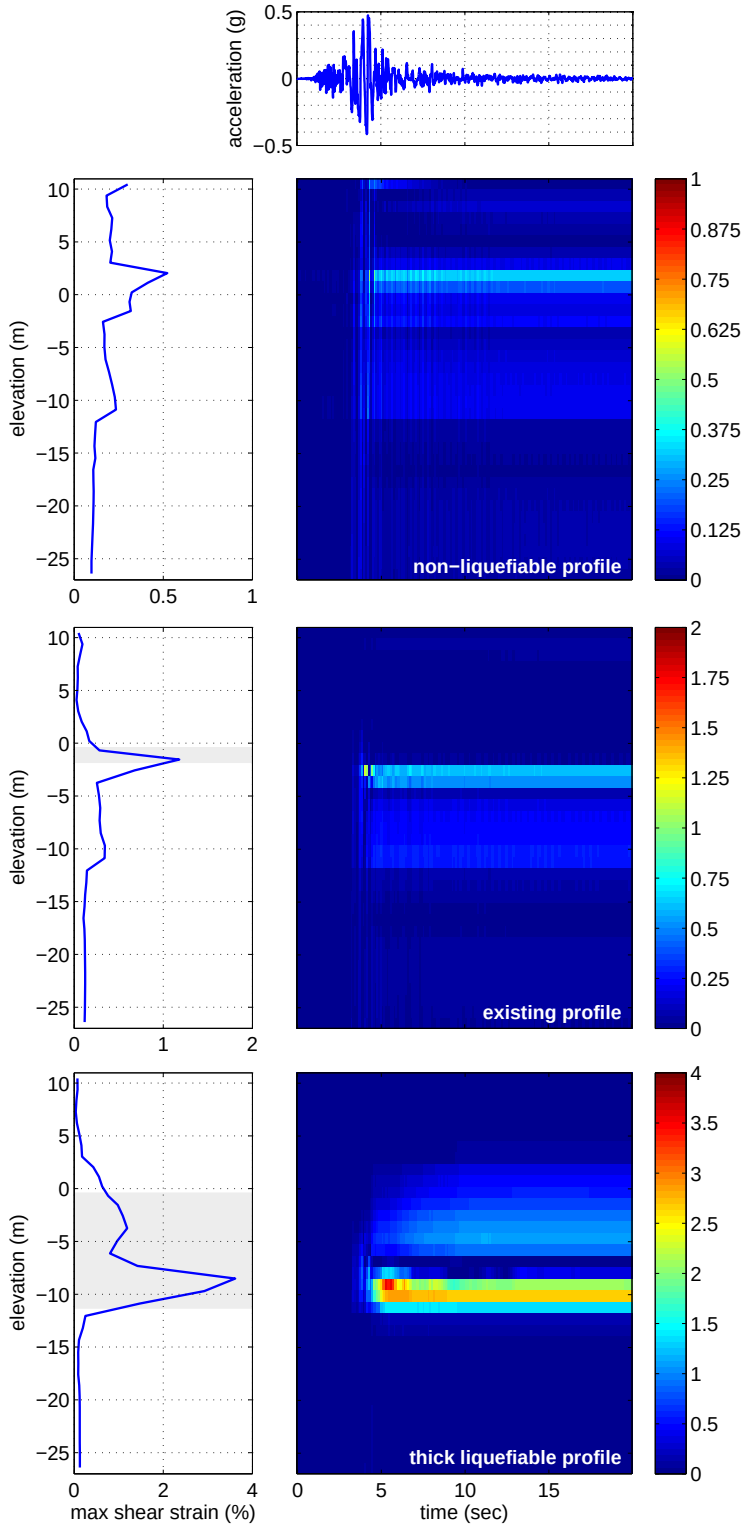

Figure 8.24: Spatial and temporal variation of shear strain in soil behind northeast abutment for three liquefaction configurations.

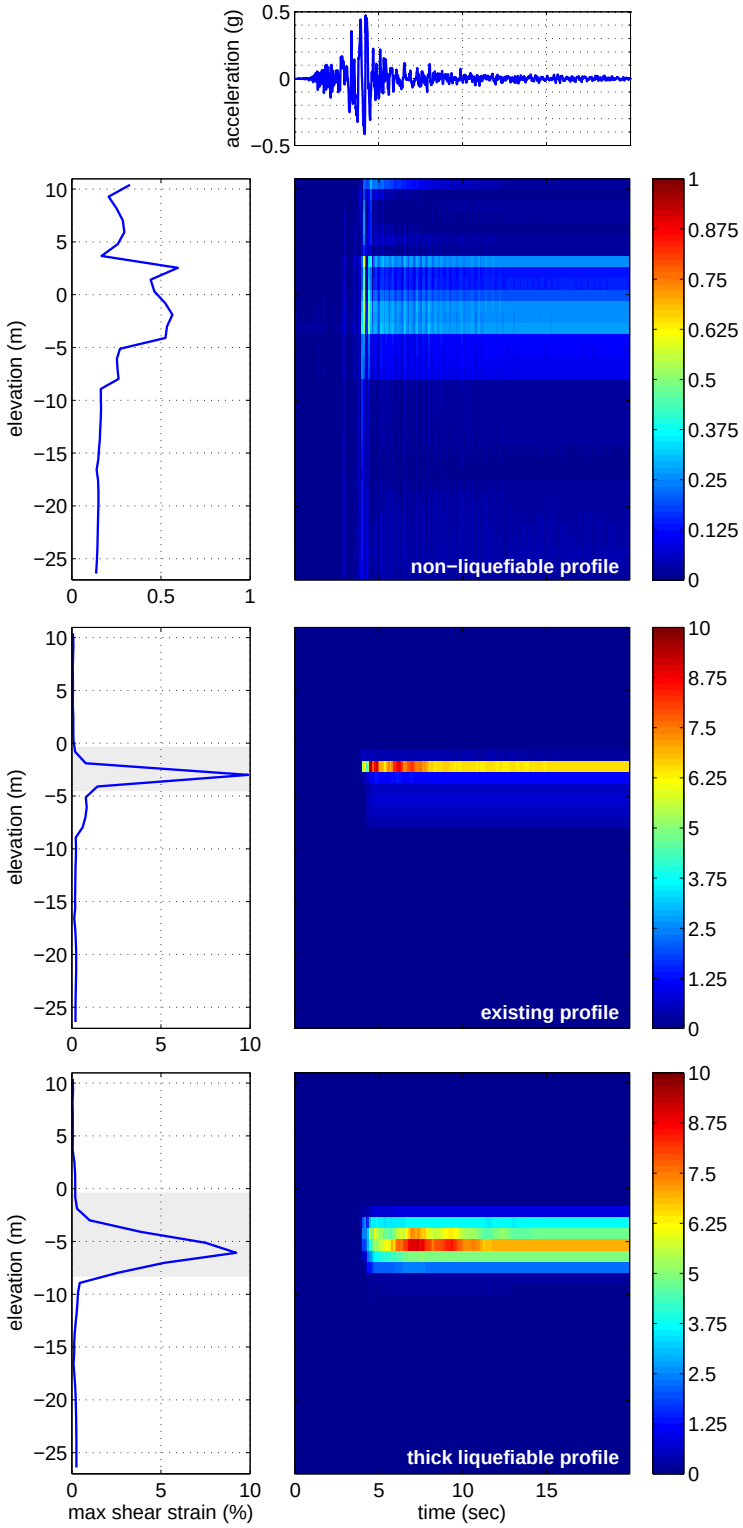

Figure 8.25: Spatial and temporal variation of shear strain in soil behind southwest abutment for three liquefaction configurations.

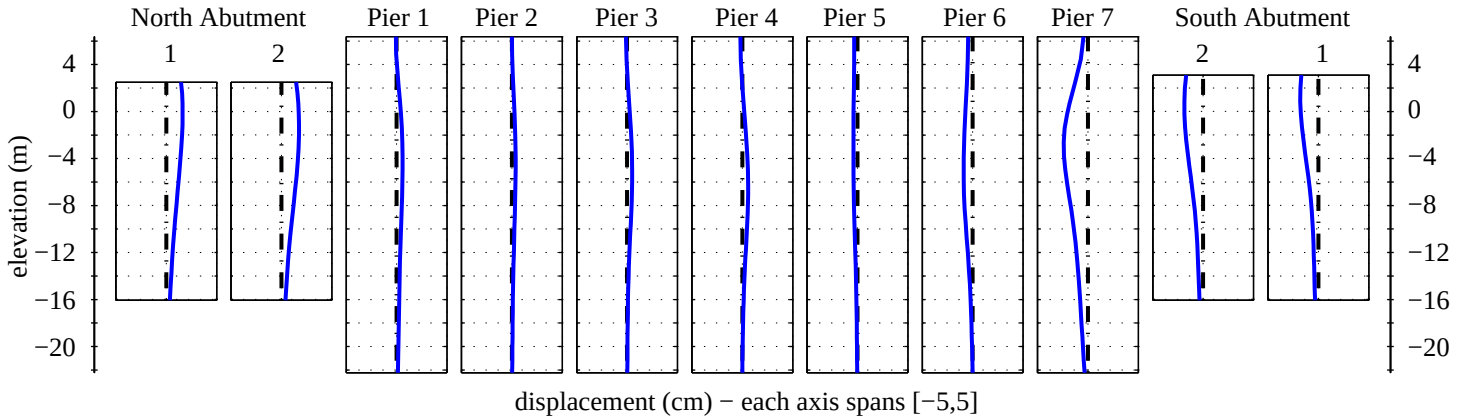

Figure 8.26: Residual shaft displacements for non-liquefiable soil profile.

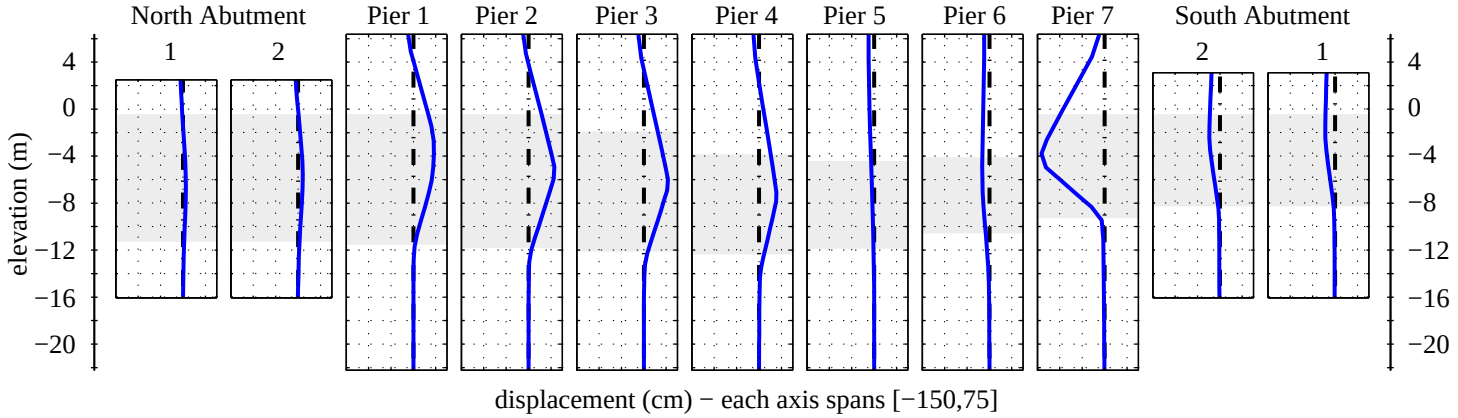

Figure 8.27: Residual shaft displacements for thick liquefiable soil profile.

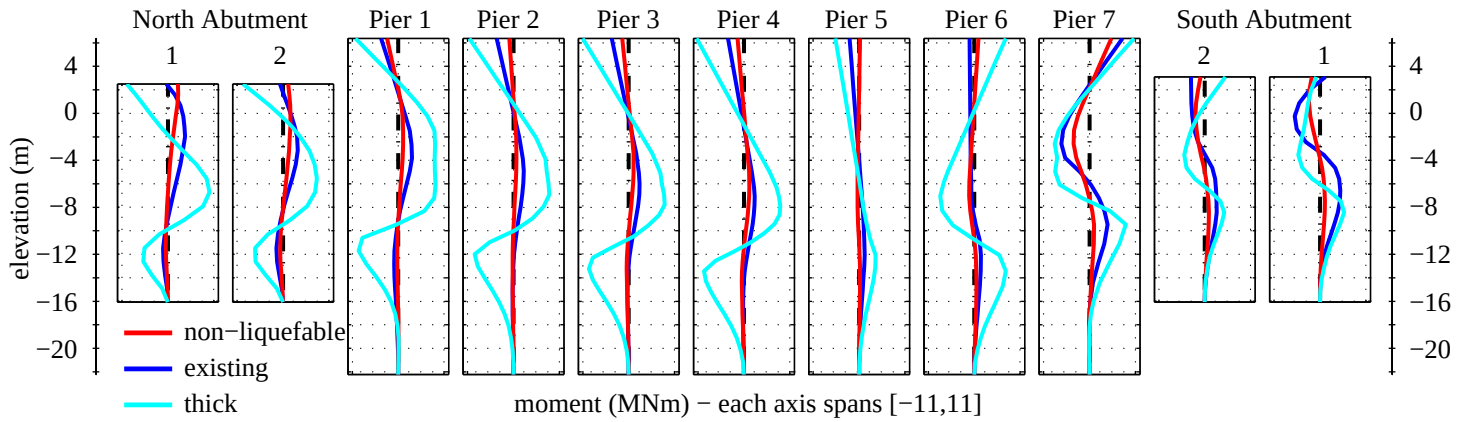

Figure 8.28: Residual bending moment profiles for three liquefaction conditions.

Based on the results for the three considered liquefiable layer configurations, it appears the layer configuration used in the idealized soil profile best represents the Puente Mataquito site response. The soil deformation in the absence of liquefaction is too minor in comparison to the site observations, while the shaft bending demands and deformations are too severe for the thickened liquefaction configuration. This small parameter study provides confidence that the idealized soil profile adequately describes the soil conditions at for the case study site.

8.3 Dynamic Plane Strain Analysis: Convento Viejo Ground Motion Record

The response of the Puente Mataquito soils to the Convento Viejo ground motion record are examined in order to gain an understanding of how the site may have responded during the Maule earthquake. It is important to establish whether or not the model predicts liquefaction to occur for this motion, and to determine the consequences of liquefaction if it does occur. This initial numerical study is used, along with the observations made during post-earthquake reconnaissance at the site, to inform the remainder of the numerical work for Puente Mataquito.

8.3.1 Global Soil Response

The residual soil deformation profiles are assessed to determine if the model predicts the development of lateral spreading due to the Convento Viejo motion. Figure 8.29 shows the residual horizontal and vertical displacement fields that exist after the ground motion has been applied to the model. As shown, the large horizontal soil deformation (> 3.0 m) occurs between the two abutments on the banks of the river and along the river bed. In comparison, relatively little horizontal deformation occurs behind the abutments, indicating that the bridge deck and foundations provided sufficient restraint. The residual vertical deformation is more uniform over the soil domain shown in Figure 8.29, with approximately 30 cm of downward displacement at the top of the embankment fill behind each abutment. The largest vertical deformations occur on the slopes of the river bank, and the horizontal and vertical soil deformation here causes the uplift of material on the southwest river bed.

The residual deformation profiles of Figure 8.29 suggest that lateral spreading has occurred due to liquefaction-induced loss of strength in the underlying soils, however, an examination of the pore pressure response in the soil is necessary to confirm this observation. Figure 8.30 shows a sequence of pore pressure ratio profiles during the application of the Convento Viejo motion. After 60 s, the material along the river bed has reached pore pressure ratios at or near 1.0, indicating that excess pore pressure has become approximately equal to the mean effective stress, and little strength remains in this region. At 120 s, the liquefiable material below the approach embankments display pore pressure ratios indica-

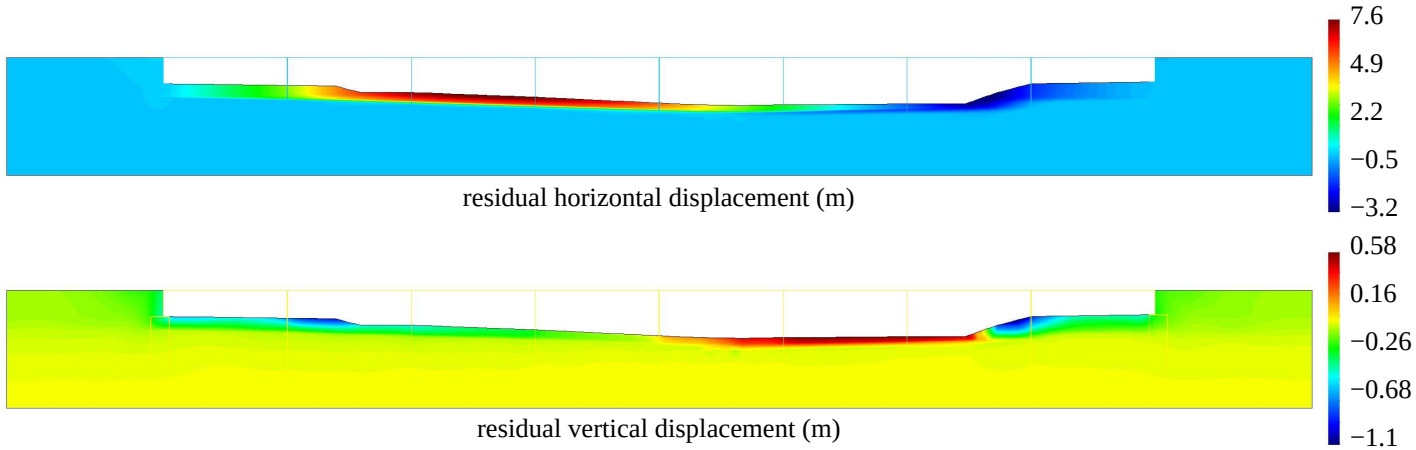

Figure 8.29: Residual horizontal and vertical displacement fields.

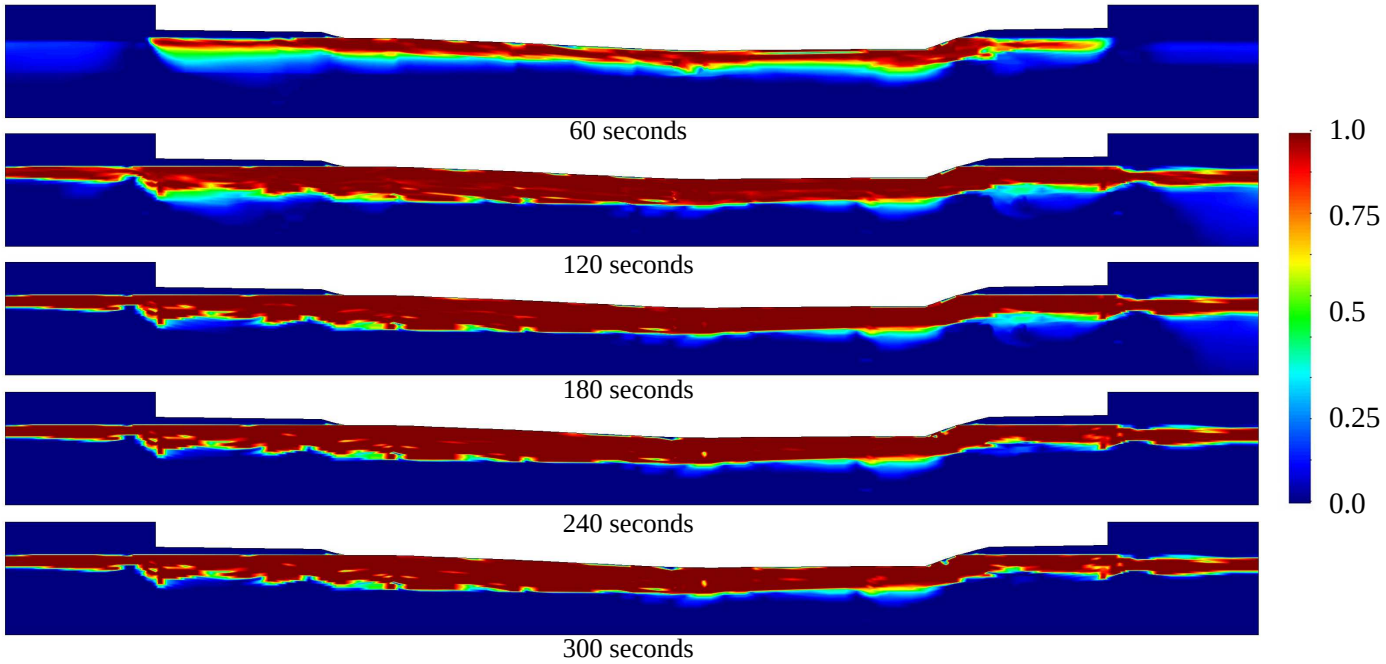

Figure 8.30: Progression of pore pressure ratio during analysis with Convento Viejo Motion.

tive of liquefaction, and this pore pressure ratio profile remains essentially constant for the remainder of the motion. Figure 8.31 shows the progression of horizontal soil deformation over the first 180 s of the motion. Lateral deformation between the abutments gradually increases over this portion of the motion, and essentially reaches a steady state value after 180 s with very little change over the remaining duration.

The pore pressure response of Figure 8.30 demonstrates a flaw in the modeling approach for this site and ground motion. When the elements in the liquefiable loose sand layer reach a strength state corresponding to $r_u \approx 1.0$, the elements deform such that the excess pore pressure does not dissipate as would be expected after the conclusion of the strong shaking in the ground motion record. The cause of this behavior is likely due to the numerical difficulty in capturing the build-up of excess pore pressure and corresponding soil shear strength loss due to the large number of high frequency cycles present in the Convento Viejo ground motion record. The results obtained using the Gilroy No. 1 record, which has a considerably lower frequency content, do not display this type of response for the same site geometry and element formulations. Additionally, this behavior is not isolated to the Q1-P1ssp element, as a secondary analysis using a standard Q1-P1 element displays a similar response.

The consequences of this undesirable element response are relatively minor in terms of the desired outcomes for this study. The absence of pore pressure dissipation likely increases the magnitude of the residual displacements in the model, however, the trends shown in the results are still valid. A soil deformation pattern and pore pressure response indicative of liquefaction-induced lateral soil deformation (lateral spreading) is evident in the results of Figures 8.29 through 8.31. Large lateral displacements in the soil in and adjacent to the river, and vertical slumping of the embankments are predicted by the model, corresponding with observations made at the site. Details of the response in the foundations and adjacent embankment fill obscured in this global view of the results are examined following discussion of the global structural response for the bridge.

8.3.2 Global Structural Response

The build-up of excess pore pressure and subsequent soil deformation observed in Figures 8.29 through 8.31 place kinematic demands on the bridge abutments and embedded shaft foundations. The residual displaced shapes of the shaft foundations for the bridge are shown in Figure 8.32, arranged to correspond with the spatial location of each pier and abutment shaft. The corresponding shear force and bending moment demands are shown in Figures 8.33 and 8.34. The extents of the liquefiable loose sand layer at each location are shown in gray in these plots. Though the soil deformation on the northeast bank is larger, Pier 7 displays the largest displacement demand of the interior piers. This makes sense in the context of the soil profile, as the large soil deformations on the northeast bank

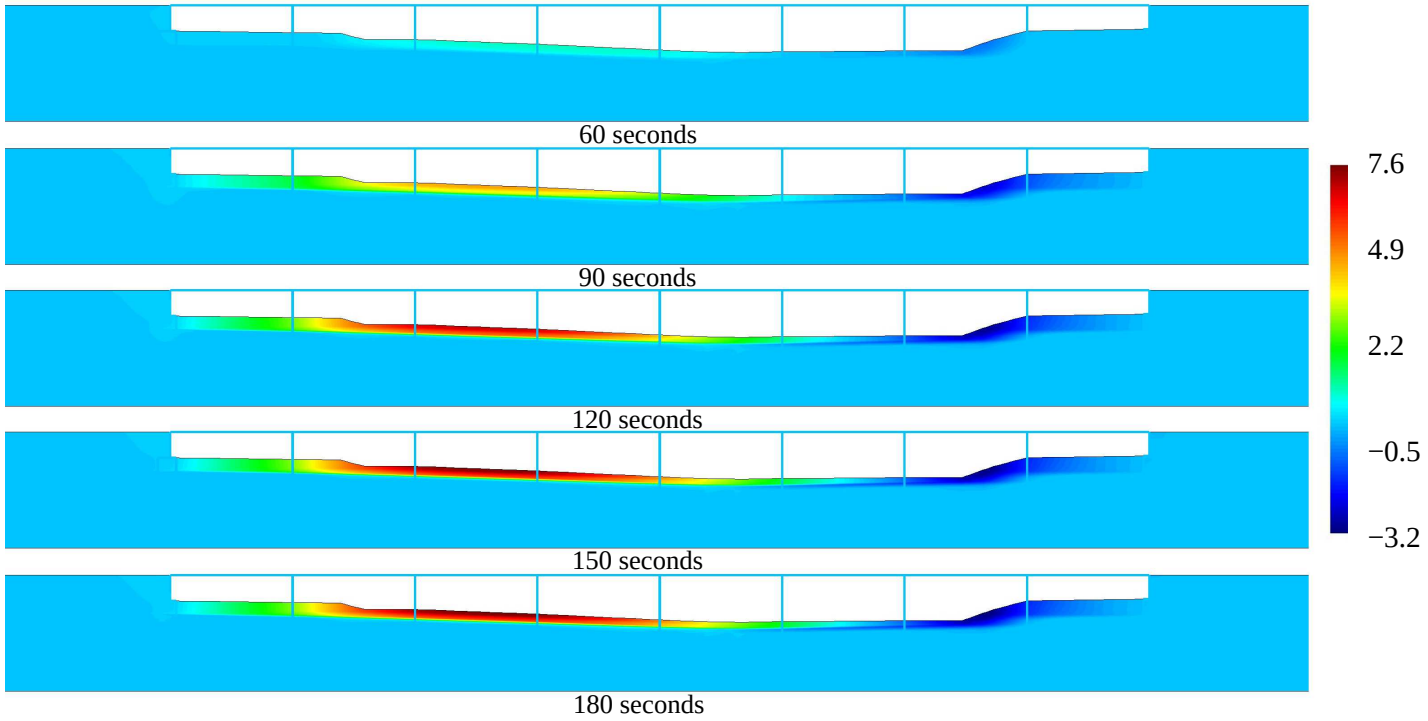

Figure 8.31: Progression of horizontal displacement during analysis with Convento Viejo motion.

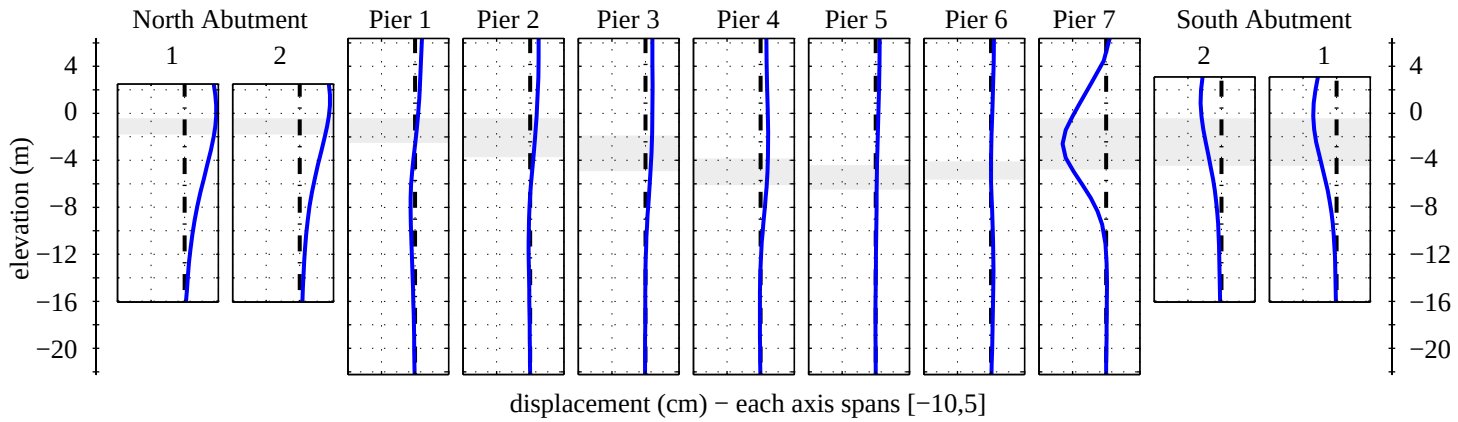

Figure 8.32: Residual shaft displacement profiles.

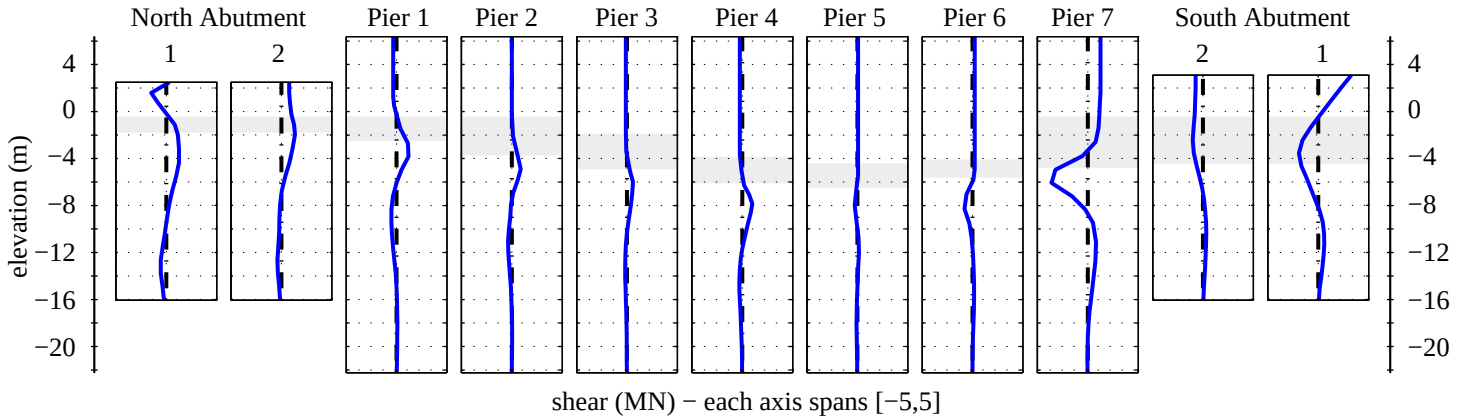

Figure 8.33: Residual shaft shear force profiles.

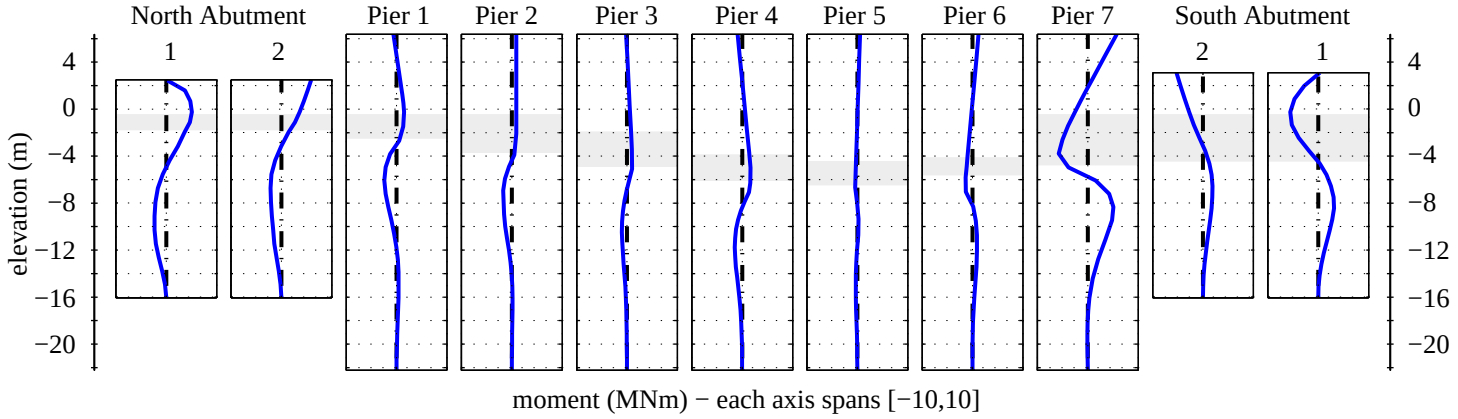

Figure 8.34: Residual shaft bending moment profiles.

Table 8.2: Maximum in-span displacement, shear force, and bending moment demands in abutment shaft foundations for Convento Viejo analysis.

shaft group	max disp (cm)	max shear (MN)	max moment (MN·m)
north abutment 1	4.7	1.5	5.1
north abutment 2	4.5	1.3	5.2
south abutment 1	3.5	1.0	5.3
south abutment 2	3.1	1.9	5.5

are shallow, indicating that the soil can flow around the piers, while the soil deformation on the southwest bank extends deeper and thus engages more resistance from the embedded foundation.

The abutments have similar maximum residual displacements, 4.7 cm at the northeast abutment and 3.5 cm at the southwest abutment, though slightly different mechanisms appear to govern their response. The shaft cap at northeast abutment tends to displace purely in a horizontal manner with only minor rotation, while the southwest shaft cap shows more rotation due to resistance from the bridge deck. These observations, along with the deformation patterns for the interior piers, which all exhibit positive displacement at the top, show that the entire bridge is translating in the positive x-direction (to the right in the plots). The moment and shear demands in the abutment shaft foundations are also reasonably similar, though, as shown in Table 8.2, the maximum in-span shear and moments are somewhat larger on the southwest side.

The observed shaft displacements correlate well with observations made at Puente Mataquito. Deformation of the northeast abutment was assumed to be around 5 cm based on superficial concrete cracking/spalling, and shear cracks in the cap for Interior Pier 1 suggest the river-ward displacement of this foundation. Measurable or visible deformation of the southwest abutment was not noted, however, displacement could have occurred without visible damage. The rotation of the southwest abutment observed in the model could also have reasonably occurred without attendant damage. Overall, it is encouraging that the trends observed in the plane strain model correlate roughly with observations made during the reconnaissance effort.

8.3.3 Abutment and Embankment Response

It is of interest to examine the response of the soil near the abutment foundations more closely in order to confirm observations made at the global level. Of particular interest is to assess the evidence of lateral spreading and associated embankment failure that may be obscured by the magnitude of the soil deformation along the river. Figure 8.35 shows the variation of pore pressure ratio with depth over the course of the motion in the soil behind the two abutments. Figures 8.36 and 8.37 show the spatial and temporal variation

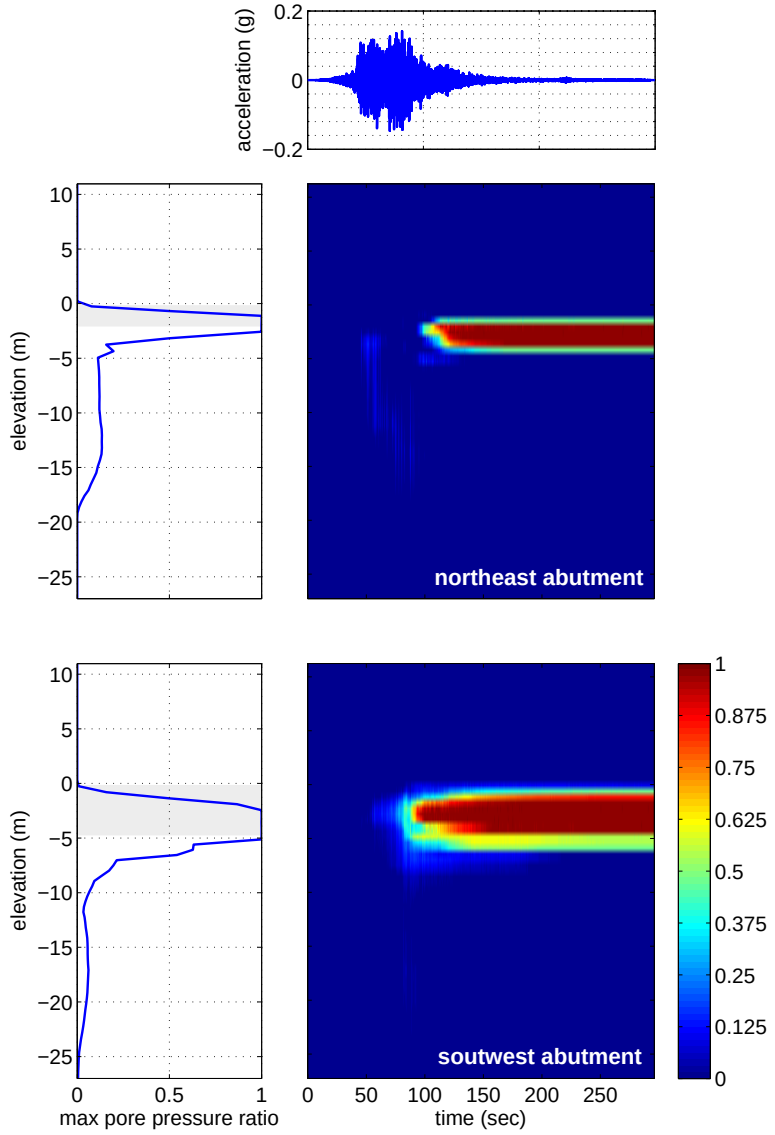

Figure 8.35: Spatial and temporal variation of pore pressure ratio in soil behind abutments.

of shear strain behind the northeast and southwest abutments, respectively. As shown in these plots, nearly half of the higher amplitude portion of the motion has elapsed before significant excess pore pressure begins to develop, with larger shear strains developing 10 to 20 s after the onset of liquefaction. As expected, the largest shear strains are found at the boundary of the liquefiable loose sand and denser sand layers.

To assess how the pore pressure ratio and shear strain profiles shown in Figures 8.35 through 8.37 are manifested as soil deformation, the displacement fields near the abutments are computed and plotted in Figure 8.38. In this plot, the size and color of the vectors indicate magnitude, and the directions of the vectors correspond with the direction of displacement. As shown, the primary component of embankment deformation is downward, and significant horizontal deformation is limited to the immediate vicinity of the abutment

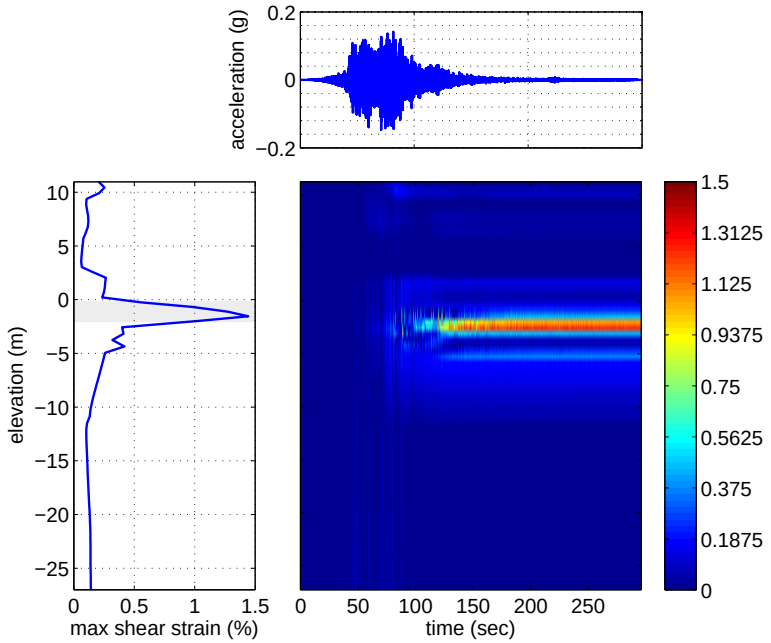

Figure 8.36: Spatial and temporal variation of shear strain in soil behind northeast abutment.

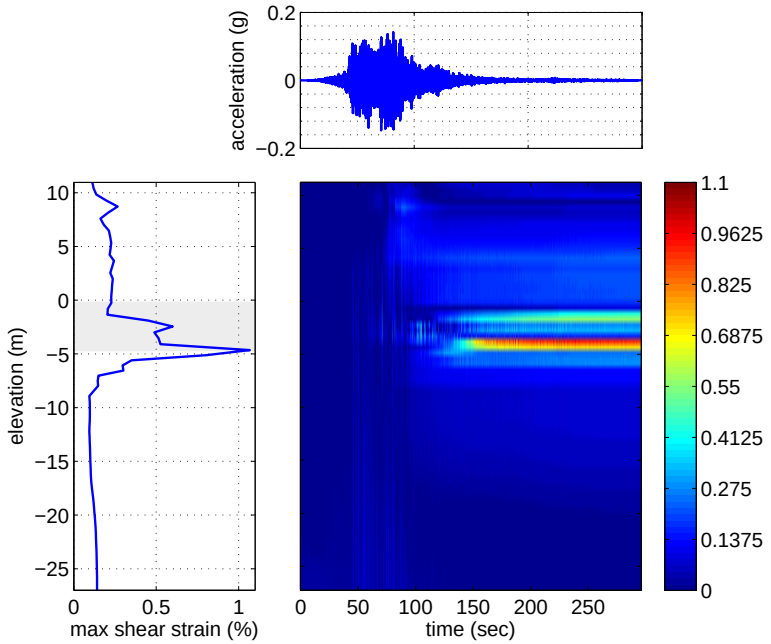

Figure 8.37: Spatial and temporal variation of shear strain in soil behind southwest abutment.

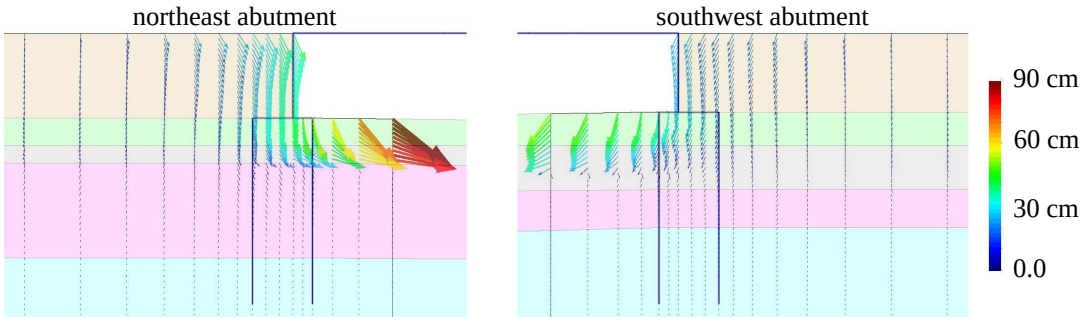

Figure 8.38: Residual displacement fields at abutments.

wall. Each of these displacement fields suggest the formation of a failure surface in the embankment, especially if the deformation in front of the abutments is considered as a part of the failure mass.

8.4 Summary

Two small parameter studies performed using the Gilroy No. 1 ground motion record have demonstrated the effects of soil element thickness and liquefiable layer configuration on the response of the Puente Mataquito plane strain model. This work has established the importance of defining a soil domain that has sufficient mass in comparison to foundation stiffness, and determined that for the site conditions used in the model, a 90 m thick soil domain appeared to be the most applicable definition for the continuum elements in this model. This work also verified that the liquefiable layer definition assumed in the idealized soil profile appropriately reflects the site conditions based on a comparison of the results in the model with observations made at the bridge site.

The results of the Convento Viejo analysis establish the susceptibility of the site to liquefaction for a ground motion that is representative of that experienced by the bridge, demonstrate that the plane strain model is able to predict trends that correspond to physical observations made at the site, demonstrate some of the mechanisms leading to liquefaction and lateral spreading, and reveal the consequences of these phenomena. Based on these results, both bridge abutments appear to be strong candidates for future study using a combination of the pile pinning approach and a 3D finite element model, but since only one will be considered, the southwest abutment is selected for further inspection. Both the Gilroy and Convento Viejo analyses predict liquefaction and attendant lateral soil deformation at this location, and the Convento Viejo analysis reveals a more interesting deformation mechanism with the rotation of the shaft cap observed at the southwest abutment. The interaction of the bridge deck, abutment walls, and shafts during lateral spreading has been identified as an important factor in determining the structural response during this type of event (Franke, 2011), a 3D model of this abutment will allow for a detailed study of these effects.

Chapter 9

SIMULATION AND ASSESSMENT OF EFFECTS OF LATERAL SPREADING ON SOUTHWEST ABUTMENT TO PUENTE MATAQUITO

The dynamic plane strain models discussed in the previous chapter confirmed the susceptibility of the site to both liquefaction and lateral spreading, and identified the southwest abutment for use in further evaluation of the effects of lateral spreading on bridge foundations. Two very distinct methods are used for this purpose: (1) the pile pinning analysis procedure adopted by Caltrans (2011) involving a combination of a BNWF model of the foundation and a slope stability model of the site, and (2) a series of 3D finite element models of the grouped shaft foundation, abutment, and surrounding soils. The results obtained through the application of these modeling approaches to the southwest abutment are presented and analyzed following discussions on the development of the necessary numerical models.

9.1 Pile Pinning Model Development

The pile pinning model of the southwest bridge abutment is created following the Caltrans (2011) procedure for the restrained ground displacement case presented in Section 5.1. This model is considered in order to assess the viability of this design approach through comparison with the observations made at the bridge site and the bending demands resulting from 3D finite element models. To this purpose, a BNWF model of the foundation is developed by converting the 4×2 pile group (Figure 7.11) into an equivalent single shaft model, and through the definition of soil-shaft interaction (p-y) curves that appropriately represent the idealized soil profile and account for group effects. In addition to this BNWF model of the foundation, a limit equilibrium slope stability model is developed for use in determining the compatible force-displacement state which defines the final design displacement in the pile pinning approach.

9.1.1 Development of Foundation Model

The southwest abutment foundation is converted into an equivalent beam model using the Caltrans recommendations for the pile pinning analysis procedure. Two versions of the equivalent beam model are created, one which considers a linear elastic shaft response, and one which considers the nonlinear section response of the shaft foundations. The properties

Table 9.1: Properties of linear elastic equivalent beam model for grouped shaft foundation.

Parameter	Single Shaft	Equivalent Shaft
E	21.3 GPa	21.3 GPa
I	0.2485 m^4	1.988 m^4
A	1.7671 m^2	14.137 m^2
G	8.52 GPa	8.52 GPa

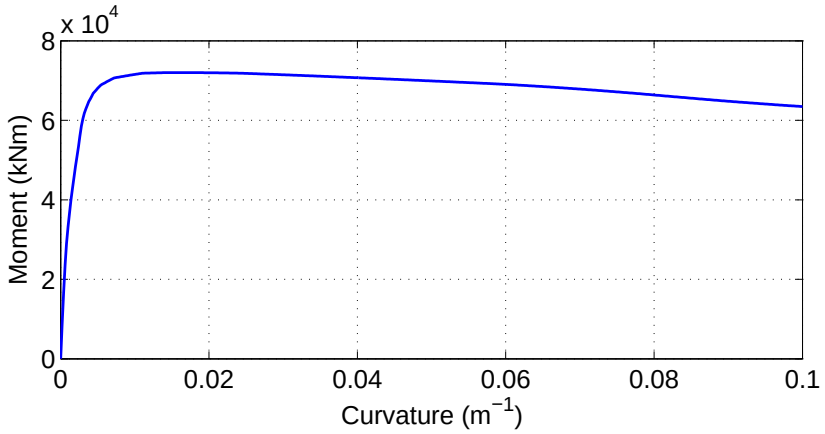

Figure 9.1: Model moment-curvature response for nonlinear equivalent beam model of grouped shaft foundation.

of the equivalent linear elastic shaft section are determined using the geometry of the shaft and the initial bending stiffness indicated in the moment-curvature plot of Figure 7.10, which, for a single shaft, is $EI = 5.295$ GN·m^2. A gross second moment of the area for a single shaft, $I_g = 0.2485$ m^4, suggests an elastic stiffness $E = 21.3$ GPa, and, for an assumed Poisson's ratio $\nu = 0.25$, a shear stiffness $G = 8.52$ GPa. The section parameters for a single shaft are scaled by the number of shafts in the group to obtain values for use in the equivalent beam model. The properties of this linear elastic equivalent beam model are provided in Table 9.1. The nonlinear equivalent beam model is defined by scaling the single shaft moment-curvature response by the number of shafts in the group, resulting in the equivalent beam model moment-curvature response shown in Figure 9.1. The stiffness of the shaft group is likely underrepresented by the scaling approach adopted for use by Caltrans, however, the intention of this study is an evaluation of the approach, thus, the modeling recommendations involved in its use are followed here.

A rotational spring is used to simulate the rotational stiffness of the shaft cap following the procedure of Mokwa and Duncan (2003). For an axial load of $P = 4120$ kN, and assuming that the axial capacity is achieved with 0.25 in of vertical displacement, the axial

stiffness for a single pile is computed as

$$k_a = \frac{0.75 \cdot 4120 \text{ kN}}{0.0063 \text{ m}} = 490 \text{ MN/m} \tag{9.1}$$

The rotational stiffness for the pile group is based on the number of rows in the shaft cap, n_{row}, the number of shafts in each row, n_{pile}, and the distance from the center of the row to the center of the shaft cap, d_c, as

$$k_\theta = n_{\text{row}} n_{\text{pile}} d_c^2 \, k_a \tag{9.2}$$

For the geometry of the abutment group at Puente Mataquito,

$$k_\theta = 2 \cdot 4 \cdot (3 \text{ m})^2 \cdot 490 \text{ MN/m} = 35.3 \text{ GN} \cdot \text{m} \tag{9.3}$$

This rotational spring is applied to the equivalent beam model at the location of the shaft cap. Above this point, the beam model is given a bending stiffness that is many times larger than the rest of the beam in order to incorporate the abutment into the equivalent beam model. This relatively rigid abutment portion of the beam is assigned linear elastic behavior for both the linear elastic and nonlinear equivalent beam models.

It should be noted that the equivalent beam models defined using the Caltrans (2011) procedure under-represent the bending stiffness of the pile group, which should fall somewhere between the values reported above and the assumption that the group acts as a single beam during the application of lateral loads. The addition of the rotational spring to the model provides some compensation, but even with this spring, the equivalent model may represent an oversimplification of the true foundation response.

9.1.2 Definition of p-y Curves

In the BNWF model, the soil response is represented by a series of *p-y* curves defined based on the idealized soil profile with the properties presented in Table 7.1. These curves are defined with ultimate lateral resistance, p_u, values computed using the method of Brinch Hansen (1961) and initial stiffness, k_T, values computed using the API (2007) recommendations corrected for overburden stress after Boulanger et al. (2003).

Group effects are incorporated into the BNWF model using the group efficiency factors of Mokwa and Duncan (2001) and the procedure recommended by Caltrans (2011). The efficiency factors for the leading and trailing rows are 0.88 and 0.67, respectively. The group effect *p*-multiplier for the equivalent shaft model is computed as the product of the number of piles with the average of the leading and trailing row values

$$p_{\text{group}} = \frac{8 \cdot (0.88 + 0.67)}{2} = 5.88 \tag{9.4}$$

The residual strength of the liquefiable soil is computed using the undrained shear strength expression recommended by Ledezma and Bray (2010)

$$\frac{S_{ur}}{\sigma'_v} = \exp\left(\frac{N_{1,60\ \mathrm{cs}}}{8} - 3.5\right)\left(1 + \frac{\left(0.3N_{1,60\ \mathrm{cs}}\right)^2}{128}\right) \qquad 0 \le N_{1,60\ \mathrm{cs}} \le 20 \qquad (9.5)$$

where S_{ur} is the undrained shear strength, σ'_v is the vertical effective stress, and $N_{1,60\ \mathrm{cs}}$ is the clean sand corrected SPT blowcount. This expression is a weighted average of the procedures proposed by Seed and Harder (1990), Olson and Stark (2002), Kramer (2008), and Idriss and Boulanger (2007). The undrained shear strength is used to define the p_u values of the *p-y* curves within the liquefiable loose sand layer, and is computed using the average SPT value assumed for this layer when defining the idealized soil profile of the site. Using this approach, the average undrained strength for the layer is 11.7 kPa, and the undrained strength varies with overburden pressure as $S_u/\sigma'_v = 0.11$. A linear smearing is used to reduce the p_u values for the *p-y* curves within one shaft diameter of the liquefiable layer boundaries per the recommendations of Caltrans (2011) and Ashford et al. (2011).

9.1.3 Definition of Abutment-Soil Interaction Curve

A tri-linear force-displacement curve is used to model abutment-embankment interaction in the BNWF model. As shown in Figure 5.3, this tri-linear curve is defined in terms of two variables, the ultimate passive force and the displacement at which this force is assumed to be fully developed. Using the geometry and properties of the embankment fill assumed for the idealized soil profile of the site, an ultimate lateral force $F_{\mathrm{ult}} = 94$ MN is computed assuming the development of a Rankine passive wedge at a displacement of $\Delta_{\max} = 0.51$ m.

9.1.4 Pseudostatic Slope Stability Model

The determination of the compatible force-displacement design state for the restrained ground displacement case requires the comparison of the results obtained from a pushover analysis of the BNWF model described in the preceding sections with the results of a slope stability analysis of the abutment site. For this purpose, a pseudostatic slope stability model is developed using Slide 6.0 (Rocscience, 2010) for the geometry and properties assumed in the idealized soil profile. This model is used to compute the horizontal resisting force required at the center of the liquefiable layer to reach a factor of safety FS = 1.0 for a series of horizontal yield accelerations $k_y = 0.05$, 0.1, 0.15, 0.2, 0.25, 0.3, 0.35, 0.4.

To assess the sensitivity of the final design result to choices made during the analysis steps, several versions of this model are developed and analyzed. Two limit equilibrium methods are considered, the simplified Bishop method (Bishop, 1955) and the simplified Janbu method (Janbu, 1973). The failure surfaces are restricted such that they do not

extend more than four times the embankment thickness behind the abutment to eliminate complex effects related to a very large slide mass per the suggestion of Ashford et al. (2011). Four cases are considered for each limit equilibrium approach:

- $F_{\text{deck}} = 0$ kN/m with constant $S_u = 11.7$ kPa in the liquefiable layer.
- $F_{\text{deck}} = 377$ kN/m with constant $S_u = 11.7$ kPa in the liquefiable layer.
- $F_{\text{deck}} = 0$ kN/m with $S_u/\sigma'_v = 0.11$ in the liquefiable layer.
- $F_{\text{deck}} = 377$ kN/m with $S_u/\sigma'_v = 0.11$ in the liquefiable layer.

The non-zero F_{deck} value is determined from the full passive resistance of the embankment fill acting over the 2.74 m depth of the bridge deck, and is applied at the centroid of the bridge deck/girder cross-section. The constant undrained strength values are the average value for the layer, and the overburden dependent values correspond to the SPT profiles assumed for the idealized soil profile.

9.2 Application of Pile Pinning Analysis Procedure to Southwest Abutment

The BNWF equivalent shaft foundation and limit equilibrium slope stability models developed for the southwestern abutment of Puente Mataquito are used to determine compatible force-displacement states for the bridge abutment and approach embankment. The viability of this design approach is assessed through comparison with observations made at the site, and in subsequent sections, with the structural demands resulting from plane strain and 3D models of the bridge. The variability in the estimated compatible state is demonstrated by considering various modeling decisions and assumptions throughout the procedure, and an approach for estimating an appropriate compatible state amidst the observed variability is proposed.

9.2.1 Initial Pushover Analysis of Foundation Model

The equivalent shaft BNWF model of the southwestern abutment is analyzed in a pushover analysis simulating the kinematic demands of lateral spreading. As discussed in Section 5.1.1, this pushover analysis is conducted by applying a set displacement profile to the soil end of the *p-y* springs supporting the foundation. The applied displacement profile used for this purpose is set at a constant 1.0 m in the upper layers, linearly-increasing from zero to 1.0 m across the liquefiable layer, and zero in the underlying material as shown in Figure 9.2.

The purpose of this analysis is to obtain a curve defining the relationship between the applied surface displacement and the foundation shear force at the center of the liquefiable

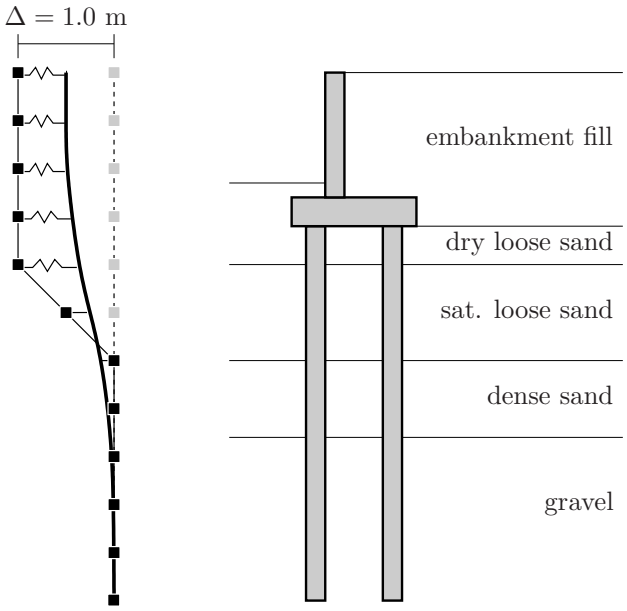

Figure 9.2: Applied displacement profile for equivalent shaft BNWF model of Puente Mataquito southwestern abutment.

loose sand layer. The unmodified shear force, V_{unmod}, recorded at this location for each step in the analysis is used to compute a corresponding running average shear force, V_{run}, which, at recorded step j, is computed as

$$V_{\text{run}}(j) = \frac{\sum_{i=1}^{j} V_{\text{unmod}}(j)}{j} \tag{9.6}$$

This running average shear force, introduced by Boulanger et al. (2006), is recommended for use in subsequent analysis steps to account for a discrepancy in how the force in the middle of the liquefied layer is treated in the pushover and slope stability phases of the procedure. In the current work, the unmodified and running average values are both considered in order to assess how each definition affects the compatible force-displacement state determined at the end of the procedure.

9.2.2 Slope Stability and Deformation Analysis

The slope stability model is used to compute the horizontal resisting force required at the center of the liquefiable loose sand layer to reach a factor of safety FS = 1.0 for a series of horizontal accelerations. As discussed in Section 9.1.4, several configurations of this model are considered in order to assess the sensitivity of the results to different modeling decisions. Table 9.2 shows the foundation resisting force values determined for each slope

Table 9.2: Foundation resisting forces (in kN/m) necessary to reach FS = 1.0.

	constant S_u				varying S_u			
	$F_{\text{deck}} = 0$		$F_{\text{deck}} = 377$ kN/m		$F_{\text{deck}} = 0$		$F_{\text{deck}} = 377$ kN/m	
k_y (g)	Bishop	Janbu	Bishop	Janbu	Bishop	Janbu	Bishop	Janbu
0.05	25	136	45	0	0	42	45	0
0.10	192	403	55	38	0	88	46	0
0.15	426	716	223	340	65	344	48	0
0.20	697	1047	476	695	290	649	87	272
0.25	973	1321	747	1039	571	996	339	619
0.30	1229	1693	1025	1325	865	1341	624	986
0.35	1511	1884	1286	1643	1216	1639	919	1352
0.40	1913	2201	1602	1911	1627	1982	1314	1651

stability analysis approach (Bishop, 1955; Janbu, 1973) with various model parameters.

As expected, using a variable strength in the liquefiable layer or a non-zero deck resistance requires less foundational resistance to achieve FS = 1.0 than the corresponding cases with constant S_u or $F_{\text{deck}} = 0$. An interesting aspect of the results in Table 9.2 is that the choice of analysis method makes a significant difference in the stabilizing force returned for a given yield acceleration. In general, the Janbu approach returns larger forces for a given combination of k_y, F_{deck}, and S_u than those computed using the Bishop approach. With $F_{\text{deck}} = 377$ kN/m, the passive force of fill acting over the depth of the bridge deck, the Bishop approach appears to have issues at lower yield accelerations, especially for the variable S_u cases, as the required resisting forces are larger than for $F_{\text{deck}} = 0$.

The displacements necessary for determination of the compatible state for the foundation are estimated using a Newmark rigid sliding block approach for each considered acceleration value. The predictive model of Bray and Travasarou (2007) is used for this purpose. Using this model, the nonzero displacement d in centimeters can be estimated for the Newmark rigid sliding block case as

$$\begin{aligned}\ln(d) = &-0.22 - 2.83\ln(k_y) - 0.333(\ln(k_y))^2 + 0.566\ln(k_y)\ln(\text{PGA}) \\ &+ 3.04\ln(\text{PGA}) - 2.44(\ln(\text{PGA}))^2 + 0.278(M-7) \pm \epsilon \end{aligned} \tag{9.7}$$

where PGA is the peak ground acceleration of the ground motion, M is the moment magnitude of the event, and ϵ is a normally distributed random variable with zero mean and a standard deviation of 0.66. The variability in this estimated displacement is considered by computing the 16 and 84% exceedance values from (9.7), thus establishing a range of estimated displacement values for each foundation resisting force. Because the standard deviation for the natural logarithm of displacement is 0.66, these values are computed as as $d_{16\%} = \exp(d - 0.66)$ and $d_{84\%} = \exp(d + 0.66)$, respectively. Table 9.3 lists the 16%, mean, and 84% displacements estimated from (9.7) using the magnitude, $\text{M}_w = 8.8$, and

Table 9.3: Displacements estimated using Bray and Travasarou (2007) procedure.

k_y (g)	$d_{16\%}$ (cm)	d (cm)	$d_{84\%}$ (cm)
0.05	42.0	80.9	155.9
0.10	13.8	26.8	51.6
0.15	3.9	10.9	22.3
0.20	0.0	3.3	9.8
0.25	0.0	0.0	3.8
0.30	0.0	0.0	0.0
0.35	0.0	0.0	0.0
0.40	0.0	0.0	0.0

peak ground acceleration, PGA = 0.4 g, of the 2010 Maule event.

9.2.3 Determination of Compatible Force-Displacement State

The foundation displacement used for design purposes is determined by finding the compatible state indicated by the initial foundation pushover and slope stability/deformation analyses. This is accomplished by plotting the force-displacement data returned from each analysis type and noting the intersection of the two curves. The foundation resisting force values determined in the slope stability analysis represent the resisting force per unit width of soil, thus, in order to compare the two data sets, the shear force values computed in the pushover analysis must be divided by an appropriate width. Two widths are considered for this purpose, the embankment crest width, $w = 12.4$ m, taken from the actual geometry at Puente Mataquito, and the tributary embankment width, $w_t = 19.9$ m, computed per the recommendations of Boulanger et al. (2006) (see Figure 5.6 for further information).

Figure 9.3 shows the compatibility plots for pushover curves defined with both the running average and unmodified shear forces, V_{run} and V_{unmod}, respectively, scaled by w and w_t and slope stability/deformation curves computed using the Janbu method with overburden dependent strength in the liquefiable layer and $F_{\text{deck}} = 377$ kN/m. The curve for the mean displacement, d, is shown as a solid line, and the $d_{16\%}$ and $d_{84\%}$ curves are shown as dashed lines. The compatible states resulting from the same set of parameters, but with the Bishop method of slope stability analysis, are shown in Figure 9.4. These plots represent only a portion of the considered cases, however, they provide and example of how the compatible state is determined for actual data, and demonstrate the variability of the compatible state for a series of modeling decisions. Tables 9.4 and 9.5 provide the compatible displacement values determined for each considered combination of model parameters. The maximum values for $F_{\text{deck}} = 0$ and $F_{\text{deck}} \neq 0$ and the minimum overall value are highlighted. The boxed values represent the range of displacements corresponding to the modeling decisions recommended by Martin et al. (2002) as modified by Boulanger et al. (2006) and Ashford et al. (2011).

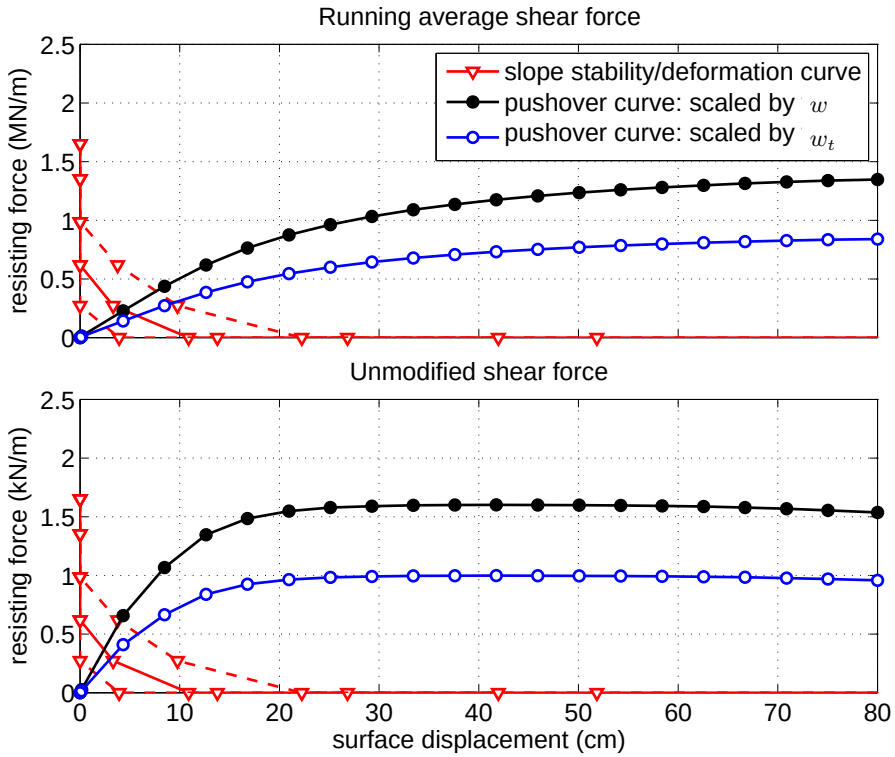

Figure 9.3: Compatible force-displacement states using the Janbu (1973) method for slope stability analysis with a varying S_u in the liquefied layer and $F_{\text{deck}} = 377$ kN/m.

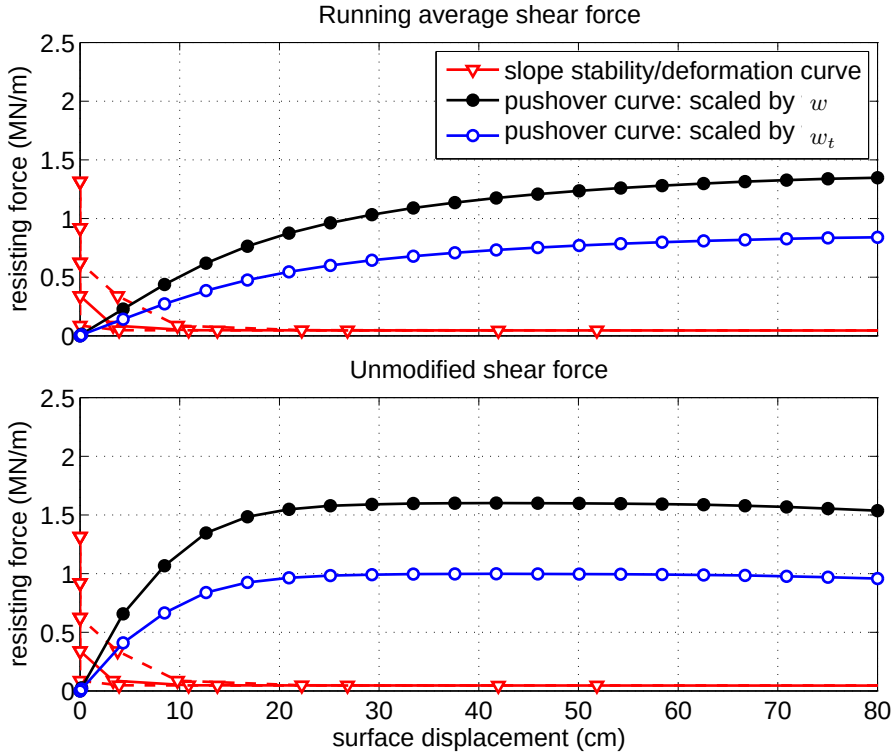

Figure 9.4: Compatible force-displacement states using the Bishop (1955) method for slope stability analysis with a varying S_u in the liquefied layer and $F_{\text{deck}} = 377$ kN/m.

Table 9.4: Compatible displacements (in cm) for various pushover and slope stability/deformation curves using the method of Janbu (1973).

16^{th} percentile displacements – $d_{16\%}$

	$F_{\text{deck}} = 0$		$F_{\text{deck}} = 377$ kN/m	
pushover curve	constant S_u	varying S_u	constant S_u	varying S_u
V_{run}/w	10.3	5.7	5.6	2.2
V_{run}/w_t	13.6	7.7	7.3	2.6
V_{unmod}/w	4.7	2.8	2.9	1.2
V_{unmod}/w_t	7.5	3.8	3.8	1.7

mean displacements – d

	$F_{\text{deck}} = 0$		$F_{\text{deck}} = 377$ kN/m	
	constant S_u	varying S_u	constant S_u	varying S_u
V_{run}/w	13.8	8.5	8.7	4.4
V_{run}/w_t	20.2	11.0	10.9	5.7
V_{unmod}/w	6.8	4.1	4.3	2.4
V_{unmod}/w_t	10.3	6.3	6.5	3.1

84^{th} percentile displacements – $d_{84\%}$

	$F_{\text{deck}} = 0$		$F_{\text{deck}} = 377$ kN/m	
	constant S_u	varying S_u	constant S_u	varying S_u
V_{run}/w	18.6	12.1	12.6	7.6
V_{run}/w_t	29.2	16.8	17.2	9.4
V_{unmod}/w	8.8	6.3	6.6	4.0
V_{unmod}/w_t	15.5	9.1	9.5	5.8

Table 9.5: Compatible displacements (in cm) for various pushover and slope stability/deformation curves using the method of Bishop (1955).

16^{th} percentile displacements – $d_{16\%}$

	$F_{\text{deck}} = 0$		$F_{\text{deck}} = 377$ kN/m	
pushover curve	constant S_u	varying S_u	constant S_u	varying S_u
V_{run}/w	6.9	2.6	4.2	1.3
V_{run}/w_t	9.4	3.2	5.9	2.0
V_{unmod}/w	3.2	1.4	2.2	0.5
V_{unmod}/w_t	4.4	1.9	3.0	0.8

mean displacements – d

	$F_{\text{deck}} = 0$		$F_{\text{deck}} = 377$ kN/m	
	constant S_u	varying S_u	constant S_u	varying S_u
V_{run}/w	9.4	4.7	6.9	2.6
V_{run}/w_t	13.1	6.3	9.0	3.1
V_{unmod}/w	4.4	2.4	3.2	1.5
V_{unmod}/w_t	6.9	3.2	4.7	2.0

84^{th} percentile displacements – $d_{84\%}$

	$F_{\text{deck}} = 0$		$F_{\text{deck}} = 377$ kN/m	
	constant S_u	varying S_u	constant S_u	varying S_u
V_{run}/w	12.9	7.6	9.6	5.3
V_{run}/w_t	18.6	9.5	13.4	6.7
V_{unmod}/w	6.3	3.8	4.8	2.7
V_{unmod}/w_t	9.5	5.6	7.3	3.7

There is significant variability in the compatible displacements for the different combinations of slope stability modeling decisions and pushover curve definition techniques. Estimated displacements range from 0.5 to 29.2 cm over the full spectrum of considered cases, and from 0.5 to 17.2 cm for those cases that consider the resistance provided by the bridge deck. This variability is apparent within the context of the boxed values in Tables 9.4 and 9.5, which range from 3.1 to 10.9 cm. Even if the scope of the study is restricted to the mean displacement cases with overburden dependent strength for the liquefied layer, as shown in Figures 9.3 and 9.4, there is variability depending on the particular slope stability analysis procedure used in the slope stability/deformation analysis.

Figures 9.5 shows the compatibility plot for all of the considered cases and 9.6 shows the compatibility plot for only the $F_{\text{deck}} \neq 0$ cases. The shaded portions of these plots represent the range of compatible displacements implied by the application of the procedure to the Puente Mataquito southwest abutment foundation and approach embankment. It is not practical to assess the foundation performance at all of the compatible states shown in these plots, however, a range of structural demands can be obtained through consideration of the minimum and maximum estimated displacements, and the average structural demands can be estimated by defining an average compatible displacement value. In order to determine a single displacement that is representative of each data set, the centroid of the shaded areas defined in the compatibility plots are computed and plotted as solid dots in Figures 9.5 and 9.6. The average displacement states computed with this approach are 11.4 cm for the full data set and 7.5 cm for the $F_{\text{deck}} \neq 0$ cases. The latter value corresponds well with the boxed displacement values of Tables 9.4 and 9.5.

9.2.4 Assessment of Foundation Performance

With a range of compatible displacements defined using the results of the initial pushover and slope stability/deformation analysis phases, the final step in the pile-pinning analysis procedure is the assessment of the foundation performance at the compatible displacement. This is accomplished using a pushover analysis with the equivalent shaft BNWF model where the applied surface displacement is set equal to the minimum, average, and maximum compatible displacement values discussed in the previous section and shown in Figures 9.5 and 9.6. Consideration of these values defines a range of estimated foundation demands that can be compared to the observed site displacements as well as the results of the 3D foundation model.

The shaft displacement profiles, shear force diagrams, and bending moment diagrams resulting from lateral spreading pushover analyses of the BNWF model for each considered surface displacement are shown in Figures 9.7 and 9.8. The shear forces and bending moments in these plots are average shaft values computed by dividing the demands returned by the equivalent foundation model by the number of shafts in the group. As expected,

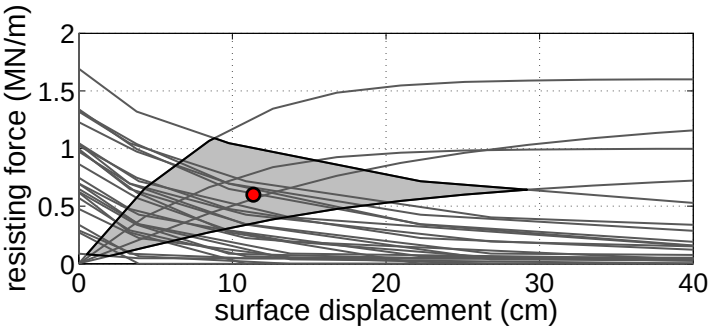

Figure 9.5: Variability in compatible state for all considered cases.

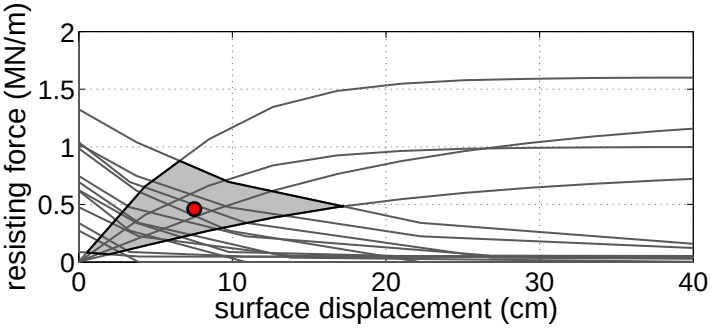

Figure 9.6: Variability in compatible state for cases with $F_{\text{deck}} \neq 0$

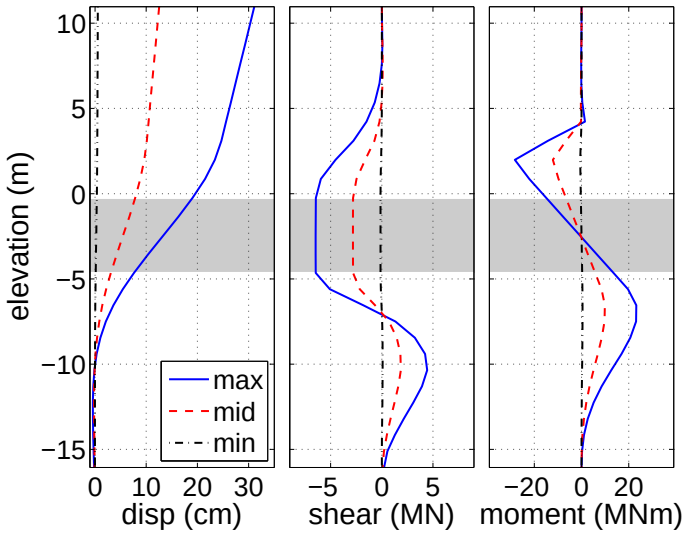

Figure 9.7: Shaft displacement, shear, and moment demands for minimum (0.5 cm), mean (11.4 cm), and maximum (29.2 cm) compatible states for full data set.

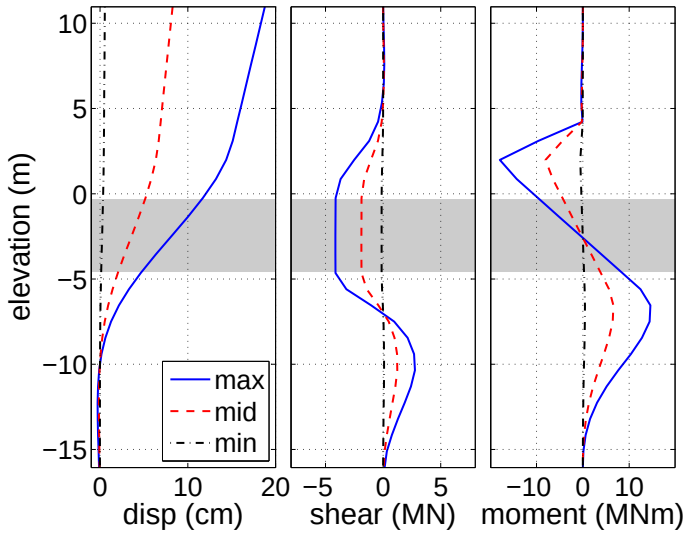

Figure 9.8: Shaft displacement, shear, and moment demands for minimum (0.5 cm), mean (7.5 cm), and maximum (17.2 cm) compatible states for $F_{\text{deck}} \neq 0$ data set.

the wide range of compatible displacements results in a wide range of estimated foundation demands, with larger applied displacements leading to larger shear and moment demands. Table 9.6 provides the maximum shaft displacement, shear force, and bending moment returned by the foundation model for each compatible displacement value.

Aside from the 0.5 and 7.5 cm cases, the maximum moments returned from this study are in excess of the 9.0 MN·m design capacity for the Puente Mataquito shaft foundations. Of the considered displacements, the average for the $F_{\text{deck}} \neq 0$ cases, 7.5 cm, is the most representative of the recommendations of Martin et al. (2002), Boulanger et al. (2006), and Ashford et al. (2011). It is encouraging that the foundation performance for this displacement correlates at least roughly with the observed foundation performance under lateral spreading. Observations at the southwest abutment indicated little or no lateral displacement of the abutment, which suggests that the shafts were able to restrain the movement of the foundation while remaining primarily in the elastic regime. For a 7.5 cm applied displacement, the BNWF model suggests shaft performance in line with the likely foundation behavior, with the shafts approaching but not reaching the plastic moment capacity. The estimated and reported abutment displacements are not in direct agreement, however, the estimated displacement is small enough for the bridge to have experienced while sustaining little visible damage, and as discussed in Section 6.2 the abutment displacement may have been underreported.

The discrepancy between the foundation demands for the average displacements resulting from full data set and the $F_{\text{deck}} \neq 0$ data set highlights the importance of the lateral resistance provided by the bridge deck in determining the foundation response to the kinematic demands of lateral spreading. This is evident in the results of this analysis, as the

Table 9.6: Maximum shaft displacement, shear, and moment demands for five considered compatible soil displacement states.

compatible disp	max disp (cm)	max shear (MN)	max moment (MN·m)
0.5 cm	0.55	0.13	0.54
7.5 cm	8.3	1.88	8.06
11.4 cm	12.5	2.82	12.11
17.2 cm	18.8	4.14	17.92
29.2 cm	31.1	6.47	28.20

inclusion or omission of F_{deck} in the slope stability analysis phase significantly changes the compatible displacement state, and is confirmed by the results from the 3D model of the southwest abutment discussed in the following sections. The inclusion of the bridge deck resistance as a constant force equal to the full passive resistance of soil acting over the area of the deck is a convenient approach, but the full passive force may not develop for all displacements and this practice may overestimate the lateral resistance provided by the bridge deck. Additionally, other site-specific factors may affect the available lateral deck resistance. Expansion gaps are typically included at the connection of the deck to the abutment, and a certain amount of displacement must occur before significant deck resistance is available. It is also possible for the deck to become unseated at larger displacements and, as discussed by Franke (2011), the factors leading to this response are obscure, as similarly constructed bridges have displayed opposing deck behavior for similar lateral spreading demands.

Further research is necessary to fully understand all of the factors contributing to the available deck resistance during lateral spreading, however, there are simpler approaches that can be incorporated into the pile pinning analysis procedure to consider the uncertainty in the contribution of the deck resistance to the compatible displacement for the foundation. One such approach is the use of a running average shear force in the definition of the pushover curve as proposed by Boulanger et al. (2006). The use of this technique adds some conservatism to the final result by lowering the pushover curve, which returns a larger compatible displacement than would be estimated for an unmodified shear force. Another approach is the consideration of multiple compatible states for which F_{deck} is set to both zero and nonzero values. The pushover and slope stability analyses used in this design procedure are relatively inexpensive in terms of time and computational effort, therefore, performing them multiple times is feasible in practice. The range of compatible displacements resulting from this approach can be used to determine a final displacement estimate, perhaps similar to the centroidal approach discussed above, or to define a range of foundation demands for use in design.

9.3 3D Finite Element Model Development

3D finite element models are created to analyze the response of the southwest approach embankment, abutment, and grouped shaft foundation to the kinematic demands of lateral spreading. A schematic of the considered domain for the southwest abutment model is shown in Figure 9.9, and the basic mesh used for the 3D model is shown in Figure 9.10. Symmetry is considered to reduce computational demand, and the mesh is selectively refined such that the elements are smaller near the foundation and the ground surface, and become larger with increasing distance from these features. Figure 9.11 shows the model with the solid bodies made transparent to demonstrate how the abutment, embankment, and shaft cap fit together, and to expose the embedded shaft foundations. For simplicity, the layer boundaries beneath the abutment in the idealized soil profile are assumed to extend horizontally over the full model domain, and the gravel layer extends only to the bottom of the shaft foundations.

The soil is modeled using the H1ssp element introduced in Chapter 4 and the constitutive models of Elgamal et al. (2003) introduced in Section 7.1. Total stress analysis is assumed as the H1ssp element makes no consideration for pore pressure effects. The bridge deck is considered using a linear elastic spring element, the abutment and shaft cap are modeled using a combination of beam-column and solid elements, and the shafts are modeled with beam-column elements that interface with the surrounding solid nodes via beam-solid contact elements.

9.3.1 Boundary and Loading Conditions

The boundary conditions for the 3D model are defined to minimize the error associated with representing only a portion of a very large soil domain. Capturing the response of the foundations and their immediate surroundings is the primary objective of the model, therefore, the locations of the mesh boundaries are selected to minimize their effect on this area. The nodes along the base of the gravel layer (light blue in Figure 9.10) are fixed against vertical translation, and elemental body forces are used to simulate the effect of gravity on the soil. The nodes on the symmetry plane are fixed against translation normal to this plane, and the nodes on the vertical boundary opposite the symmetry plane are fixed against all horizontal translation. The nodes on the two remaining vertical boundaries are fixed against out-of-plane translation only. The nodes at the base of the beam-column elements representing the shaft foundations are supported on Q-z springs to consider end bearing effects.

The kinematic demands of lateral spreading are achieved in the model by gradually imposing a set displacement profile to the vertical mesh boundaries as shown in Figure 9.12. This displacement profile represents the free-field kinematic demands on the soil system,

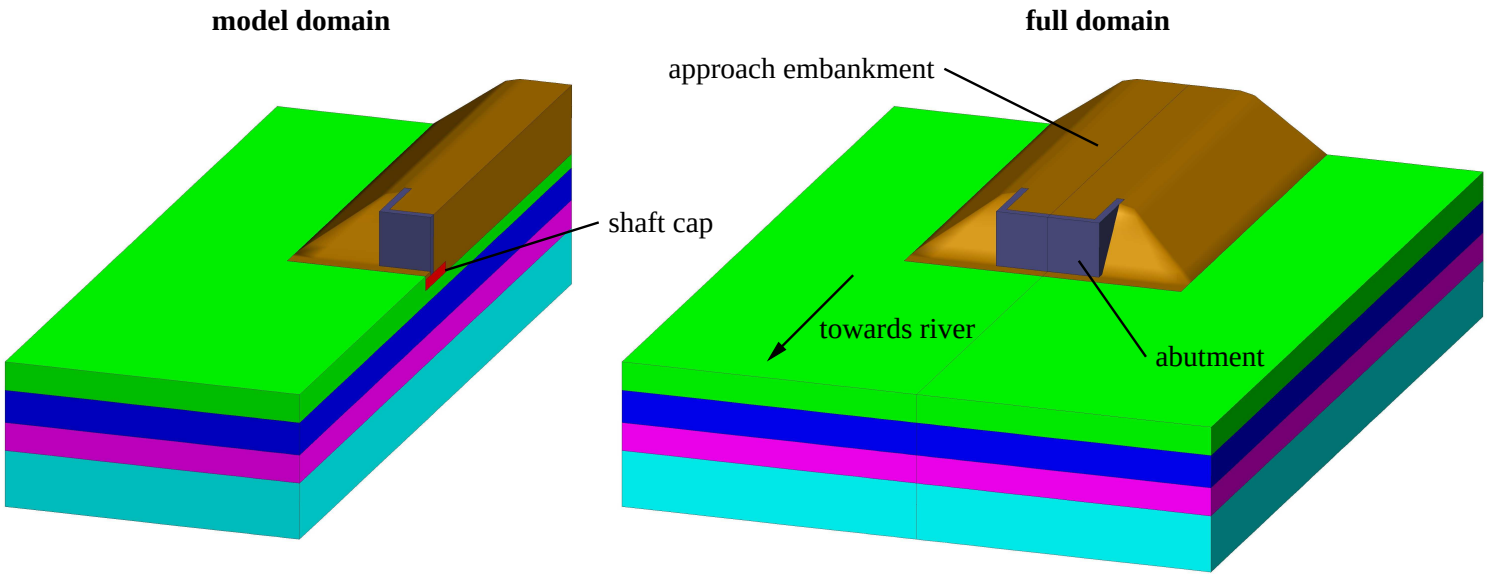

Figure 9.9: Schematic of Puente Mataquito southwest abutment demonstrating symmetry considerations.

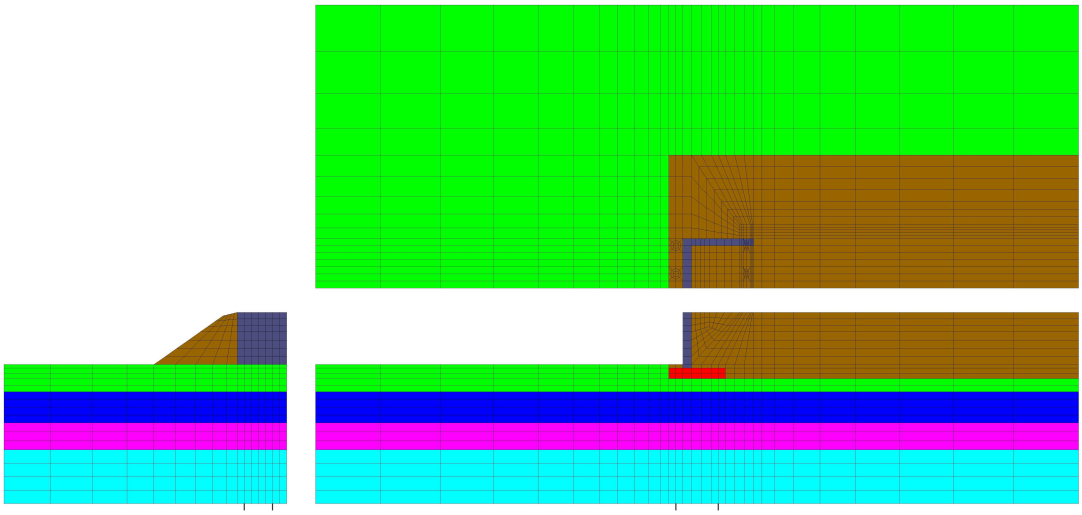

Figure 9.10: Base 3D finite element mesh for southwest abutment of Puente Mataquito.

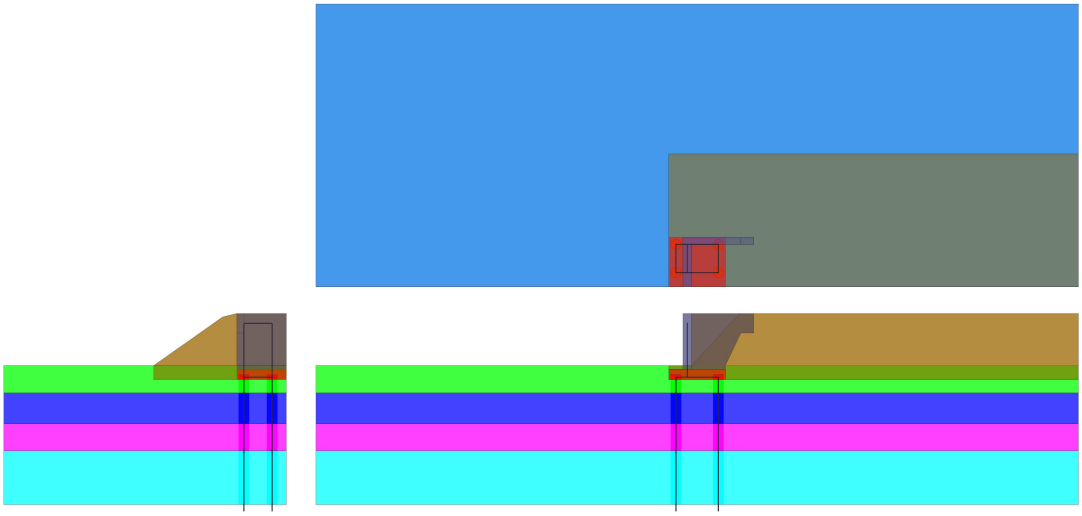

Figure 9.11: Transparent view of base 3D finite element mesh.

with the material above the liquefiable layer translating laterally in relation to the material below. Applied displacements are constant on the boundaries of the dry loose sand and embankment fill layers, linearly increasing across the liquefiable saturated loose sand layer, and held at zero in on the boundaries of the dense sand and gravel layers. No displacements are imposed on the nodes in the symmetry plane not shared with other vertical boundaries.

9.3.2 Modified Soil Properties

The focus of the 3D modeling effort is to simulate the response of the bridge foundation to the kinematic demands of a lateral spreading event. It is assumed that effects related

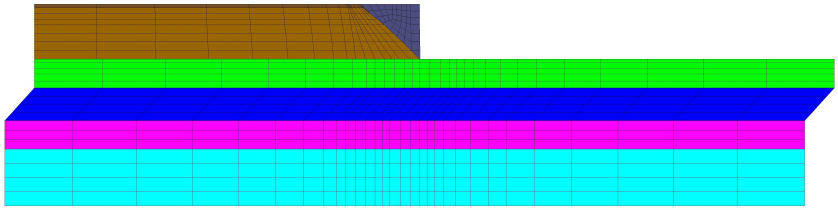

Figure 9.12: Displacement profile applied to mesh boundaries used to simulate kinematic demands of lateral spreading.

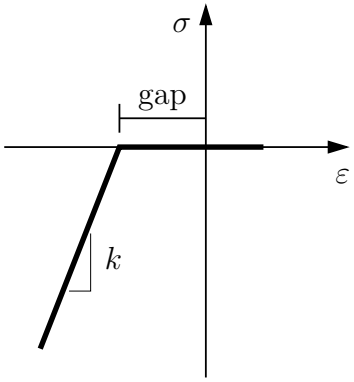

Figure 9.13: Linear elastic constitutive model with gap used in bridge deck spring.

to the initiation of liquefaction are irrelevant to this goal, therefore, the properties of the liquefiable loose sand are modified to reflect the reduction in strength and stiffness associated with a liquefied state. This layer is modeled as a pressure independent (J2) material with a reduced shear modulus $G = 6000$ kPa, and an undrained shear strength of 18.0 kPa. The bulk modulus is unmodified, resulting in a nearly incompressible state that reflects the incompressibility of water. The remaining soil layers in the 3D model (embankment fill, dry loose sand, dense sand, and gravel) are assigned the soil properties discussed in Section 7.1.

9.3.3 Consideration of the Bridge Deck

The bridge deck is not explicitly considered in the 3D model for Puente Mataquito, instead the presence of the deck is modeled using a linear elastic spring. An elastic constitutive model with a gap, Figure 9.13, is used to define the response of the deck spring. This constitutive model considers zero tensile stiffness and zero compressive stiffness prior to gap closure. The spring stiffness, $k = EA/L$, is assigned based on a smeared reinforced concrete elastic modulus, $E_{\text{deck}} = 63.2$ GPa, the bridge deck gross cross-sectional area, $A_{\text{deck}} = 7.25$ m^2, and the span length $L = 40$ m. The nodes on the abutment coinciding with the location of the bridge deck, see Figure 9.14, are constrained to have equal degrees-of-freedom in the direction of loading, and are connected to the free end of the spring element. The sensitivity of the results to the magnitude of the expansion gap is assessed by considering a series of expansion gap values.

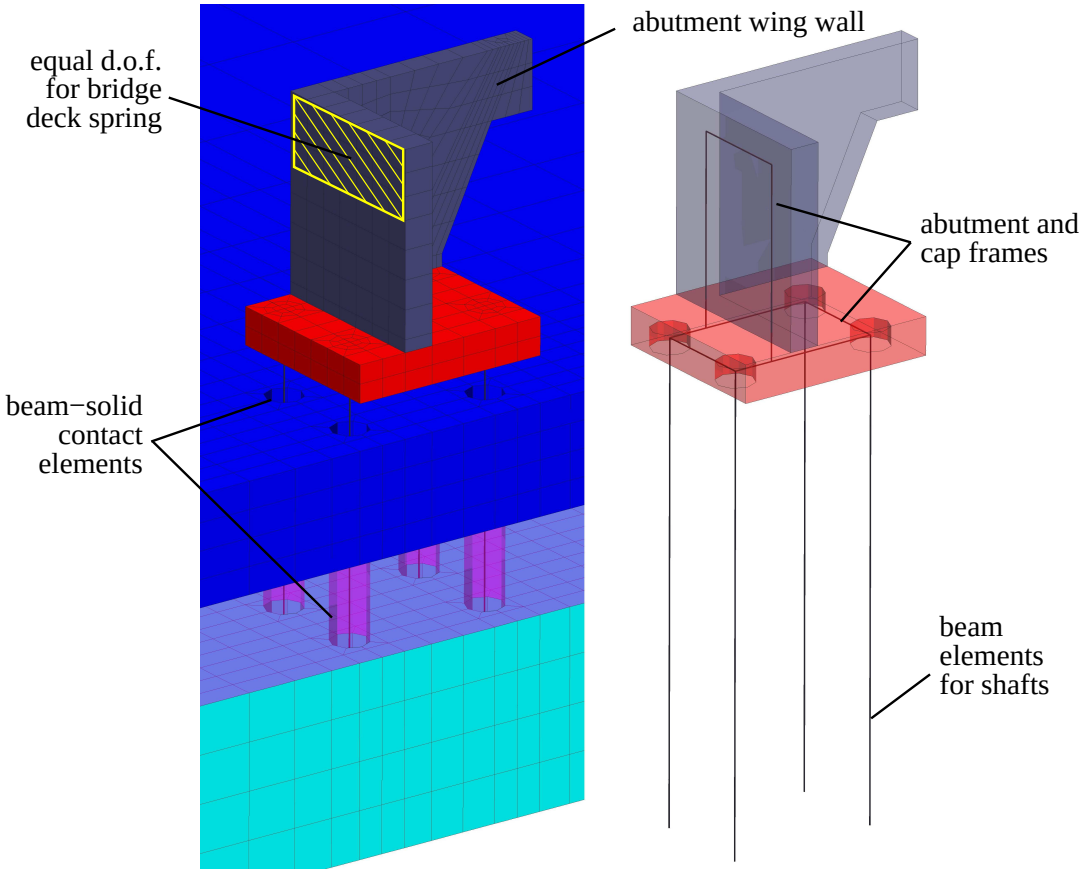

Figure 9.14: Incorporation of grouped shaft foundation into 3D model.

9.3.4 Abutment and Grouped Shaft Foundation

Figure 9.14 shows how the grouped shaft foundation is incorporated in to the 3D model. Displacement-based beam-column elements are used to model the shaft foundations, with the foundation model discussed in Section 7.2 used to describe the section response. The shaft foundations consider linear elastic section response in order to determine the theoretical structural demands independent of strength. No scaling of the section behavior is necessary in the 3D model, as each column of beam elements represents a single shaft foundation. Each shaft is loaded vertically with the foundation design axial load $P = 4120$ kN and supported at the base by a Q-z spring with parameters computed based on the vertical stress and soil properties at the base of the shafts. A circular space surrounding the beam-column elements is built into the mesh to represent the size of the foundation modeled using the beam-column elements. The beam-solid contact elements of Petek (2006) are used to enforce a contact condition with the solid element nodes on the outer circumference of this space. The beam elements are extended beyond the bottom of the solid element mesh to ensure contact is enforced with the nodes at the base of the mesh.

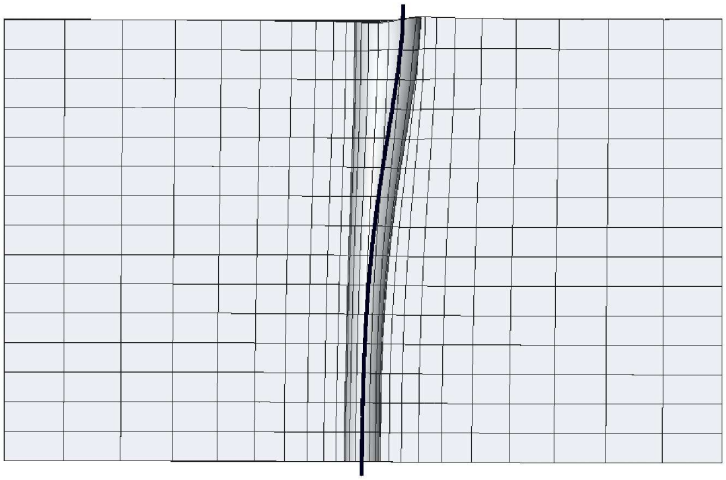

Figure 9.15: Example of gapping behavior simulated with beam-solid contact elements.

The shaft cap and abutment are modeled primarily using solid elements. These elements are assigned a linear elastic constitutive response, with elastic parameters $G = 1.3$ GPa and $K = 2.5$ GPa. As shown in Figure 9.14, beam elements are used to form a frame inside of the cap and abutment bodies. The beam elements inside the shaft cap serve to rigidly tie the shafts together within the cap. The beam elements inside the front wall of the abutment are used to transmit forces acting on the abutment into the grouped shaft foundation, and the nodes at the top of these elements are constrained to have equal degrees-of-freedom in the direction of loading with the bridge deck spring. All of the beam elements in the abutment/cap frame are assigned linear elastic behavior with a large enough bending stiffness such that these elements are rigid in comparison to the shaft section model.

The beam-solid contact element of Petek (2006) is very advantageous in the context of the 3D model. This element allows the shaft foundations to be modeled using beam-column elements, thus enabling the use of fiber section models and the interpretation of results in the context of traditional beam theory, and creates a contact interface capable of capturing frictional stick-slip and gapping behaviors. Figure 9.15 shows an application of this element to a pile pushover analysis. As shown, the beam elements do not come into direct contact with the surrounding solid elements, and a gap develops on the trailing edge of the pile while the soil deformation on the leading edge matches the pile deformation. For the purposes of efficiency, the original beam-solid contact elements of Petek (2006) are extended to include a penalty formulation in the enforcement of the contact condition. This extended version of the element is used in all of the 3D modeling presented in this work, and the necessary modifications are summarized in the following discussion.

9.3.4.1 Extension of Beam-Solid Contact Element to Penalty Constraints

The current formulation for the beam-solid contact element developed by Petek (2006) uses the method of Lagrange multipliers to enforce the contact constraints. Using this approach,

the virtual work for the contact system is expressed in terms of the gap, g, the slip, $\mathbf{s}$, normal force, t_n, and tangential force $\mathbf{t}_s$, as

$$\delta W_c = t_n \delta g + \delta t_n g - \mathbf{t}_s \dot{\delta} \mathbf{s} \tag{9.8}$$

From this expression and its linearization, the element force vector,

$$\mathbf{R} = \left\{ \begin{array}{c} t_n \mathbf{B}_n - \mathbf{B}_s \mathbf{t}_s \\ g \end{array} \right\} \tag{9.9}$$

where $\mathbf{B}_n$ and $\mathbf{B}_s$ are terms related to the variation of the gap and slip, respectively, and the element tangent stiffness matrix,

$$\mathbf{K} = \left[\begin{array}{cc} -\mathbf{B}_s \mathbb{C}_{ss} \mathbf{B}_s^T & \mathbf{B}_n - \mathbf{B}_s \mathbb{C}_{sn} \\ \mathbf{B}_n^T & \mathbf{0} \end{array} \right] \tag{9.10}$$

where $\mathbb{C}_{ss}$ and $\mathbb{C}_{sn}$ are constitutive terms for a frictional contact interface, are obtained using an augmented nodal degrees-of-freedom vector defined as

$$\mathbf{q}^* = \left\{ \begin{array}{c} \mathbf{q} \\ t_n \end{array} \right\} \tag{9.11}$$

where $\mathbf{q}$ is the nodal degrees-of-freedom vector for the element. Please refer to Petek (2006) for further definition of terms and a discussion on the full formulation and implementation of the beam-solid contact elements.

The Lagrange multiplier technique used in the original element formulation is effective in enforcing the contact constraints, however, the OpenSees implementation of the element requires an additional node to provide the necessary extra degree-of-freedom. This increases the size of the global system of equations, and complicates mesh generation. Additionally, the enforcement of the constraints is absolute under the Lagrange multiplier approach, which can lead to numerical issues for certain problems. For the current work, the beam-solid contact element of Petek (2006) is extended to use a penalty approach for constraint enforcement. Use of the penalty method relaxes the constraint enforcement, creating a more forgiving contact surface and removing the requirement for additional degrees-of-freedom in the elemental and global systems.

The transition to penalty constraint enforcement begins with a reformulation of the virtual work expression to

$$\delta W_c = \epsilon \bar{g} \delta \bar{g} + \mathbf{t}_s \dot{\delta} \mathbf{s} \tag{9.12}$$

where $\bar{g}$ is the penetration, and $\epsilon > 0$ is the penalty parameter. Under penalty constraints, the bodies in contact are able to interpenetrate, thus the substitution of a penetration

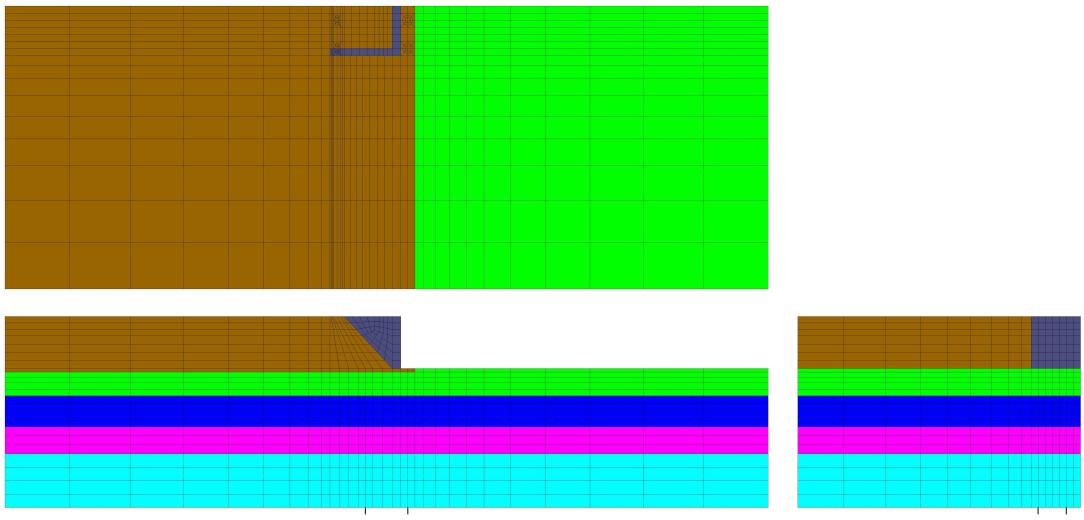

Figure 9.16: Mesh for wide embankment geometry intended to simulate 2D assumptions.

function for the gap used in the Lagrange multiplier approach. The amount of penetration allowed depends on the magnitude of the penalty parameter. The reformulated virtual work expression and its linearization lead to new expressions for the element force vector,

$$\mathbf{R} = \epsilon \bar{g} \mathbf{B}_n - \mathbf{B}_s \mathbf{t}_s \tag{9.13}$$

and the element tangent stiffness matrix,

$$\mathbf{K} = \epsilon \mathbf{B}_n \mathbf{B}_n^T + \mathbf{B}_s \mathbb{C}_{ss} \mathbf{B}_s^T + \mathbf{B}_s \mathbb{C}_{sn} \mathbf{B}_n^T \tag{9.14}$$

Beyond replacing the augmented nodal degrees-of-freedom vector, $\mathbf{q}^*$, with the natural vector of nodal degrees-of-freedom for the element, $\mathbf{q}$, no other aspect of the original element formulation must be changed in the extension to penalty constraints. Changes to the element implementation must be made, however, these modifications are relatively minor as they are primarily related to changing the input parameters for the element, and the sizes of some of the internal variables.

9.3.5 Alternative Configurations

One alternative mesh configuration is considered for the 3D model. This mesh, shown in Figure 9.16, is identical to the base mesh for the site with the exception of the embankment geometry. Instead of using the embankment geometry existing at the bridge site, the alternative mesh considers an embankment that extends to the boundary of the model. This wide embankment geometry is intended to simulate the assumptions made in a plane strain treatment of the site, and is used to compare the foundation demands due to lateral spreading to those resulting from the existing embankment geometry. The kinematic demands of

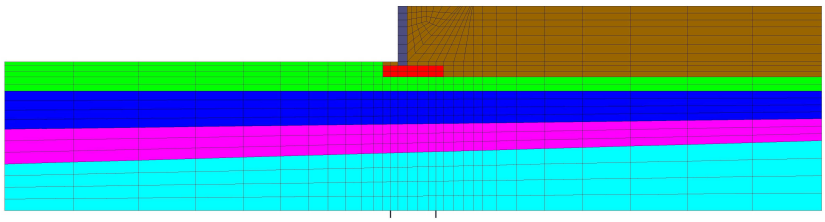

Figure 9.17: Mesh for bridge foundation strength reduction model.

lateral spreading are simulated in the manner described previously, with a set displacement profile imposed on the non-symmetry vertical boundaries of the mesh. Displacements are not imposed on the side of the embankment across from the symmetry plane, and these nodes are left free to displace in the loading direction.

For each embankment geometry, lateral spreading analyses are conducted for two deck expansion gap values to test the sensitivity of the results to this parameter. According to construction drawings of the bridge, a 20 cm expansion gap is built in to the connection of the bridge deck and abutment. The two gap magnitudes considered in the applied kinematic model are based on this value. The first gap, 5 cm, is chosen on the assumption that the deck is moving towards the abutment due to lateral spreading on the opposite river bank as observed in the plane strain models. The second gap, 25 cm, is based on the assumption that the bridge deck may be moving slightly away from the abutment as lateral soil movement affects the interior piers.

9.3.6 Strength Reduction Model

A second approach to simulating the kinematic demands of lateral spreading on the embedded bridge foundation is considered to provide verification of the results obtained from the applied kinematic model, and to aid in the identification of lateral load reduction mechanisms that may be obscured by the applied kinematic approach. In this second model, instead of applying a set displacement profile to the model boundaries, the shear strength and stiffness of the liquefiable layer are gradually reduced to nearly zero (G = 1.0 kPa and S_u = 0.05 kPa) over a series of analysis steps, with the model being allowed to reach equilibrium for each new set of parameters before proceeding to the next state. Using this approach, the effects of liquefaction in the saturated loose sand layer on the soil-foundation-bridge system can be considered in a simplified manner. This new model is referred to as the strength reduction model in all subsequent discussion in reference to the technique used to simulate the kinematic demands of lateral spreading. Based on similar reasoning, the 3D model discussed in the preceding sections is referred to as the applied kinematic model.

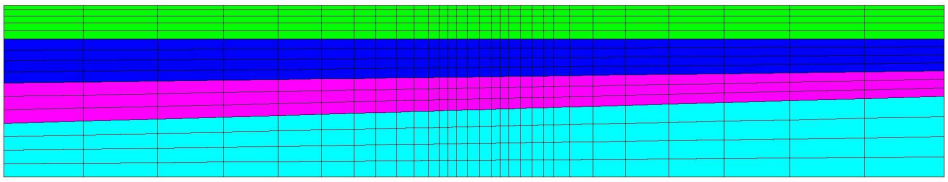

Figure 9.18: Mesh for soil-only strength reduction model.

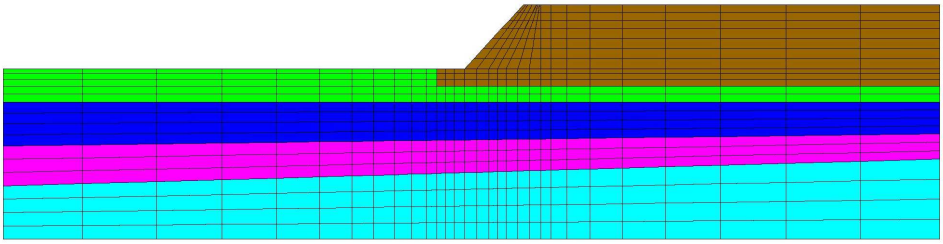

Figure 9.19: Mesh for embankment-only strength reduction model.

The strength reduction model is created with a slightly modified soil geometry to facilitate the alternative approach to simulating the kinematic demands associated with lateral spreading. The mesh for this case, shown in Figure 9.17, considers soil layer boundaries that slope down towards the river. The orientations of these sloped boundaries are defined by extrapolating the slopes of the layers at the center of the foundation in the idealized soil profile to the model boundaries. Two additional complementary meshes are considered for the strength reduction model, one without an embankment, bridge, or foundation, Figure 9.18, and one with an embankment but no foundation or bridge deck, Figure 9.19. The mesh extents and layer geometry of the native soils in both models, and the embankment in the latter model, match those of the base bridge mesh of Figure 9.17.

In all three meshes, the soil nodes above the bottom of the liquefiable layer on the boundary away from the river and the boundary opposite the symmetry plane are allowed to translate towards the river, but are held fixed against translation is the opposite direction. All other boundary conditions are as previously defined. Three global slopes are considered for the strength reduction model. These slopes are simulated by applying gravitational body forces consistent with 0°, 2.5°, and 5.0° rotations of the mesh. These rotated body forces are applied only to the solid elements above the liquefied layer. The lower soil layers consider vertical body forces as in the applied kinematic model. The non-zero global slopes are not intended to simulate conditions at the site, but they are useful in that they encourage the soil above the liquefiable layer to move towards the river, placing larger kinematic demands

on the embedded foundations, and allowing deformation mechanisms to be more clearly identified.

9.4 3D FEA of Southwest Abutment with Applied Kinematic Model

The applied kinematic model is used to examine the response of the southwest abutment and approach embankment to the kinematic demands of lateral spreading, and to compare these demands to those predicted by a plane strain description of the problem. To accomplish this, two embankment geometries are considered: the embankment geometry existing at the site shown in Figure 9.10, and a widened embankment geometry where the embankment fill extends to the boundary of the mesh as shown in Figure 9.16. In addition to the these two geometries, two expansion gap values are considered in order to assess the effect of the size of the gap between the bridge deck and abutment on the response of the model. The results of the lateral spreading simulations for each embankment geometry and expansion gap value are compared to each other in terms of the global response of the soils and foundations, the overall behavior of the abutment and foundation, and the displacement, shear force, and bending moment demands developed in the shaft foundations.

9.4.1 Global Model Response

Figures 9.20 and 9.21 show the deformed mesh at the end of the analysis for the 5 cm and 25 cm gap applied kinematic models with the existing embankment geometry. The deformed meshes are magnified 4 times for visualization, and contours of displacement magnitude (units of cm) are plotted on each mesh. Figures 9.22 and 9.23 are the corresponding plots for the wide embankment geometry. For all cases, the displacements in the direction of loading are generally larger than those in other directions, and the deformation magnitude contours shown in these figures are primarily influenced by this displacement component.

The deformation fields for these models show that with the existing embankment geometry, the bridge foundation provides more resistance to riverward deformation in the immediately adjacent soil and affects a larger lateral expanse of soil. With the wide geometry, there is increased overburden stress at the lateral free-field boundary due to the presence of the embankment. This increases the available shear strength and stiffness of the soil in this location, leading to a larger kinematic demand on the foundation as the free-field displacement is propagated closer to the bridge. This is manifested in the smaller lateral zone of foundation influence for these cases, and in the larger deformations present below the connection of the bridge deck to the abutment.

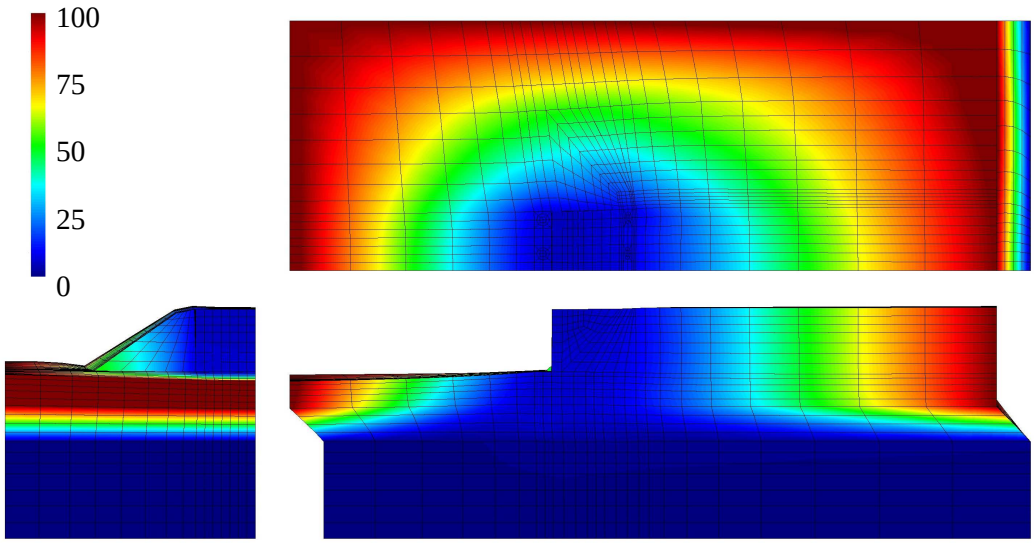

Figure 9.20: Deformed mesh (magnified 4 times) for existing geometry 5 cm gap applied kinematic model with contours of displacement magnitude (in cm).

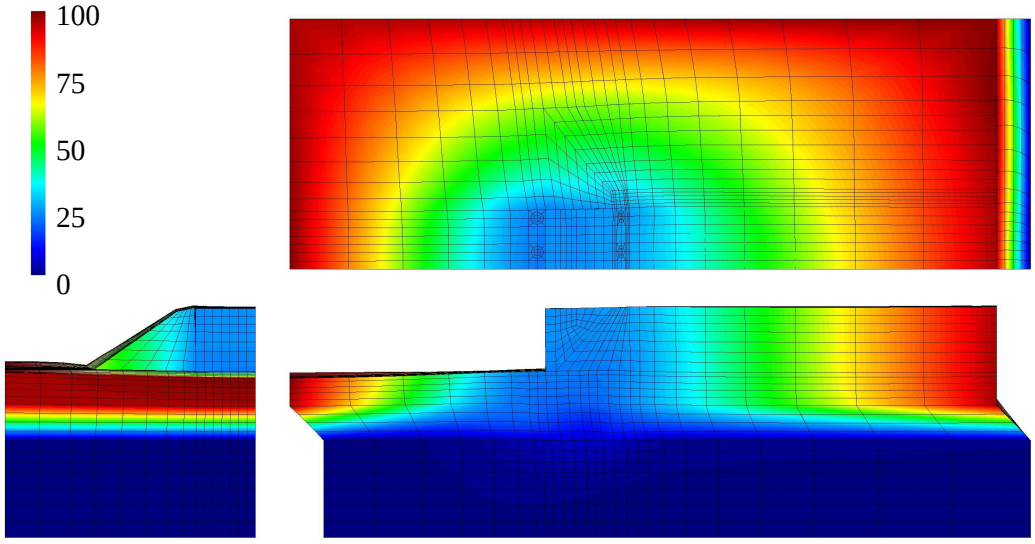

Figure 9.21: Deformed mesh (magnified 4 times) for existing geometry 25 cm gap applied kinematic model with contours of displacement magnitude (in cm).

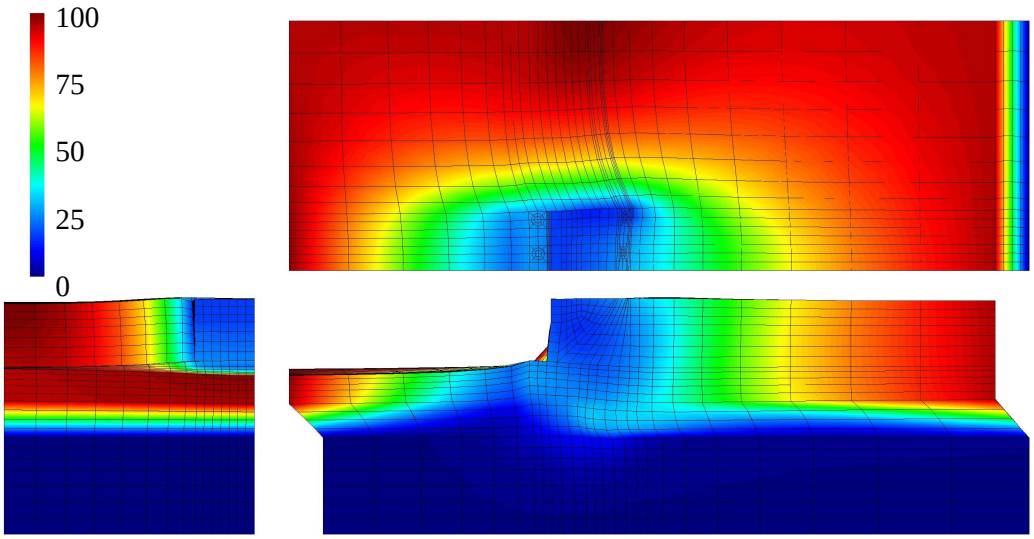

Figure 9.22: Deformed mesh (magnified 4 times) for wide geometry 5 cm gap applied kinematic model with contours of displacement magnitude (in cm).

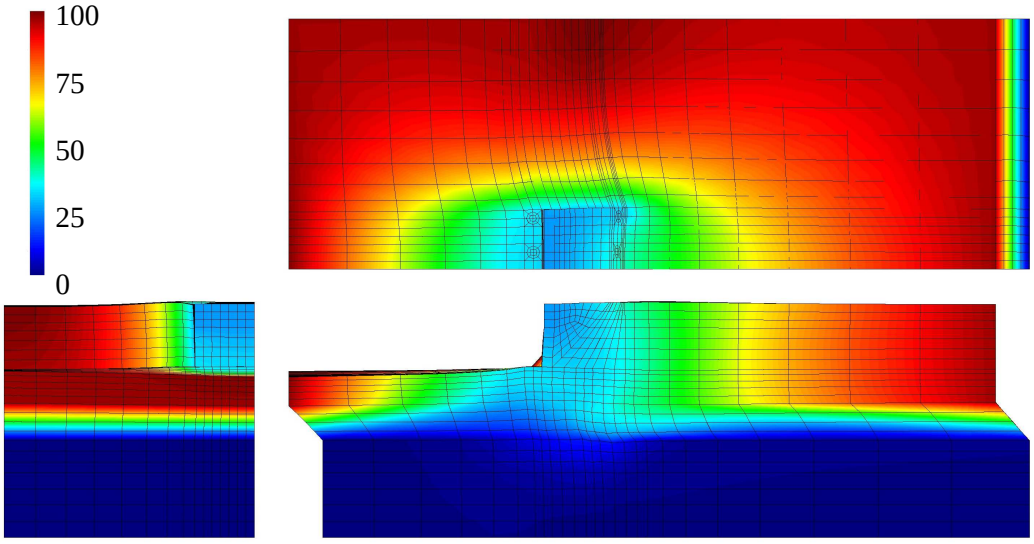

Figure 9.23: Deformed mesh (magnified 4 times) for wide geometry 25 cm gap applied kinematic model with contours of displacement magnitude (in cm).

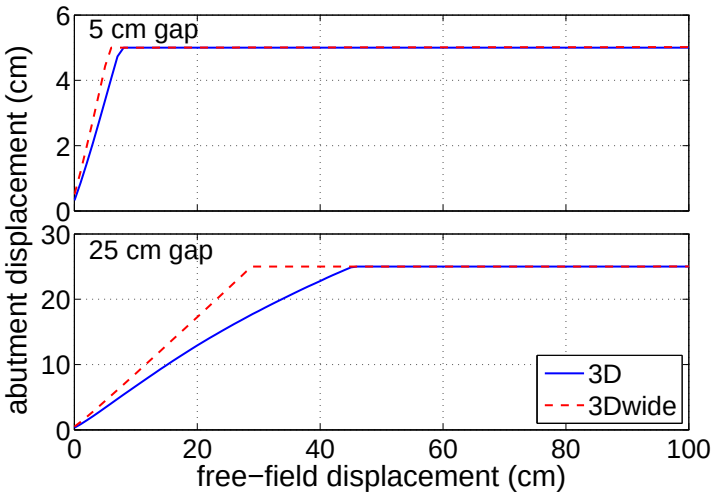

Figure 9.24: Evolution of abutment displacement in direction of loading for 5 cm and 25 cm gap cases.

9.4.2 Abutment and Foundation Response

Figure 9.24 shows how the displacement at the top of the abutment changes over the course of the free-field displacement application. Prior to gap closure for both gap magnitudes, the abutment displacement in the wide geometry case is essentially equal to the free-field displacement, indicating that the foundation is unable to provide significant resistance to the lateral soil deformation. In contrast, the abutment displacements for the existing embankment geometry are less than the applied values, indicating that the foundation is resisting the lateral soil demands. The difference between the free-field and abutment displacement for this geometry increases with increasing free-field displacement. After the gap has closed, the displacement at the top of the abutment remains essentially constant due to the resistance provided by the bridge deck spring.

The deformation mechanism for the foundation changes after the closure of the gap. Figures 9.25 and 9.26, which show the deformed shapes of the model foundations for the 5 cm and 25 cm gap cases, respectively, demonstrate this difference in deformation mechanism. After the gap has closed, the lateral deformation of the shaft cap continues to increase, resulting in a rotation about the bridge deck connection point. This effect is most clearly observed for the wide embankment geometry cases, though it is present in all considered configurations. This type of rotational foundation response to lateral spreading corresponds to observations made at numerous bridge sites, including the New Zealand bridges discussed in Chapter 1, and demonstrates the importance of the bridge deck in defining the overall foundation response. It also demonstrates the need for 3D (or 2D) simulation, as a simplified analysis may not capture this effect.

The effects of approach embankment geometry are also evident from the deformed foun-

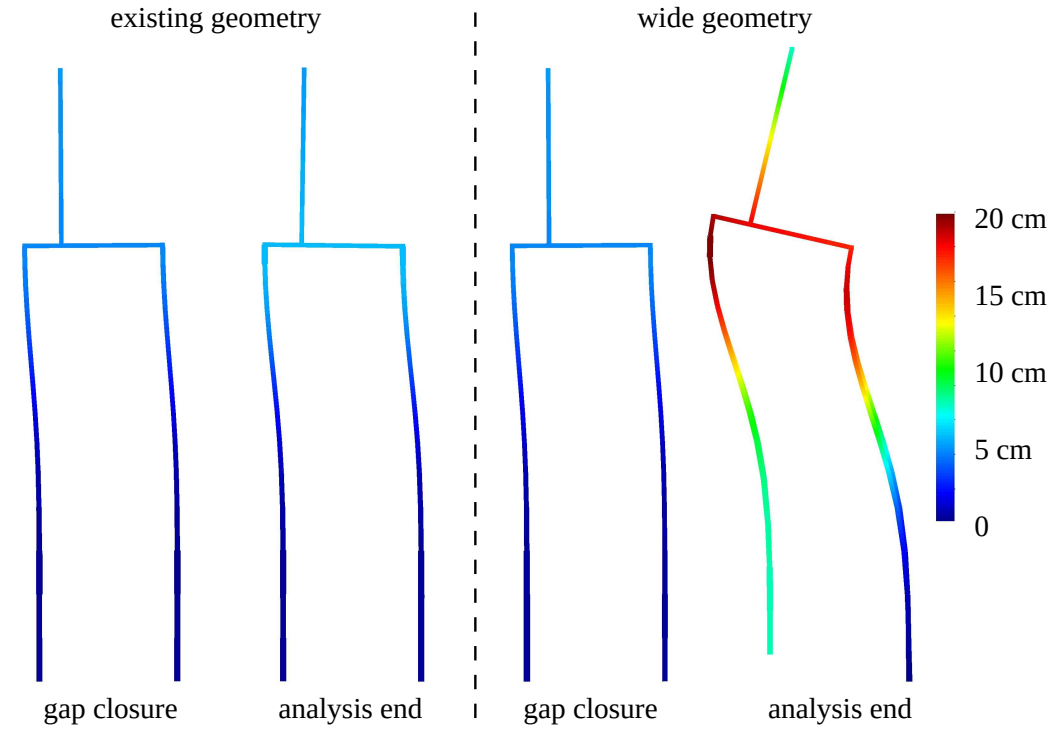

Figure 9.25: Foundation deformations (magnified 15 times) at gap closure and analysis end for 5 cm gap models.

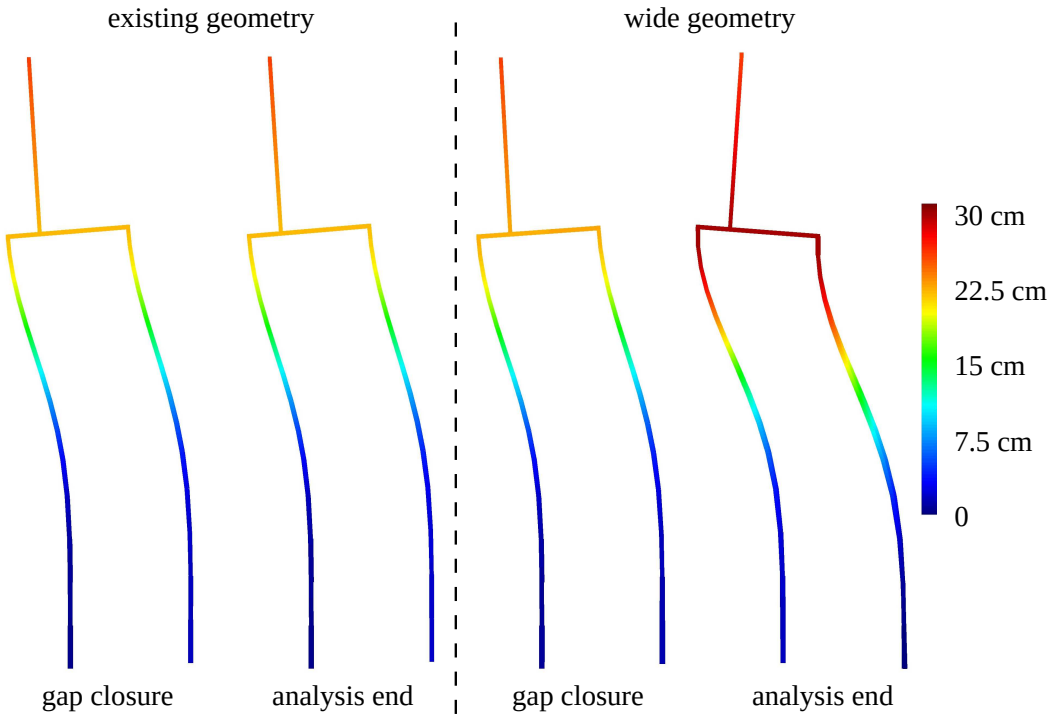

Figure 9.26: Foundation deformations (magnified 15 times) at gap closure and analysis end for 25 cm gap models.

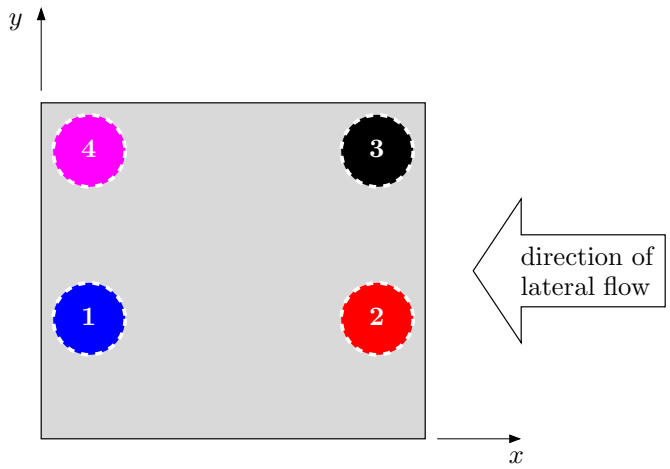

Figure 9.27: Numbering and color scheme used for foundation shafts.

dations of Figures 9.25 and 9.26. Prior to gap closure, the foundation deformations for each embankment geometry are similar, with the existing geometry inducing slightly less lateral movement in the foundation. After the gap has closed, the differences in how the embankment configuration affects the bridge foundation become apparent, as the end of analysis foundation deformations for the widened embankment cases are significantly larger than those for the corresponding existing geometry cases.

9.4.3 Foundation Bending Demands

The shaft bending demands developed in the applied kinematic model vary for each of the four shafts in the foundation, especially at larger displacements. To aid in identifying these shafts in the subsequent discussion, Figure 9.27 establishes a numbering and color coding scheme for the shaft group. The shaft displacement profiles, shear force diagrams, and bending moment diagrams at the closure of the 5 cm and 25 cm gaps are shown in Figures 9.28 and 9.29. These plots demonstrate that prior to gap closure, the foundation demands for the existing and wide embankment geometries are nearly the same, though it is important to note that, as shown in Figure 9.24, gap closure occurs at different levels of free-field displacement for the two geometries.

Figures 9.30 and 9.31 show summaries of the shaft bending demands at the end of the analysis (i.e., 1 m free-field displacement in upper layers) for the 5 cm and 25 cm gaps, respectively. These plots demonstrate the importance of the bridge deck resistance in defining the magnitude of the shaft bending demands due to lateral spreading, especially with respect to three-dimensional effects. For the existing embankment geometry, the bending demands at the end of the analysis are only slightly larger than at gap closure. This indicates that the lateral resistance provided by the grouped shaft foundation and bridge deck

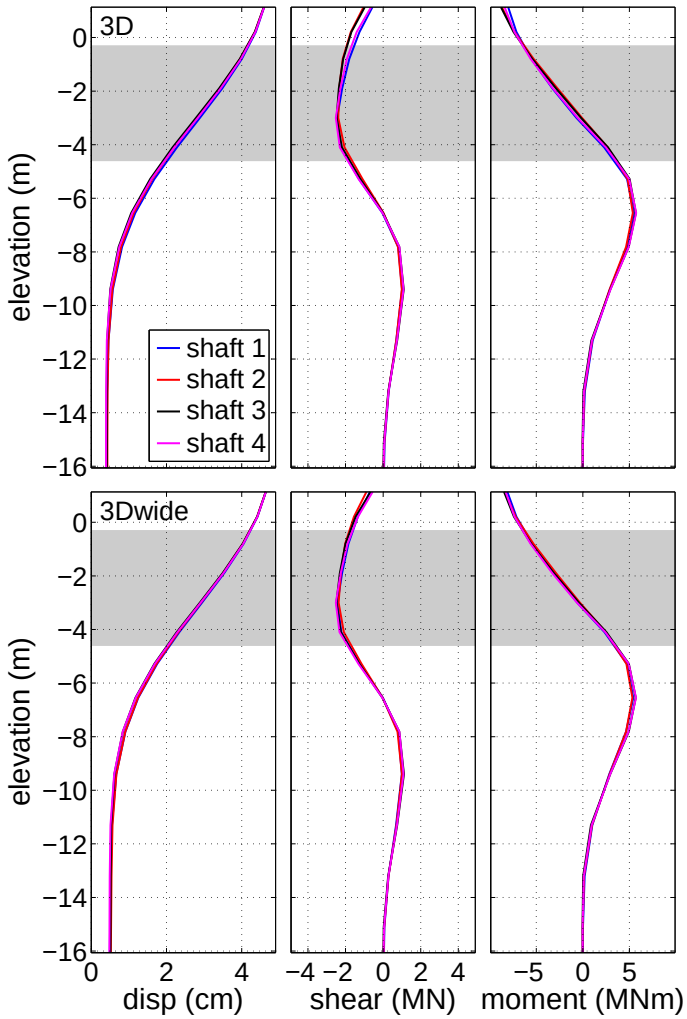

Figure 9.28: Shaft bending demands for existing and wide embankment geometries at closure of 5 cm gap.

is sufficient to resist the kinematic demands imposed by the soil given the limited footprint of the approach embankment. In contrast, for the wide embankment geometry the foundation rotates about the essentially horizontally stationary deck connection as the free-field displacements increase past the gap closure point. As shown in Figures 9.30 and 9.31 this results in significantly larger shear and moment demands in the shafts.

The change in the foundation deformation mode after the gap has closed also results in a change in the individual shaft response within the group. Whereas initially all four shafts responded similarly, after gap closure two distinct responses appear, with shafts 2 and 3 sharing one response, and shafts 1 and 4 sharing the other. The leading shafts (2 and 3)

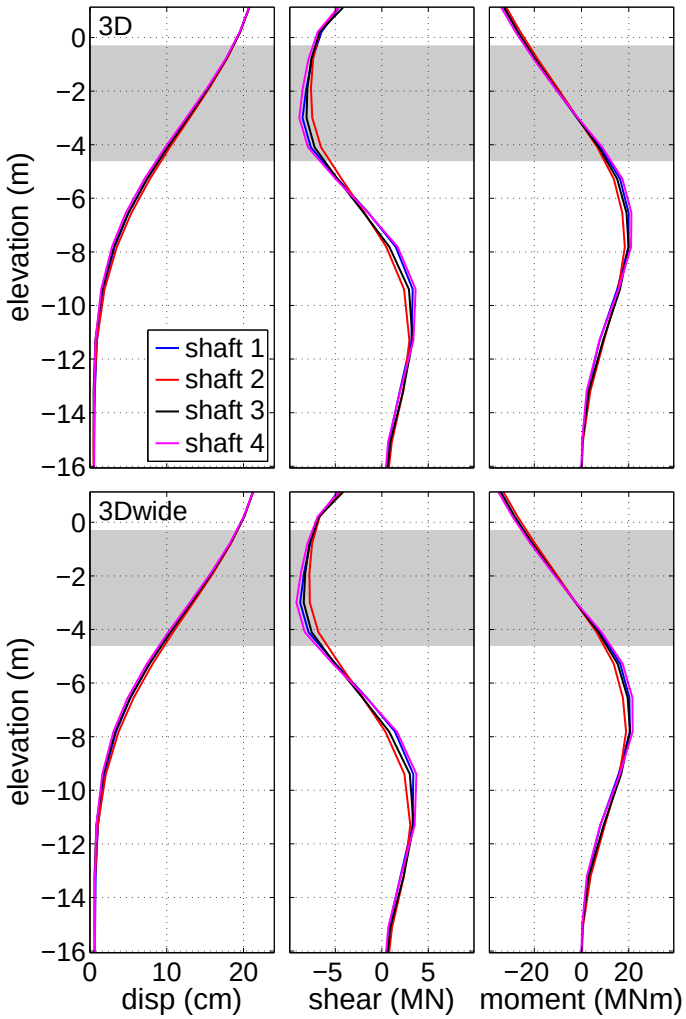

Figure 9.29: Shaft bending demands for existing and wide embankment geometries at closure of 25 cm gap.

display larger displacements with depth than the trailing shafts (1 and 4), resulting larger shear force demands in the lower soil layers and slightly lower moment demands overall. In both cases, the outer shafts (3 and 4) develop somewhat larger shear and moment demands than the inner shafts (1 and 2), with shaft 4 typically displaying the largest bending demands of the four shafts.

To further examine the difference between the bending demands for the two embankment geometries, the progressions of maximum shear force and bending moment above (or within) and below the liquefied layer are shown in Figures 9.32 through 9.35 for the 5 cm gap, and in Figures 9.36 through 9.39 for the 25 cm gap. These plots confirm and clarify several

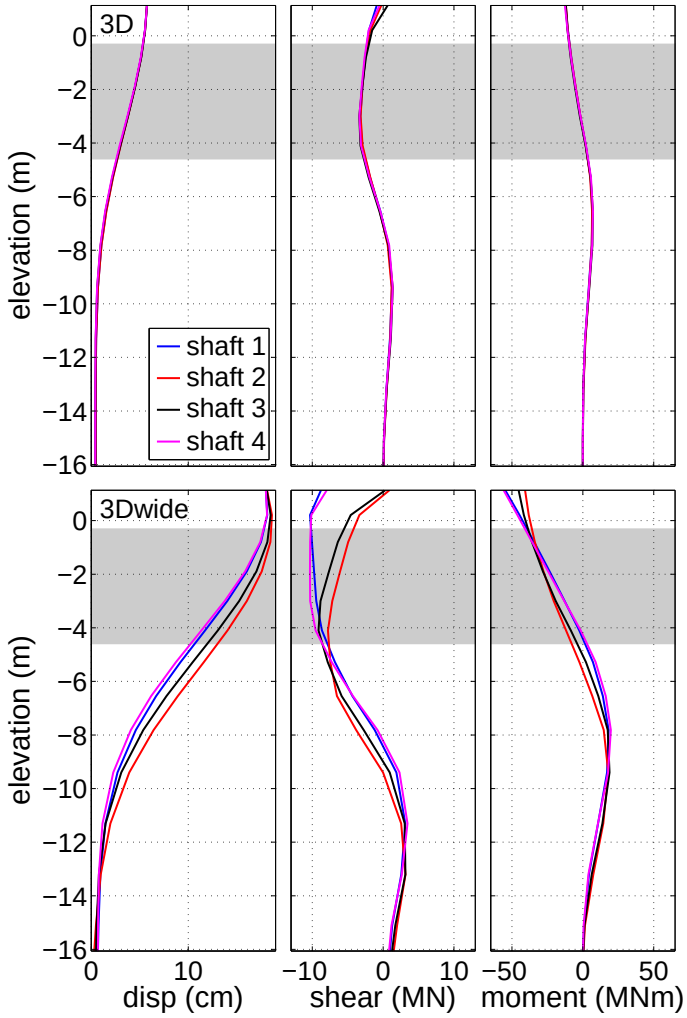

Figure 9.30: Shaft bending demands for existing and wide embankment geometries at analysis end for 5 cm gap.

observations made from the previously discussed bending demand summary plots. For the existing geometry, the maximum bending demands level off after the gap has closed, reaching ultimate values that are not significantly larger than those at the closure of the gap. For the wide embankment geometry, the maximum shear and moment demands do not level off after gap closure. These demands continue to increase with increasing free-field displacement, though at a lesser rate of increase than in the pre-closure regime. The group effects noted in Figures 9.30 and 9.31 are also apparent in these maximum demand evolution plots, and as clearly indicated in Figures 9.36, 9.38, and 9.39, the group effects are manifested prior to gap closure in certain cases.

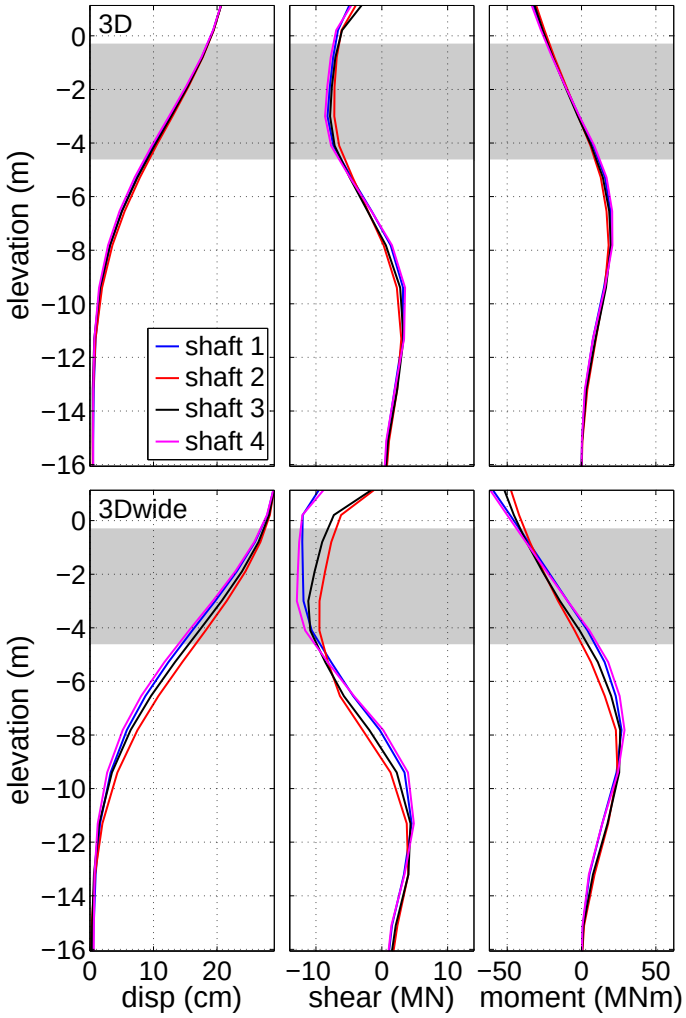

Figure 9.31: Shaft bending demands for existing and wide embankment geometries at analysis end for 25 cm gap.

9.4.4 Summary of Applied Kinematic Model Results

The results obtained from the various configurations of the applied kinematic model have established that there is a tangible difference in the foundation response depending on the geometry of the approach embankment. The soil deformation near the foundation, the general foundation response, and the shaft bending demands are all significantly larger for the wide embankment case, especially after the closure of the deck expansion gap. This indicates that consideration for the 3D geometry of the embankment is critical in order to determine appropriate structural foundation demands for the lateral spreading load case.

These results also highlight the importance of the bridge deck and expansion gap in defining the response of the foundation to lateral spreading. Prior to expansion gap closure, the differences between the two geometries are less significant, as the lateral soil movement

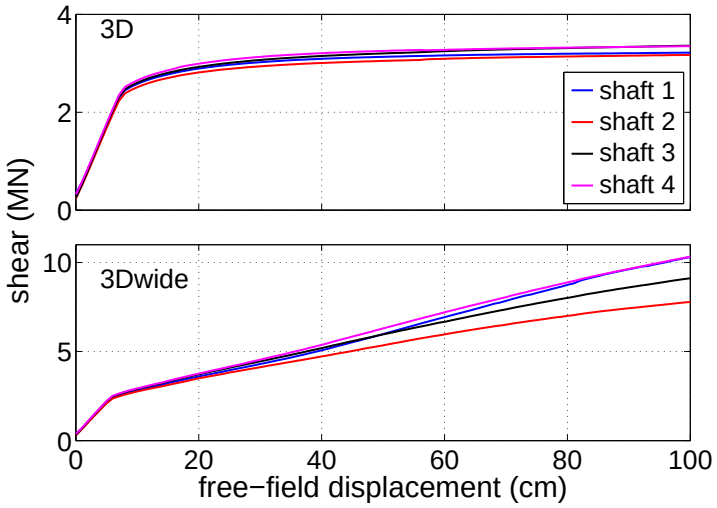

Figure 9.32: Evolution of maximum shear force above the liquefiable layer for existing and wide embankment geometries with 5 cm gap.

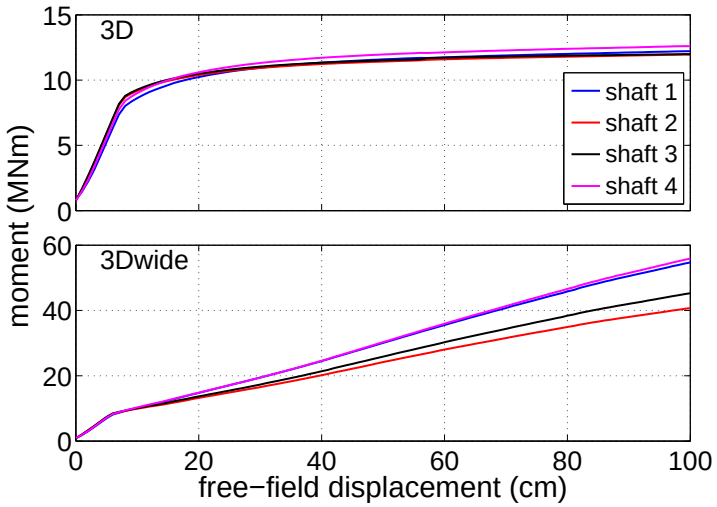

Figure 9.33: Evolution of maximum moment above the liquefiable layer for existing and wide embankment geometries with 5 cm gap.

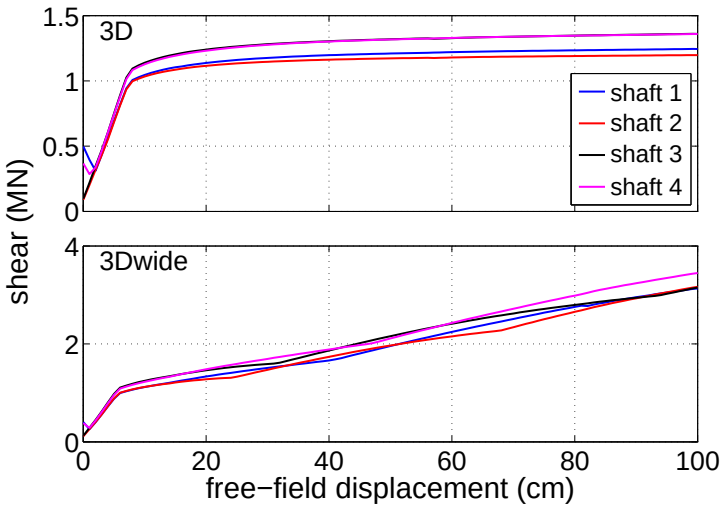

Figure 9.34: Evolution of maximum shear force below the liquefiable layer for existing and wide embankment geometries with 5 cm gap.

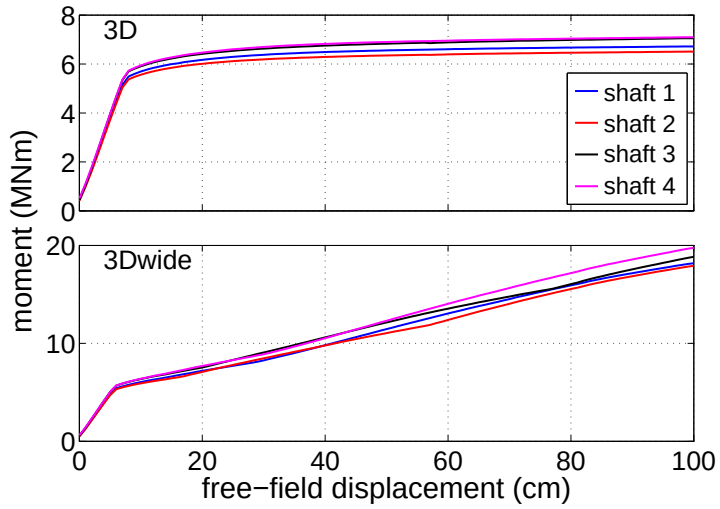

Figure 9.35: Evolution of maximum moment below the liquefiable layer for existing and wide embankment geometries with 5 cm gap.

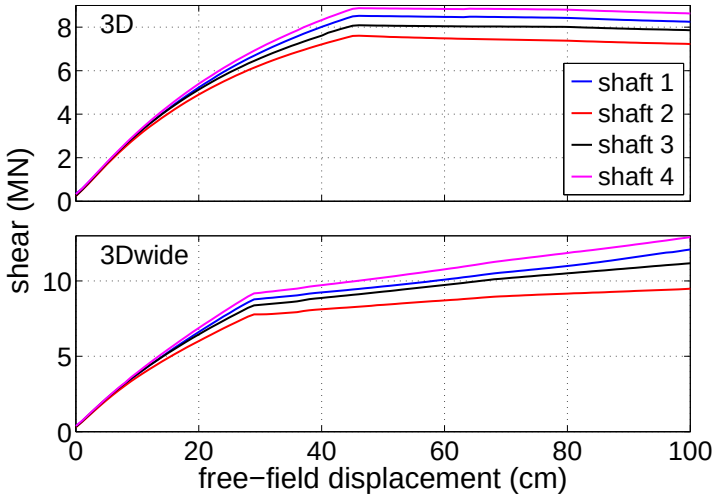

Figure 9.36: Evolution of maximum shear force above the liquefiable layer for existing and wide embankment geometries with 25 cm gap.

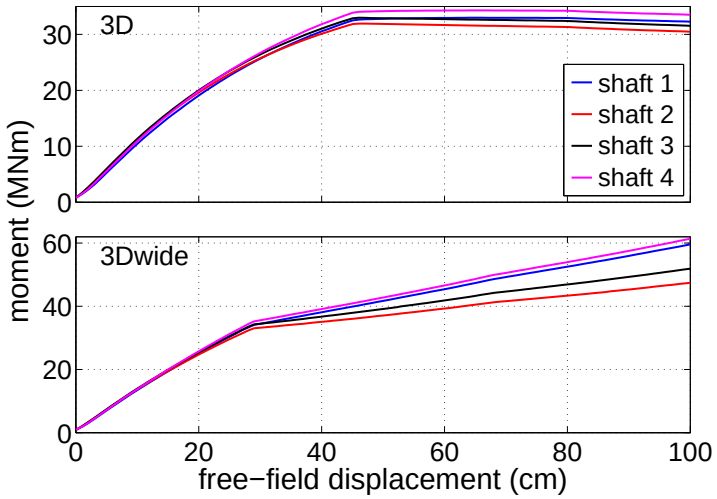

Figure 9.37: Evolution of maximum moment above the liquefiable layer for existing and wide embankment geometries with 25 cm gap.

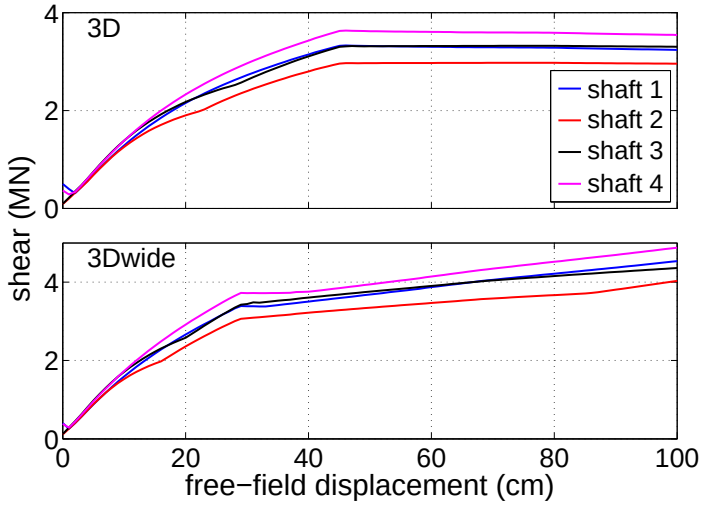

Figure 9.38: Evolution of maximum shear force below the liquefiable layer for existing and wide embankment geometries with 25 cm gap.

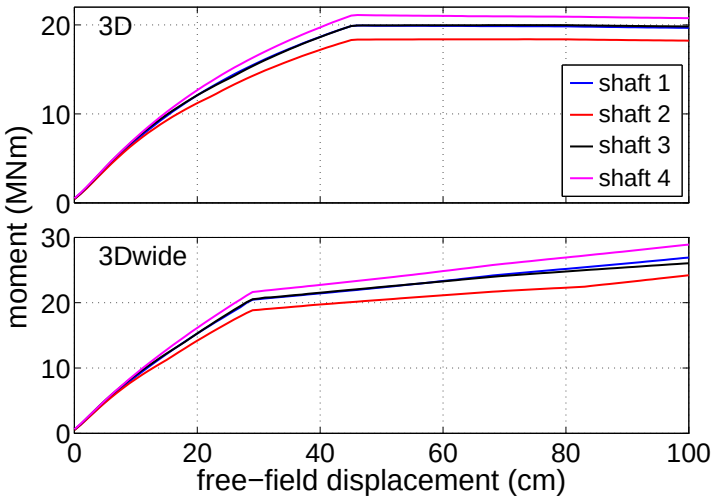

Figure 9.39: Evolution of maximum moment below the liquefiable layer for existing and wide embankment geometries with 25 cm gap.

imposes nearly matching movement in the foundation. After expansion gap closure, the three-dimensional effects become more prominent. The addition of the lateral deck stiffness to the bending stiffness of the foundation is sufficient to resist most of the remaining kinematic demands for the existing embankment geometry, leading to relatively minor increases in the structural foundation demands as the free-field displacement continues past the closure of the gap. This is not the case for the simulated 2D conditions of the wide embankment geometry, as significant foundation demands develop after gap closure.

9.5 3D FEA of Southwest Abutment with Strength Reduction Model

The strength reduction models are advantageous in that they allow for an evaluation of how the system responds as the saturated loose sand layer loses shear strength and stiffness. Consideration of the three model configurations (foundation and embankment, soil-only, embankment-only) shown in Figures 9.17, 9.18, and 9.19 allows for an assessment of the impact of the embankment and foundation on the response of the site. This set of models also serves as an independent evaluation of the results of the applied kinematic model, especially with respect to the foundation bending demands. The kinematic demands of lateral spreading are simulated in a completely different manner for these models, and correlation between the bending demands obtained from each approach increases confidence in the observations and conclusions made from the models.

9.5.1 Global Model Response

Figures 9.40 and 9.41 show the deformed mesh at the end of the analysis for the bridge foundation and embankment only model configurations with flat slope conditions. The mesh deformations are magnified 25 times for visualization purposes, and displacement magnitudes (units of cm) are indicated as contours with the same scale in each figure. A similar figure for the soil-only case is not included here, as the deformations for the flat slope condition are negligible in comparison. The results shown in Figures 9.40 and 9.41 reflect the general trends indicated for all considered slopes. The loss of shear strength and stiffness in the loose sand layer results in a tendency for the embankment to slump downward and expand laterally in both directions as shown in Figure 9.41. With the bridge foundation in place, the riverward deformation of the embankment is resisted, which results in less overall slumping. The bridge foundation also reduces lateral deformation in the second lateral direction in the adjacent embankment fill, however, the free-field lateral deformation is much less affected.

Table 9.7 shows the maximum soil displacements in the x-, y-, and z-directions ($u_{\max}$, $v_{\max}$, and $w_{\max}$, respectively) for each of the considered strength reduction model configurations. For these models, the x-axis is oriented towards the river and corresponds with the

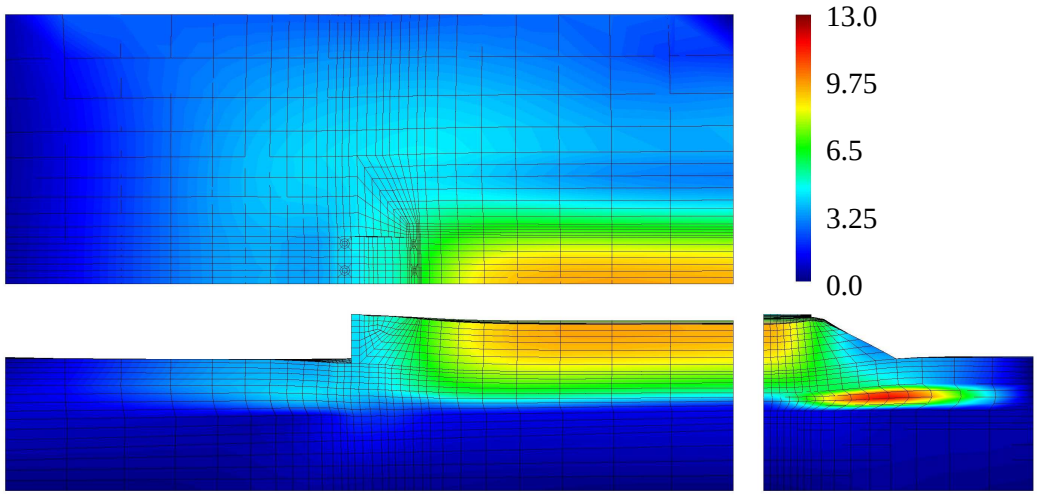

Figure 9.40: Deformed mesh (magnified 25 times) for flat slope foundation strength reduction model with contours of displacement magnitude (in cm).

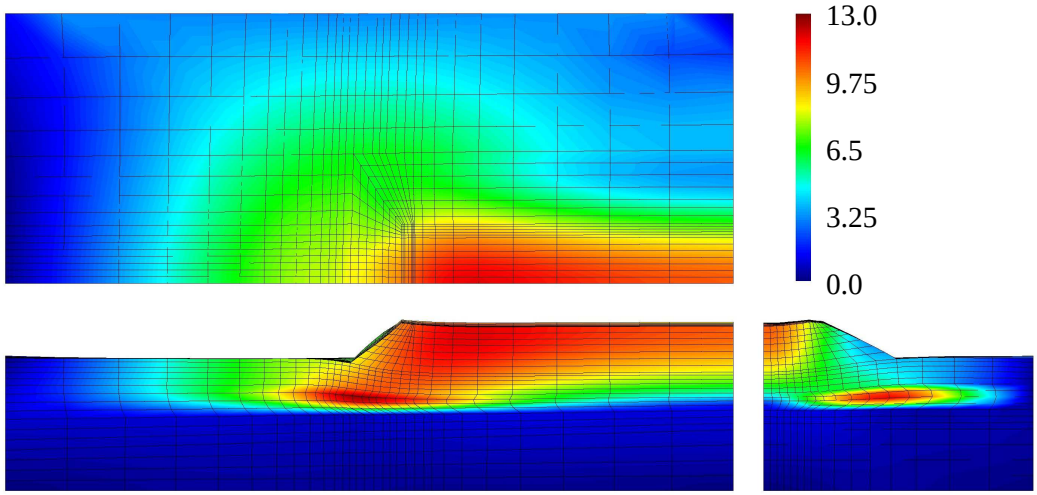

Figure 9.41: Deformed mesh (magnified 25 times) for flat slope embankment-only strength reduction model with contours of displacement magnitude (in cm).

primary direction of the kinematic soil demands, the y-axis is oriented perpendicularly to the symmetry plane, and the z-axis is oriented vertically. These maximum displacements provide further evidence of how the presence of the embankment and bridge foundation affect the overall deformation pattern for the site. Adding the approach embankment without a foundation to restrain its deformation results in the largest deformations in all three directions. The unbalanced loading applied by the embankment causes relatively large de-

Table 9.7: Maximum soil displacements for three strength reduction model configurations at each considered slope.

model type	slope	u_{max} (cm)	v_{max} (cm)	w_{max} (cm)
soil-only	0°	0.5	0.0	1.1
	2.5°	13.4	0.0	4.0
	5°	23.2	0.0	5.0
embankment	0°	12.6	12.3	11.2
	2.5°	22.2	13.1	16.9
	5°	32.8	13.5	22.9
foundation	0°	4.4	12.0	9.5
	2.5°	8.8	12.7	13.1
	5°	13.6	13.1	16.8

formation out from the embankment centerline, and these deformations are only slightly reduced by the presence of the foundation. Vertical slumping of the embankment is more significantly affected by the addition of the foundation, likely due to reductions in the deformations in both lateral directions. The most dramatic effect of the bridge foundation on the site is in reducing the riverward displacements of the soil. As expected, the u_{max} values in the foundation model for each slope are smaller than the corresponding results in the embankment model, but perhaps unexpectedly, these deformations are also smaller than those for the native soil alone at the larger slopes.

The global model results for three strength reduction model configurations demonstrate the importance of the bridge foundation in defining the overall lateral displacement of the system, lending credence to the compatibility-based approach used in the pile pinning analysis procedure. These models also show that the outward displacement of the soil away from the bridge centerline is largely due to the approach embankment alone. The slumping mechanism displayed by these models is a response that was observed at the Puente Mataquito site, and appears to be due primarily to the overall settling of the embankment as the liquefiable layer loses strength, though there is likely an additional component of loss in embankment height due to material moving laterally. This vertical slumping is present in the applied kinematic models, however, the magnitude is small in comparison to the lateral deformations, and the compression of the embankment under the applied displacement profile further obscures any slumping in that set of models.

9.5.2 Foundation Bending Demands

Figures 9.42, 9.43, and 9.44 show the shaft foundation displacement, shear force, and bending moment demands developed for the flat, 2.5°, and 5° slope cases in the strength reduction model. The bending demands shown in these plots are averaged across the four shafts to

get a single set of demands for each case that is representative of the whole. As expected, the larger slopes lead to larger abutment displacements and correspondingly larger shear and moment dema

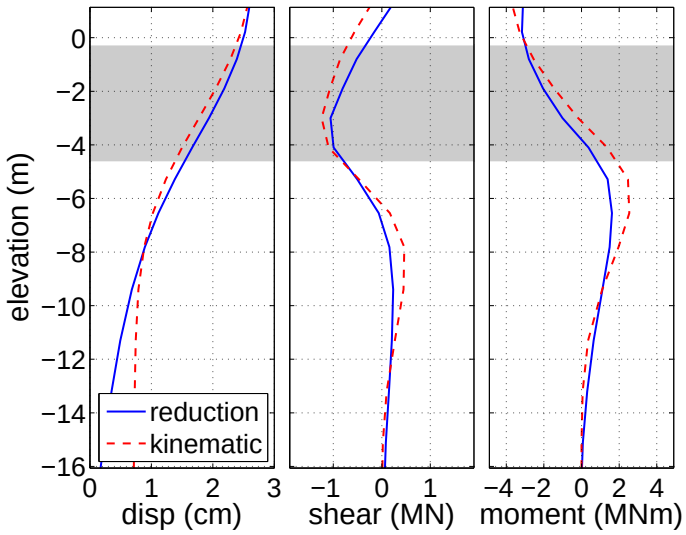

Figure 9.42: Average shaft bending demands for flat strength reduction model. Demands at matching abutment displacement in applied kinematic model are shown for reference.

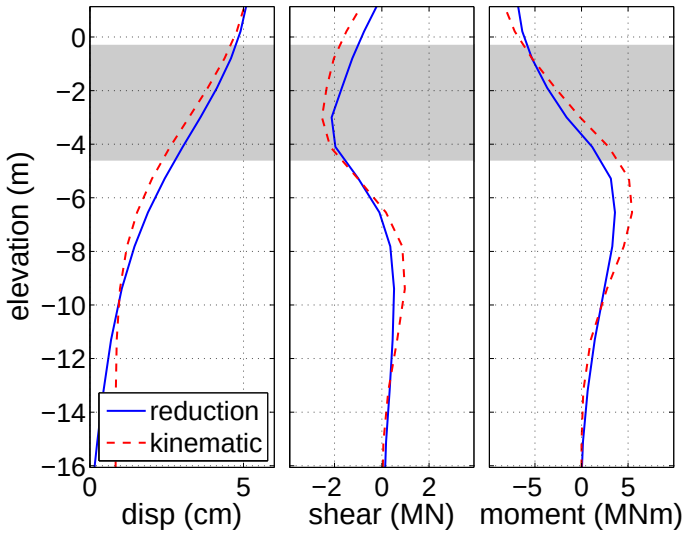

Figure 9.43: Average shaft bending demands for 2.5° strength reduction model. Demands at matching abutment displacement in applied kinematic model are shown for reference.

The bending demands at equivalent abutment displacements in the applied kinematic model are provided in these plots to compare how the two approaches for modeling lateral spreading affect the foundation response. The displacement profiles shown in Figures

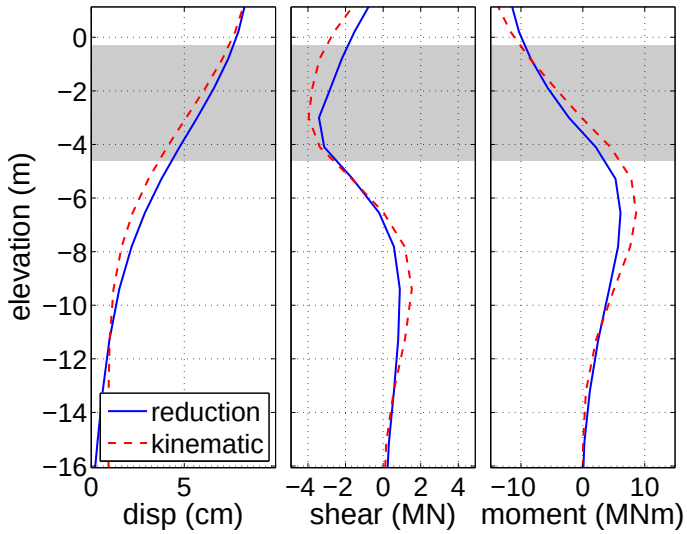

Figure 9.44: Average shaft bending demands for 5° strength reduction model. Demands at matching abutment displacement in applied kinematic model are shown for reference.

9.42, 9.43, and 9.44 demonstrate the primary difference between the two approaches. In the strength reduction models, there is more of a rigid body rotation aspect to the shaft deformation profile. This serves to lessen the shear force and bending moment demands as compared to the applied kinematic model, even though the displacement at the top of the abutment is the same in each case. However, the overall form of shear and moment diagrams correspond between the two approaches, and the maximum demands are of the same order of magnitude.

The evolution of the maximum shear force and bending moment demands in the shaft foundations in the strength reduction model are compared to the corresponding demands in the applied kinematic model in Figures 9.45 through 9.50. These plots reveal some differences between the two lateral spreading modeling approaches that are obscured by considering only the average shaft demands as in Figures 9.42 through 9.44. Group effects are more prominent in the reduction model results, with shafts 2 and 3 on the leading row carrying consistently larger maximum moment demands, and shafts 3 and 4 on the outside of the group carrying larger shear force demands. The form of the maximum shear and moment evolution for the flat case differs from that displayed by the applied kinematic model, however, the difference is minor, and as the abutment displacement increases, the overall similarity between the two data sets increases. Overall, the two modeling approaches return very similar foundation demands for corresponding abutment displacements.

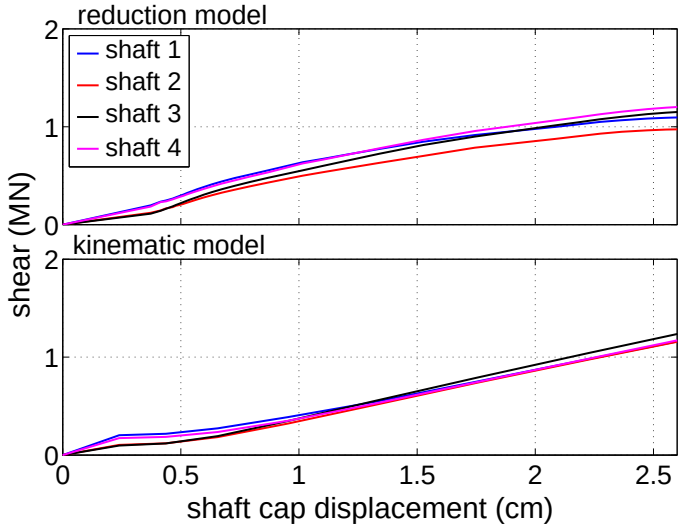

Figure 9.45: Evolution of maximum shear forces for flat strength reduction model and applied kinematic model at matching cap displacement.

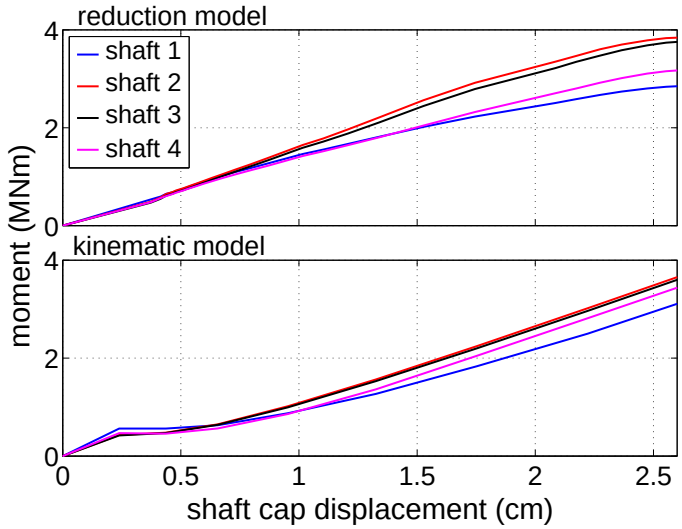

Figure 9.46: Evolution of maximum bending moments for flat strength reduction model and applied kinematic model at matching cap displacement.

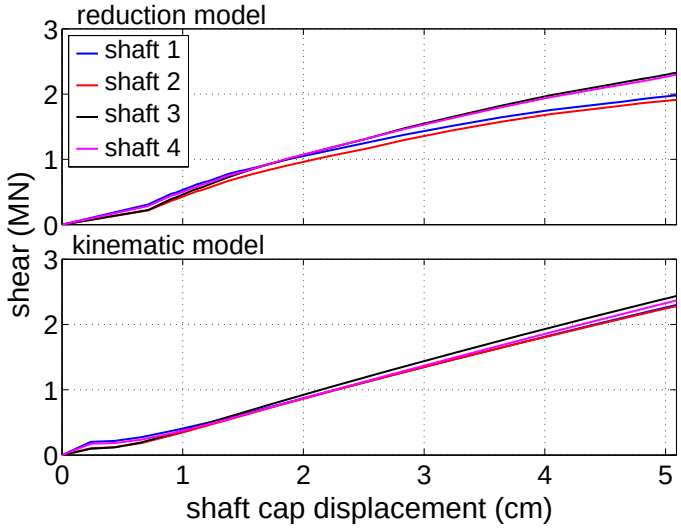

Figure 9.47: Evolution of maximum shear forces for 2.5° slope strength reduction model and applied kinematic model at matching cap displacement.

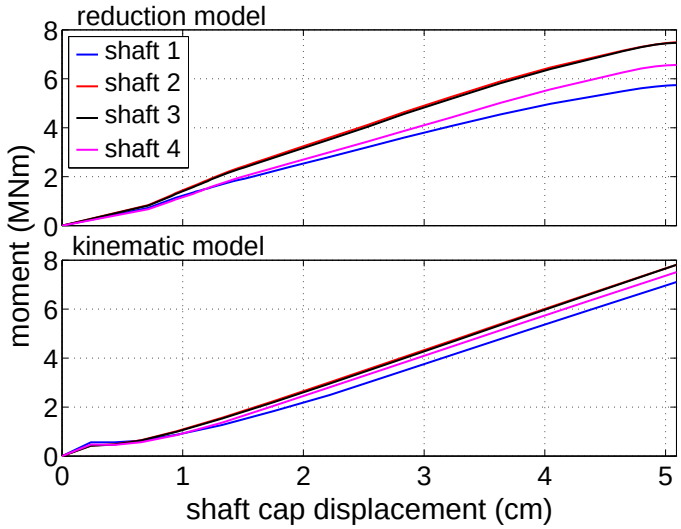

Figure 9.48: Evolution of maximum bending moments for 2.5° slope strength reduction model and applied kinematic model at matching cap displacement.

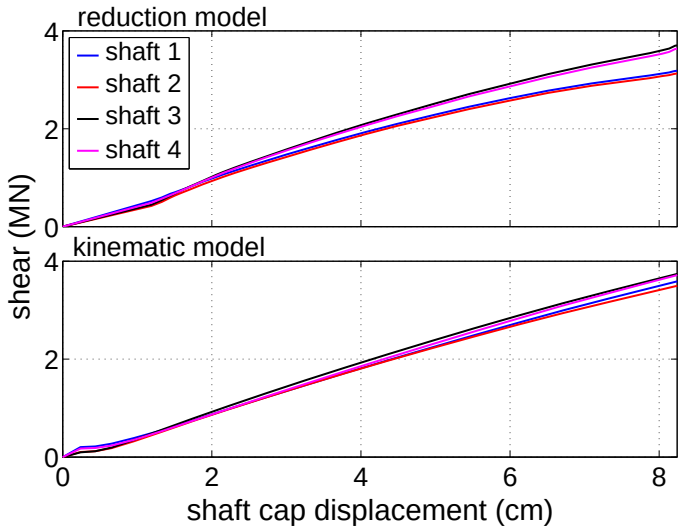

Figure 9.49: Evolution of maximum shear forces for 5° slope strength reduction model and applied kinematic model at matching cap displacement.

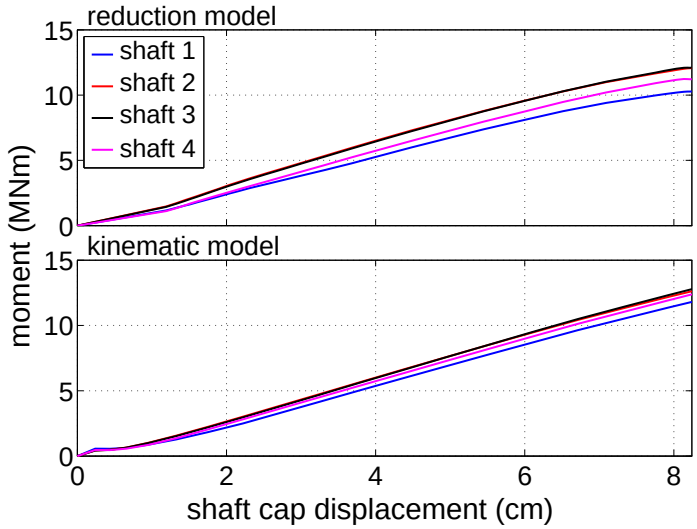

Figure 9.50: Evolution of maximum bending moments for 5° slope strength reduction model and applied kinematic model at matching cap displacement.

9.5.3 Summary of Strength Reduction Model Results

The results obtained from the strength reduction models have identified several significant features related to how a bridge foundation responds to the kinematic demands of lateral spreading, as well as how the presence of the foundation alters the global response of the site. The foundation bending demands obtained from the strength reduction models are essentially the same as those returned from the applied kinematic model at corresponding abutment displacements. This provides increased confidence in the results and observations obtained from the 3D modeling effort.

9.6 Comparison of 3D FE and Pile Pinning Analysis Approaches

The pile pinning model discussed in Section 9.2 and the applied kinematic version of the 3D finite element model discussed in Section 9.4 represent two separate approaches to model the effects of lateral spreading on the southwest abutment and grouped shaft foundation for Puente Mataquito. The shaft foundation bending demands obtained from these two modeling approaches are compared to each other in order to comment on their relative similarities and differences, to demonstrate positive aspects of the pile pinning analysis procedure, and to identify potential flaws or shortcomings of the simplified approach as compared to the 3D model.

9.6.1 Comparison to 5 cm Gap Applied Kinematic Model

Figure 9.51 shows the average shaft bending demands at the closure of the 5 cm gap in the existing and wide embankment geometry cases alongside the shaft bending demands determined from lateral spreading pushover analyses with the BNWF model for the minimum and maximum compatible displacements (0.5 and 29.2 cm, respectively) resulting from all of the cases considered in the pile pinning analysis (see Section 9.2.4). The shaded zones in this plot are the shaft displacement, shear force, and bending moment demands bounded by the minimum and maximum compatible states, and represent the range of demands suggested by the pile pinning analysis. The demands for the mean (11.4 cm) compatible displacement are shown for reference and labeled as *1Davg*. Figure 9.52 shows a similar comparison between the two analysis approaches, however, here the minimum, mean, and maximum compatible displacements for those cases in which $F_{\text{deck}} \neq 0$ (compatible displacements of 0.5, 7.5, and 17.2 cm, respectively) are used to determine the bending demands for the pile pinning approach. Figures 9.53 and 9.54 are constructed similarly, however, the bending demands from the 3D applied kinematic model are those at the end of the analysis when the full 1 m free-field displacement profile has been applied.

The bending demands at the closure of the 5 cm gap in the 3D model fall within the range of demands suggested by the pile pinning analysis, and as shown in Figure 9.52, these

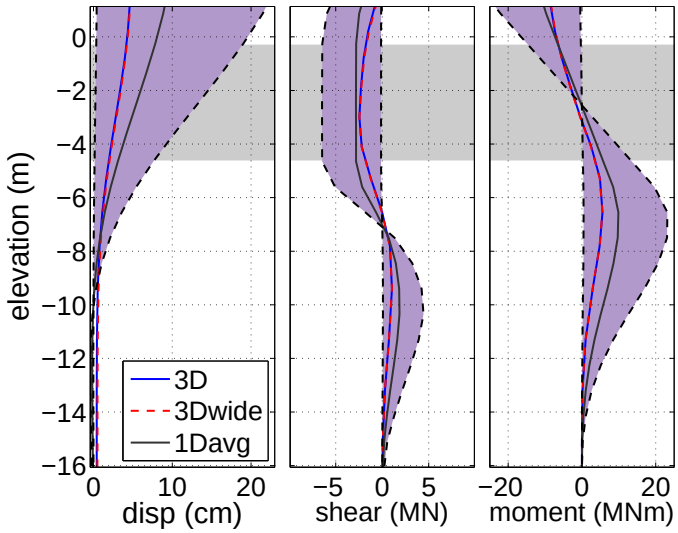

Figure 9.51: Average shaft bending demands at closure of 5 cm gap in applied kinematic model with zone of bending demands suggested by all cases considered in pile pinning model.

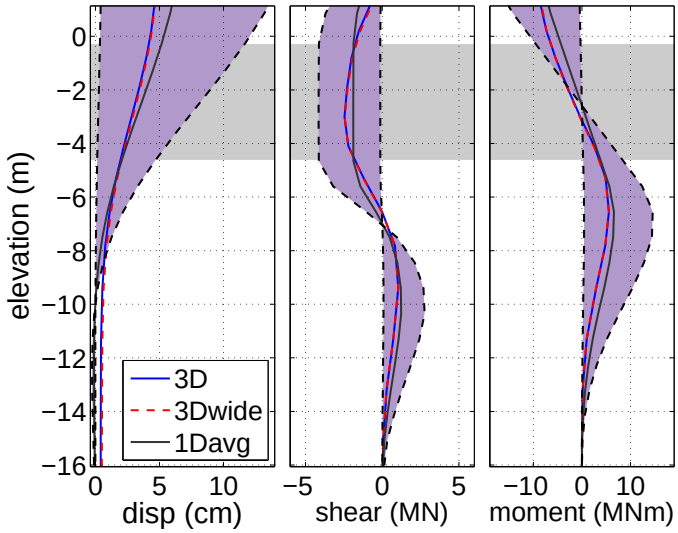

Figure 9.52: Average shaft bending demands at closure of 5 cm gap in applied kinematic model with zone of bending demands suggested by $F_{\text{deck}} \neq 0$ cases considered in pile pinning model.

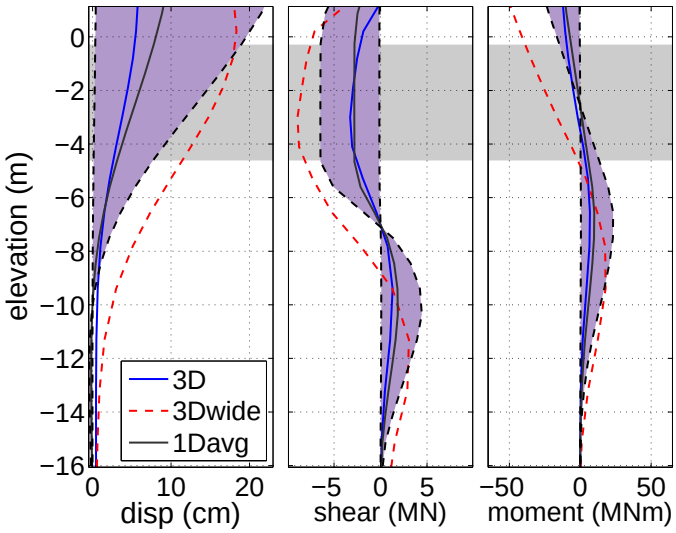

Figure 9.53: Average shaft bending demands at analysis end with 5 cm gap in applied kinematic model with zone of bending demands suggested by all cases considered in pile pinning model.

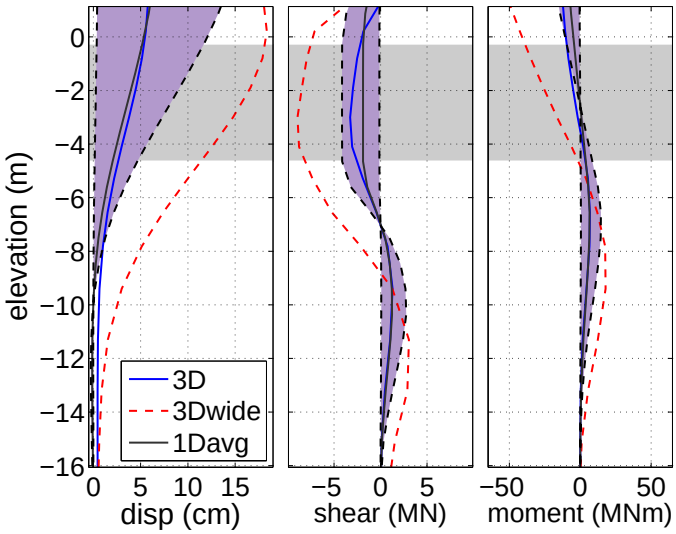

Figure 9.54: Average shaft bending demands at analysis end with 5 cm gap in applied kinematic model with zone of bending demands suggested by $F_{\text{deck}} \neq 0$ cases considered in pile pinning model.

demands are reasonably similar to the mean compatible displacement results from the cases with $F_{\text{deck}} \neq 0$. As previously discussed, and as shown in Figures 9.51 and 9.52, at the closure of the gap, there is little difference between the foundations demands for the two embankment geometries, and both sets of curves correspond reasonably well with the mean pile pinning results. Neither of these observations apply to the end of analysis bending demands shown in Figures 9.53 and 9.54, where the results for the wide embankment geometry fall outside the range of pile pinning demands for both data sets, while the existing embankment geometry demands remain within the suggested ranges and retain their similarity to the mean compatible state for the $F_{\text{deck}} \neq 0$ cases. It is encouraging that the bending demands at the end of the free-field displacement application for the wide embankment geometry, which are similar to what would be expected from a 2D description of the problem, do not correspond to the pile pinning results. This indicates that the pile pinning analysis procedure is capable of estimating foundation bending demands that are consistent with three-dimensional embankment geometry effects.

9.6.2 Comparison to 25 cm Gap Applied Kinematic Model

The pile pinning results do not compare as favorably to the 25 cm gap cases in the applied kinematic model. Figures 9.55 and 9.56 show the bending demand comparisons at the closure of the gap, and Figures 9.57 and 9.58 show these comparisons at the end of the free-field displacement application. At gap closure, the 3D bending demands are slightly larger than those for the maximum considered compatible displacement (29.2 cm), and are well outside of the range defined by the $F_{\text{deck}} \neq 0$ cases. After gap closure, the existing embankment geometry results remain essentially the same relative to the ranges obtained in the pile pinning analysis, while the wide geometry demands become even larger in comparison.

The discrepancies between the two modeling approaches demonstrated in Figures 9.55 through 9.58 emphasize the importance of consideration for the presence of an expansion gap when determining foundation demands developed during lateral spreading. The 25 cm of displacement required to close the gap in the 3D models is larger than all but one of the compatible displacements considered in this comparison, therefore, even the most conservative estimate of foundation bending demands obtained from the pile pinning procedure may be too small when the magnitude of the gap is relatively large. For bridges where the foundation alone does not provide sufficient lateral resistance to embankment deformation, it is likely that the expansion gap will be closed due to lateral movement of the foundation. In this case, a better estimation of the foundation bending demands may be obtained by considering the magnitude of the expansion gap in the compatible displacement used for the final evaluation of the foundation.

A potential solution to this problem may be to consider $F_{\text{deck}} \neq 0$ in the determination of the compatible state, then simply add the gap magnitude to the estimated compatible

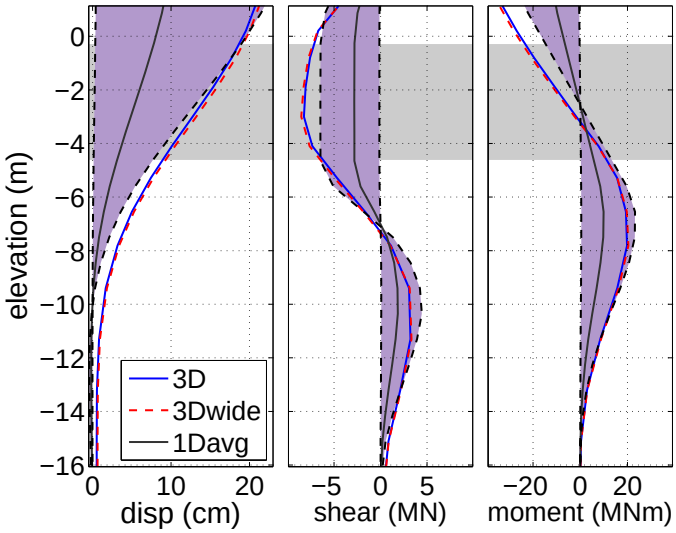

Figure 9.55: Average shaft bending demands at closure of 25 cm gap in applied kinematic model with zone of bending demands suggested by all cases considered in pile pinning model.

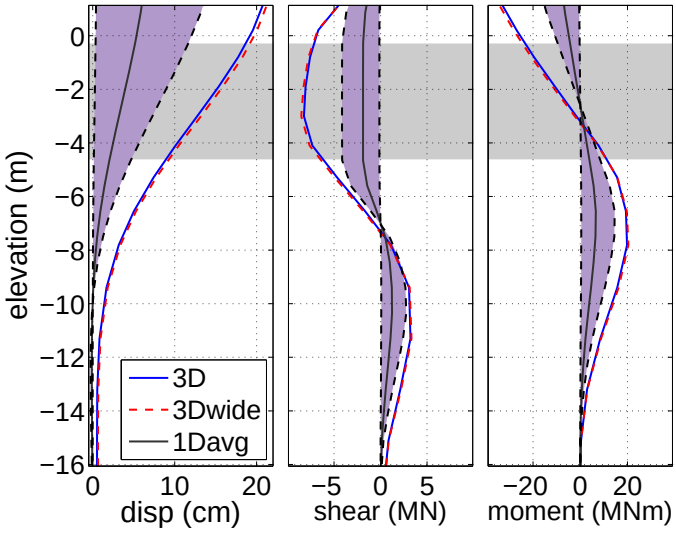

Figure 9.56: Average shaft bending demands at closure of 25 cm gap in applied kinematic model with zone of bending demands suggested by $F_{\text{deck}} \neq 0$ cases considered in pile pinning model.

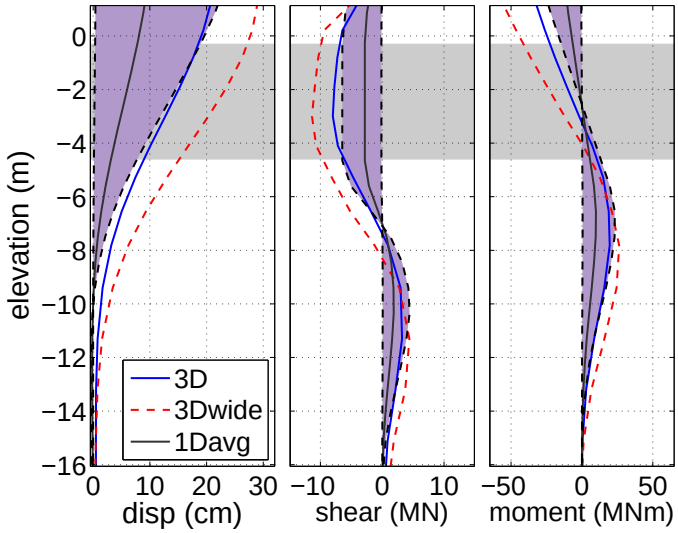

Figure 9.57: Average shaft bending demands at analysis end with 25 cm gap in applied kinematic model with zone of bending demands suggested by all cases considered in pile pinning model.

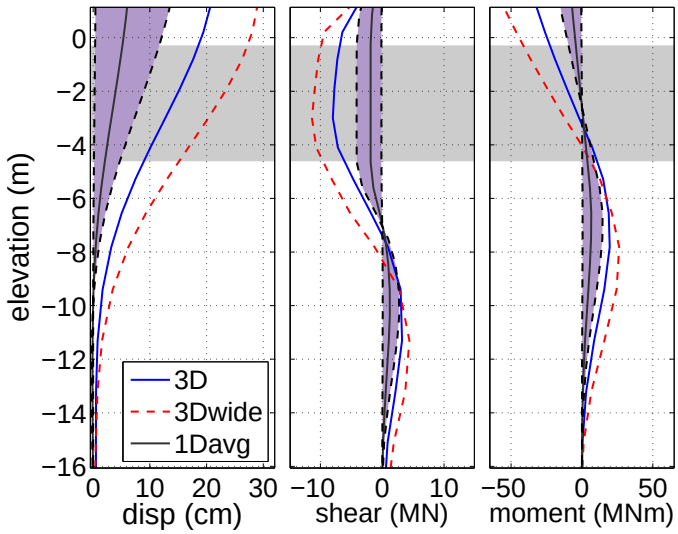

Figure 9.58: Average shaft bending demands analysis end with 25 cm gap in applied kinematic model with zone of bending demands suggested by $F_{\text{deck}} \neq 0$ cases considered in pile pinning model.

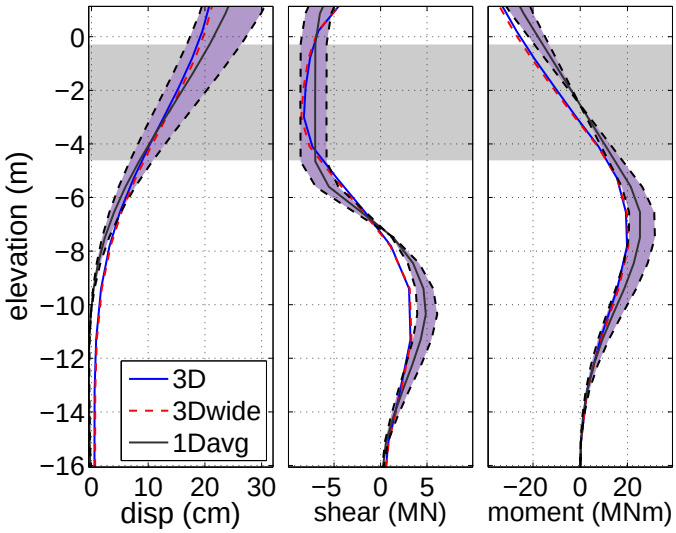

Figure 9.59: Average shaft bending demands at closure of 25 cm gap in applied kinematic model with zone of bending demands suggested by the sum of the compatible displacements for the $F_{\text{deck}} \neq 0$ cases with the gap magnitude.

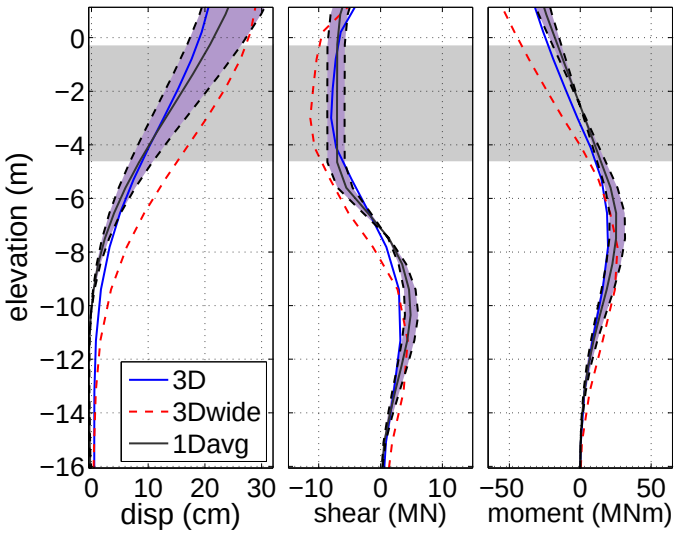

Figure 9.60: Average shaft bending demands analysis end with 25 cm gap in applied kinematic model with zone of bending demands suggested by the sum of the compatible displacements for the $F_{\text{deck}} \neq 0$ cases with the gap magnitude.

displacement and use the resulting displacement to determine the design foundation bending demands in the final BNWF analysis phase. Figures 9.59 and 9.60 demonstrate an application of this approach to the Puente Mataquito foundation. These plots compare the 3D results at the closure of the gap and the end of the analysis, respectively, to the bending demands resulting from adding 25 cm to the compatible displacements for the $F_{\text{deck}} \neq 0$ cases. With this modification to the pile pinning analysis, the shear force and bending demands moment for the 3D embankment geometry now compare more favorably to the pile pinning demands. Figure 9.60 also shows that the structural demands resulting from the wide embankment geometry in the 3D model remain larger than those predicted by the modified pile pinning approach, though the difference is not as great as for the unmodified pile pinning results and the smaller expansion gap.

The potential solution demonstrated here is rather simplistic, and further comparative studies are required to determine if this is a viable solution for general use, however, it appears to effectively introduce the effects of the 25 cm expansion gap into the pile pinning analysis for the foundation and site geometry at Puente Mataquito. With further research, the proposed solution of adding the gap distance to the compatible displacement value may prove to be a successful approach for dealing with lateral spreading design of bridges with larger expansion gaps.

9.7 Summary

The response of the southwest abutment at Puente Mataquito to lateral spreading was evaluated using two analysis approaches: simplified pile pinning analyses in which the foundation is represented using a BNWF approach, and 3D finite element analyses that consider the full geometry of the site. The results from these analyses were used to gain insights into the mechanisms that govern the response of abutment and foundation during the kinematic loading of lateral spreading.

The 3D FEA for the abutment demonstrated that there is a tangible difference in the foundation demands and soil deformation due to consideration of the three-dimensional embankment geometry. These analyses identified important mechanisms leading to this reduction in demands. During the simulated lateral spreading events, rather than pushing directly into the abutment and foundation, the embankment slumps vertically and deforms in the outward lateral direction, thus reducing the foundation demands. The pinning resistance of the foundation was also demonstrated using 3D models that considered gradual loss of shear strength and stiffness in the liquefied layer. The 3D modeling effort also showed how the presence of a bridge deck expansion gap affects the response of the system and the foundation, and identified the importance of the lateral resistance of the bridge deck on the response of the site during lateral spreading.

The pile pinning analysis for the abutment was used to demonstrate that the application

of this approach to an actual problem is not quite as simple as it may seem from a theoretical viewpoint, as seemingly minor changes in modeling choices, e.g., the chosen method of slope stability analysis, resulted in different compatible solutions. To overcome the observed variability in the compatible displacements predicted by this procedure, an approach is proposed in which the final design displacement is obtained as an average value from an array of compatible states computed using different assumptions. This proposed method requires many individual analyses for the design of a single foundation, however, the pushover and slope stability analyses involved in the pile pinning procedure are relatively inexpensive in terms of time and computational resources. Through comparison to the results from 3D FEA, it was shown that when applied carefully, the pile pinning procedure is able to predict foundation bending demands that correspond to a three-dimensional description of the problem, especially for smaller deck expansion gaps.

When performing the design of a bridge foundation using the pile pinning analysis procedure, it would be useful to have an independent prediction of how much pinning resistance can be expected for a particular combination of foundation, soil profile, and embankment geometry. The parameter study introduced in the following chapter addresses an approach to estimating the expected difference between the foundation displacement, shear force, and bending moment demands resulting from 2D and 3D descriptions of the problem. This difference can be interpreted as an indication of the amount of lateral pinning resistance available for a particular site.

Chapter 10

3D PARAMETER STUDY OF GEOMETRIC EFFECTS ON FOUNDATION RESPONSE TO LATERAL SPREADING

The 3D finite element models created and analyzed for Puente Mataquito have identified that the approach embankment geometry can greatly influence the response of a bridge foundation to the kinematic demands of lateral spreading. Consideration for 3D embankment geometry was shown to produce structural foundation demands that are reduced in comparison to a two-dimensional description of the problem. The results obtained from the Mataquito case study provide a useful evaluation of how these 3D effects are manifested at that particular site, however, a general description of the problem cannot be gained from a single combination of bridge foundation, embankment size, and soil profile. In order to further analyze how the site geometry affects foundation response, a parameter study is considered using a series of 3D finite element models with various combinations of shaft diameter and site geometry. These models are simplified in comparison to the Puente Mataquito models, however, the fundamental aspects of the approach embankment problem are captured.

10.1 Parameter Study Model Overview

The parameter study models consider a single pile or shaft foundation embedded in a layered soil profile with an embankment placed above the upper soil layer. This embankment is built with a 2H:1V side slope and extends across the length of the mesh as shown in Figure 10.1. Different combinations of embankment width, shaft diameter, liquefied layer depth, and liquefied layer thickness are considered to characterize the influence of site geometry on the response of the single shaft to lateral spreading.

10.1.1 Considered Site Geometries

Figure 10.2 shows a summary of the soil profiles and embankment geometries considered in the parameter study. The soil profile is varied with respect to the liquefied layer thickness, t, and the depth, z, to the top of the liquefied layer (dark blue layer in the plot). Three values of each parameter are selected: $t = 1.0,\ 2.0,\ 3.0$ m and $z = 1.0,\ 2.0,\ 3.0$ m. For each of these nine soil profiles, three embankment crest widths, $w = 4.0,\ 8.0,\ 16.0$ m, are considered in addition to a fourth case in which the embankment extends across the full width of the model (35.0 m). These full width cases are used to simulate a two-dimensional description

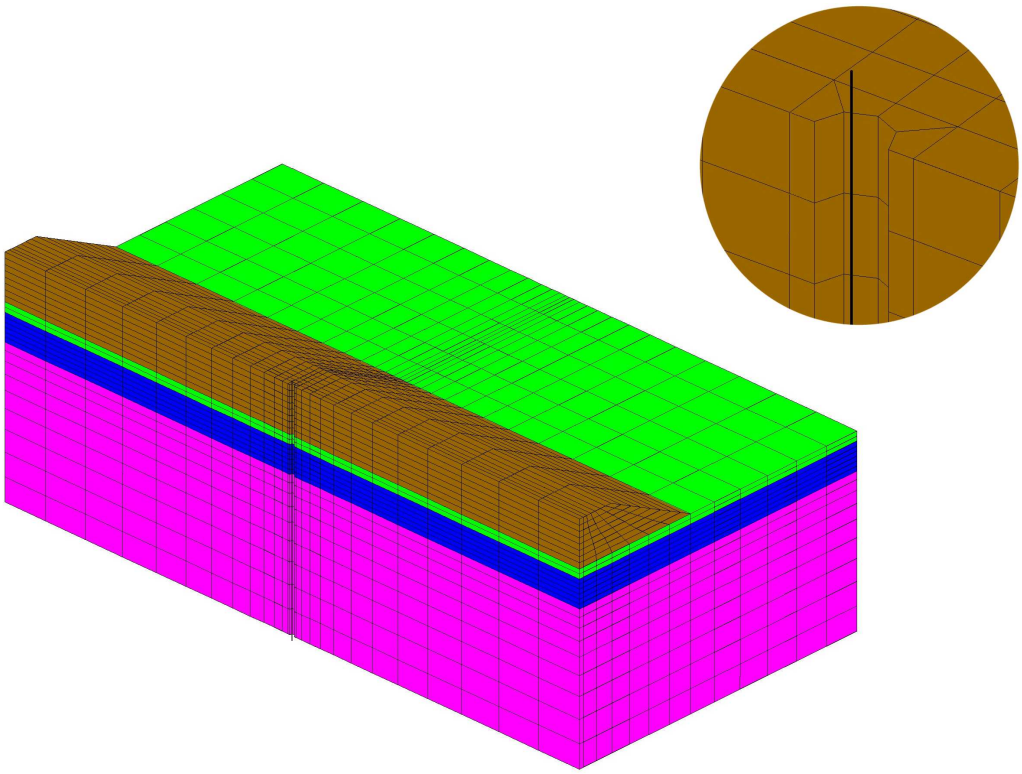

Figure 10.1: Example 3D finite element mesh used in the parameter study.

of the problem, and are compared to the other embankment configurations in order to assess the reduction in foundation bending demands relative to the plane strain case. Models are generated for each of the 36 site geometric configurations with consideration of two shaft foundation designs, leading to 72 distinct cases in the parameter study. Two shaft diameters are considered, $D = 0.6,\ 1.4$ m, to assess the effects of foundation size, and each shaft is based on a separate template cross-section design to assess the effects of foundation bending stiffness on the response of the system.

10.1.2 Boundary and Loading Conditions

The boundary and loading conditions for the parameter study models are similar to those used in the applied kinematic model for Puente Mataquito. The nodes on the base of the mesh are fixed against vertical translation, and elemental body forces are used to consider the effects of gravity on the soil continuum. Symmetry is considered as shown in Figure 10.1, with the symmetry plane cutting through the center of the shaft foundation such that only one half of the shaft is considered in the model. The nodes on the vertical boundary opposite the symmetry plane are fixed against all horizontal translation, and the nodes on the remaining non-symmetry vertical boundaries are fixed against out-of-plane translations only. The effects of lateral spreading are simulated using the applied kinematic approach introduced in the discussion of the Puente Mataquito modeling effort, in which a set dis-

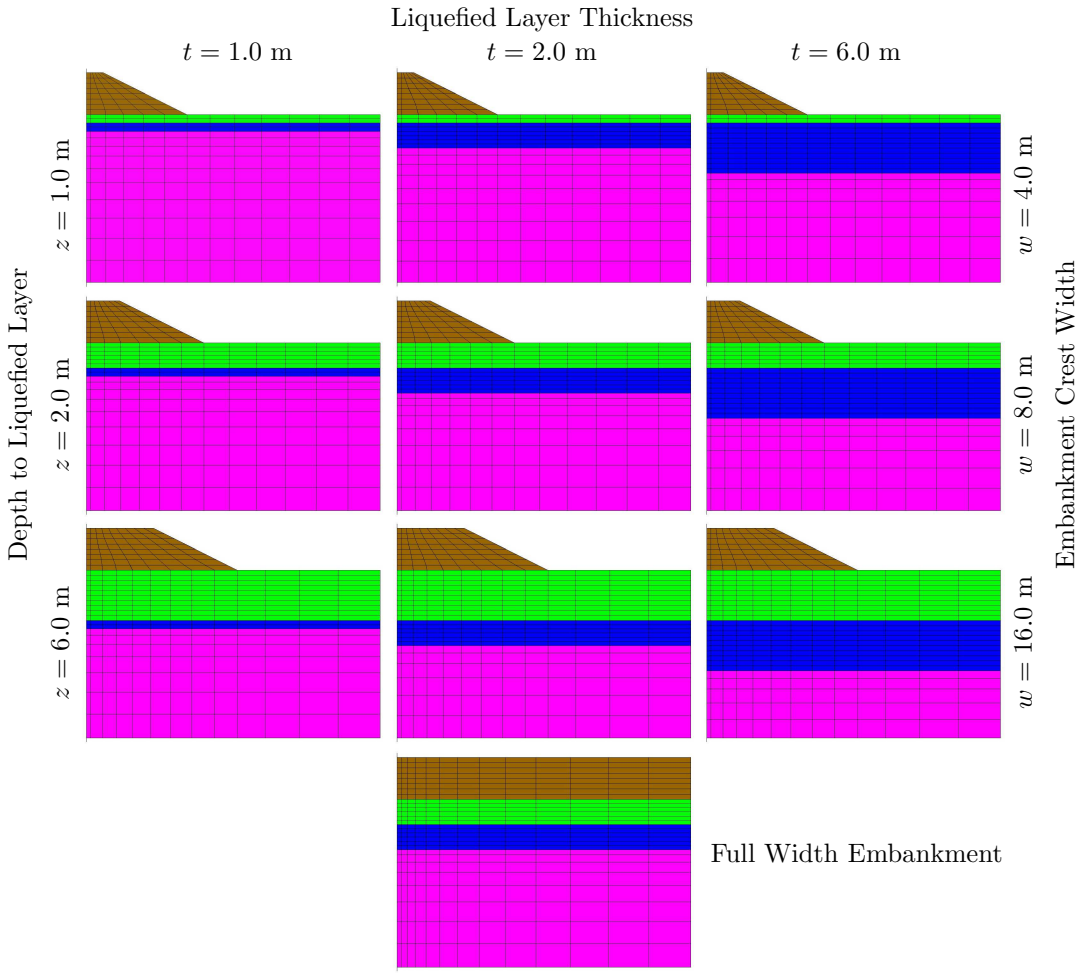

Figure 10.2: Summary of cases considered in the parameter study.

placement profile is gradually applied to the non-symmetry vertical boundaries of the mesh. This displacement profile is constant above the assumed liquefied layer, linearly-increasing across the liquefied layer, and zero below this point. The soil mesh boundaries are placed 35 m away from the shaft centerline in both horizontal directions, and the mesh is 20 m deep vertically with a 5 m tall embankment for all configurations.

The shaft foundation is modeled with a displacement-based beam-column element that interfaces with the surrounding solid elements via the beam-solid contact elements of Petek (2006). A detail of the mesh immediately surrounding the shaft centerline is provided in Figure 10.1. As shown, a semi-circular space is built-in to the solid element mesh to consider the physical size of the shafts considered in the study. The nodes for the beam-column elements are fixed against translation normal to the symmetry plane, and rotations about the direction of loading and the axis of the shaft. The beam node at the base of the model is fixed against vertical translation, and the beam node at the top of the model is fixed against rotations in the plane of loading to represent a rigid connection to a hypothetical shaft cap or superstructure body.

Table 10.1: Model properties for soil layers in parameter study.

Layer	ρ (Mg/m^3)	ϕ (°)	$G_{\max}$ (MPa)	$K_{\max}$ (MPa)	S_u (kPa)
dry loose sand	1.7	32	75	200	–
sat. loose sand	1.7	–	6.0	175	5.0
dense sand	2.0	38	100	300	–
embankment fill	1.9	48	130	390	–

Table 10.2: Model material and section properties in parameter study shaft foundations.

Shaft diameter	A (m^2)	E (GPa)	G (GPa)	I (m^4)
0.6 m	0.15	31.3	12.5	0.0038
1.4 m	0.74	28.7	11.5	0.0869

10.1.3 Soil Properties

Generic soil properties are assumed for the various soil layers in the model. Four layers are defined: the embankment fill, a dry crustal sand layer, a liquefiable saturated loose sand layer, and an underlying denser sand layer. The constitutive models of Elgamal et al. (2003) discussed in Section 7.1 are used to model the material response of all considered soils. The embankment fill, crust, and dense sand layers are modeled with Drucker-Prager type failure surfaces with friction angle dependent strengths, while the liquefied loose sand layer is modeled as a pressure independent material with a residual undrained shear strength defining the bounds of the failure surface. As with the applied kinematic model for Puente Mataquito, the liquefied layer is assigned residual shear strength and stiffness properties at the beginning of the analysis, as it is assumed that liquefaction has already occurred.

10.1.4 Shaft Foundation Models

Two template shaft models are used in the parameter study, a 0.6 m diameter shaft and a 1.4 m diameter shaft. These shaft models are based on actual deep foundation designs, and consider linear elastic bending stiffness values determined from the initial tangent of the nonlinear moment curvature responses of the template cross-sections. The material and section properties used to define the shaft models are provided in Table 10.2. For each shaft, the cross-sectional area, A, and second moment of the area, I, are determined based on half of the shaft cross-section for consistency with the symmetry conditions assumed in the model. The shaft elastic modulus values are chosen such that the linear elastic bending stiffness, EI, corresponds to the initial bending stiffness of the template cross-sections, and the elastic shear modulus, G, for each shaft is based on an assumed Poisson's ratio of 0.25. Further details on the template cross-section designs used to define these shaft models are discussed in McGann et al. (2012).

10.2 General Effects of Site Geometry on Foundation Response

The effects of approach embankment and soil profile geometry on the flexural response of the shaft foundations are assessed through comparisons of the results obtained from the various cases considered in the parameter study. These comparisons are made both qualitatively and quantitatively, and the discussion of the observed effects is organized into several sections in order to isolate the individual effects of each considered geometric aspect.

10.2.1 Summary of Global Model Response

In general, the results of the parameter study demonstrate that the presence of the shaft foundation alters the soil deformation field such that only the material near the boundaries experiences the full free-field displacement applied to the model. This resistance varies depending on the geometric configuration of the site, as certain combinations lead to greater and more widespread resistance, while others indicate a less significant effect. To demonstrate the range of responses obtained, Figures 10.3 and 10.4 show the deformed mesh for two models in which the only difference is the embankment width. The soil profiles shown in these plots consider a 0.6 m diameter shaft with a 3 m thick liquefied layer located 1 m below the base of the embankment fill.

The mesh shown in Figure 10.3 considers an embankment defined with $w = 8$ m. In this case, the shaft provides substantial resistance to the lateral deformation of the soil, as the deformations near the shaft are approximately one-quarter of the free-field displacement, and this effect is manifested over a fairly large portion of the soil domain. In contrast, Figure 10.4, which shows the same results for the full width embankment, demonstrates that with the 2D geometry, the shaft offers only minimal lateral resistance as nearly the entire soil domain experiences the free-field deformation profile. This general trend of increased embankment width leading to a more homogeneous soil deformation field corresponds to observations made using the Puente Mataquito models.

10.2.2 Effects of Embankment Crest Width

The general effects of increasing embankment width are demonstrated through a comparison of Figures 10.3 and 10.4, however, it is also of interest to assess the differences in how the three considered embankment crest widths affect the embedded shaft foundations. The effects of the different embankment sizes on the foundation demands are demonstrated in Figures 10.5 through 10.10, which show the shaft bending demand profiles (displacement, shear force, and bending moment) for the indicated parameter combinations. In these plots, *w1* through *w4* correspond to the four embankment crest widths ordered from low to high (4, 8, 16, and 35 m, respectively), and the liquefied layer thickness is indicated by the extents of the gray shaded zones. Each individual figure considers the combination of liquefied layer

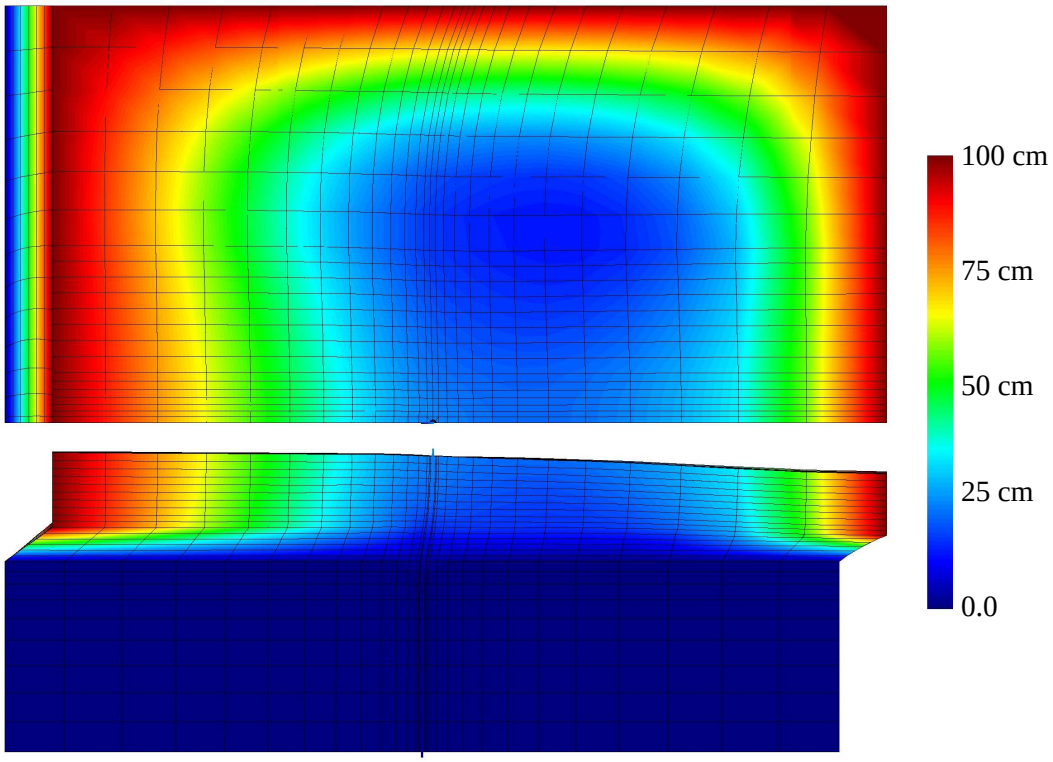

Figure 10.3: Deformed mesh (magnified 4 times) with contours of horizontal deformation for $w = 8$ m case with $D = 0.6$ m, $z = 1$ m, and $t = 3$ m.

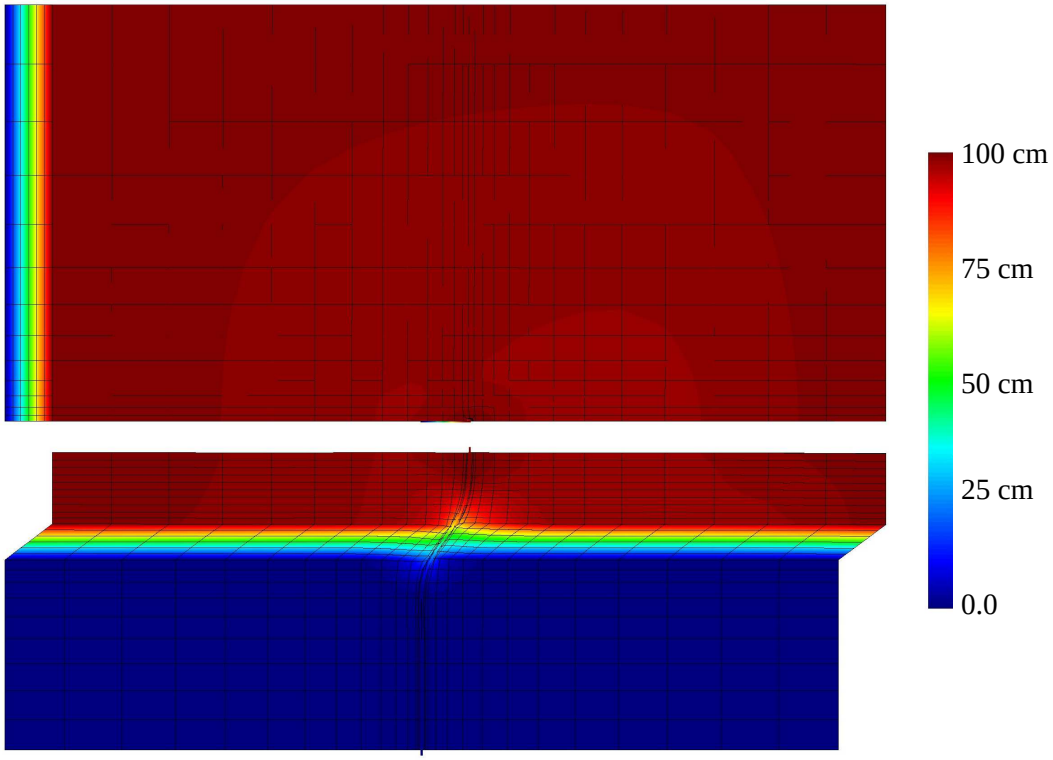

Figure 10.4: Deformed mesh (magnified 4 times) with contours of horizontal deformation for full width case with $D = 0.6$ m, $z = 1$ m, and $t = 3$ m.

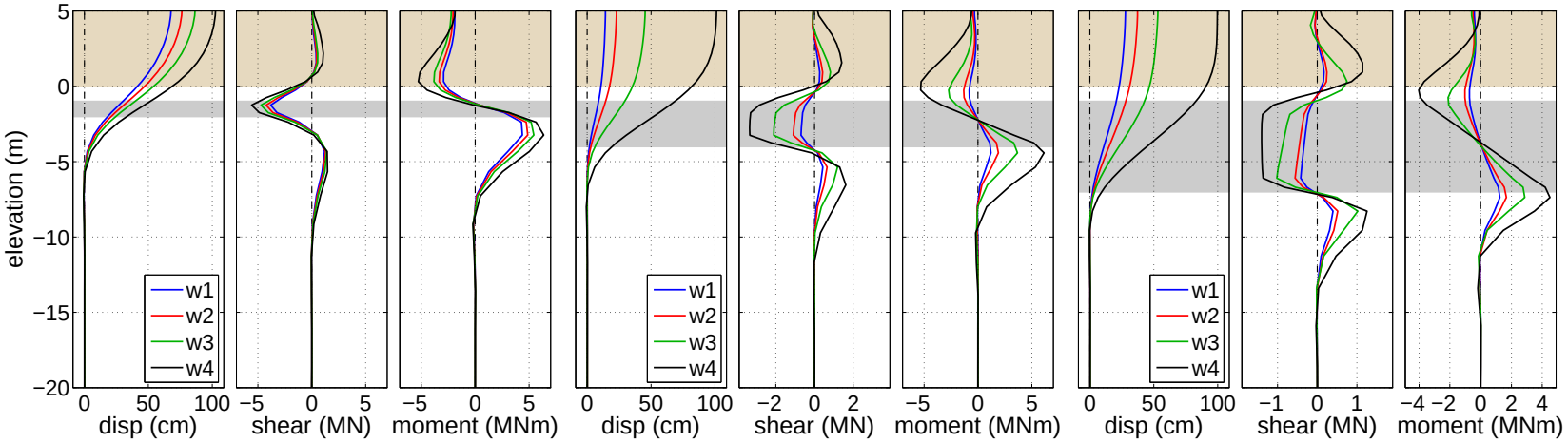

Figure 10.5: 0.6 m dia. shaft bending demands for three liquefied layer thicknesses and four embankment widths with $z = 1$ m.

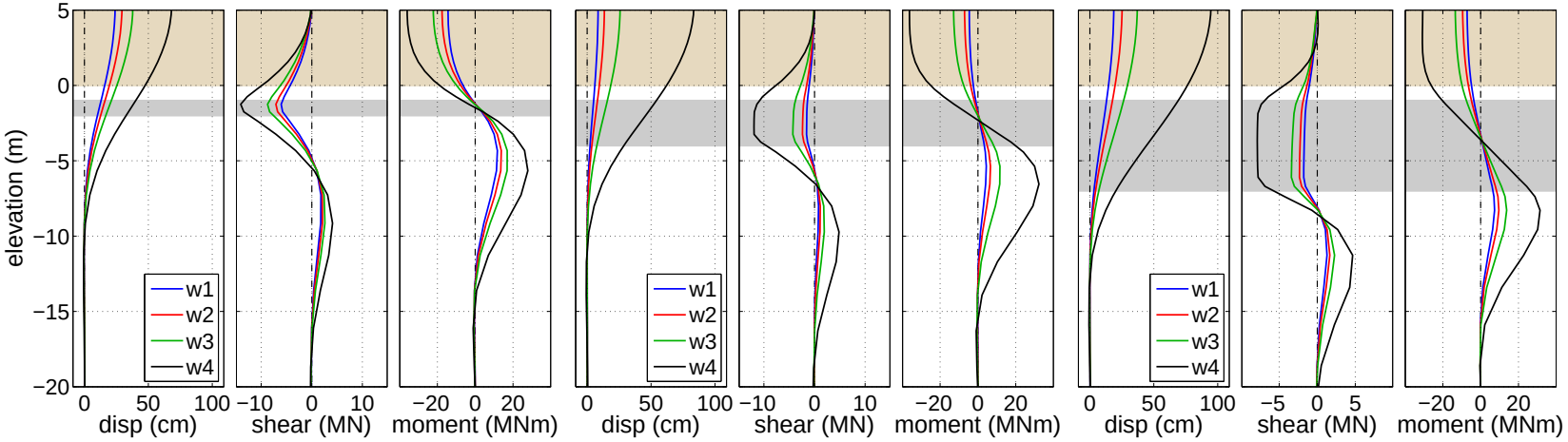

Figure 10.6: 1.4 m dia. shaft bending demands for three liquefied layer thicknesses and four embankment widths with $z = 1$ m.

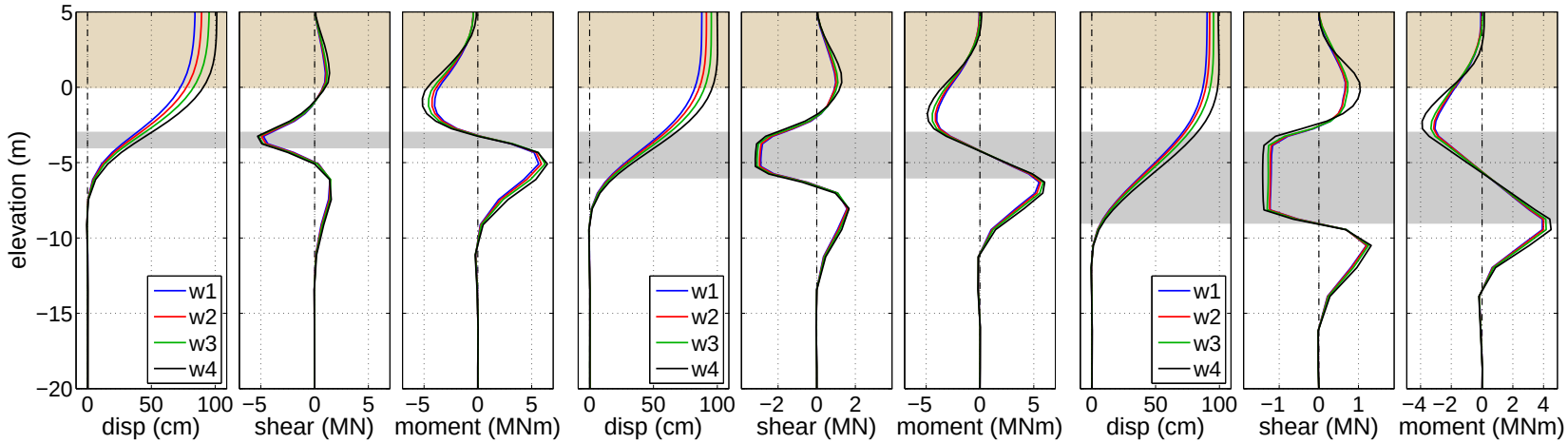

Figure 10.7: 0.6 m dia. shaft bending demands for three liquefied layer thicknesses and four embankment widths with $z = 3$ m.

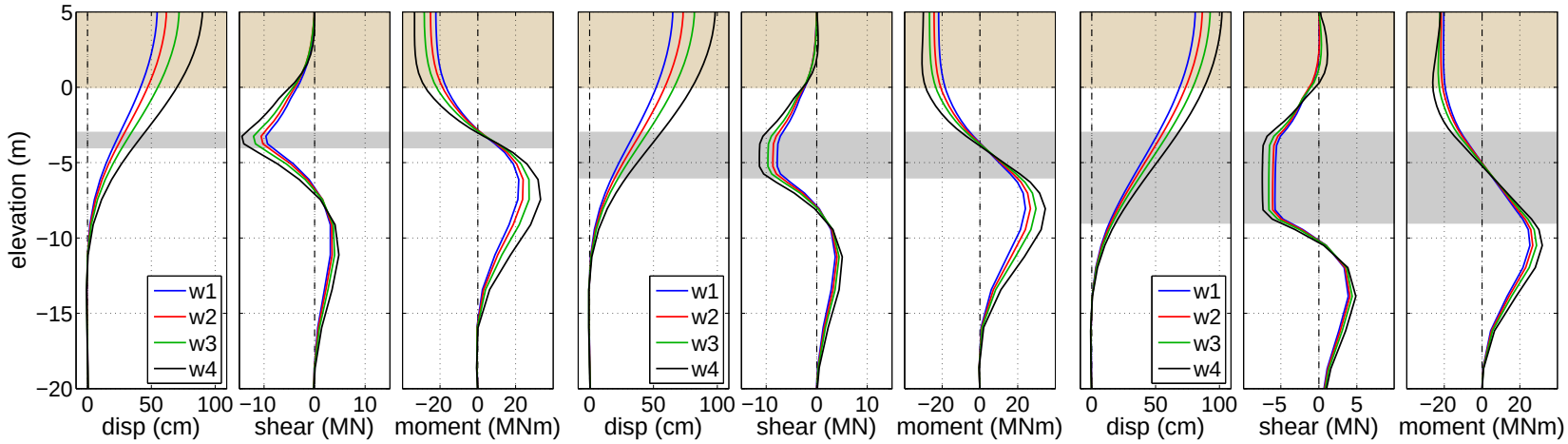

Figure 10.8: 1.4 m dia. shaft bending demands for three liquefied layer thicknesses and four embankment widths with $z = 3$ m.

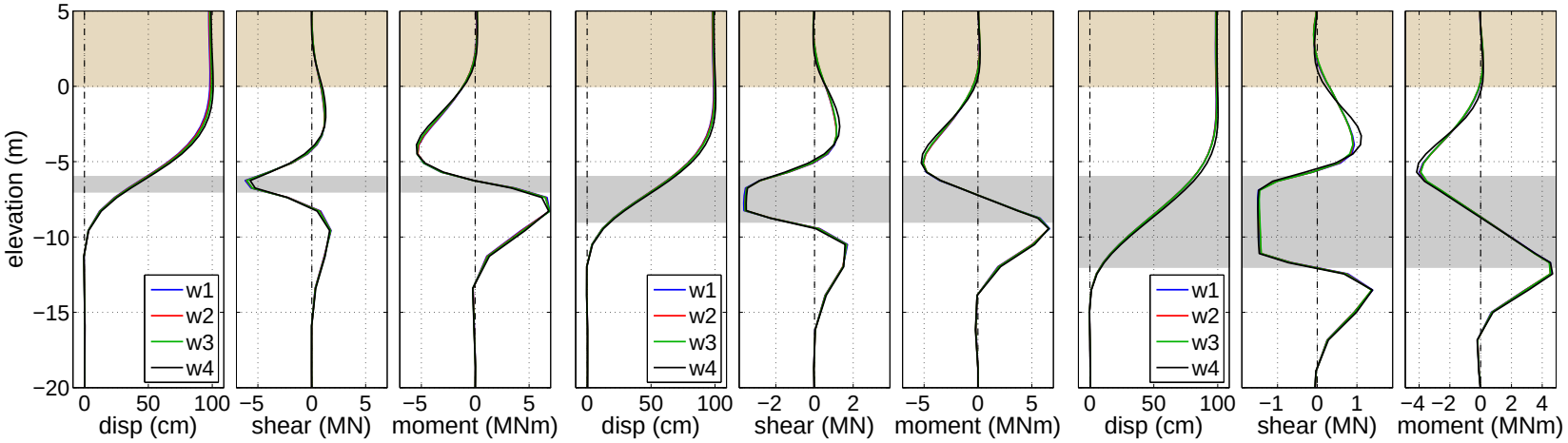

Figure 10.9: 0.6 m dia. shaft bending demands for three liquefied layer thicknesses and four embankment widths with $z = 6$ m.

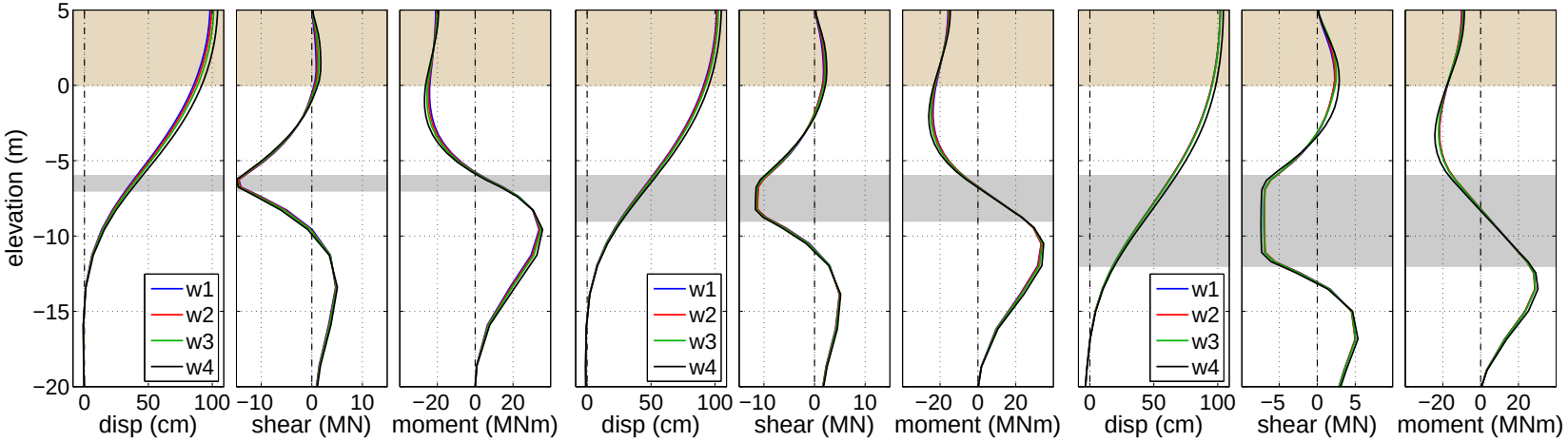

Figure 10.10: 1.4 m dia. shaft bending demands for three liquefied layer thicknesses and four embankment widths with $z = 6$ m.

depth, z, and shaft diameter, D, noted in its caption, and the portion of the soil profile corresponding to the approach embankment is shaded in brown for reference.

As expected based on the Puente Mataquito results and the soil deformation fields of Figures 10.3 and 10.4, increased embankment width leads to increased shaft bending demands. This is most clearly seen in Figures 10.5 and 10.6, which consider the shallowest liquefied layer depth, though it can been seen to some extent in all of the bending demand summary plots. The general forms of the displacement, shear force, and bending moment profiles remain similar for the four widths, however, the magnitudes become larger, and, in general, for constant D, z, and t, the locations of the shear and moment inflection points move further apart as the embankment becomes wider.

Figures 10.11 through 10.16 support some of these observations by showing how the maximum displacement, shear force, and bending moment demands change with increasing free-field displacement for each considered combination of shaft design and soil configuration. As shown, perhaps with the exception of the first few analysis steps, for all levels of free-field displacement, larger embankment widths lead to larger maximum bending demands. The maximum displacement, shear, and moment demands are affected similarly by changes in w, and it appears that for constant values of D, z, and t, the relative difference between the results for each embankment width remains nearly constant over the course of the free-field displacement application. In all cases, the bending demands obtained from the wide embankment geometry are greater than or equal to the bending demands for the 3D embankment geometries.

10.2.3 Effects of Liquefied Layer Depth

The depth of the liquefied layer plays an important role in defining how changes in embankment crest width affect the embedded foundation during lateral spreading. For the cases with shallow liquefied layers, the width of the embankment is very influential to the shaft response. As shown in Figures 10.5 and 10.11 for the 0.6 m shaft, and Figures 10.6 and 10.14 for the 1.4 m shaft, there are significant differences in the shaft bending demand profiles and in the maximum bending demands for the four considered crest widths. As the depth to the liquefied layer is increased, the differences between the shaft bending demands resulting from the four widths become less significant. With $z = 3$ m (e.g., Figures 10.7 and 10.12), there is less variation in the shaft demands for increasing values of w than for the corresponding cases with $z = 1$. With $z = 6$ m (e.g., Figures 10.9 and 10.13), there is almost no difference in the demands manifested by the four crest widths.

These observations suggest that for these single shaft cases, there is a limiting liquefied layer depth at which the 3D embankment effects are no longer a significant factor in defining the structural demands in the foundation. When the liquefied layer is relatively shallow, the approach embankment is the primary source of kinematic demands on the shaft foundation

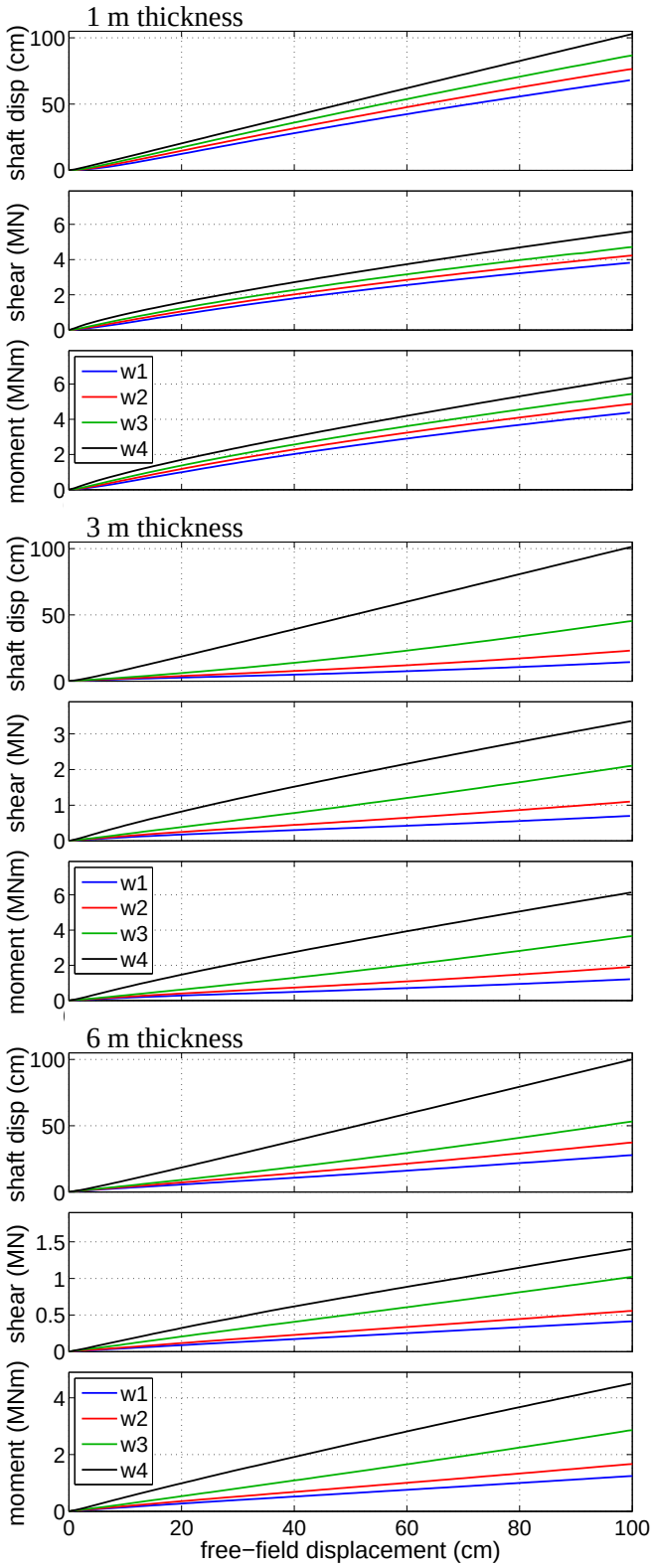

Figure 10.11: Maximum shaft bending demands for three liquefied layer thicknesses and four embankment widths with $D = 0.6$ m and $z = 1$ m.

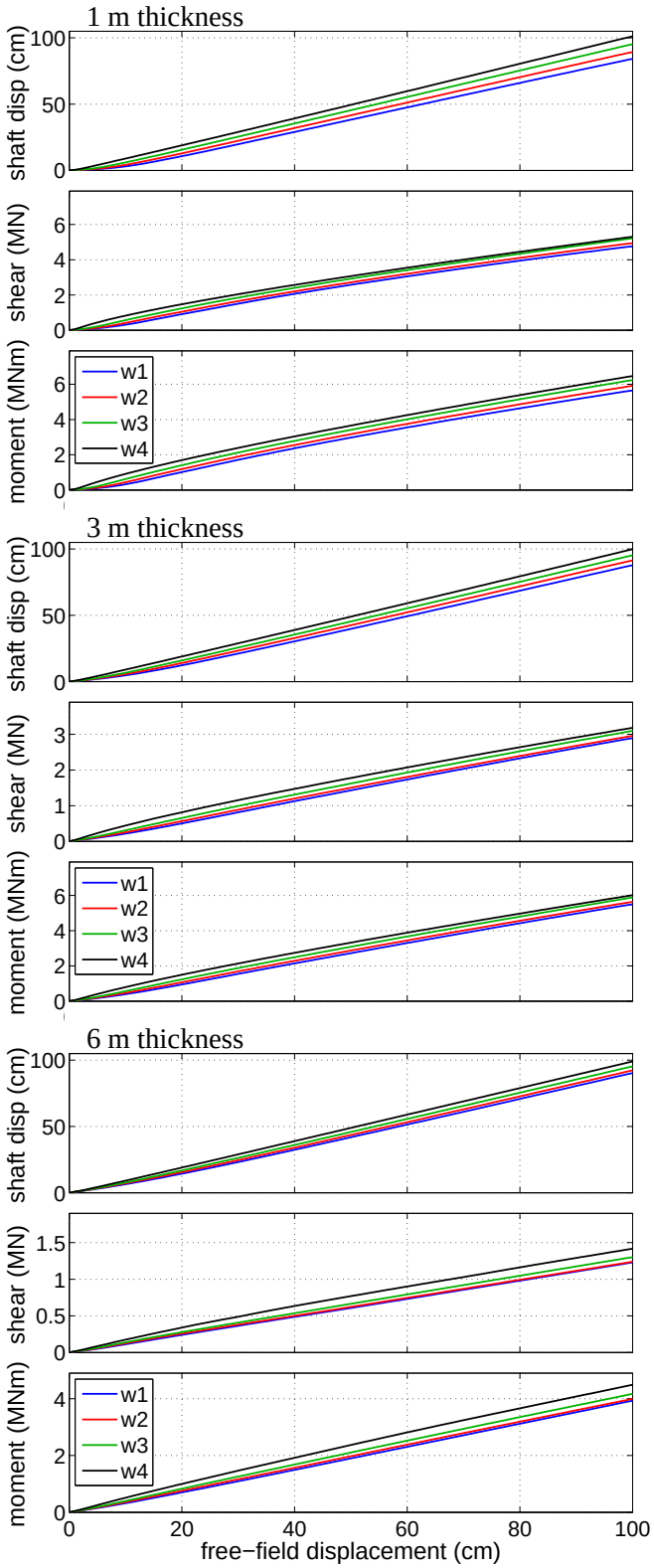

Figure 10.12: Maximum shaft bending demands for three liquefied layer thicknesses and four embankment widths with $D = 0.6$ m and $z = 3$ m.

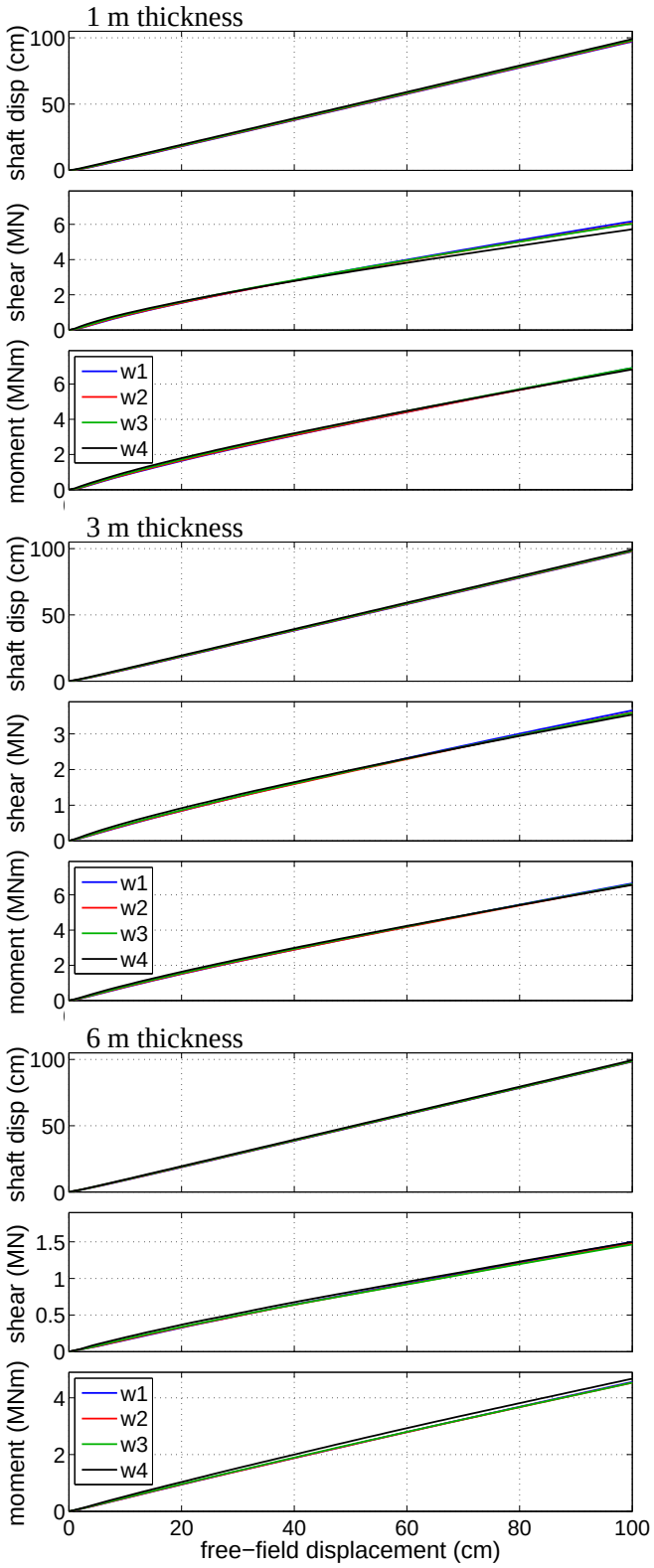

Figure 10.13: Maximum shaft bending demands for three liquefied layer thicknesses and four embankment widths with $D = 0.6$ m and $z = 6$ m.

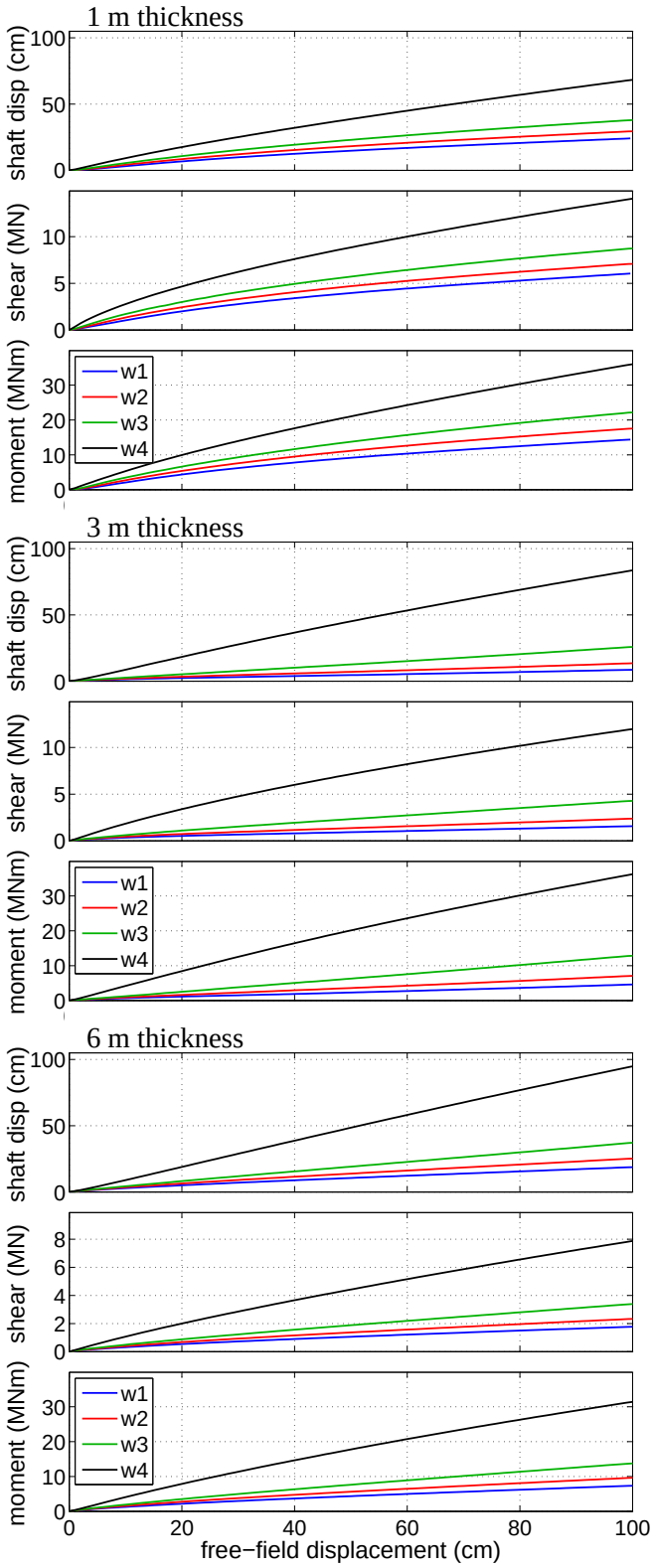

Figure 10.14: Maximum shaft bending demands for three liquefied layer thicknesses and four embankment widths with $D = 1.4$ m and $z = 1$ m.

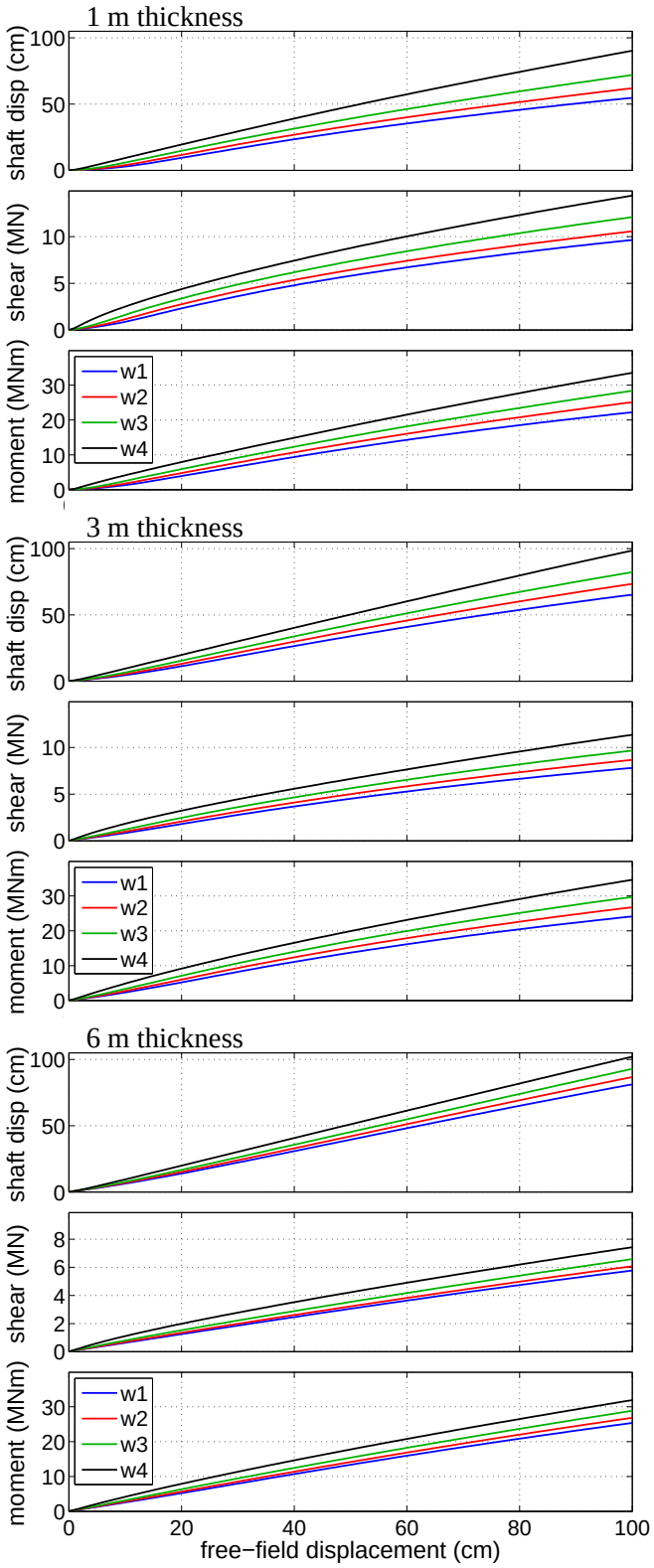

Figure 10.15: Maximum shaft bending demands for three liquefied layer thicknesses and four embankment widths with $D = 1.4$ m and $z = 3$ m.

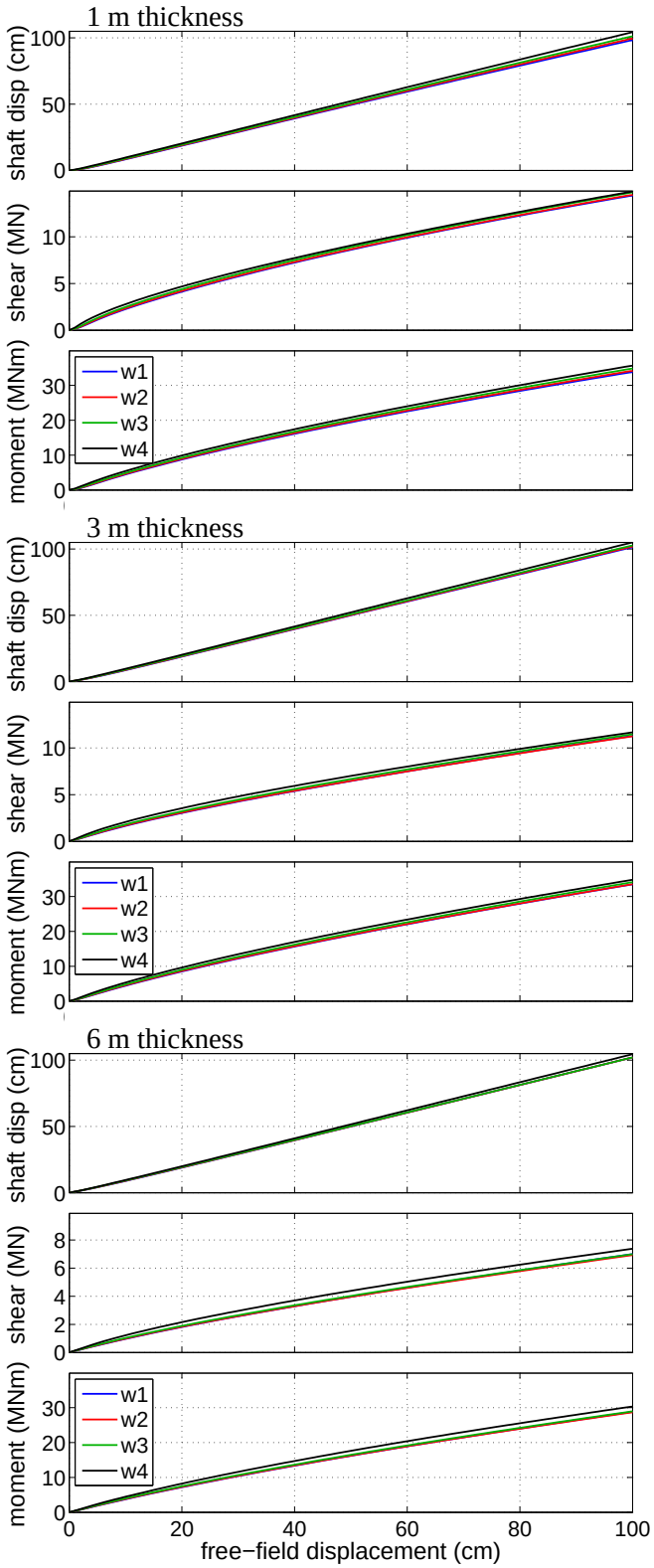

Figure 10.16: Maximum shaft bending demands for three liquefied layer thicknesses and four embankment widths with $D = 1.4$ m and $z = 6$ m.

during lateral spreading, and thus, differences in the geometry of the embankment are very influential on the foundation response. As the amount of crustal soil is increased, a greater amount of soil below the embankment is mobilized during the simulated lateral spreading event, and the kinematic demands placed on the foundation by the lateral movement of this crustal layer begins to control the overall shaft response.

10.2.4 Effects of Liquefied Layer Thickness

The effects of liquefied layer thickness are more subtle than those observed for the embankment crest width and liquefied layer depth. Based on the results shown in Figures 10.5 through 10.16, it does not appear that there is a clear trend that holds for all cases demonstrated by changes in t, however, there are differences in how the foundation is affected for the considered liquefied layer thickness values. One effect of the liquefied layer thickness is manifested in the foundation shear force diagrams. As shown in Figures 10.5 and 10.6, for the same values of D, w, and z, thinner liquefied layers lead to larger shear force demands. This is primarily due to how the applied displacement profile changes for thinner layers. As the thickness of the liquefied layer decreases, the shear demands on the shaft should approach the maximum possible value that would result in the absence of the linearly-distributed portion of the displacement profile. In contrast, the bending moment demands are much less affected by changes in t, though the distance between the maximum moment demands naturally increases with liquefied layer thickness.

The thickness of the liquefied layer also appears to affect how the embankment width influences the foundation response, and these effects show a depth dependence. As shown in Figures 10.11 and 10.14, the relative differences between the maximum bending demands for the four crest widths are not uniform for the three thicknesses considered. With $t = 1$ m, there is less variation with width than for the 3 and 6 m layer thicknesses. For deeper layer configurations, e.g., Figures 10.12 and 10.15, this effect is not as apparent and there is more consistency in the relative demands for the four widths at each thickness value.

10.2.5 Effects of Shaft Bending Stiffness

Some of the differences observed for the two shaft designs are expected effects of the two bending stiffness values represented by the shafts. The smaller shaft has a lower bending stiffness in comparison to the soil stiffness ($EI_{0.6} = 119$ MN·m^2 compared to $EI_{1.4} = 2494$ MN·m^2), therefore, for corresponding soil profiles the displacements of the 0.6 m shaft are larger and more closely resemble the applied displacement profile, while the larger shaft design offers more resistance to the lateral soil deformation. Since the larger shaft has a larger stiffness, for similar levels of shaft displacement, the shear and moment demands in the 1.4 m shaft are much larger than those in the 0.6 m shaft.

The liquefied layer depth effects discussed in the preceding sections appear to change based on the shaft bending stiffness. A comparison of Figures 10.12 and 10.15 demonstrates this effect; with $z = 3$ m, there is more variation with width in the maximum bending demands for the 1.4 m shaft than for the 0.6 m shaft. This observation also holds for the $z = 6$ m cases of Figures 10.13 and 10.16, as there is almost no variation with w for the 0.6 m shaft design, while the larger shaft still shows some visible differences for the considered crest widths. The implications of these observations make sense in the context of the problem, as it seems natural that the amount of crustal soil necessary to negate the three-dimensional effects of the embankment on the foundation response depends on the stiffness of the foundation itself.

10.3 Characterization of Geometric Site Effects

The basic observations made in the previous discussion demonstrate that geometric site effects during lateral spreading are not exclusive to the approach embankment. The amount of lateral pinning resistance that can be expected from a given foundation is not only dependent on the width of the embankment, but on the arrangement of the soil profile and stiffness of the foundation as well. The simplified pile pinning analysis approach discussed throughout this work likely captures the depth and thickness effects in the slope stability/deformation phase. A deeper liquefied layer results in a larger failure mass and correspondingly larger resisting forces required to contain the failure. This shifts the compatible design displacement to the right, indicating that there is less available foundation resistance for the system. The foundation stiffness effects should be captured by altering the pushover curve obtained from the foundation model. Therefore, while it is likely that the geometric effects observed in the parameter study are captured in the pile pinning analysis approach, an independent prediction of the expected amount of lateral pinning resistance for a given foundation and site geometry represents a useful supplementary design tool.

In order to characterize the expected amount of lateral resistance for a particular case, the problem is framed in terms of a reduction in foundation bending demands from those returned by the pseudo plane strain geometry of the full width embankment cases. These reductions are characterized in terms of a reduction ratio computed by dividing the displacement, shear force, and bending moment demands at each analysis step by the corresponding demands for the wide embankment case with matching soil profile and shaft design. Figures 10.17 through 10.22 show these computed ratios plotted against the free-field displacement in the model. In these plots, a reduction ratio of 1.0 implies no reduction from the plane strain case, while a reduction ratio less than 1.0 indicates that the bending demands are less than those in the plane strain case. For example, a reduction ratio of 0.2 indicates bending demands that are 20% of those predicted using a two-dimensional description of the site geometry.

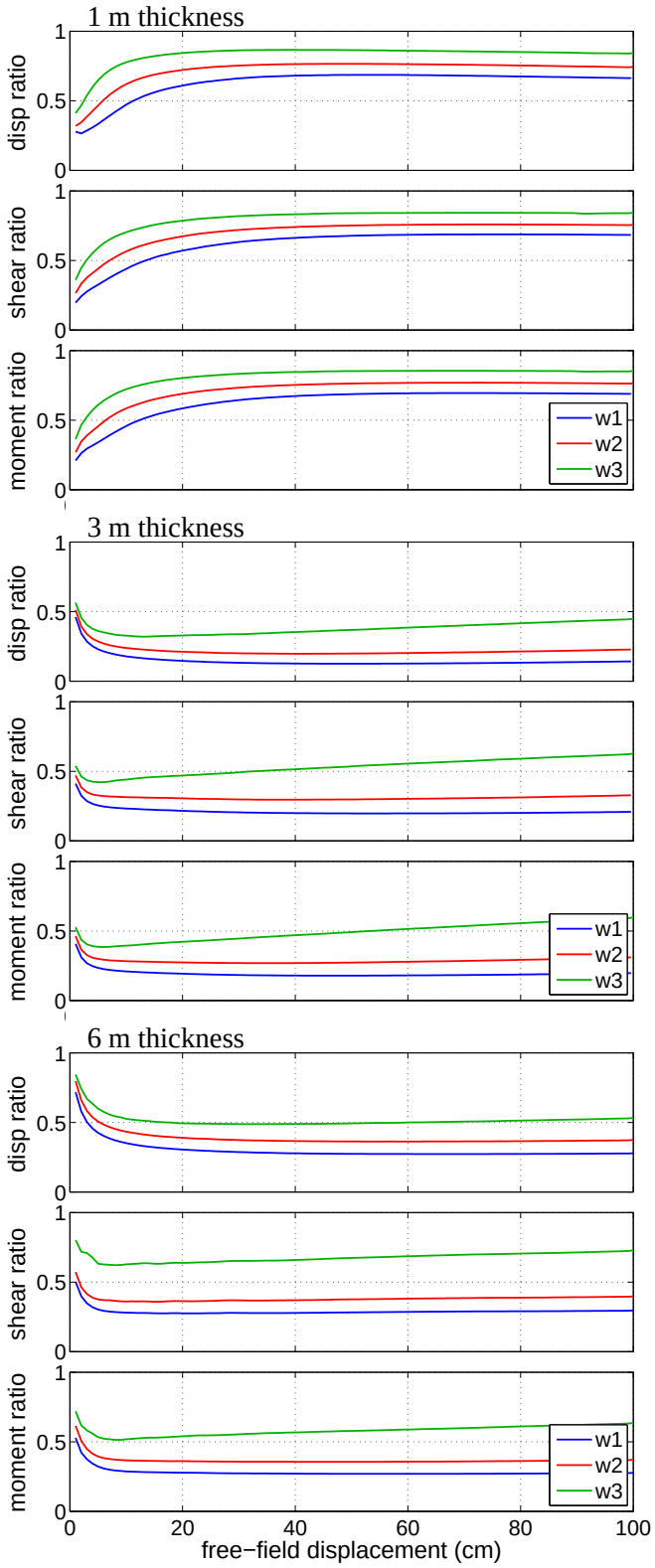

Figure 10.17: Bending demand ratios for three liquefied layer thicknesses and three embankment widths with $D = 0.6$ m and $z = 1$ m.

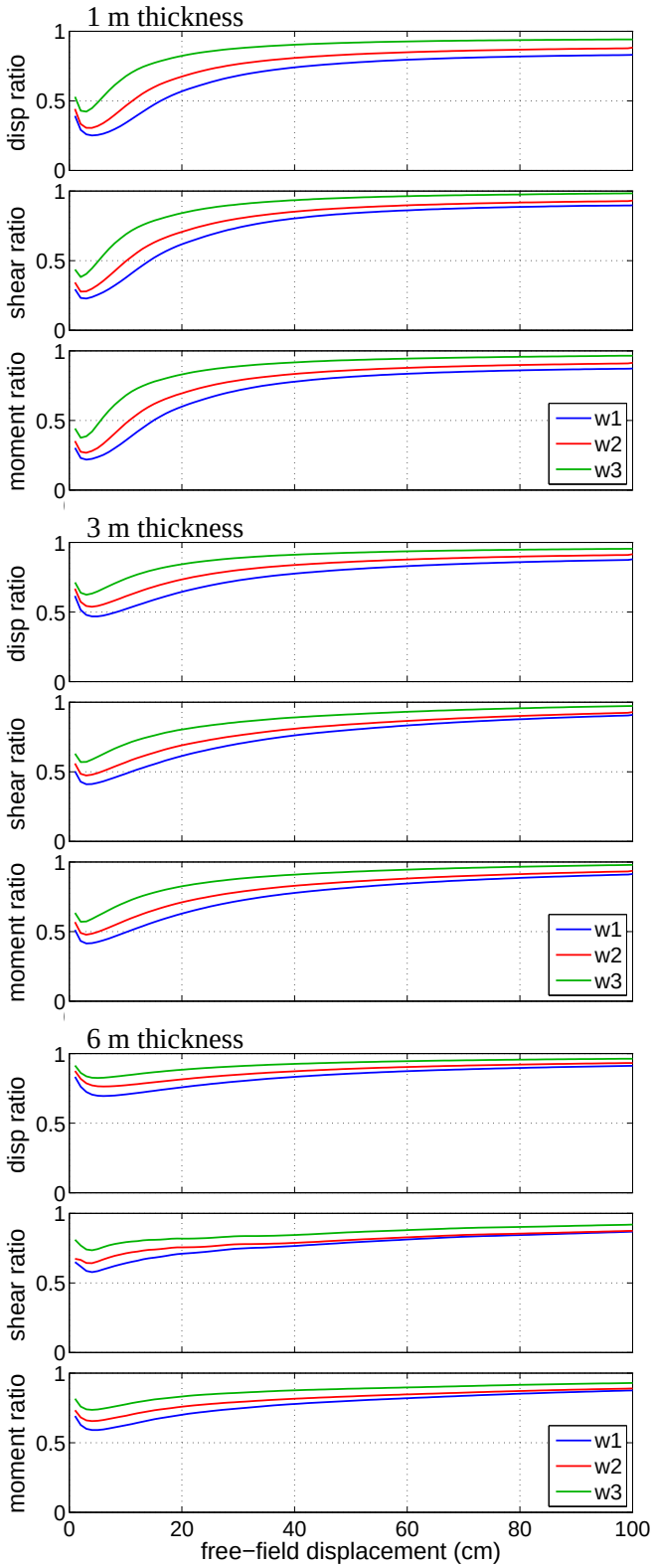

Figure 10.18: Bending demand ratios for three liquefied layer thicknesses and three embankment widths with $D = 0.6$ m and $z = 3$ m.

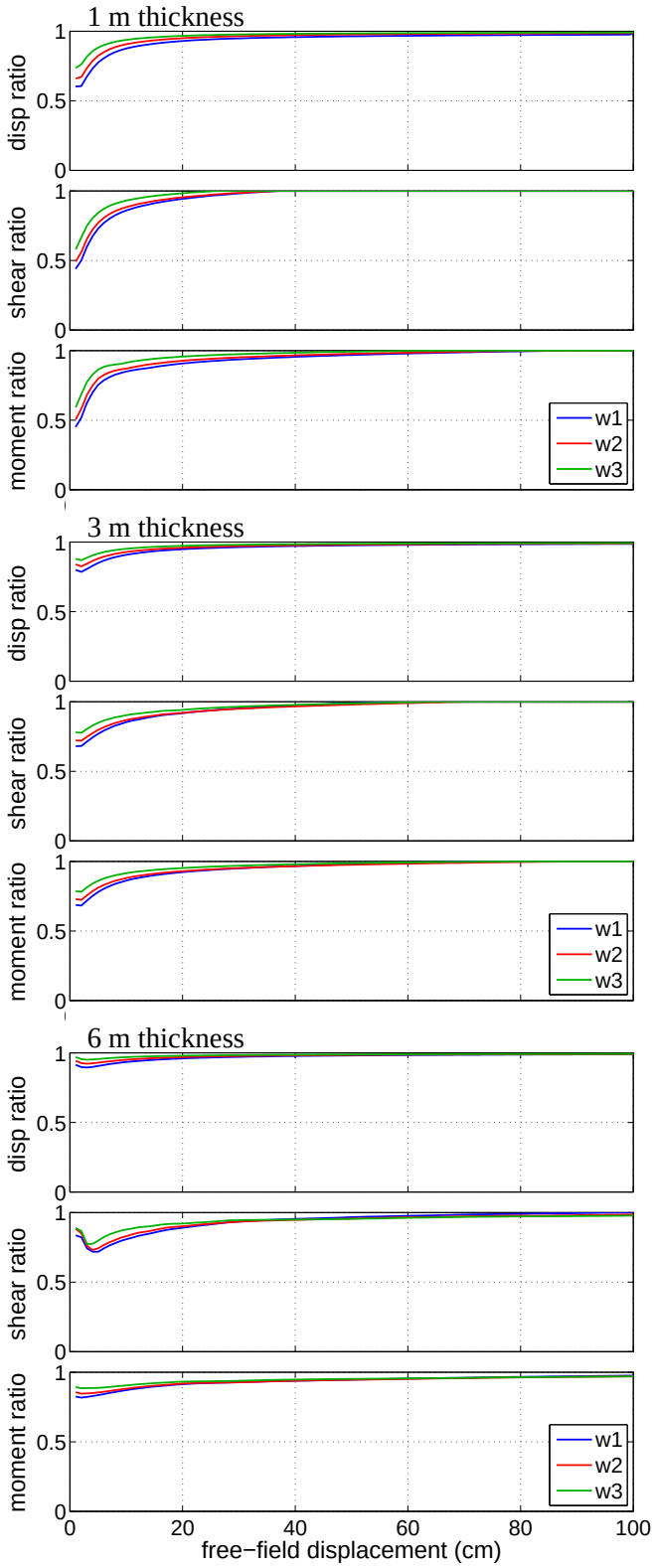

Figure 10.19: Bending demand ratios for three liquefied layer thicknesses and three embankment widths with $D = 0.6$ m and $z = 6$ m.

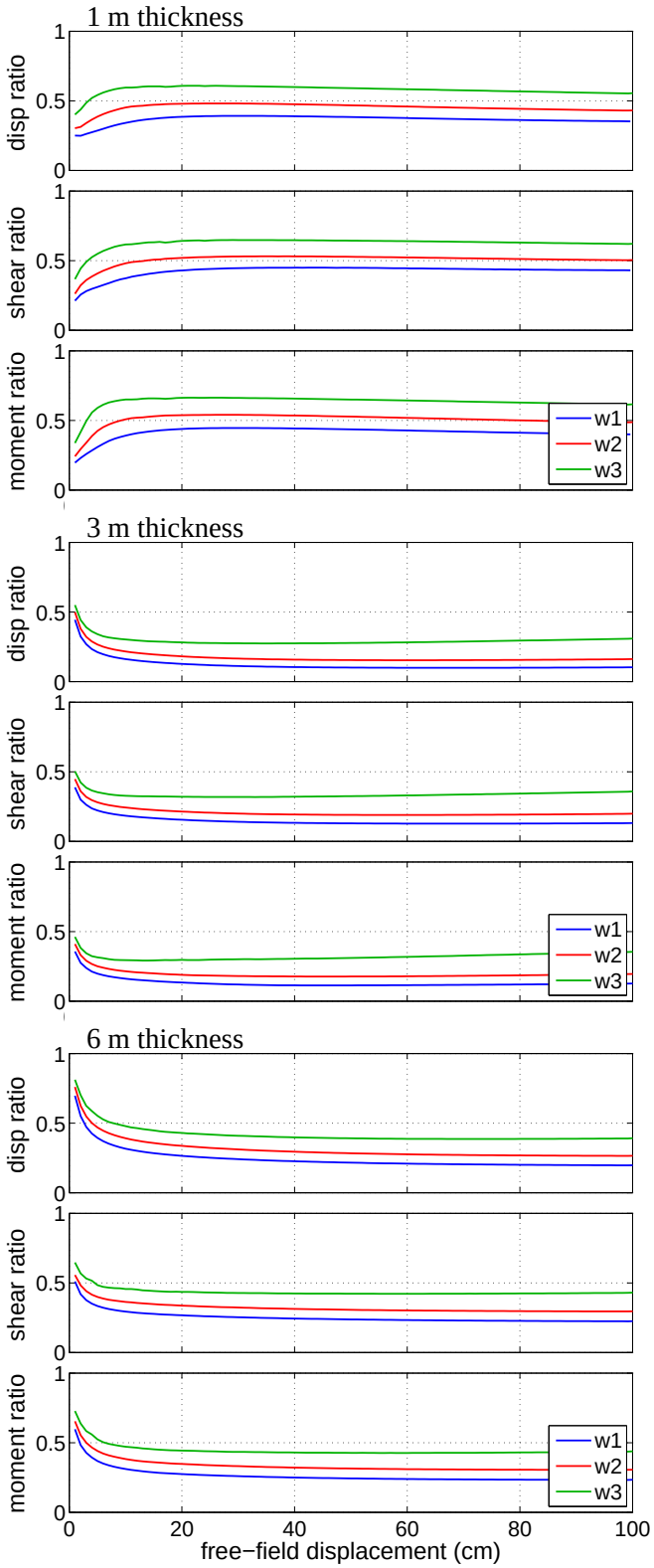

Figure 10.20: Bending demand ratios for three liquefied layer thicknesses and three embankment widths with $D = 1.4$ m and $z = 1$ m.

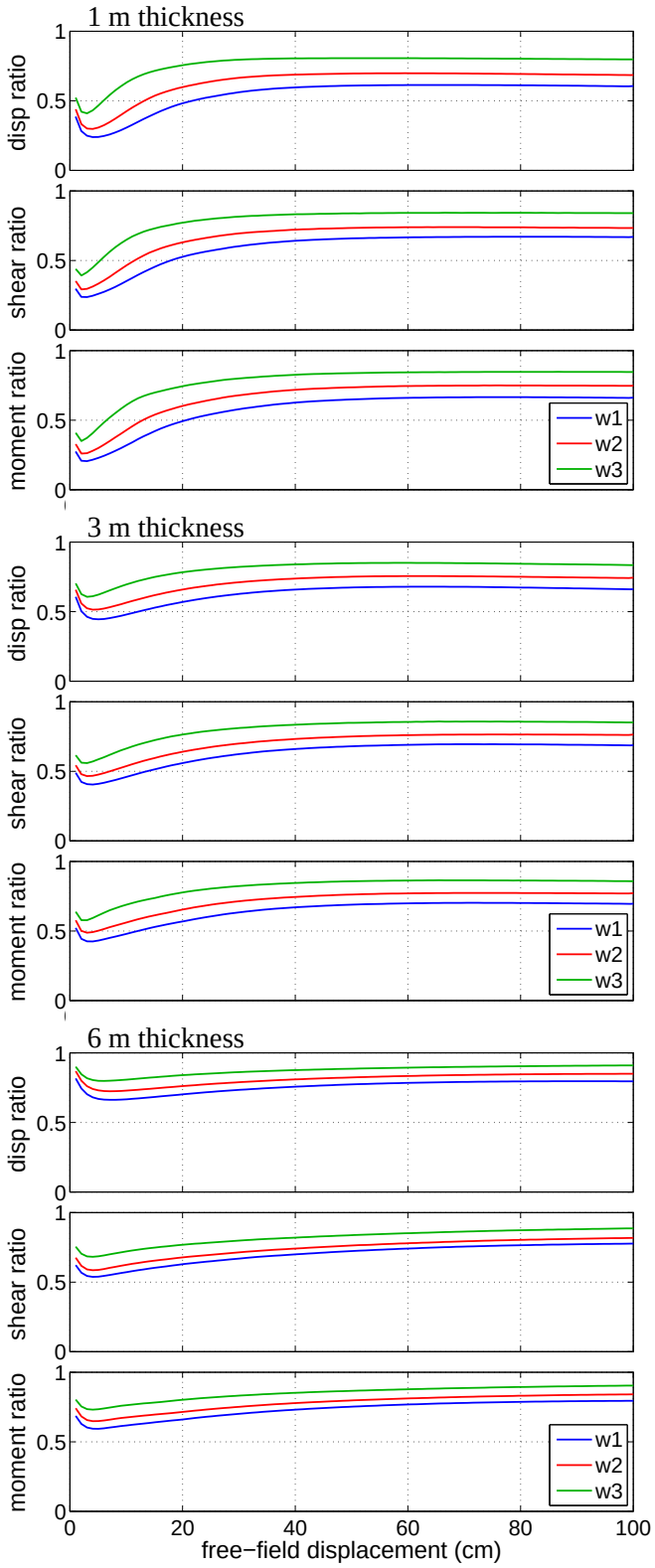

Figure 10.21: Bending demand ratios for three liquefied layer thicknesses and three embankment widths with $D = 1.4$ m and $z = 3$ m.

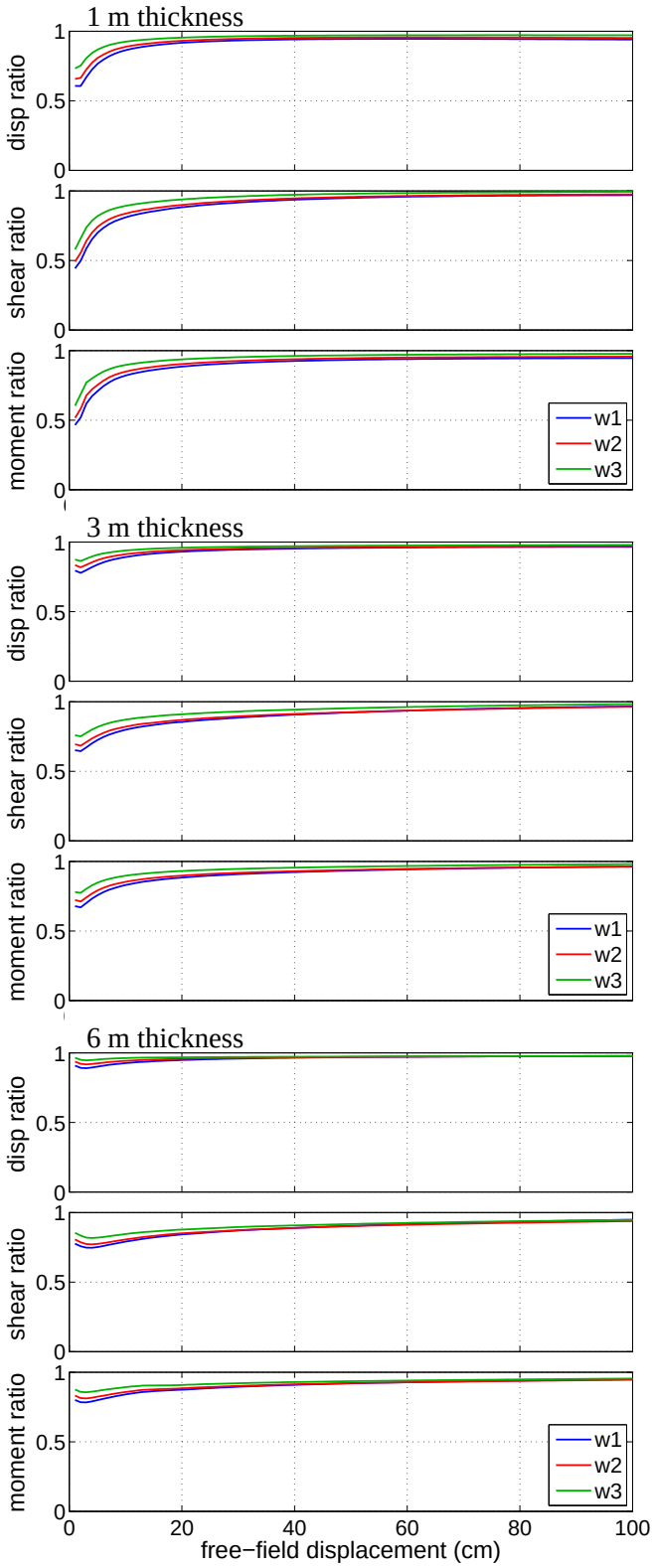

Figure 10.22: Bending demand ratios for three liquefied layer thicknesses and three embankment widths with $D = 1.4$ m and $z = 6$ m.

The reduction ratio plots of Figures 10.17 through 10.22 support the observations made in the previous sections, while providing a better representation of how the bending demands relate to each other over the full span of the free-field displacement, and thus illuminating aspects of the geometric site effects that are obscured in previous plots. Most of the site configurations display a similar trend in how the reduction ratios develop; the ratios are lower over the initial portion of the free-field displacement, and then gradually increase before reaching an essentially steady final value. There are some exceptions to this general trend, particularly for the $z = 1$ m configurations with $t > 1$ m, which, as shown in Figures 10.17 and 10.20, display the opposite ratio development pattern, with initially higher ratios becoming smaller with increasing free-field displacement and, for the 0.6 m diameter shaft cases, the reduction ratios do not all reach a steady value prior to the end of the analysis. The other exceptions to the general trend of reduction ratio evolution are displayed for the $z = 3$ m cases shown in Figures 10.18 and 10.21. Here, the ratios initially become smaller before they begin to gradually increase to their steady-state values. It is not yet clear whether this is a relevant effect due to these geometric conditions or a numerical effect due to differences in the model between the initial state and the loading state.

10.3.1 Reduction Model

The residual reduction ratio values (i.e., those at the end of the free-field displacement), are used to establish a means to predict expected reductions in shaft displacement, shear force, and bending moment demands for a given site geometry. By plotting the residual reduction ratios, R, against various combinations of liquefied layer depth, z, liquefied layer thickness, t, embankment width, w, and foundation bending stiffness, EI, in a natural-log plot, dimensionless relations are established that relate the reduction ratio to the site parameters. For this purpose, the tributary width introduced by Boulanger et al. (2006)

$$w = w_c + \frac{2}{m}h \tag{10.1}$$

where w_c is the crest width, m is the embankment side slope, and h is the embankment height, is used to describe the width of the embankment. The parameter study models all consider a 2H:1V side slope and a 5 m height, thus, the tributary widths are simply the sum of the crest widths and the height. This consideration results in a modified set of widths, $w = 9,\ 13,\ 21$ m.

Other than the unit weight of the crustal soil layer, γ, considered to provide a set of force units to offset those in EI, soil properties are not considered when constructing the relations between the reduction ratio and site parameters. All of the parameter study models consider the same set of soil properties, and since the problem has been framed in terms of reduction ratios for shaft bending demands, any effects related to the strength and stiffness of the soil

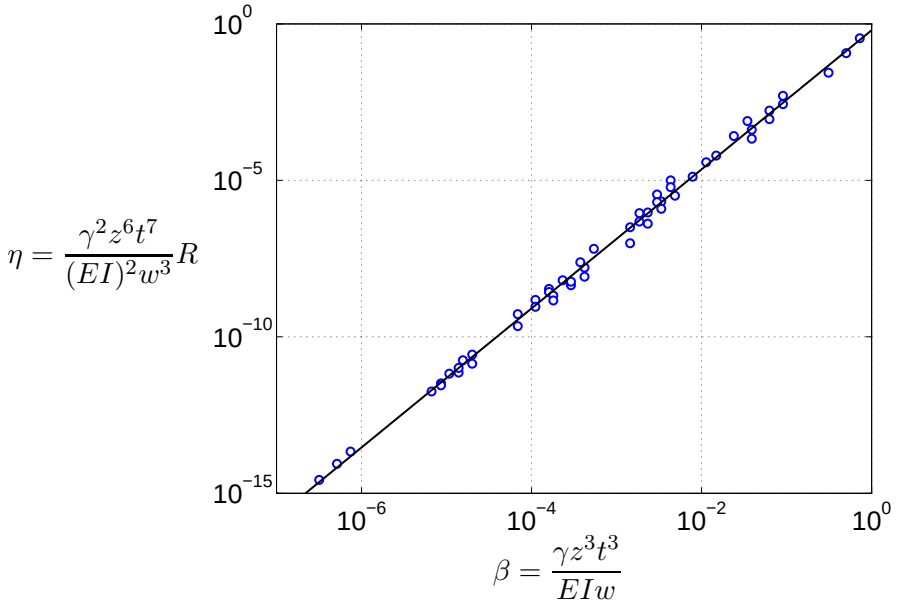

Figure 10.23: Dimensionless relationship between reduction ratio, R, and maximum shaft displacement.

should cancel out when the ratios between the various cases are computed.

The relations for which the data displayed the best correlation in the natural-log plots define two dimensionless parameters: the dimensionless reduction ratio,

$$\eta = \frac{\gamma^2 z^6 t^7}{(EI)^2 w^3} R \tag{10.2}$$

and the dimensionless site parameter,

$$\beta = \frac{\gamma z^3 t^3}{EIw} \tag{10.3}$$

These dimensionless parameters are computed for the 54 sets of residual reduction ratios for the maximum shaft displacement, maximum shaft shear force, and maximum shaft bending moment demands shown in Figures 10.17 through 10.22, as well as an additional 72 residual reduction ratios computed as the ratio of the shaft head displacement in each case to the applied free-field displacement.

Figures 10.23 through 10.26 show the relations between the dimensionless reduction ratio and site parameters for each of these four cases. As shown, the data points for each reduction ratio type display a strong linear trend when plotted using the dimensionless parameters, β and η. Lines are fit to the data using least squares in order to establish expressions for the observed trends. A straight line in natural-log space represents

$$\ln \eta = b \ln \beta + \ln a \tag{10.4}$$

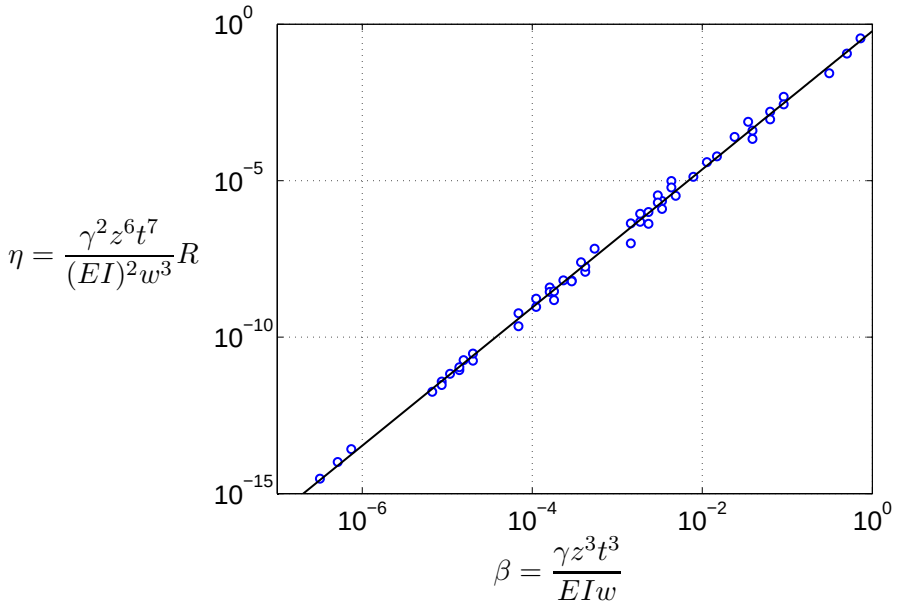

Figure 10.24: Dimensionless relationship between reduction ratio, R, and maximum shaft shear force.

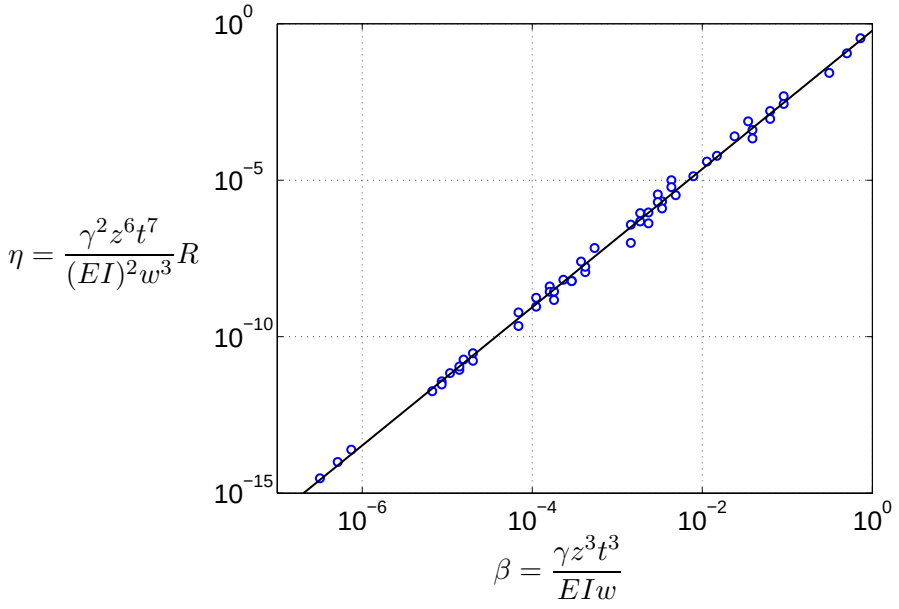

Figure 10.25: Dimensionless relationship between reduction ratio, R, and maximum shaft bending moment.

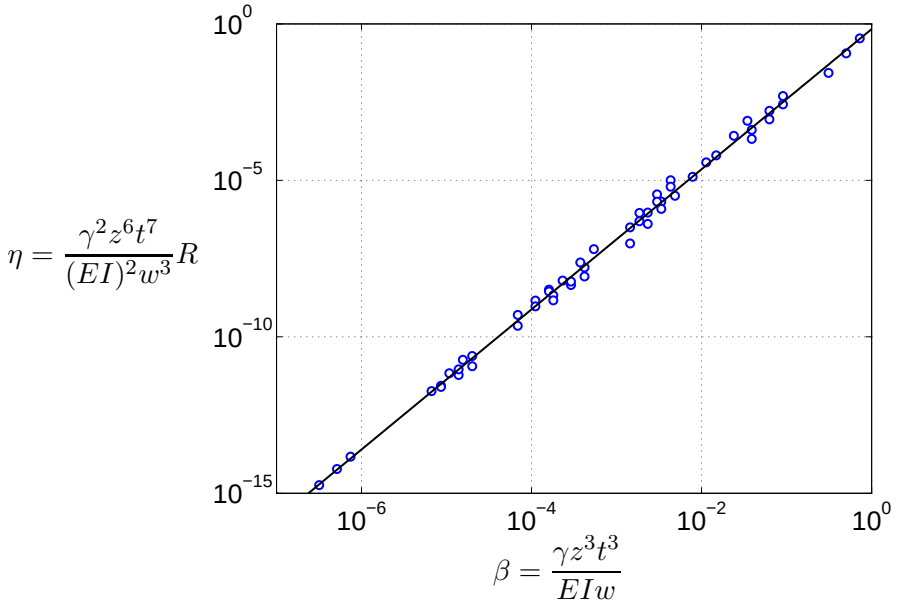

Figure 10.26: Dimensionless relationship between reduction ratio, R, and free-field displacement.

where the coefficients a and b are determined from the linear least squares procedure for the reduction ratios. Solving this expression for η gives

$$\eta = a\beta^b \tag{10.5}$$

which, when combined with (10.2) and (10.3) defines the following expression for the reduction ratio in terms of the site parameters and the least squares coefficients

$$R = aw^{3-b}\gamma^{b-2}z^{3b-6}t^{3b-7}(EI)^{2-b} \quad \leq \quad 1.0 \tag{10.6}$$

A reduction ratio greater than 1.0 implies an increase in the shaft bending demands as compared to 2D conditions, therefore, the expression is defined such that $R \leq 1.0$ to ensure that such values are not considered.

As shown in Figures 10.23 through 10.26, the dimensionless reduction ratio relationships for each of the four considered cases display nearly identical trends. This appears reasonable based on the reduction ratios plotted in Figures 10.17 through 10.22, which display little difference in the residual values for each maximum bending demand. As expected based on the observed similarity between the four reduction ratio types, the least squares coefficients computed for each case and shown in Table 10.3 are all nearly the same. Due to this similarity between the reduction ratio types, it is proposed that a single reduction ratio model that uses average least squares coefficients can be applied to determine reductions in any of the considered quantities without resulting in significant error. The a- and b-

Table 10.3: Least squares coefficients for each reduction ratio type.

Reduction ratio type	a	b
max shaft displacement	0.63	2.22
max shear force	0.60	2.21
max bending moment	0.60	2.21
free-field displacement	0.68	2.22

coefficients computed for the maximum shaft displacement reduction ratio are used to define this master model, which can now be expressed as

$$R = 0.63\frac{w^{0.8}\gamma^{0.2}z^{0.6}}{(EI)^{0.2}\,t^{0.4}} \quad \leq \quad 1.0 \tag{10.7}$$

By multiplying the value of R computed from (10.7) with the maximum bending demands obtained from a simplified analysis of a bridge foundation, e.g., the initial BNWF pushover phase of the pile pinning analysis procedure, a designer can obtain a first-order approximation of the foundation bending demands with consideration for the 3D geometry of a given site. Alternatively, given a particular set of site parameters, the reduction ratio can be applied to the free-field lateral spreading displacement value estimated using a predictive method (e.g., Baska, 2002; Youd et al., 2002; Idriss and Boulanger, 2008) in order to estimate the expected shaft cap displacement at the site. The scope of the current data set used to establish this reduction model is not sufficiently large and diverse as to suggest that the reductions predicted by its application are definitive results, however, this reduction model can be an effective tool if used in support of an independent analysis, with the reductions computed from (10.7) serving as an estimate of the amount of lateral resistance a foundation may provide during lateral spreading.

10.3.2 Effects of Site Parameters on Reduction Model

It is of interest to evaluate the effects of each of the four primary site parameters on the reduction ratio estimated from (10.7). These observations overlap somewhat with those made previously, but evaluating the effects of these parameters in the context of the reduction ratio allows for them to be isolated further. In order to make these evaluations, a generic site profile is assumed where $EI = 10$ MN·m, $t = 4$ m, $z = 2$ m, $\gamma = 17$ kN/m^2, and $w = 10$ m. In the discussion that follows, unless otherwise stated, these parameters apply to the results shown.

Figure 10.27 shows how the reduction ratio varies with foundation bending stiffness, and also demonstrates how the relationship between R and EI is affected by changes in the other site parameters. These plots generally show the expected effects of foundation bending

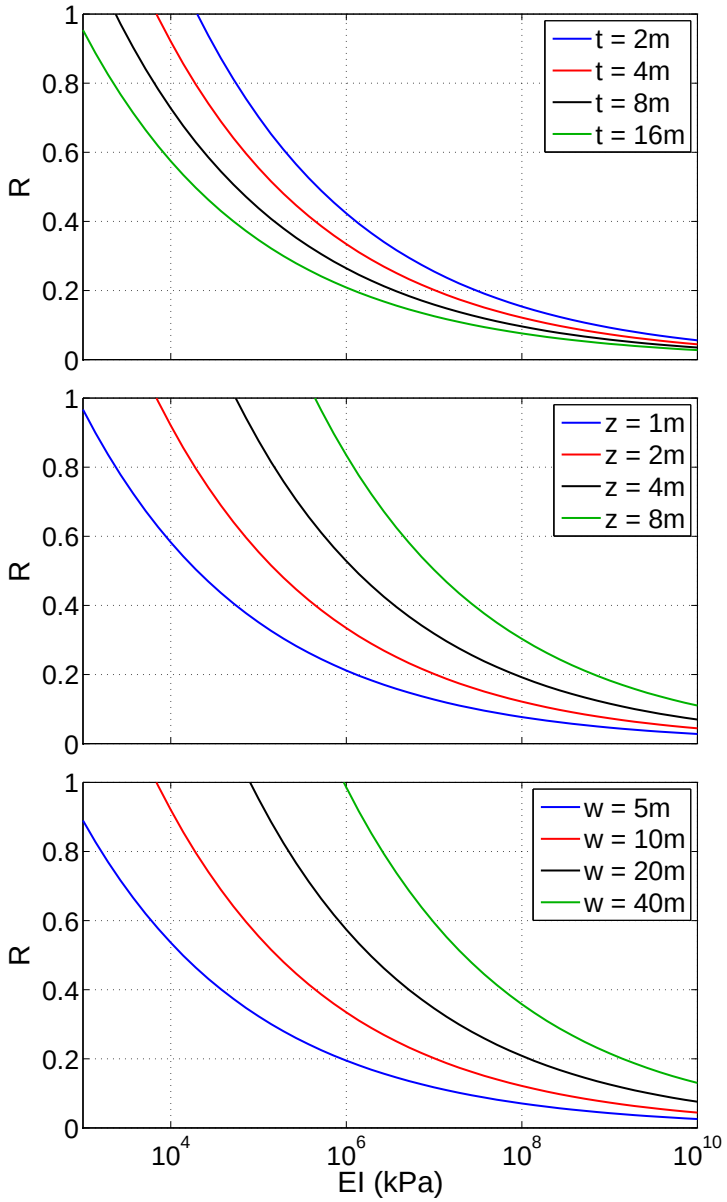

Figure 10.27: Variation of reduction ratio, R, with shaft bending stiffness, EI, and effects of changing t, z, and w on this relationship.

stiffness on the reduction ratio. As EI is increased, R becomes smaller, implying a greater reduction from the plane strain case. As the depth to the liquefied layer or the embankment width are increased, larger values of EI are required to affect a similar reduction in the system. The inverse relation holds for changes in liquefied layer thickness, as larger values of t decrease the amount of foundation stiffness required to achieve a particular reduction. Additionally, these plots show that for the assumed generic site parameters, the thickness of the liquefied layer is less influential on the R-EI relationship than the other parameters.

To assess the effects of liquefied layer thickness on the computed reduction ratio, the

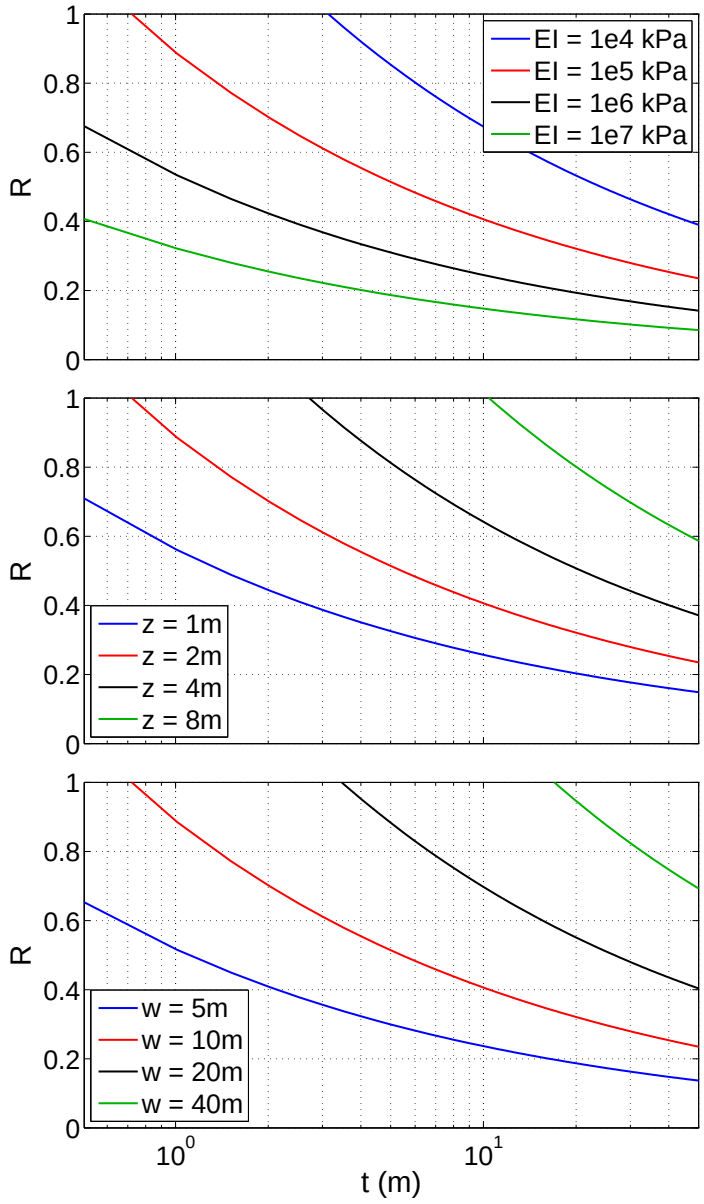

Figure 10.28: Variation of reduction ratio, R, with liquefied layer thickness, t, and effects of changing EI, z, and w on this relationship.

relations between t and R are similarly plotted in Figure 10.27. Because t and EI are both located in the denominator of (10.7), they share a similar overall trend in relation to R, and in how the other parameters influence this relation. Increases in embankment width and liquefied layer depth necessitate a larger liquefied layer thickness to maintain a steady reduction ratio, while increasing the foundation bending stiffness decreases the thickness necessary to maintain a certain level of reduction. The amount of influence of the non-thickness site parameters on the R-t relation appears to be similar based on the spread

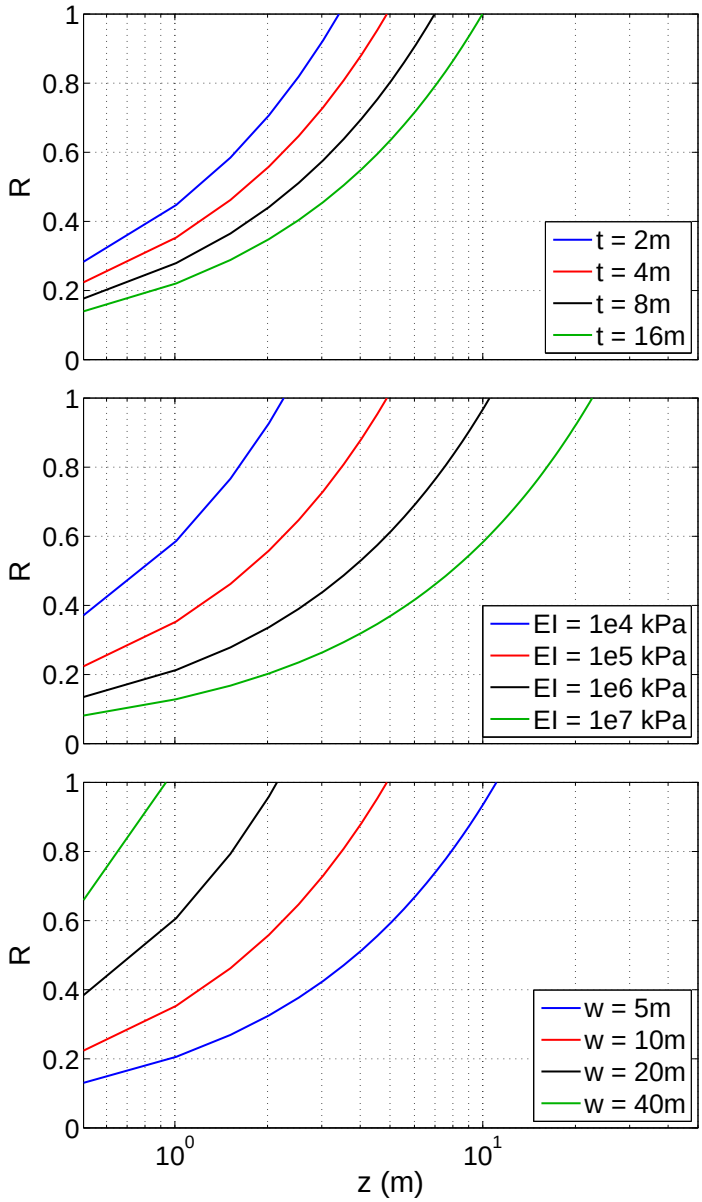

Figure 10.29: Variation of reduction ratio, R, with liquefied layer depth, z, and effects of changing t, EI, and w on this relationship.

between the individual curves in the plots of Figure 10.27.

The relations between the reduction ratio and the liquefied layer depth and embankment width shown in Figures 10.29 and 10.30 confirm the previously observed effects of these parameters on the amount of lateral foundation resistance available for a given site configuration. Decreasing either of these parameters leads to larger reductions in foundation demands as compared to the 2D site description, and this is manifested in the plots as smaller reduction ratios for smaller values of z and w. Increasing either the liquefied layer thickness or foundation stiffness increases the amount of crustal soil which can be present in

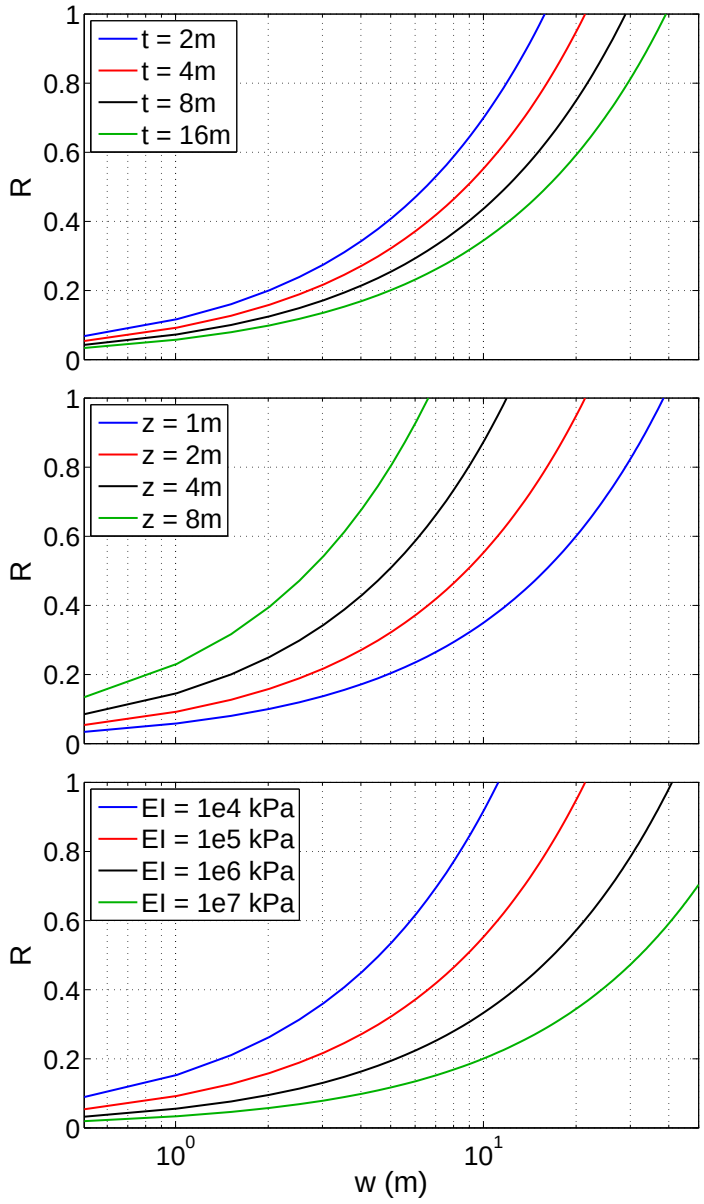

Figure 10.30: Variation of reduction ratio, R, with embankment tributary width, w, and effects of changing t, z, and EI on this relationship.

the soil profile before the reduction becomes negligible, with EI demonstrating the greater amount of influence on this effect. Increases in t and EI affect the embankment width similarly, demonstrating that as these parameters become larger, the embankment width at which 3D effects become insignificant also becomes larger. The influence of w on the depth effect and z on the width effect are also evident in these results, with Figures 10.29 and 10.30 demonstrating that larger embankment widths require shallower liquefied layers to affect a similar level of reduction in the foundation demands. These observations correspond with those made qualitatively from previous plots, lending confidence to the final form of the

reduction ratio model.

10.4 Summary

A series of 3D finite element models was used to examine the influence of various site parameters on the response of a single deep foundation to the kinematic demands of lateral spreading. These models focused on assessing the effects of changes in the embankment width, the depth to the liquefied layer, the thickness of the liquefied layer, and the bending stiffness of the foundation. The observed effects were framed within the context of a reduction in foundation bending demands as compared to a plane strain description of the site. Based on this parameter study, it was determined that the interaction of the geometric site parameters defines the overall lateral response of the system.

Reductions ratios were computed by comparing the foundation demands from the cases with 3D geometries to corresponding results obtained from wide geometry configurations that mimic plane strain conditions. The residual reduction ratios were compared to various combinations of the site parameters in order to establish dimensionless parameters, which, when plotted in natural-log space, demonstrated a strong correlation for the data set. A mathematical model that describes the residual reduction ratio in terms of the site parameters was obtained from this plotted data using least squares. Using this proposed reduction model, a first-order approximation can be obtained for the expected amount of pinning resistance available for a particular site configuration. This reduction model represents a valuable tool to the designer, especially when used in concert with a simplified analysis procedure, as it provides an independent assessment of the general foundation response to lateral spreading.

Chapter 11

RESEARCH OUTCOMES

This dissertation presents an extensive research program performed in the pursuit of identifying and quantifying mechanisms that lead to reductions in bridge foundation demands during lateral spreading with consideration for three-dimensional site geometry effects. This research encompasses the development of efficient finite element formulations, the review of current design procedures, the identification of an appropriate case history bridge, and the development and analysis of numerical models to study the response of the case history bridge foundations to the kinematic demands of lateral spreading.

11.1 Summary and Conclusions

A summary of the completed work and a discussion of the related research findings are presented for each of the primary topics considered in the work. The following sections reiterate the fundamental aspects of each topic and identify any conclusions drawn from that portion of the research.

11.1.1 Finite Element Development

Four efficient continuum finite element formulations were developed and implemented to support the modeling effort involved in the remainder of this work. These elements include both displacement and coupled fluid solid formulations for use in 2D and 3D. The solid elements, and the solid phase of the coupled elements, use hourglass stabilized single-point integration schemes to reduce computational expense, and take advantage of assumed strain fields to eliminate volumetric and shear locking phenomena. The coupled elements use a **u**-p formulation to consider the coupled response of a pore fluid and solid skeleton under the assumptions of mixture theory, and use a direct stabilization technique to enhance element stability in the incompressible-impermeable limit.

The beam-solid contact element of Petek (2006) was extended to include an alternative constraint enforcement approach. The original element formulation uses the method of Lagrange multipliers to enforce the contact constraints for the element. In this work, the formulation was modified to include enforcement of the contact constraints using a penalty approach. This modification results in a relaxation of the constraint enforcement that is beneficial in certain analysis configurations.

11.1.2 Review of Current Simplified Design Procedures

The design procedures used by the California Department of Transportation and Washington State Department of Transportation for bridge foundations subject to liquefaction-induced lateral ground deformation were reviewed to assess the state of current design practice for this load case. These two approaches are based off of the same underlying documents, and consider similar analysis components such as beam on nonlinear Winkler foundation and slope stability models, however, due to key differences in assumptions, they lead to different outcomes for certain site configurations.

The Caltrans procedure makes a distinction between cases for which it is expected that the foundation will provide lateral pinning resistance, and cases for which no resistance is assumed. For the cases where assuming foundational restraint appears to be reasonable, the pile pinning analysis procedure (Martin et al., 2002; Boulanger et al., 2006; Ashford et al., 2011), which is based on the assumption of compatibility between the foundation resistance and embankment deformation during lateral spreading, is adopted by Caltrans. The WSDOT design procedure makes no explicit distinction between these two types of cases, and instead assumes that the bridge foundation shall be designed to withstand the soil deformation and attendant lateral forces that would occur due to liquefaction-induced flow failure or lateral spreading in the absence of a foundation.

11.1.3 Case History Evaluation

A series of Chilean bridge sites affected by lateral spreading due to the 2010 offshore Maule earthquake were examined for potential use as a case study to support this research. These bridge sites were evaluated in terms of the evidence of three-dimensional soil deformation effects, the sufficiency of the available structural and geotechnical data, and the applicability of the bridge design details to newly designed structures. Based on this evaluation, Puente Mataquito was selected for use as the primary case study site for this research, while several other bridges were identified as candidates for future consideration.

11.1.4 Numerical Analysis of Case Study Site

Three numerical modeling techniques were used to examine the effects of lateral spreading on the selected case study bridge. These models vary in complexity and in their intended use. A summary of each technique and the associated findings follows.

11.1.4.1 Plane Strain Models

Dynamic plane strain effective stress models of the Puente Mataquito site were developed and analyzed to evaluate the response of the bridge and soils to seismic excitation. This model was used to demonstrate the effects of the soil domain thickness on the response

of the bridge foundations, and to verify assumptions made during the development of the idealized soil profile used for the numerical models of the site. A version of the plane strain model was used to assess the performance of the bridge to a ground motion similar to what may have been experienced at Puente Mataquito. This analysis returned results that were reasonably similar to observations made following the Maule earthquake, and confirmed the susceptibility of the site to liquefaction. Lateral spreading deformations associated with liquefaction were observed in these models, and the abutment foundations were found to be affected more significantly by this soil deformation than most of the interior pier foundations. Based on the scope of liquefaction and lateral spreading in the soil near the two abutments, and a comparison of the foundation demands imposed upon the bridge foundations due to these paired phenomena, the southwest abutment was identified for further study.

11.1.4.2 Three-Dimensional Models

Three-dimensional finite element models of the southwestern abutment of Puente Mataquito were developed and analyzed in an effort to identify the mechanisms leading to the reductions in foundation demands implied by the combination of large free-field lateral spreading deformation and minimal structural damage observed at the site. Overall, the results obtained from the 3D modeling effort compared favorably to the site observations. The general soil deformation patterns were the same, with the approach embankment tending to slump vertically and spread outwards instead of moving only in the direction of lateral spreading. The magnitudes of these deformations did not directly correspond with the reported site response, however, the similarity in the trends captured by the model to those observed increases confidence in the results obtained from the model.

The primary goal of these models is to assess the response of the foundation to a set of demands similar to those that would occur during an actual lateral spreading event. All of the 3D analysis was conducted pseudo statically, working from the assumptions that liquefaction has already developed and inertial effects can be ignored. The validity of these assumptions was addressed through the consideration of two distinct approaches to simulating the kinematic demands of lateral spreading. The foundation bending demands resulting from each approach were found to be similar, further increasing confidence in the results from the 3D modeling effort.

Models that simulated lateral spreading using an applied kinematic approach demonstrated a reduction in the soil and foundation demands when 3D site geometry was considered. These models identified the importance of the lateral resistance provided by the bridge superstructure in defining the response of the foundation, and demonstrated the differences in foundation response before and after the deck expansion gap was closed due to lateral foundation movement. The models that simulated lateral spreading through gradual reductions in the shear strength and stiffness of the liquefiable soil layer identified how

the presence of the approach embankment creates instability in the liquefied soil system. Further evidence of the foundation pinning effect was obtained through the comparison of models both with and without the bridge foundation.

11.1.4.3 Simplified Models

The pile pinning analysis procedure (Martin et al., 2002; Boulanger et al., 2006; Ashford et al., 2011) was assessed through an application of the Caltrans (2011) version of the procedure to the southwest abutment of Puente Mataquito. The compatible displacements obtained from the pile pinning analysis were shown to possess great variability with respect to the particular assumptions and modeling choices made in the individual analysis phases that comprise the pile pinning approach. It was proposed that the compatible displacement used in the final foundation design phase be selected as an average of the compatible displacements resulting from a series of different modeling configurations and assumptions. In this manner, the design solution that is most representative of the site conditions can be obtained.

The pile pinning analysis procedure was shown to produce foundation demands that were consistent with the results obtained from certain 3D model configurations. When a smaller deck expansion gap was considered in the 3D model, the two approaches produced reasonably similar foundation bending demands. When the 3D models considered a larger expansion gap, comparisons of the two sets of foundation demands were not as favorable. A potential solution to this problem was proposed and demonstrated in which the design displacement is defined as the sum of the gap magnitude and the compatible displacement obtained from the pile pinning approach. With this modification, the pile pinning results were much more similar to those obtained from the large expansion gap 3D models

11.1.5 Parameter Study of Geometric Site Effects

A series of 3D finite element models was developed and analyzed to investigate the effects of various site parameters on the response of a single deep foundation to the kinematic demands of lateral spreading. This modeling effort provided further evidence that consideration for the 3D geometry of the site is an important factor in this type of analysis. It was determined that the lateral response of the foundation for a particular site is governed by the interaction of multiple site parameters, including the location and size of the liquefied layer, the width of the approach embankment, and the size and stiffness of the foundation.

A predictive model was developed from the parameter study data set that can be used to estimate the reductions in foundation demands as compared to a two-dimensional description of the site. The reductions returned by this model can be applied to the foundation shear force and bending moment demands obtained from a simplified analysis in order to get a first-order approximation of the expected demands with consideration for 3D site effects.

The reduction model can also be used to inform a simplified analysis approach by providing an estimate of how much lateral pinning resistance can be expected for a particular case.

11.2 Directions for Future Research

The research discussed in this document has identified several avenues for further study into the effects of lateral spreading on bridge foundations. This future research is divided into two broad groups: (1) the further numerical evaluation of case history bridges with consideration for 3D effects, and (2) the expansion and refinement of the parameter study data set for the evaluation of geometric site effects.

11.2.1 Case Study Evaluation

The 3D finite element simulations related to Puente Mataquito have demonstrated the effectiveness of this approach for learning about the behavior of bridge foundations during lateral spreading, however, the results obtained from these models need further verification and validation that can only be gained through the consideration of one or more different bridges. Several potential bridge sites have been identified for this purpose, both in Chile (see Chapter 6), and elsewhere in the world (see Chapter 1), and there are undoubtedly other bridges not identified in this work that would be suitable for the purpose.

The selection of any future case study bridge for use in a numerical evaluation of this problem should focus on site configurations and modeling aspects that were not considered in the Puente Mataquito work. The parameter study presented in Chapter 10 has identified the importance of consideration for the full geometry of the site in determining the response of the foundation to lateral spreading. A bridge that is constructed in a different manner than Puente Mataquito would be useful for furthering the understanding of this problem. The current work has identified the influence of the bridge deck as a major factor in defining the lateral response of the foundation, therefore, it could be useful to incorporate a more rigorous description of the bridge deck, the expansion gap, and the deck to abutment connection in future models.

A dynamic analysis is another modeling refinement that holds potential for a three-dimensional assessment of the effects of lateral spreading on bridge foundations. The current work has focused simulating the kinematic demands of lateral spreading through simplified techniques. While this has shown to be an effective method with which to study foundation response to lateral soil deformation, the pseudo static approach employed in the models ignores certain aspects of the problem such as inertial forces and pore pressure generation effects. A dynamic effective stress model could allow for a more natural consideration of the problem, though such a model would present several challenges for the hypothetical future researcher.

In addition to the potential for modeling refinements or alternative configurations in advancing the understanding of the mechanisms governing the lateral spreading problem, future case study models could be used to support the further validation of the pile pinning analysis approach. This work has shown that this approach compared favorably with certain 3D models for Puente Mataquito, but it is of interest to expand the scope of this validation effort to different bridge configurations and soil profiles. The pile pinning approach holds great potential for use as the primary simplified design technique for bridge foundation subject to lateral spreading, and any improvements or refinements that can be achieved through comparison to 3D models will greatly benefit the profession.

11.2.2 Parameter Study Expansion/Refinement

Another direction for future work lies in furthering the ideas obtained from the parameter study presented in Chapter 10. Specifically, it is of interest to determine whether a new series of models that considers a new set of site parameters produces bending demands that correspond to those obtained in this work. This future parameter study effort could focus on parameters that were not explicitly considered here, such as the height of the approach embankment, or on further variations in the parameters that were considered, such as more liquefied layer arrangements and different shaft designs. The consideration of more liquefied layer depths closer to the ground surface would be particularly useful, as this would expand the number of cases with smaller reduction ratios.

Other potential effects that may be beneficial to include in future studies of this nature are the effect of shaft groups or deck resistance on the influence of the geometric site parameters. The current data set includes only a single deep foundation, and it is not clear whether the addition of shaft foundations will affect the reduction in a manner similar to increases in foundation bending stiffness, or whether it will manifest as some other effect entirely. It is likely conservative to generate the reduction ratio data set in the absence of the additional lateral resistance provided by the bridge deck, however, it may be useful to include this aspect of the problem in order to be able to predict how this resistance affects the overall behavior of the system.

BIBLIOGRAPHY

Abdoun, T. and Dobry, R. (2002). "Evaluation of pile foundation response to lateral spreading." *Soil Dynamics and Earthquake Engineering*, 22, 1051–1058.

American Association of State Highway and Transportation Officials (AASHTO) (2010a). *Guide Specifications for LRFD Seismic Bridge Design*. Washington, D.C., 1st edition.

American Association of State Highway and Transportation Officials (AASHTO) (2010b). *LRFD Bridge Design Specifications*. Washington, D.C., 5th edition.

American Concrete Institute (ACI) Committee 318 (2011). *Building Code Requirements for Structural Concrete (ACI 318-11) and Commentary (ACI 318R-11)*. Farmington Hills, MI.

American Petroleum Institute (API) (2007). *Recommended Practice for Planning, Designing and Constructing Fixed Offshore Platforms–Working Stress Design*. API Recommended Practice 2A-WSD (RP 2A-WSD), 21st edition. Errata and Supplement 3, October 2007.

ARCADIS (2010). *Geostudies for infrastructure, mining & energy*. Trifold Brochure, ARCADIS Chile S.A., Providencia, Santiago, Chile.

Arduino, P., Kramer, S. L., Li, P., and Horne, J. C. (2006). "Stiffness of piles in liquefiable soils." *Seismic Performance and Simulation of Pile Foundations in Liquefied and Laterally Spreading Ground*, R. W. Boulanger and K. Tokimatsu, eds., GSP 145, ASCE. 134–148.

Armstrong, R. J. (2010). *Evaluation of the Performance of Piled Bridge Abutments Affected by Liquefaction-Induced Ground Deformations Through Centrifuge Tests and Numerical Analysis Tools*. Ph.D. Dissertation, University of California at Davis.

Armstrong, R. J., Boulanger, R. W., Galerce, U., Kutter, B. L., and Wilson, D. W. (2008). "Centrifuge modeling of pile pinning effects." *Geotechnical Earthquake Engineering and Soil Dynamics IV*, D. Zeng, M. T. Manzari, and D. R. Hiltunen, eds., GSP 181, ASCE.

Ashford, S. A., Boulanger, R. W., and Brandenberg, S. J. (2011). "Recommended design practice for pile foundations in laterally spreading ground." *PEER Report No. 2011/04*, Pacific Earthquake Engineering Research Center, University of California, Berkeley.

Ashford, S. A. and Juirnarongrit, T. (2006). "Push-over analyses of piles in laterally spreading soil." *Seismic Performance and Simulation of Pile Foundations in Liquefied and Laterally Spreading Ground*, R. W. Boulanger and K. Tokimatsu, eds., GSP 145, ASCE. 109–120.

Ashour, M. and Ardalan, H. (2011). "Piles in fully liquefied soils with lateral spread." *Computers and Geotechnics*, In Press, Corrected Proof.

Ashour, M., Norris, G., and Pilling, P. (1998). "Lateral loading of a pile in layered soil using the strain wedge model." *Journal of Geotechnical and Geoenvironmental Engineering, ASCE*, 124(4), 303–315.

Ashour, M., Norris, G., and Pilling, P. (2002). "Strain wedge model capabiity of analyzing behavior of laterally loaded isolated piles, drilled shafts, and pile groups." *Journal of Bridge Engineering, ASCE*, 7(4), 245–254.

Ates, S. and Constantinou, M. C. (2011). "Example of application of response history analysis for seismically isolated curved bridges on drilled shaft with springs representing soil." *Soil Dynamics and Earthquake Engineering*, 31, 334–350.

Aviram, A., Mackie, K. R., and Stojadinovic, B. (2008a). "Effect of abutment modeling on the seismic response of bridge structures." *Earthquake Engineering and Engineering Vibration*, 7(4), 395–402.

Aviram, A., Mackie, K. R., and Stojadinovic, B. (2008b). "Guidelines for nonlinear analysis of bridge structures." *PEER Report No. 2008/03*, Pacific Earthquake Engineering Research Center, University of California, Berkeley.

Basha, B. M. and Babu, G. L. S. (2009). "Computation of sliding displacements of bridge abutments by pseudo-dynamic method." *Soil Dynamics and Earthquake Engineering*, 29, 103–120.

Baska, D. A. (2002). *An analytical/emirical model for prediction of lateral spreading displacements*. Ph.D. Dissertation, University of Washington.

Bathe, K.-J. (1996). *Finite Element Procedures*. Prentice Hall, Upper Saddle River, New Jersey.

Belytschko, T. and Bachrach, W. E. (1986). "Efficient implementation of quadrilaterals with high coarse-mesh accuracy." *Computer Methods in Applied Mechanics and Engineering*, 54, 279–301.

Belytschko, T. and Bindeman, L. P. (1991). "Assumed strain stabilization of the 4-node quadrilateral with 1-point quadrature for nonlinear problems." *Computer Methods in Applied Mechanics and Engineering*, 88, 311–340.

Belytschko, T. and Bindeman, L. P. (1993). "Assumed strain stabilization of the eight node hexahedral element." *Computer Methods in Applied Mechanics and Engineering*, 105, 225–260.

Belytschko, T., Liu, W. K., and Moran, B. (2000). *Nonlinear Finite Elements for Continua and Structures*. John Wiley & Sons, Ltd., West Sussex, England.

Belytschko, T., Ong, J.-S., Liu, W. K., and Kennedy, J. M. (1984). "Hourglass control in linear and nonlinear problems." *Computer Methods in Applied Mechanics and Engineering*, 43, 251–276.

Berrill, J. and Yasuda, S. (2002). "Liquefaction and piled foundations: Some issues." *Journal of Earthquake Engineering*, 6(Special Issue 1), 1–41.

Berrill, J. B., Christensen, S. A., Keenan, R. P., Okada, W., and Pettinga, J. R. (2001). "Case study of lateral spreading forces on a piled foundation." *Géotechnique*, 51(6), 501–517.

Bhattacharya, S., Bolton, M. D., and Madabhushi, S. P. G. (2005). "A reconsideration of the safety of piled bridge foundations in liquefiable soils." *Soils and Foundations*, 45(4), 13–25.

Bielak, J., Loukakis, K., Hisada, Y., and Yoshimura, C. (2003). "Domain reduction method for three-dimensional earthquake modeling in localized regions, Part I: Theory." *Bulletin of the Seismological Society of America*, 93(2), 817–824.

Biot, M. A. (1941). "General theory of three dimensional consolidation." *Journal of Applied Physics*, 12, 155–164.

Biot, M. A. (1956). "Theory of propagation of elastic waves in a fluid saturated porous solid." *Journal of the Acoustical Society of America*, 28, 168–191.

Biot, M. A. (1962). "Mechanics of deformation and acoustic propagation in porous media." *Journal of Applied Physics*, 33, 1482–1498.

Bishop, A. W. (1955). "The use of the slip circle in the stability analysis of slopes." *Géotechnique*, 5(1), 7–17.

Bochev, P. B., Dohrmann, C. R., and Gunzburger, M. D. (2006). "Stabilization of low-order mixed finite elements for the Stokes equations." *SIAM Journal on Numerical Analysis*, 44(1), 82–101.

Boroschek, R., Soto, P., and León, R. (2010). *Registros del Terremoto del Maule, Mw=8.8, 27 de Febrero de 2010*. RENADIC Report 10/05.

Boulanger, R. W., Chang, D., Gulerce, U., Brandenberg, S. J., and Kutter, B. L. (2006). "Evaluating pile pinning effects on abutments over liquefied ground." *Seismic Performance and Simulation of Pile Foundations in Liquefied and Laterally Spreading Ground*, R. W. Boulanger and K. Tokimatsu, eds., GSP 145, ASCE. 306–318.

Boulanger, R. W., Kutter, B. L., Brandenberg, S. J., Singh, P., and Chang, D. (2003). *Pile Foundations in liquefied and laterally spreading ground during earthquakes: Centrifuge experiments and analyses*. Center for Geotechnical Modeling, University of California at Davis, Davis, CA. Rep. UCD/CGM-03/01.

Bozorgzadeh, A., Ashford, S. A., and Restrepo, J. I. (2008). "Effect of backfill soil type on stiffness and ultimate capacity of bridge abutments." *Geotechnical Earthquake Engineering and Soil Dynamics IV*, D. Zeng, M. T. Manzari, and D. R. Hiltunen, eds., GSP 181, ASCE.

Bradley, B. A., Cubrinovski, M., Dhakal, R. P., and MacRae, G. A. (2009). "Intensity measures for the seismic response of pile foundations." *Soil Dynamics and Earthquake Engineering*, 29, 1046–1058.

Bradley, B. A., Cubrinovski, M., Dhakal, R. P., and MacRae, G. A. (2010). "Probabilistic seismic performance and loss assessment of a bridge-foundation-soil system." *Soil Dynamics and Earthquake Engineering*, 30, 395–411.

Bradley, B. A., Cubrinovski, M., and Haskell, J. J. M. (2011). "Probabilistic pseudo-static analysis of pile foundations in liquefiable soils." *Soil Dynamics and Earthquake Engineering*, 31, 1414–1425.

Brandenberg, S. J., Boulanger, R. W., Kutter, B. L., and Chang, D. (2005). "Behavior of pile foundations in laterally spreading ground during centrifuge tests." *Journal of Geotechnical and Geoenvironmental Engineering, ASCE*, 131(11).

Brandenberg, S. J., Boulanger, R. W., Kutter, B. L., and Chang, D. (2007a). "Liqufaction induced softening of load transfer between pile groups and laterally spreading crusts." *Journal of Geotechnical and Geoenvironmental Engineering, ASCE*, 133(1), 91–103.

Brandenberg, S. J., Boulanger, R. W., Kutter, B. L., and Chang, D. (2007b). "Static pushover analyses of pile groups in liquefied and laterally spreading ground in centrifuge tests." *Journal of Geotechnical and Geoenvironmental Engineering, ASCE*, 133(9), 1055–1066.

Brandenberg, S. J., Zhang, J., Kashighandi, P., Huo, Y., and Zhao, M. (2011). "Demand fragility surfaces for bridges in liquefied and laterally spreading ground." *PEER Report No. 2011/01*, Pacific Earthquake Engineering Research Center, University of California, Berkeley.

Bray, J. D. and Travasarou, T. (2007). "Simplified procedure for estimating earthquake-induced deviatoric slope displacements." *Journal of Geotechnical and Geoenvironmental Engineering, ASCE*, 133(4), 381–392.

Brezzi, F. and Fortin, M. (1991). *Mixed and Hybrid Finite Element Methods*. Springer-Verlag, New York.

Brezzi, F. and Pitäkaranta, J. (1984). "On the stabilization of finite element approximations of the Stokes problem." *Efficient Solutions of Elliptic Systems*, W. Hackbusch, ed., Notes on Numerical Fluid Mechanics, Vieweg, Braunschweig. 11–19.

Brinch Hansen, J. (1961). "The ultimate resistance of rigid piles against transversal forces." *Bulletin No. 12*, Geoteknisk Institute, Copenhagen, 5–9.

Brown, D. A. and Shie, C. F. (1990). "Three-dimensional finite element model of laterally loaded piles." *Computers and Geotechnics*, 10(1), 59–79.

Brown, D. A. and Shie, C. F. (1991). "Some numerical experiments with a three-dimensional finite element model of a laterally loaded pile." *Computers and Geotechnics*, 12, 149–162.

Brown, D. A., Shie, C. F., and Kumar, M. (1989). "*p-y* curves for laterally loaded piles derived from three-dimensional finite element model." *Proceedings of the III International Symposium, Numerical Models in Geomechanics (NUMOG III)*. Elsevier Applied Sciences, 683–690.

California Department of Transportation (Caltrans) (2011). *Guidelines on Foundation Loading and Deformation Due to Liquefaction Induced Lateral Spreading*. Internal Policy Proposal, February 2011.

Cetin, K. O., Seed, R. B., Der Kiureghian, A., Tokimatsu, K., Harder, L. F., Kayen, R. E., and Moss, R. E. S. (2004). "Standard penetration test-based probabilistic and deterministic assessment of seismic soil liquefaction potential." *Journal of Geotechnical and Geoenvironmental Engineering, ASCE*, 130(12), 1314–1340.

Chang, D., Boulanger, R. W., Brandenberg, S. J., and Boulanger, R. W. (2006). "Dynamic analyses of soil-pile-structure interaction in laterally spreading ground during earthquake shaking." *Seismic Performance and Simulation of Pile Foundations in Liquefied and Laterally Spreading Ground*, R. W. Boulanger and K. Tokimatsu, eds., GSP 145, ASCE. 218–229.

Chang, D. W., Lin, B. S., Yeh, C. H., and Cheng, S. H. (2008). "FD solutions for static and dynamic winkler models with lateral spread induced earth pressures on piles." *Geotechnical Earthquake Engineering and Soil Dynamics IV*, D. Zeng, M. T. Manzari, and D. R. Hiltunen, eds., GSP 181, ASCE.

Cheng, Z. and Jeremic, B. (2009). "Numerical modeling and simulation of pile in liquefiable soil." *Soil Dynamics and Earthquake Engineering*, 29(11-12), 1405–1416.

Commend, S., Truty, A., and Zimmermann, T. (2004). "Stabilized finite elements applied to elasto-plasticity: I. Mixed displacement-pressure formulation." *Computer Methods in Applied Mechanics and Engineering*, 193, 3559–3586.

Cowan, M. (2011). *R101 South Brighton – Bridge Status Summary Report.* Opus International Consultants, Wellington, New Zealand.

Cubrinovski, M. and Ishihara, K. (1998a). "Modeling of sand behavior based on state concept." *Soils and Foundations*, 38(3), 115–127.

Cubrinovski, M. and Ishihara, K. (1998b). "State concept and modified elastoplasticity for sand modeling." *Soils and Foundations*, 38(4), 213–225.

Cubrinovski, M. and Ishihara, K. (2004). "Simplified method for analysis of piles undergoing lateral spreading in liquefied soils." *Soils and Foundations*, 44(5), 119–133.

Cubrinovski, M. and Ishihara, K. (2006). "Assessment of pile group response to lateral spreading by single pile analysis." *Seismic Performance and Simulation of Pile Foundations in Liquefied and Laterally Spreading Ground*, R. W. Boulanger and K. Tokimatsu, eds., GSP 145, ASCE. 242–254.

Cubrinovski, M. and Ishihara, K. (2007). "Simplified analysis of piles subjected to lateral spreading: Parameters and uncertainties." *Proceedings of the 4th International Conference on Earthquake Geotechnical Engineering*, Thessaloniki, Greece, June 25-28, Paper No. 1385.

Cubrinovski, M., Kokusho, T., and Ishihara, K. (2006). "Interpretation from large-scale shake table tests on piles undergoing lateral spreading in liquefied soils." *Soil Dynamics and Earthquake Engineering*, 26, 275–286.

Cubrinovski, M., Uzuoka, R., Sugita, H., Tokimatsu, K., Sato, M., Ishihara, K., Tsukamoto, Y., and Kamata, T. (2008). "Prediction of pile response to lateral spreading by 3-D soil-water coupled dynamic analysis: Shaking in the direction of ground flow." *Soil Dynamics and Earthquake Engineering*, 28, 421–435.

Dafalias, Y. F. and Manzari, M. T. (2004). "Simple plasticity sand model accounting for fabric change effects." *Journal of Engineering Mechanics*, 130(6), 622634.

Dash, S. R., Bhattacharya, S., and Blakeborough, A. (2010). "Bending-buckling interaction as a failure mechanism of piles in liquefiable soils." *Soil Dynamics and Earthquake Engineering*, 30, 32–39.

Deibels, S. and Ehlers, W. (1996). "Dynamic analysis of a fully saturated porous medium accounting for geometrical and material non-linearities." *International Journal for Numerical Methods in Engineering*, 39, 81–97.

Desai, C. S. and Appel, G. C. (1976). "3D analysis of laterally loaded structures." *Proceedings of the 2nd International Conference on Numerical Methods in Geomechanics*, Blacksburg, VA.

DFSAP (2006). *Deep Foundation System Analysis Program.* JP Singh & Associates *in association with* M. Ashour and G. Norris, *Prepared for* Washington State Department of Transporation (WSDOT).

Dicleli, M. (2005). "Integral abutment-backfill behavior on sand soil-pushover analysis approach." *Journal of Bridge Engineering, ASCE*, 10(3), 354–364.

Dicleli, M. and Erhan, S. (2005). "Effect of soil and substructure properties on live-load distribution in integral abutment bridges." *Journal of Bridge Engineering, ASCE*, 13(5), 527–539.

Doherty, W. P., Wilson, E. L., and Taylor, R. L. (1969). "Stress analysis of axisymmetric solids utilizing higher order quadrilateral finite elements." *SESM Report No. 69-3*, Dept. of Civil Engineering, University of California, Berkeley.

Duncan, J. M. and Chang, C. Y. (1970). "Nonlinear analysis oof stress and strain in soil." *Journal of the Soil Mechanics and Foundations Division, ASCE*, 96, 1629–1653.

Dungca, J. R., Kuwano, J., Takahashi, A., Saruwatari, T., Izawa, J., Suzuki, H., and Tokimatsu, K. (2006). "Shaking table tests on the lateral response of a pile buried in liquefied sand." *Soil Dynamics and Earthquake Engineering*, 26, 287–295.

Elgamal, A., He, L., Lu, J., Abe, A., Abdoun, T., Dobry, R., Sato, M., Takimatsu, K., and Shantz, T. (2006). "Liquefaction-induced lateral loads on piles." *Proceedings of the 4th International Conference of Earthquake Engineering*, Taipei, Taiwan, October 12-13, Paper No. 42.

Elgamal, A., Yan, L., Yang, Z., and Conte, J. P. (2008). "Three-dimensional seismic response of Humbolt Bay bridge-foundation-ground system." *Journal of Structural Engineering, ASCE*, 134(7), 1165–1176.

Elgamal, A., Yang, Z., Parra, E., and Ragheb, A. (2003). "Modeling of cyclic mobility in saturated cohesionless soils." *International Journal of Plasticity*, 19, 883–905.

Faraji, S., Ting, J. M., Crovo, D. S., and Ernst, H. (2001). "Nonlinear analysis of integral bridges: Finite element model." *Journal of Geotechnical and Geoenvironmental Engineering, ASCE*, 127(5), 454–461.

Faris, A. T., Seed, R. B., Kayen, R. E., and Wu, J. (2006). "A semi-empirical model for the estimation of maximum horizontal displacement due to liquefaction-induced lateral spreading." *Proceedings, 8th U.S. National Conference on Earthquake Engineering*, San Franciso, CA, April 18-22, Paper No. 1323.

Faruque, M. O. and Desai, C. S. (1982). "3D material and geometric nonlinear analysis of piles." *Proceedings of the 2nd International Conference on Numerical Methods in Offshore Piling*, University of Texas at Austin. 553–576.

Federal Highway Administration (FHWA) (1978). *Guidelines for Cone Penetration Test Performance and Design*. J. H. Schmertmann, Report FHWA-TS-78-209, U.S. Department of Transportation, Washington.

Federal Highway Administration (FHWA) (2011). *Post-Earthquake Reconnaissance Report on Transportation Infrastructure: Impact of the February 27, 2010, Offshore Maule Earthquake in Chile*. W.-H. P. Yen, G. Chen, I. Buckle, T. Allen, D. Alzamora, J. Ger, and J. G. Arias, Publication No. FHWA-HRT-11-030, U.S. Department of Transportation, McLean, VA.

Finn, W. D. L. (2005). "A study of piles during earthquakes: Issues of design and analysis." *Bulletin of Earthquake Engineering*, 3(2), 141–234.

Flanagan, D. P. and Belytschko, T. (1981). "A uniform strain hexahedron and quadrilateral with orthogonal hourglass control." *International Journal for Numerical Methods in Engineering*, 17, 679–706.

Franke, K. W. (2011). *A Performance-Based Model for the Computation of Kinematic Pile Response Due to Lateral Spread and its Application on Select Bridges Damaged During the M7.6 Earthquake in the Limon Province, Costa Rica*. Ph.D. Dissertation, Brigham Young University.

Geo-Engineering Extreme Events Reconnaissance (GEER) Association (2010a). *Geo-engineering Reconnaissance of the 2010 Maule, Chile Earthquake*. J. Bray and D. Frost, eds., Report No. GEER-022.

Geo-Engineering Extreme Events Reconnaissance (GEER) Association (2010b). *Geotechnical Reconnaissance of the 2010 Darfield (New Zealand) Earthquake*. R. A. Green and M. Cubrinovski, eds., Report No. GEER-024.

Geo-Engineering Extreme Events Reconnaissance (GEER) Association (2011). *Geotechnical Reconnaissance of the 2011 Christchurch, New Zealand Earthquake*. M. Cubrinovski, R. A. Green, and L. Wotherspoon, eds., Report No. GEER-027.

Gonzalez Lagos, L. L., Abdoun, T., and Dobry, R. (2007). "Centrifuge modeling of permeability and pinning reinforcement effects on pile response to lateral spreading." *Technical Report MCEER-07-0020*, Multidisciplinary Center for Earthquake Engineering Research, University at Buffalo, The State University of New York.

M. Hamada and T. O'Rourke, eds. (1992). *Case Studies of Liquefaction and Lifeline Performance During Past Earthquakes, Volume 1, Japanese Case Studies*. Technical Report NCEER-92-0001, National Center for Earthquake Engineering Research, Buffalo, NY.

Hara, T., Yu, Y., and Ugai, K. (2004). "Behavior of piled bridge abutments on soft ground: A design method proposal based on 2D elasto-plastic-consolidation coupled FEM." *Computers and Geotechnics*, 31, 339–355.

Hashiguchi, K. and Chen, Z.-P. (1998). "Elastoplastic constitutive equation of soils with the subloading surface and the rotational hardening." *International Journal for Numerical and Analytical Methods in Geomechanics*, 22(3), 197–227.

Huang, M., Wu, S., and Zienkiewicz, O. C. (2001). "Incompressible or nearly incompressible soil dynamic behavior – a new staggered algorithm to circumvent restrictions of mixed formulation." *Soil Dynamics and Earthquake Engineering*, 21, 169–179.

Huang, M., Yue, Z. Q., Tham, L. G., and Zienkiewicz, O. C. (2004). "On the stable finite element procedures for dynamic problems of saturated porous media." *International Journal for Numerical Methods in Engineering*, 61, 1421–1450.

Hughes, T. J. R. (1995). "Multiscale phenomena: Green's functions, the Dirichlet to Neumann formulation, subgrid scale models, bubbles and the origin of stabilized methods." *Computer Methods in Applied Mechanics and Engineering*, 127, 387–401.

Hughes, T. J. R., Feijóo, G. R., Mazzei, L., and Quincy, J. B. (1998). "The variational multiscale method – A paradigm for computational mechanics." *Computer Methods in Applied Mechanics and Engineering*, 186, 3–24.

Hughes, T. J. R., Franca, L. P., and Balestra, M. (1986). "A new finite element formulation for computational fluid dynamics: V. Circumventing the Babuška-Brezzi condition: A stable Petrov-Galerkin formulation of the Stokes problem accommodating equal-order interpolations." *Computer Methods in Applied Mechanics and Engineering*, 59, 85–99.

Idriss, I. M. and Boulanger, R. W. (2007). "Residual shear strength of liquefied soils." *Proceedings of the 27th USSD Annual Meeting and Conference, Modernization and Optimization of Existing Dams and Reservoirs.*

Idriss, I. M. and Boulanger, R. W. (2008). *Soil Liquefaction During Earthquakes.* Earthquake Engineering Research Institute (EERI), MNO-12.

Ingeniería Cuatro Ltda. (2006). *Ruta Costera, Proyecto de Modificación de Estribo Sur del Puente Mataquito, Proyecto de Construcción.* Documento No. 286-Mataquito MOD-ES-010, 06 de Octubre.

International Center for Numerical Methods in Engineering (CIMNE) (2008). *GiD The Personal Pre and Post Processor.* `http://gid.cimne.upc.es/`.

Jacquotte, O.-P. and Oden, J. T. (1984). "Analysis of hourglass instabilities and control in underintegrated finite element methods." *Computer Methods in Applied Mechanics and Engineering*, 44, 339–363.

Janbu, N. (1973). "Slope stability computations." *Embankment Dam Engineering – Casagrande Volume*, R. C. Hirschfeld and S. J. Poulos, eds., John Wiley & Sons, New York. 47–86.

Jeremic, B., Guanzhou, J., Preisig, M., and Tafazzoli, N. (2009). "Time domain simulation of soil-foundation-structure interaction in non-uniform soils." *Earthquake Engineering and Structural Dynamics*, 38(5), 699–718.

Joyner, W. B. and Chen, A. T. F. (1975). "Calculation of nonlinear ground response in earthquakes." *Bulletin of the Seismological Society of America*, 65(5), 1315–1336.

Katayama, S., Fujii, T., and Takahashi, Y. (1966). "Damage caused by the Niigata Earthquake and the geological features of national highway in the suburbs of Niigata City." *Soil and Foundation*, VI(1), 54–70.

Kent, D. C. and Park, R. (1971). "Flexural members with confined concrete." *Journal of the Structural Mechanics Division, ASCE*, 97(ST7), 1969–1990.

Khalili-Tehrani, P., Ahlberg, E., Rha, C., Lemnitzer, A., Salamanca, A., Nigbor, R., Stewart, J. P., Wallace, J., and Taciroglu, E. (2007). "Field-testing and modeling of soil-structure interaction for highway support structures." *Proceedings of the 2007 Structures Congress*, R. Lyons, J. W. Wallace, and E. Stovner, eds., Long Beach, CA. ASCE.

Knappett, J. A. and Madabhushi, S. P. G. (2006). "Modelling of liquefaction-induced instability in pile groups." *Seismic Performance and Simulation of Pile Foundations in Liquefied and Laterally Spreading Ground*, R. W. Boulanger and K. Tokimatsu, eds., GSP 145, ASCE. 255–267.

Knappett, J. A., Mohammadi, S., and Griffin, C. (2010). "Lateral spreading forces on bridge piers and pile caps in laterally spreading soil: Effect of angle of incidence." *Journal of Geotechnical and Geoenvironmental Engineering, ASCE*, 136(12), 1589–1599.

Kondoh, M. and Tamura, K. (2003). "Experimental study on liquefaction-induced earth pressure on bridge abutment." *Proceedings of the 19th U.S.-Japan Bridge Engineering Workshop*, Tsukuba, Japan, October 27-30.

Kotsoglou, A. N. and Pantazopoulou, S. J. (2009). "Assessment and modeling of embankment participation in the seismic response of integral abutment bridges." *Bulletin of Earthquake Engineering*, 7(2), 343–361.

Kraft, L. M., Ray, R. P., and Kagawa, T. (1981). "Theoretical t-z curves." *Journal of the Geotechnical Engineering Division, ASCE*, 107(11), 1543–1561.

Kramer, S. L. (2008). *Evaluation of Liquefaction Hazards in Washington State*. Washington State Department of Transportation (WSDOT), WA-RD 668.1.

Kramer, S. L. and Mayfield, R. T. (2007). "Return period of soil liquefaction." *Journal of Geotechnical and Geoenvironmental Engineering, ASCE*, 133(7), 802–813.

Kulhawy, F. H. (1991). "Drilled shaft foundations." *Foundation Engineering Handbook, 2nd Ed.*, H.-Y. Fang, ed., New York. Van Nostrand Reinhold.

Land Information New Zealand (LINZ) (2011). *Christchurch Post-Earthquake Aerial Photos (24 February 2011).* 10cm colour orthophotography of the area affected by the 22 February 2011 Christchurch earthquake. `http://http://koordinates.com/layer/3185-christchurch-post-earthquake-aerial-photos-24-feb-2011/#`. Accessed 17 February 2012.

Ledezma, C. (2012). "Case study of three pile-supported bridges affected by liquefaction-induced lateral spreading after the M8.8 2010 Maule Chile earthquake." *Second International Conference on Performance-Based Design in Earthquake Geotechnical Engineering*, Taormina, Italy, May 28-30, Paper No. 6.13.

Ledezma, C. and Bray, J. D. (2008). "Factors that affect the performance of bridge foundations undergoing liquefaction-induced lateral spreading." *Geotechnical Earthquake Engineering and Soil Dynamics IV*, D. Zeng, M. T. Manzari, and D. R. Hiltunen, eds., GSP 181, ASCE.

Ledezma, C. and Bray, J. D. (2010). "Probabilistic performance-based procedure to evaluate pile foundations at sites with liquefaction-induced lateral displacement." *Journal of Geotechnical and Geoenvironmental Engineering, ASCE*, 136(3), 464–476.

Lemitzer, A., Ahlberg, E. R., Nigbor, R. L., Wallace, A. S. J. W., and Stewart, J. P. (2009). "Lateral performance of full-scale bridge abutment wall with granular backfill." *Journal of Geotechnical and Geoenvironmental Engineering*, 135(4), 506–514.

Lemitzer, A., Khalili-Tehrani, P., Ahlberg, E. R., Rha, C., Taciroglu, E., Wallace, J. W., and Stewart, J. P. (2010). "Nonlinear efficiency of bored pile group under lateral loading." *Journal of Geotechnical and Geoenvironmental Engineering*, 136(12), 1673–1685.

LPILE (2010). *A Program for the Analysis & Design of Piles and Drilled Shafts Under Lateral Loads.* `http://www.ensoftinc.com`. Ensoft, Inc. Engineering Software, Austin, Texas.

Lysmer, J. and Kuhlemeyer, A. M. (1969). "Finite dynamic model for infinite media." *Journal of the Engineering Mechanics Division, ASCE*, 95, 859–877.

MacNeal, R. H. and Harder, R. L. (1985). "A proposed standard set of problems to test finite element accuracy." *Finite Elements in Analysis and Design*, 1(1), 3–20.

Malkus, D. S. and Hughes, T. J. R. (1978). "Mixed finite element methods - Reduced and selective integration techniques: A unification of concepts." *Computer Methods in Applied Mechanics and Engineering*, 15, 63–81.

Manzari, M. T. and Dafalias, Y. F. (1997). "A critical state two-surface plasticity model for sands." *Géotechnique*, 47(2), 255–272.

Martin, G. R. (2004). "The seismic design of bridges - Geotechnical and foundation design issues." *Geotechnical Engineering for Transportation Projects*, M. K. Yegian and E. Kavazanjian, eds., GSP 126, ASCE. 137–166.

Martin, G. R., March, M. L., Anderson, D. G., Mayes, R. L., and Power, M. S. (2002). "Recommended design approach for liquefaction induced lateral spreads." *Proc., 3rd Natl. Seismic Conf. and Workshop on Bridges and Highways*, MCEER-02-SP04, Buffalo, NY.

Matlock, H. (1970). "Correlations for design of laterally loaded piles in soft clay." *Proceedings of the 2nd Offshore Technology Conference*, Houston, TX. (OTC 1204), 577–594.

McGann, C. R. (2009). "Analysis and evaluation of single piles in laterally spreading soil. Master's thesis, University of Washington.

McGann, C. R., Arduino, P., and Mackenzie-Helnwein, P. (2010). "Lateral resistance reduction for static analysis of lateral spreading." *Joint Conference Proceedings, 7th International Conference on Urban Earthquake Engineering (7CUEE) & 5th International Conference on Earthquake Engineering (5ICEE)*, Tokyo Institute of Technology, Tokyo, Japan. 593–600.

McGann, C. R., Arduino, P., and Mackenzie-Helnwein, P. (2011). "Applicability of conventional p-y relations to the analysis of piles in laterally spreading soil." *Journal of Geotechnical and Geoenvironmental Engineering, ASCE*, 137(6), 557–567.

McGann, C. R., Arduino, P., and Mackenzie-Helnwein, P. (2012). "Development of simplified analysis procedure for piles in laterally spreading layered soils." *PEER Report No. 2012/05*, Pacific Earthquake Engineering Research Center, University of California, Berkeley.

Meera, R. S., Shanker, K., and Basudhar, P. K. (2007). "Flexural response of piles under liquefied soil conditions." *Geotechnical and Geological Engineering*, 25(4), 409–422.

Meyerhof, G. G. (1956). "Penetration tests and bearing capacity of cohesionless soils." *Journal of the Soil Mechanics and Foundations Division, ASCE*, 82(SM1), 1–19.

Meyerhof, G. G. (1976). "Bearing capacity and settlement of pile foundations." *Journal of the Soil Mechanics and Foundations Division, ASCE*, 102, 197–228.

Mid-America Earthquake (MAE) Center (2010). *The Maule (Chile) Earthquake of February 27, 2010 Consequence Assessment and Case Studies.* A. S. Elnashai, B. Gencturk, O.-S. Kwon, I. L. Al-Qadi, Y. Hashash, J. R. Roesler, S.-J. Kim, S.-H. Jeong, J. Dukes, and A. Valdivia, Report No. 10-04.

Ministerio de Obras Públicas (MOP) (2002). *Manual de Carreteras, Vol. 3, Instrucciones y Criterios de Diseńo.* Santiago, Chile.

Miwa, S., Ikeda, T., and Sato, T. (2006). "Damage process of pile foundation in liquefied ground during strong motion." *Soil Dynamics and Earthquake Engineering*, 26, 325–336.

Mokwa, R. L. and Duncan, J. M. (2000). *Investigation of the Resistance of Pile Caps and Intregral Abutments to Lateral Loading.* Publication No. FHWA/VTRC 00-CR4, Virginia Transportation Research Council, Charlottesville, VA.

Mokwa, R. L. and Duncan, J. M. (2001). "Laterally loaded pile groups and *p-y* multipliers." *Foundations and Ground Improvement: Proceedings of a specialty conference: June 9-13, Blacksburg, VA*, T. L. Brandon, ed., Geotechnical Special Publication No. 113. ASCE, 728–742.

Mokwa, R. L. and Duncan, J. M. (2003). "Rotational restraint of pile caps during lateral loading." *Journal of Geotechnical and Geoenvironmental Engineering, ASCE*, 129(9), 829–837.

Mosher, R. L. (1984). *Load transfer criteria for numerical analysis of axial loaded piles in sand*. Army Engineer Waterways Experiment Station, Vickburg, MS.

Moss, R. E. S., Seed, R. B., Kayen, R. E., Stewart, J. P., Der Kiureghian, A., and Cetin, K. O. (2006). "CPT-based probabilistic and deterministic assessment of in situ seismic soil liquefaction potential." *Journal of Geotechnical and Geoenvironmental Engineering, ASCE*, 132(8), 1032–1051.

Muqtadir, A. and Desai, C. S. (1986). "Three-dimensional analysis of a pile-group foundation." *International Journal for Numerical and Analytical Methods in Geomechanics*, 10, 41–58.

National Cooperative Highway Research Program (NCHRP) (2002). *Comprehensive Specification for the Seismic Design of Bridges*. NCHRP Report 472, National Academy Press, Washington, D.C.

Naylor, D. J. (1974). "Stresses in nearly incompressible materials by finite elements with application to the calculation of excess pore pressures." *International Journal for Numerical Methods in Engineering*, 8, 443–460.

Newmark, N. M. (1959). "A method of computation for structural dynamics." *Journal of the Engineering Mechanics Division, ASCE*, 85(EM3), 67–94.

Olson, S. M. and Stark, T. D. (2002). "Liquefied strength ratio from liquefaction flow failure case histories." *Canadian Geotechnical Journal*, 39, 629–647.

Ooi, P. S. K., Lin, X., and Hamada, H. S. (2010). "Numerical study of an integral abutment bridge supported on drilled shafts." *Journal of Bridge Engineering, ASCE*, 15(1), 19–31.

OpenSees (2007). *Open System for Earthquake Engineering Simulation*. `http://opensees.berkeley.edu`. Pacific Earthquake Engineering Research Center (PEER), University of California, Berkeley.

Park, R. and Paulay, T. (1975). *Reinforced Concrete Structures*. Wiley & Sons, New York.

Peck, R. B., Hanson, W. E., and Thornburn, T. H. (1974). *Foundation Engineering*. John Wiley & Sons, New York. 2nd Edition.

PEER (2010). *PEER Ground Motion Database for Shallow Crustal Earthquakes in Active Tectonic Regimes*. `http://peer.berkeley.edu/peer_ground_motion_database`. Pacific Earthquake Engineering Research Center, University of California, Berkeley.

Pender, M. J. and Robertson, T. W. (1987). "Edgecumbe earthquake: Reconnaissance report." *Bulletin of the New Zealand National Society for Earthquake Engineering*, 20(3), 201–249.

Petek, K. A. (2006). *Development and Application of Mixed Beam-Solid Models for Analysis of Soil-Pile Interaction Problems*. Ph.D. Dissertation, University of Washington.

Petrus Consultores Geotecnicos (2006). *Informe Complementario de Mecánica de Suelos, Puente Mataquito (Ruta Costera), Camino Quivolgo-Iloca (Cruce J-60)*. Informe No. 2619-ING-SGC-150/2006 (Rev 1).

Prevost, J. H. (1977). "Mathematical modeling of monotonic and cyclic undrained clay behavior." *International Journal for Numerical and Analytical Methods in Geomechanics*, 1, 195–216.

Prevost, J. H. (1982). "Nonlinear transient phenomena in saturated porous media." *Computer Methods in Applied Mechanics and Engineering*, 30, 3–8.

Prevost, J. H. (1985a). "A simple plasticity theory for frictional cohesionless soils." *Soil Dynamics and Earthquake Engineering*, 4, 9–17.

Prevost, J. H. (1985b). "Wave propagation in fluid-saturated porous media: An efficient finite element procedure." *Soil Dynamics and Earthquake Engineering*, 4, 183–202.

Priestley, M. J. N., Singh, J. P., Youd, T. L., and Rollins, K. M. (1991). "Costa Rica Earthquake Reconnaissance Report: Bridges (EERI)." *Earthquake Spectra*, 7(S2), 59–91.

Reese, L. C., Cox, W. R., and Koop, F. D. (1974). "Analysis of laterally loaded piles in sand." *Proceedings of the 6th Offshore Technology Conference*, Vol. 2, Houston, TX. 473–483.

Reese, L. C., Isenhower, W. M., and Wang, S.-T. (2006). *Analysis and Design of Shallow and Deep Foundations*. John Wiley & Sons, Inc., Hoboken, New Jersey.

Reese, L. C. and Van Impe, W. F. (2001). *Single Piles and Pile Groups Under Lateral Loading*. A.A. Balkema, Rotterdam, Netherlands.

Reese, L. C. and Welch, R. C. (1975). "Lateral loading of deep foundations in stiff clay." *Journal of the Geotechnical Engineering Division, ASCE*, 101(GT7), 633–649.

Reese, S. (2003). "On a consistent hourglass stabilization technique to treat large inelastic deformations and thermo-mechanical coupling in plane strain problems." *International Journal for Numerical Methods in Engineering*, 57, 1095–1127.

Reese, S. (2005). "On a physically stabilized one point finite element formulation for three-dimensional finite elasto-plasticity." *Computer Methods in Applied Mechanics and Engineering*, 194, 4685–4715.

Rocscience (2010). *Slide 6.0 Slope Stability and Groundwater Software*. `http://www.rocscience.com`. Rocscience, Inc., Toronto, Ontario.

Rollins, K. M., Gerber, T. M., Lane, J. D., and Ashford, S. A. (2005). "Lateral resistance of a full-scale pile group in liquefied sand." *Journal of Geotechnical and Geoenvironmental Engineering, ASCE*, 131(1), 115–125.

Romstad, K., Kutter, B., Maroney, B., Vanderbilt, E., Griggs, M., and Chai, Y. H. (1995). "Experimental measurements of bridge abutment behavior." *Report No. UCD-STR-95-1*, Dept. of Civil and Environmental Engineering, University of California, Davis, CA.

Seed, H. B. and Reese, L. C. (1957). "The action of soft clay along friction piles." *Transactions, ASCE*, 122, 731–754.

Seed, R. B. and Harder, L. F. (1990). "Spt-based analysis of cyclic pore pressure generation and undrained residual strength." *Proceedings of the H. Bolton Seed Memorial Symposium, Vol. 2*, Vancouver, BC, Canada. BiTech Pub, Ltd., 351–376.

Sextos, A. G. and Taskari, O. (2008). "Comparative assessment of advanced computational tools for embankment-abutment-bridge superstructure interaction." *Proceedings of the 14th World Conference on Earthquake Engineering*, Beijing, China, October 12-17.

Shamsabadi, A., Ashour, M., and Norris, G. (2005). "Bridge abutment nonlinear force-displacement-capacity prediction for seismic design." *Journal of Geotechnical and Geoenvironmental Engineering*, 131(2), 151–161.

Shamsabadi, A., Khalili-Tehrani, P., Stewart, J. P., and Taciroglu, E. (2010). "Validated simulation models for lateral response of bridge abutments with typical backfills." *Journal of Bridge Engineering, ASCE*, 15(3), 302–311.

Shamsabadi, A., Rollins, K. M., and Kapuskar, M. (2007). "Nonlinear soil-abutment-bridge structure interaction for seismic performance-based design." *Journal of Geotechnical and Geoenvironmental Engineering, ASCE*, 133(6), 707–720.

Shin, H. (2007). *Numerical Modeling of a Bridge System & Its Application for Performance-Based Earthquake Engineering*. Ph.D. Dissertation, University of Washington.

Shin, H., Arduino, P., Kramer, S. L., and Mackie, K. (2008). "Seismic response of a typical highway bridge in liquefiable soil." *Geotechnical Earthquake Engineering and Soil Dynamics IV*, D. Zeng, M. T. Manzari, and D. R. Hiltunen, eds., GSP 181, ASCE.

Silva, P. F. and Manzari, M. T. (2008). "Soil-structure interaction analysis of bridge columns supported on CISS piles." *Geotechnical Earthquake Engineering and Soil Dynamics IV*, D. Zeng, M. T. Manzari, and D. R. Hiltunen, eds., GSP 181, ASCE.

Simo, J. C. and Armero, F. (1992). "Geometrically nonlinear enhanced strain mixed methods and the method of incompatible modes." *International Journal for Numerical Methods in Engineering*, 33, 1413–1449.

Simo, J. C., Armero, F., and Taylor, R. L. (1993). "Improved versions of assumed enhanced strain tri-linear elements for 3d finite deformation problems." *Computer Methods in Applied Mechanics and Engineering*, 110, 359–386.

Stewart, J. P., Taciroglu, E., Wallace, J. W., Ahlberg, E. R., Lemnitzer, A., Rha, C., and Khalili-Tehrani, P. (2007). "Full scale cyclic large deflection testing of foundation support systems for

highway bridges. Part I: Drilled shaft foundations." *UCLA - SGEL Report 2007/01*, Department of Civil and Environmental Engineering, University of California, Los Angeles.

Suzuki, H., Tokimatsu, K., Sato, M., and Abe, A. (2006). "Factor affecting horizontal subgrade reaction of piles during soil liquefaction and lateral spreading." *Seismic Performance and Simulation of Pile Foundations in Liquefied and Laterally Spreading Ground*, R. W. Boulanger and K. Tokimatsu, eds., GSP 145, ASCE. 1–10.

Takahashi, A., Sugita, H., and Tanimoto, S. (2006a). "Beam on Winkler foundation methods for piles in laterally spreading soils." *Seismic Performance and Simulation of Pile Foundations in Liquefied and Laterally Spreading Ground*, R. W. Boulanger and K. Tokimatsu, eds., GSP 145, ASCE. 230–241.

Takahashi, A., Sugita, H., and Tanimoto, S. (2006b). "Permanent deformation of bridge abutment on liquefiable soils." *Technical Memorandum of Public Works Research Institute*, 4009, 411–424.

Takahashi, A., Sugita, H., and Tanimoto, S. (2010). "Forces acting on bridge abutments over liquefied ground." *Soil Dynamics and Earthquake Engineering*, 30, 146–156.

Timoshenko, S. and Goodier, J. N. (1951). *Theory of Elasticity.* McGraw-Hill Book Company, Inc., New York, second edition.

Tobita, T., Iai, S., Sugaya, M., and Kaneko, H. (2006). "Analysis of group pile behavior under lateral spreading." *Seismic Performance and Simulation of Pile Foundations in Liquefied and Laterally Spreading Ground*, R. W. Boulanger and K. Tokimatsu, eds., GSP 145, ASCE. 294–305.

Tokimatsu, K., Suzuki, H., and Sato, M. (2005). "Effects of inertial and kinematic interaction on seismic behavior of pile with embedded foundation." *Soil Dynamics and Earthquake Engineering*, 25, 753–762.

Truty, A. (2001). "A galerkin/least-squares finite element formulation for consolidation." *International Journal for Numerical Methods in Engineering*, 52, 763–786.

Truty, A. and Zimmermann, T. (2006). "Stabilized mixed finite element formulations for materially nonlinear partially saturated two-phase media." *Computer Methods in Applied Mechanics and Engineering*, 195, 1517–1546.

Uzuoka, R., Cubrinovski, M., Sugita, H., Sato, M., Tokimatsu, K., Sento, N., Kazama, M., Zhang, F., Yashima, A., and Oka, F. (2008). "Prediction of pile response to lateral spreading by 3-D soil-water coupled dynamic analysis: Shaking in the direction perpendicular to ground flow." *Soil Dynamics and Earthquake Engineering*, 28, 436–452.

Valsamis, A., Bouckovalas, G., and Chaloulos, Y. (2011). "Simplified design of single piles under liquefaction induced lateral spreading." *Proceedings of the 5th International Conference on Earthquake Geotechnical Engineering*, Santiago, Chile, January 10-13, Paper No. SDOVA.

Vijayvergiya, V. N. (1977). "Load movement characteristics of piles." *Proceedings of the Ports '77 Conference, ASCE, Vol II.* 269–284.

Wallace, J. W., Fox, P. J., Stewart, J. P., Janoyan, K., Qiu, T., and Lermitte, S. (2001). "Cyclic large deflection testing of shaft bridges Part I: Background and field test results." *Report to California Department of Transportation.*

Wan, J. (2002). *Stabilized Finite Element Methods for Coupled Geomechanics and Multiphase Flow.* Ph.D. Dissertation, Stanford University.

Wang, C.-H. (2003). *Prediction of the Residual Strength of Liquefied Soils.* Ph.D. Dissertation, University of Washington.

Washington State Department of Transportation (WSDOT) (2011a). *Bridge Design Manual (LRFD).* Technical Manual M 23-50.05, May 2011.

Washington State Department of Transportation (WSDOT) (2011b). *Geotechnical Design Manual (LRFD).* Technical Manual M 46-03.04, April 2011.

White, J. A. and Borja, R. I. (2008). "Stabilized low-order finite elements for coupled solid-deformation/fluid-diffusion and their application to fault zone transients." *Computer Methods in Applied Mechanics and Engineering*, 197, 4353–4366.

Wissmann, J. W., Becker, T., and Möller, H. (1987). "Stabilization of the zero-energy modes of under-integrated isoparametric finite elements." *Computational Mechanics*, 2, 289–306.

Wotherspoon, L., Bradshaw, A., Green, R., Wood, C., Palermo, A., Cubrinovski, M., and Bradley, B. (2011). "Performance of bridges during the 2010 Darfield and 2011 Christchurch earthquakes." *Seismological Research Letters*, 82(6), 950–964.

Wriggers, P. (2008). *Nonlinear Finite Element Methods.* Springer-Verlag, Berlin.

Xia, K. and Masud, A. (2009). "A stabilized finite element formulation for finite deformation elastoplasticity in geomechanics." *Computers and Geotechnics*, 36, 396–405.

Yang, Z. and Jeremic, B. (2002). "Numerical analysis of pile behavior under lateral loads in layered elastic-plastic soils." *International Journal for Numerical and Analytical Methods in Geomechanics*, 26(14), 1385–1406.

Yang, Z. and Jeremic, B. (2003). "Numerical study of the effective stiffness of pile groups." *International Journal for Numerical and Analytical Methods in Geomechanics*, 27(15), 1255–1276.

Yang, Z. and Jeremic, B. (2005). "Study of soil layering effects on lateral loading behavior of piles." *Journal of Geotechnical and Geoenvironmental Engineering, ASCE*, 131(6), 762–770.

Yoshimura, C., Bielak, J., Hisada, Y., and Fernández, A. (2003). "Domain reduction method for three-dimensional earthquake modeling in localized regions, Part II: Verification and applications." *Bulletin of the Seismological Society of America*, 93(2), 825–840.

Youd, T. L. (1993). "Liquefaction-induced damage to bridges." *Transportation Research Record No. 1411*, 35–41.

Youd, T. L., Hansen, C. M., and Bartlett, S. F. (2002). "Revised multilinear regression equations for prediction of lateral spread displacement." *Journal of Geotechnical and Geoenvironmental Engineering, ASCE*, 128(12), 1007–1017.

Youd, T. L., Idriss, I. M., Andrus, R. D., Arango, I., Castro, G., Christian, J. T., Dobry, R., Finn, W. D., Harder, L., Haynes, M. E., Ishihara, K., Koester, J. P., Liao, S. S. C., Marcuson, W. F., Martin, G. R., Mitchell, J. K., Moriwaki, Y., Power, M. S., Robertson, P. K., Seed, R. B., and Stokoe, K. H. (2001). "Liquefaction resistance of soils: Summary report from the 1996 NCEER and 1998 NCEER/NSF workshops on evaluation of liquefaction resistance of soils." *Journal of Geotechnical and Geoenvironmental Engineering, ASCE*, 127(10), 817–833.

Yuan, K. Y., Huang, Y. S., Yang, H. T., and Pian, T. H. H. (1994). "The inverse mapping and distortion measures for 8-node hexahedral isoparametric elements." *Computational Mechanics*, 14(6), 189–199.

Zha, J. (2004). "Lateral spreading forces on bridge abutment walls/piles." *Geotechnical Engineering for Transportation Projects*, M. K. Yegian and E. Kavazanjian, eds., GSP 126, ASCE. 1711–1720.

Zha, J. (2006). "Lateral spreading forces on bridge piles." *Seismic Performance and Simulation of Pile Foundations in Liquefied and Laterally Spreading Ground*, R. W. Boulanger and K. Tokimatsu, eds., GSP 145, ASCE. 71–82.

Zhang, G., Robertson, P. K., and Brachman, R. W. I. (2004). "Estimating liquefaction-induced lateral displacements using the standard penetration test or cone penetration test." *Journal of Geotechnical and Geoenvironmental Engineering, ASCE*, 130(8), 861–871.

Zienkiewicz, O. C. (1981). "Basic formulation of static and dynamic behavior of soil and other porous media." *Numerical Methods in Geomechanics*, J. B. Martins, ed., Dordrecht, Holland. D. Reidel Publishing Company.

Zienkiewicz, O. C., Huang, M., and Pastor, M. (1994). "Computational soil dynamics – a new algorithm for drained and undrained conditions." *Computer Methods and Advances in Geomechanics*, H. J. Siriwardane and M. M. Zaman, eds., Rotterdam. A.A. Balkema, 47–59.

Zienkiewicz, O. C. and Shiomi, T. (1984). "Dynamic behavior of saturated porous media; the generalized Biot formulation and its numerical solution." *International Journal for Numerical Methods in Geomechanics*, 8, 71–96.

Zienkiewicz, O. C., Taylor, R. L., and Too, J. M. (1971). "Reduced integration technique in general analysis of plates and shells." *International Journal for Numerical Methods in Engineering*, 3, 275–290.

Zienkiewicz, O. C., Taylor, R. L., and Zhu, J. Z. (2005). *The Finite Element Method - Its Basis and Fundamentals (6th Edition)*. Elsevier Butterworth-Heinemann, Oxford.